TECHNISCHE
UNIVERSITÄT
WIEN
Vienna University of Technology

DISSERTATION

Relevance of the irreversible degradation of superconducting Nb_3Sn wires and cables caused by transverse stress at room temperature within the FCC study at CERN

Ausgeführt zum Zwecke der Erlangung des akademischen Grades eines Doktors der technischen Wissenschaften unter der Leitung von

Priv.Doz. Dipl.-Ing. Dr.tech. Michael Eisterer
E141
Atominstitut

eingereicht an der Technischen Universität Wien
Fakultät für Physik

von

Dipl.-Ing. Patrick Ebermann
Matrikelnummer 0825085
Hofuren 49
4574 Nennigkofen, Schweiz

Wien, 17. Mai 2020

Acknowledgment

I am very thankful to Michael Eisterer, my university supervisor at the Vienna University of Technology, Atominstitut, as well as Friedrich Lackner, my supervisor at CERN. I am also grateful to Michael Benedikt, head of the Austrian CERN PhD programme.

In addition, a thank you to my colleagues at the CryoLab (CERN), especially to Torsten Köttig, who continuously supported me during the design, build-up and improvement of the cryostat insert for the wire measurements. I also thank Jérôme Fleiter and his colleagues from the FRESCA cable test station (CERN) for the collaboration regarding the cable measurements.

Also a warm thanks to Carmine Senatore, University of Geneva, and Lucio Rossi, University of Milan respectively CERN, for serving as examiners and for their comments, which led to the presented revised version.

Finally, I would like to thank my student and post-doctoral colleagues at CERN and the Atominstitut for the countless technical and scientific discussions as well as the collaboration in various projects.

My special gratitude goes to my life partner Doris for her loving support and patience.

Kurzfassung

Die **Future Circular Collider (FCC)** Studie ist eine Forschungsstudie, die die Realisierbarkeit und das Konzept eines zukünftigen Teilchenbeschleunigers als Nachfolger des Large Hadron Colliders (LHC) erarbeitet. Die Studie untersucht den Bau eines ringförmigen Beschleunigers mit einem Umfang von 80 km bis 100 km und soll für Anwendungen über den Kapazitäten des High Luminositiy LHC (HL-LHC), voraussichtlich nach 2035, dienen. Als endgültige Betriebsart ist ein Protonenbeschleuniger (FCC-hh) mit einer Kollisionsenergie von bis zu 100 TeV und einer Luminosität von $5 \cdot 10^{38}\,\mathrm{m}^{-2}\,\mathrm{s}^{-1}$ bis $30 \cdot 10^{38}\,\mathrm{m}^{-2}\,\mathrm{s}^{-1}$ vorgesehen.

Ein Teil der Sudie ist die Forschung und Entwicklung von **supraleitenden Ablenkmagneten** mit einem nominalen Feld von 16 T bis 20 T bei einer Betriebstemperatur zwischen 4.3 K und 1.9 K. **Nb_3Sn-Multifilamentdrähte** wurden als Grundlage für den Leiter ausgewählt. Um den Bau und Betrieb solcher Beschleunigermagnete zu erforschen und zu entwickeln, wurde ein 16 T Dipol-Programm gestartet. Neben vielen anderen Aspekten wird die Fertigung dieser Beschleunigermagneten untersucht. Das geplante supraleitende Material Nb_3Sn ist sehr spröde und seine Eigenschaften sind druckabhängig. Aus diesem Grund ist eine Charakterisierung des mechanischen Verhaltens sowie der Degradation der supraleitenden Eigenschaften auf Grund der mechanischen Belastungen für die Fertigung der Spulen sowie den Bau der Magnete entscheidend.

Die supraleitenden Spulen werden aus unreagierten Nb_3Sn Rutherford-Kabeln gewickelt und anschließend einer Wärmebehandlung mit Temperaturen von bis zu 650 °C unterzogen, wodurch sich die supraleitende A-15 Phase Nb_3Sn bildet („wind and react"-Technik). Anschließend werden die Spulen inklusive Instrumentierung und Quench-Heizern mittels Vakuum-Druck-Verfahren mit Epoxidharz imprägniert, wobei die Rutherford-Kabel zuvor mit einer Fieberglas-Isolation umwickelt worden sind. Jegliche Bewegungen des Leiters können zu einer Störung des Betriebes oder im ungünstigsten Fall zur Zerstörung des Magneten führen. Aus diesem Grund werden die imprägnierten Spulen dauerhaft vorgespannt. So können die stromführenden Leiter der enormen Lorentzkraft während des Betriebes standhalten. Die Vorspannvorrichtung supraleitender Magnete, realisiert durch beispielsweise Collars oder Bladder-and-Key Systeme, spannen die Spulen beim Zusammensetzen des Magneten mit 70 MPa bis 150 MPa vor, woraus eine beabsichtigte bleibende Vorspannung von 50 MPa bis 120 MPa resultiert. Abhängig von den Fertigungsgenauigkeiten kann es entlang der Spule während des Vorspannungsprozesses zu lokalen Stressspitzen kommen, die den Supraleiter beschädigen und somit eine unbeabsichtigte irreversible Degradation hervorrufen können.

Ziel dieser Arbeit ist die Analyse der irreversiblen Degradation des Supraleiters, verursacht durch transversalen Stress bei Raumtemperatur, der repräsentativ für die mechanischen Belastungen während der Fertigung, im Speziellen des Vorspannungsprozesses, steht. Ein Experiment an Kabeln wurde ausgearbeitet, um so den Degradationsvorgang nahe der realen Situation während des Vorspannungsprozesses nachzubilden. Zusätzlich wurde ein Experiment mit Drähten durchgeführt, um den Mechanismus und die Ursache des Degradationsprozesses im Detail zu analysieren. Dazu wurde die Arbeit in folgende **Teilbereiche** aufgeteilt:

- Eine existierende **hydraulische Presse** wurde modernisiert, um einen homogenen Druck auf Kabel- und Drahtproben auszuüben. Hydraulische Steuerkomponenten sowie Instrumentierungen wurden erneuert, um einen genauen und zuverlässigen Betrieb zu gewährleisten. Um die Homogenität der Druckverteilung auf die Proben zu optimieren, wurden druckempfindliche Folien in Kombination mit einer selbstentwickelten Evaluierungssoftware genutzt. Die hydraulische Presse wurde für die beiden in der Folge beschriebenen Experimente verwendet.

- **Imprägnierte Rutherford-Kabel** wurden mit transversalem Druck bei Raumtemperatur belastet und anschließend wurde ihr kritischer Strom in der FRESCA Kabelteststation des CERN bei Tieftemperatur gemessen. Dieser Vorgang wurde iterativ mit steigendem Drucklevel wiederholt. Die FRESCA Kabelteststation verfügt über eine Stromquelle mit bis zu 32 kA und einen Dipolmagneten mit einem nominalen Feld von 9.6 T. Die Probe kann mittels Kühlung mit flüssigem oder supraflüssigem Helium bei einer Temperatur von 4.3 K oder 1.9 K gemessen werden.

- Um den Degradationseffekt genauer zu untersuchen sowie auch das Spektrum an Messmethoden zu erweitern, wurden ebenso die Auswirkungen des transversalen Stresses auf **einzelne Drähte** bei Raumtemperatur untersucht. Dazu wurden Drähte mittels der oben erwähnten hydraulischen Presse mit Druck belastet. Nach jedem Drucklevel wurde eine Transportstrommessung von bis zu 150 A im Selbstfeld mittels eines **selbstentwickelten Kryostatenaufbaus** durchgeführt. Der supraleitende Draht wurde konduktiv, mittels flüssigen Heliums eines Phasenseparators und Wärmetauschern, gekühlt. Anstatt eines außen angelegten Magnetfeldes wurde die Probentemperatur

bis nahe der kritischen Temperatur erhöht, um so den kritischen Strom in einen realisierbaren Bereich zu schieben. Dieses unübliche Konzept wurde zum einem gewählt um mechanisches Beanspruchen, d.h. Lorentz Kräfte, während den Tieftemperaturmessungen zu vermeiden. Zum anderen wurde eine **alternative kosteneffiziente Messmethode zur Charakterisierung supraleitender Drähte** mit hohem Durchsatz demonstriert. Der Kryostatenaufbau diente als Machbarkeitsstudie einer Messstation für Drähte ohne zusätzlichen Magneten und ohne kontinuierliche Versorgung von flüssigem Helium, d.h. eine Realisierung mit einem kryogenen Kühlsystem (zweistufigem Cryocooler). Ergänzend wurden kurze Probenstücke mit äquivalentem Druck belastet und einer Magnetisierungsmessung mit einem SQUID Magnetometer unterzogen, um die Transportstrommessungen zu überprüfen. Weiters wurde eine Röntgentomographie belasteter und unbelasteter Proben veranlasst, um mittels Finite-Elemente-Analyse die Druckverteilung im Draht, im Speziellen auf die supraleitenden Sub-Elemente, zu simulieren.

- Zusätzlich wurden belastete und unbelastete Kabel- sowie Drahtproben einer metallographischen Studie unterzogen, um so in einer **Elektronenrastermikroskopie** die Degradation der (Mikro-) Struktur zu untersuchen.

Die Messung des kritischen Stroms der **imprägnierten Rutherford-Kabel** zeigte eine erste Degradation nach einer Belastung von 175 MPa. Dies geht einher mit den Ergebnissen der Mikroskopie, die erste Brüche in den supraleitenden Sub-Elementen nach einer Belastung von 175 MPa nachgewissen hat. Die Brüche verlaufen vorwiegend in longitudinaler Richtung, im Gegensatz zu Brüchen, die von Biege- oder Axialbelastung verursacht werden.

Im Rahmen des **Drahtprojekts** konnte der Degradationsprozess des kritischen Stroms und weiterer intrinsischer supraleitender Eigenschaften grundlegender untersucht werden. Die Mikroskopie zeigte eine erste plastische Deformation nach einer Belastung von 50 MPa und eine Entstehung von Brüchen in den fragilen Sub-Elementen nach einer Belastung von 100 MPa. Die plastische Deformation der Kupfermatrix erzeugt eine verbleibende Vorspannung auf die supraleitenden Sub-Elemente, wodurch eine Veränderung der druckabhängigen Eigenschaften festgestellt werden konnte. Ab einer Belastung von 100 MPa beginnt die Degradation, verursacht durch Brüche im supraleitenden Material.

Sowohl die realisierte Transportstrommessung nahe der kritischen Temperatur als auch die Magnetisierungsmessungen zeigten sich als geeignet um irreversible Auswirkungen von transversalem Stress bei Raumtemperatur auf die supraleitenden Eigenschaften zu beobachten.

Abstract

The **Future Circular Collider (FCC)** study aims to develop a conceptual design for a future particle accelerator as a successor of the Large Hadron Collider (LHC). The study investigates the feasibility of a circular collider with a circumference of between 80 km and 100 km. It is planned to serve for objectives beyond the capabilities of the High Luminosity LHC (HL-LHC) prospectively after 2035. The final operating mode is a hadron collider (FCC-hh) to achieve a collision energy of up to 100 TeV and a luminosity of $5 \cdot 10^{38}\,\mathrm{m^{-2}\,s^{-1}}$ to $30 \cdot 10^{38}\,\mathrm{m^{-2}\,s^{-1}}$.

One part of the study is the research and development of **superconducting bending magnets** with a nominal field of 16 T to 20 T at an operational temperature of between 4.3 K and 1.9 K. **Multi-filamentary Nb_3Sn wires** are considered as the baseline for the conductor. Therefore, a 16 T dipole development programme was launched to investigate the feasibility of fabricating and operating high-field accelerator magnets with the required performance. Among other research topics, the magnet manufacturing process is examined. The high brittleness and strain sensitivity of Nb_3Sn make it essential to research the mechanical limits of the coil at magnet manufacturing and its effects on the electrical performance. One objective of this technology programme is to investigate the degradation of the conductor during the magnet assembly.

The Nb_3Sn coils are made of non-reacted Rutherford cables and subjected to a reaction heat treatment of up to 650 °C, in which the superconducting A-15 phase Nb_3Sn is formed ("wind and react" technique). Afterwards, the coil including the instrumentation and quench heaters are impregnated with epoxy resin to ensure electrical insulation between the cable coils, which are initially separated by braided fibreglass. Regardless of the coil geometry, enormous Lorentz forces during operation require mechanical force-restraining structures to prevent movements of the superconductor. These movements can cause training or disturbance quenches followed by a failure of the magnet. Force-restraining structures apply high nominal stress on the order of 70 MPa to 150 MPa to the coil during magnet assembly. This is implemented, for example, with collars or bladder-and-key concepts, resulting in a desired residual pre-stress of between 50 MPa and 120 MPa. Depending on the homogeneity of the stress and the production accuracy, the application of the load may cause even higher local stresses, leading to undesirable and irreversible damage to the superconductor.

The objective of this thesis is to analyse the irreversible performance loss of the superconductor caused by transverse compressive stress exerted at room temperature during magnet assembly, especially during the force-restraining procedure. First, a cable study was launched to obtain quantitative results of the degradation under conditions mimicking the real situation during magnet assembly. Additionally, the degradation mechanism was investigated in detail on single wires. Following this approach, the presented thesis consists of the following **subtasks**:

- An existing **hydraulic press** was refurbished to guarantee a well-defined homogeneous stress application on the specimens. State-of-the-art hydraulic components and calibrated instrumentation were used to ensure accurate and reliable operation. To facilitate the optimisation of the stress homogeneity on the specimen's surface, an evaluation software for pressure-sensitive films was developed. The refurbished press served as a necessary and essential tool in the major experiments explained below.

- **Impregnated Rutherford cable** double stacks were exposed to transverse compressive stress, and their electrical performance was tested in the FRESCA cable test station. FRESCA-compatible samples were iteratively exposed to homogeneous stress at room temperature using the above-mentioned hydraulic press. Subsequently, their critical current was measured at low temperature. The FRESCA cable test station supplies a test current of up to 32 kA and a nominal background magnetic field of 9.6 T. The sample can be cooled to a temperature of 4.3 K or 1.9 K by using liquid or superfluid helium, respectively.

- To investigate the effect of degradation in a more general case and to widen the spectrum of measurement methods, the degradation of **single wires** due to transversal stress at room temperature was also measured. For this purpose, single wires were exposed to stress by the above-mentioned hydraulic press. Subsequently, transport current measurements were performed in a **self-designed cryostat setup** with a test current of up to 150 A. The sample was conductively cooled with liquid helium, a phase separator and heat exchangers. Instead of using an applied magnetic field to shift the critical current into the accessible range, the temperature was adjusted close to the critical temperature. On the one hand, this unusual measurement principle was chosen to avoid additional forces, i.e. Lorentz force, during the low-temperature measurements. On the other hand, **an alternative method was demonstrated to characterise superconducting wires** in

a cost-efficient way with high throughput. The setup served as a feasibility study for a measurement station for wires without a background magnet and without continually supplying liquid helium, i.e. an implementation with a cryogenic refrigerator system (two-stage cryocooler). For confirmation of these transport current measurements, a magnetisation measurement campaign of short samples was performed with a SQUID magnetometer. Moreover, an X-ray tomography following a finite element analysis was performed to obtain the stress distribution within the wire, especially on the sub-elements.

- Finally, a supplementary metallographic preparation of specimens, wires and cables after stress exertion was performed with a **scanning electron microscope** to investigate the changes in the (micro-)structure.

The measurement of a **double cable stack** with a particular configuration and impregnation showed that the critical current began to degrade at 175 MPa. These results are correlated with the crack initiation in the Nb_3Sn sub-elements revealed by the metallographic observation, leading to current sharing within the cable. The induced cracks are mainly in longitudinal direction, with contrasting fracture shapes caused by bending or axial loads.

The **wire investigation** provided a detailed picture of the degradation process of the critical current as well as the intrinsic properties of the superconductor, independent of the cable or coil properties. The microscopy analysis revealed that the plastic deformation of the wire started at 50 MPa and the crack initiation at 100 MPa. The plastic deformation of the copper matrix below the crack initiation threshold generated a residual strain on the superconducting sub-elements, which changed the strain-dependent properties of the superconductor. After applying 100 MPa, the wire performance deteriorated due to the fracture of the sub-elements.

The implemented transport current measurements close to the critical temperature as well as the magnetisation measurements proved to be suitable to monitor irreversible effects after the application of transverse stress at room temperature.

Contents

List of abbreviations & symbols **1**

1 Introduction **3**
1.1 CERN & FCC design study . . . 3
1.2 Applied superconductivity & Nb_3Sn wires . . . 6
1.3 Accelerator magnets & their manufacturing . . . 15
1.4 Former investigations & literature research . . . 22
1.5 Scope & overview of thesis . . . 24

2 Specimen specification & preparation **28**
2.1 Wire for transport current & magnetisation measurements . . . 28
2.2 Impregnated cables for transport current measurements . . . 30
2.3 Metallographic preparation techniques . . . 32

3 Measurement procedures **35**
3.1 Application of transverse stress at room temperature . . . 35
3.2 Measurements of cables with the FRESCA test station . . . 38
3.3 Measurements of wire with the NearT_c setup . . . 46
3.4 Measurements of wires with the SQUID magnetometer . . . 56
3.5 Microscopy of metallographically prepared cables & wires . . . 63

4 Results & discussion **64**
4.1 Results of cable investigations . . . 64
4.2 Results of wire investigations . . . 74
4.3 Conclusion . . . 89
4.4 Outlook . . . 91

Bibliography **102**

List of abbreviations & symbols

Frequently-used abbreviations and symbols in the presented thesis are summarised here.

Abbreviations

BSE	Backscattered electron
EDX	Energy dispersive X-ray spectroscopy
FCC	Future circular collider
FEM	Finite element method
FRESCA	Facility for reception test of superconducting cables
HL-LHC	High luminosity LHC
HTS	High-temperature superconductors
LHC	Large hardon collider
LTS	Low-temperature superconductors
MQE	Minimum quench energy
MQXF	Low-β^* quadrupoles in the intersection region of the planned HL-LHC
NPZ	Normal propagation zone
ODE	Ordinary differential equation
OM	Optical microscope
PID	Piping and instrumentation diagram, Proportional-integral-derivative
PIT	Power-In-Tube
RHT	Reaction heat treatment
RRP	Restacked-Rod Process
RSO	Reciprocating sample option
RT	Room temperature
SE	Secondary electron
SEM	Scanning electron microscope
SQUID	Superconducting quantum interference device
USL	Unified scaling law

Symbols

The magnetic flux density B in Tesla is commonly designated as the magnetic field in the literature of applied superconductivity, which is performed in this work as well. All quantities are in SI units, except stated otherwise.

Constants

h	Planck's constant
μ_0	Vacuum permeability
Φ_0	Magnetic flux quantum

Notation

$\mathbf{F}$	Vector F
F	Amount of vector $\mathbf{F}$
$\mathbf{e}_\mathrm{i}$	Unit vector in direction of i

Variables

A	Area
$A_{\text{A-15}}$	Average A-15 area of Nb_3Sn composite wire
A_{proj}	Central longitudinal cross-section of a cylindrical wire
A_{nom}	Nominal area of cable
b	Reduced magnetic field
B	Magnetic field inside the material
B_{c}	(Thermodynamic) critical field
B_{c1}	Lower critical field
B_{c2}	Upper critical field
$B_{\text{c2}}{}^{*}$	Effective upper critical field
c	Specific heat capacity
E	Electrical field
E_{c}	Electrical field criterion
F	Force
$f(b)$	General pinning force function
f	Frequency
$g(\varepsilon)$	Strain scaling law
$h(t)$	Temperature scaling law
I	Electrical current
I_{c}	Critical current
J	Electrical current density
J_{c}	Critical current density
l	Electronic mean free path
L	Length of sample,
	Machine luminosity,
	Voltage tape distance
n	Resistive transition index
N	Number of sub-element
m	Magnetic moment
m'	In-phase magnetic moment of AC measurement
m''	Out-of-phase magnetic moment of AC measurement
m_{irr}	Irreversible magnetic moment
Q	Heat energy
RRR	Residual resistance ratio
t	Time,
	Reduced temperature
T	Temperature
T_{c}	Critical temperature
$T_{\text{c}}{}^{*}$	Effective critical temperature
T_{cs}	Current sharing temperature
ε	Strain
ε_0	Intrinsic strain
ε_{m}	Thermal-induced pre-strain
V	Electrical voltage
ΔT_{c}	Width of resistive transition
$\varkappa$	Ginzburg-Landau parameter
λ	Thermal conductivity
λ_{L}	London penetration depth
ρ	Electrical resistivity
ρ_{m}	Volume mass density
ρ_{i}	Inner radius of superconducting sub-element
ρ_{o}	Outer radius of superconducting sub-element
σ	Mechanical stress
σ_{nom}	Nominal (target) stress
$\sigma_{\text{LC},\Sigma}$	Actual stress evaluated by installed load cells
ξ	Ginzburg-Landau coherence length
ξ_{BCS}	BCS coherence length
χ'	In-phase magnetic AC susceptibility
χ''	Out-of-phase magnetic AC susceptibility

Chapter 1

Introduction

The first chapter of this thesis gives an introduction to the physical background, the motivation for the topic as well as an overview of the performed experiments. Section 1.1 introduces the aims and tasks of CERN and the currently ongoing FCC design study for a new circular particle collider, at which this work is targeted. Section 1.2 gives an overview of superconductivity as well as the technical implementation of superconducting Nb_3Sn wires, especially the Restacked-Rod Process (RRP), and the specified assessment criteria. An overview of superconducting magnets and their manufacturing process is given in Section 1.3. It will highlight the challenges and potential difficulties of building Nb_3Sn accelerator magnets. Specifically, the ongoing fabrication of the 11 T dipole magnets for the HL-LHC project will lead to the task definition given in Section 1.5. This allows to develop the described strategy of how to investigate the degradation as closely as possible to the real conditions during magnet assembly in correlation with a fundamental analysis of the degradation process and its reasons.

1.1 CERN & FCC design study

The European Organisation of Nuclear Research (CERN) was established in 1954 at the French border in the western Swiss canton of Geneva. It has more than 20 member states and employs 2600 scientists, engineers and technicians together with 14000 visiting users. The core competence of CERN is accelerator science and particle physics. It operates various accelerators, a decelerator and further necessary infrastructure needed for high-energy physics research.

1.1.1 LHC

An overview of CERN's current high-energy physics infrastructure can be seen in Figure 1.1, which serves for various experiments with different objectives.

The currently largest accelerator is the Large Hadron Collider (LHC), having a collision energy of 7 TeV and a maximal luminosity of $10^{38}\,\mathrm{m^{-2}\,s^{-1}}$ at its full commissioning in 2010 [29]. It is housed in the civil engineering infrastructure of the former Large Electron Positron Collider (LEP) [184], which was in operation between 1989 and 2000. In the period from 2010 to 2023, the LHC is planned to reach a collision energy of up to 14 TeV and a luminosity of up to $2 \cdot 10^{38}\,\mathrm{m^{-2}\,s^{-1}}$.

The best-known purpose is the experimental validation of the standard model of particle physics, especially the Higgs mechanism, as well as aspects regarding super-symmetric partners of particles. A remarkable achievement of the LHC, besides demonstrating large-scale accelerator technology, was the experimental confirmation of the theoretically predicted Higgs boson in July 2012, leading ultimately to the Nobel prize in physics in October 2013.

The two most comprehensive identification parameters of particle colliders are collision energy and machine luminosity. Collision energy, i.e. the available energy to produce new particles as a collision product, is given by the sum of the beam energies in the case of the LHC, a circular collider. Luminosity L is the ratio of the number of detected events N_D per second to the interaction cross section σ given by

$$\frac{\mathrm{d}N_\mathrm{D}}{\mathrm{d}t} = L\,\sigma \tag{1.1}$$

in $\mathrm{m^{-2}\,s^{-1}}$, which depends only on the beam parameters. Hence it is a measure of the beam focusing conditions at the interaction point (IP) surrounded by the experimental detector [29].

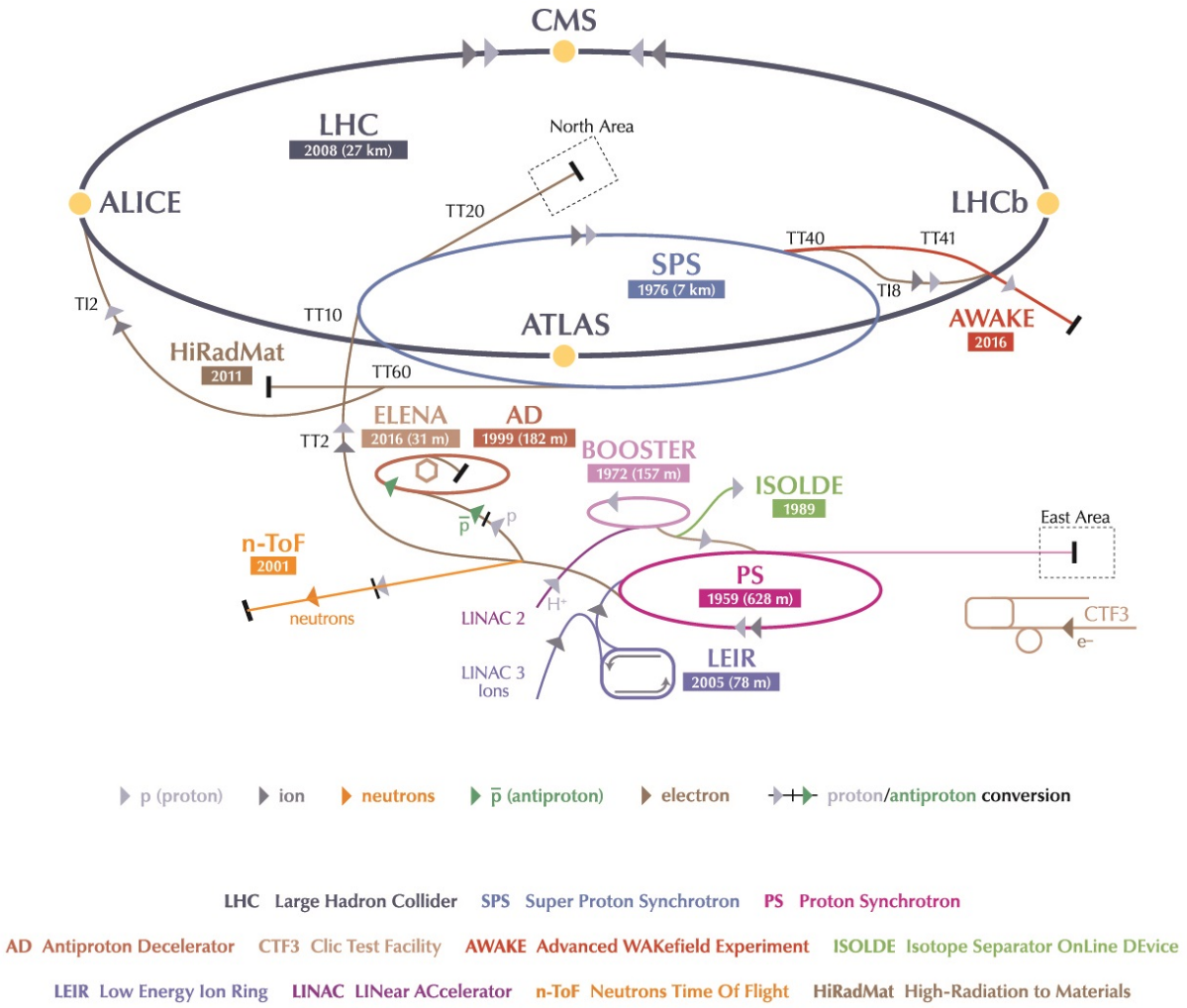

Figure 1.1: Overview of the current accelerator infrastructure of CERN. The largest accelerator, the LHC, a circular collider for protons and heavy ions, had a nominal collision energy of 7 TeV and a luminosity of $10^{38}\,\mathrm{m}^{-2}\,\mathrm{s}^{-1}$ at the full commissioning in 2010. Information taken from Reference [29].

In general, the LHC is a circular twin-aperture proton collider, an alternative-gradient synchrotron with two counter-rotating proton beams and four major collision experiments. The particle beams are steered on the circular trajectory by using superconducting twin-aperture Nb-Ti dipole magnets with a nominal field of 8.3 T operating at 1.9 K in superfluid helium.

The alternative-gradient concept [24, 38, 39, 40], also-called the strong focusing scheme, focuses the particle beam by using quadrupole magnets. A quadrupole magnet in combination with an additional quadrupole magnet rotated by a quarter-turn is called a FODO cell in the context of beam optics. It performs alternatively a focusing of the beam in horizontal and vertical directions, which ensures the required bundling of the beam and hence affects the luminosity. This is performed by Nb-Ti quadrupole magnets with a field gradient of up to $215\,\mathrm{T\,m}^{-1}$ operating at 1.9 K in addition to sextuple, decapole and octupole magnets for additional beam corrections.

The protons are cascade-accelerated by using the other accelerators within the CERN infrastructure, as shown in Figure 1.1:

- The linear accelerator LINAC 2 initially accelerates the protons, which are extracted from hydrogen gas by a duoplasmatron proton ion source, to a kinetic energy of 50 MeV.
- Then they are transferred to the Proton Synchrotron Booster (PSB), where they gain further energy and are extracted at 1.4 GeV.
- Injected into the Proton Synchrotron (PS), the particles are further accelerated to a kinetic energy of 25 GeV.
- Subsequently, the Super Proton Synchrotron (SPS) increases the proton energy to 450 GeV and forwards the particles finally to the LHC.

The LHC is thus iteratively filled with proton bunches within a duration of approximately 15 min by using fast-pulsed kicker magnets and additional deflecting systems to change the trajectory for injection. After the LHC is fully filled with 2808 bunches and a nominal spacing of 25 ns, high-frequency cavities accelerate the beams from the injected 450 GeV to 7 TeV in approximately 30 min. This also requires a continuous ramp-up of the bending (dipole) magnets to their nominal field.

Afterwards, the two beams are pointed against each other at the interaction points in physics operation of the LHC, which are located in the experimental detectors. The outcome of a particle collision is a shower of different types of particles, which are intended to be identified by the detectors. Recording the collision experiments allows the trajectory, momentum and energy of the resulting particles to be reconstructed. The largest detector systems installed at the LHC are ATLAS [96] and CMS [97] with the highest luminosity followed by the ALICE [95] and LHCb detectors [98]. In order to process the tremendous amount of measurement data generated by the LHC experiments, CERN created the LHC computer grid [50], which uses various computing centres of more than 40 countries.

After around 10 h to 20 h, the quality of the beams is decayed due to the many collisions. Consequently the beams are disposed via the beam dumping system near the CMS infrastructure so that the refill for the next run of the LHC can start.

Finally, it has to be mentioned that the LHC is also constructed for heavy ion collision experiments. Highly charged lead ions are produced by an ECR ion source and initially accelerated by the linear accelerator LINAC 3 before reaching their final kinetic energy in the LHC via the above-mentioned accelerator chain. The collision of the particles is detected, for example, by the ALICE experiment [95] (cf. Figure 1.1) and the emerged temperatures and energy densities are intended to prove and study the quark-gluon plasma.

The currently large-scale development obligation of CERN is to enhance the LHC within the High Luminosity LHC project (HL-LHC) [7]. The primary objectives are to increase the luminosity to $5 \cdot 10^{38}\,\mathrm{m^{-2}\,s^{-1}}$ in addition to many other upgrades by around 2025, as indicated in Figure 1.2(b). This includes multiple upgrades of accelerator technology, such as new technologies for beam collimation and upgrades of the cryogenic infrastructure. Furthermore, some improvements to prevent accelerator ageing are planned, for instance, improving quench protection and exchanging radiation-exposed electronics. The most relevant work within the HL-LHC regarding this thesis are the development of state-of-the-art Nb_3Sn accelerator magnets, which was originally performed in collaboration with the U.S. LHC accelerator research program (US-LARP) [75]. More specifically, the 11 T dipole magnet [139] and the MXQF quadrupole magnets [92] are being developed for the following purpose:

- Dispersion suppressor (DS) regions:
  The developed 5.8-m-long 11 T dipole magnets are planned to replace the longer LHC main dipole magnets (14.2 m, 8.3 T) in the dispersion suppressor regions by generating the same bending angle within a shorter distance. The retained longitudinal space will be used to install additional beam collimation systems to raise the beam quality. Collimators are passive accelerator components to protect the beam tube and magnets from particles that deviate from the desired beam trajectory.

- Inner triplets:
  The inner triplets are the group of focusing magnets closest to the interaction point. Owing to the high luminosity upgrade, these magnets are exposed to higher radiation. An early failure due to radiation damage is planned to be prevented by exchanging the existing quadrupole in the critical region to low-β^* quadrupole magnets, the so-called MQXF magnets with lengths of 4.2 m and 7.15 m. The parameter β^* refers to the distance from the interaction point at which the beam width is twice as wide as the interaction point.

The specimens used to produce data for the present thesis originated from the projects mentioned above. The development and research of Nb_3Sn accelerator magnets is a valuable gain of knowledge for the next large-scale project of CERN, described in the next section.

1.1.2 FCC design study

The next long-term goal of CERN to discover high-energy physics beyond the LHC capabilities is to extend their infrastructure by adding a new particle accelerator, the so-called Future Circular Collider (FCC) [1, 2, 3]. Its objectives and feasibility have been investigated within the FCC study since 2014, which focuses on the potential of a hadron and a lepton circular collider. A hadron-lepton scenario is also being considered as a possible operation mode. Therefore, an underground tunnel with a circumference of 80 km to 100 km including caverns for experimental detectors in the Geneva region is studied, as indicated in Figure 1.2(a). The final goal is the FCC-hh, a hadron collider, followed after the operation

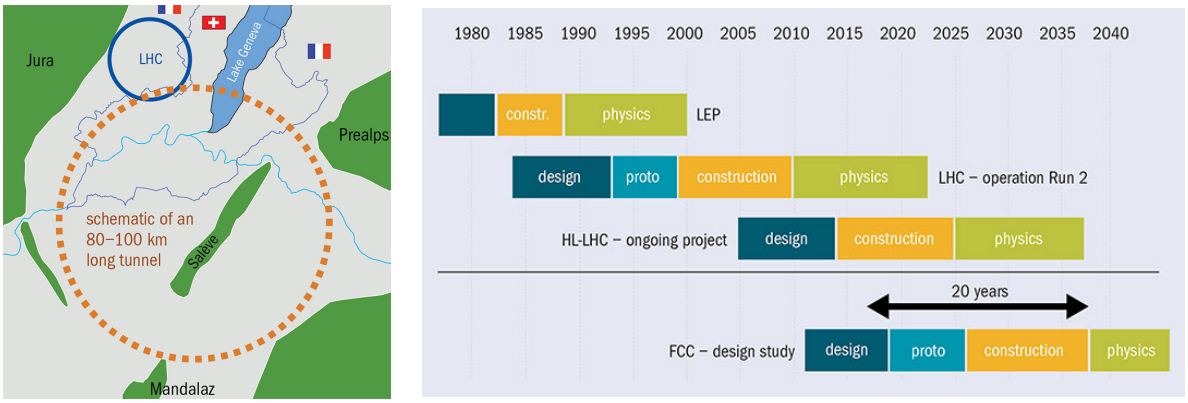

(a) **(b)**

Figure 1.2: Future circular collider study. **(a)** Schematic of planned tunnel **(b)** Planned time schedule in contrast with past and ongoing projects. Information taken from Reference [106, p.34].

end of the FCC-ee, a lepton collider. The conceptual design for the FCC-hh targets a collision energy of 100 TeV and a luminosity in the range of $5 \cdot 10^{38}\,\mathrm{m^{-2}\,s^{-1}}$ to $30 \cdot 10^{38}\,\mathrm{m^{-2}\,s^{-1}}$ with a possible physics operation starting at around 2040. To reach these parameters with an 100 km circumstance collider, bending magnets with a nominal field of 16 T to 20 T and focusing magnets with a field gradient of around $360\,\mathrm{T\,m^{-1}}$ are targeted.

Achieving a particle collider of this scale requires a wide-range technology programme. The magnet research is covered by the 16 T dipole development programme [145, 168, 169]. A comprehensive investigation regarding the magnet types and the conductor is launched. Therefore a re-evaluation of possible magnet designs, such as $\cos(\vartheta)$ [107], canted-$\cos(\vartheta)$ [34] and block coil [102], is performed. The superconducting material Nb_3Sn is considered as the baseline material. Therefore, CERN engineers are striving to achieve a nonCu critical current density[1] of $1.5 \cdot 10^9\,\mathrm{A\,m^{-2}}$ at 16 T and 4.2 K for Nb_3Sn wires, which requires research and development of the superconducting material on a fundamental level. Recently, a feasibility was published by S. Balachandran *et al.* [10], and further scientific approaches have been discussed, for example, by M. Eisterer [51].

One of the studies within the framework of the 16 T dipole development programme is the manufacturing of Nb_3Sn accelerator magnets [90]. The brittleness and strain sensitivity of Nb_3Sn make research on the mechanical limits for the coil winding process and magnet assembly substantial. The mechanical properties of Nb_3Sn wires require a sophisticated manufacturing concept with higher demands on fabrication processes and tolerances compared to the LHC magnets using Nb-Ti superconductors. One of the objectives of this sub-task is the degradation analysis of the conductor during magnet assembly, which initiated the present work.

1.2 Applied superconductivity & Nb_3Sn wires

This section gives a compact overview of applied superconductivity focusing on the knowledge applied in this work. In order to keep this section to a suitable length, the literature of M. Tinkham [167] on the theory of superconductivity, R. Flückiger *et al.* [65] on the scientific research on Nb_3Sn wires as well as that of J.W. Ekin [55] on the critical current measurements and data analysis is recommended.

1.2.1 Superconductivity

Technical superconductors for high-field magnets, i.e. superconductors with an adequate critical current in the form of wires, were researched and developed in several steps:

- The first liquefaction of helium performed by H. Kamerlingh Onnes in 1908 made a previously unexplored low-temperature range accessible for material characterisation. The superconducting phase was first discovered by G. Holst and H. Kamerlingh Onnes [77, 173] while performing resistivity measurements of high-purity mercury at these temperatures. Certain materials lose their resistivity if they are cooled below a specific so-called critical temperature T_c. Furthermore, they

[1] The nonCu critical current density $J_{c,\mathrm{nonCu}}$ of a Nb_3Sn wire is equal to the critical current over the non-copper area of the wire's cross section (cf. Section 3.2.3).

must not be exposed to an external magnetic field higher than a certain level, i.e. the critical field B_c, to remain superconducting. For instance, mercury is in the superconducting state below 4.2 K and 0.04 T. Unfortunately, the low critical fields inhibit the technical use of mercury at that stage. Another insightful discovery was made in 1933 by W. Meißner and R. Ochsenfeld [111]. They discovered that the materials in superconducting state expel applied magnetic fields, i.e. exhibit perfect diamagnetism (so-called Meißner effect), which differentiates superconductivity from ideal conductivity. The behaviour of these so-called type-I superconductors, i.e. the Meißner phase, is described phenomenologically by F. and H. London [101]. A.B. Pippard [123] later introduced a non-local generalisation of the London equations and introduced a coherence length.

One of the most revealing theories about superconductivity is the Bardeen–Cooper–Schrieffer (BCS) theory published in 1957 [12]. It describes the so-called conventional superconductors, i.e. phonon-mediated superconductivity. Crudely put, the microscopy theory describes superconductivity as an interaction between electrons via the vibration of the crystal lattice, i.e. phonon-mediated electron–electron interaction, confirmed by various subsequent experiments. At $T = 0$, the electron density of state $N(E)$ around the Fermi level $E_F \pm \Delta$ is equal to zero, whereby the energy gap $\Delta < 2\hbar\omega_D$ with ω_D as the Debye frequency is typically two or three orders of magnitude smaller than the Fermi level. Two electrons with opposite spin and momentum occupied in this energy gap combine to a so-called Cooper pair, coupled by a phonon. These pairs with a whole-numbered spin, condensate to a coherent matter wave, which prevents them from scattering with the crystal lattice. Thus, it enables current flow without resistivity. The superconducting state is energetically favourable, and an excitation of the electrons must exceed the binding energy the Cooper pairs to break them. It was possible to derive a relation between the critical temperature T_c and the observable energy gap Δ. The energy gap depends primary on the Debye energy ω_D, the electron density of states at the Fermi level $N(E_F)$ and the electron–phonon coupling potential V. It should be mentioned that the BCS theory is limited to the weak-coupling approximation. G.M. Eliashberg [60] introduced and W.L. McMillan [110] further developed an extension beyond the weak-coupling superconductivity, which describes superconductivity in Nb_3Sn more accurately. The theory defines the attractive electon–phonon coupling constant λ_{EP} as well as the repulsive Coulomb interaction between the electrons μ^* to describe an expression for T_c. The material parameter λ_{EP} depends on the so-called Eliashberg function $\alpha^2(\omega)F(\omega)$, whereby $F(\omega)$ is the density states of phonons and $\alpha(\omega)$ is the electron–phonon coupling.

- In 1935, so-called type-II superconductors were discovered by J.N. Rjabinin and L.W. Shubnikov [130, 153]. These materials adopt in a mixed phase, the so-called Shubnikov phase, between the Meißner and normal-conducting phase. Consequently, the materials expel the applied magnetic field until the lower critical field B_{c1}, equivalent to type-I superconductors before transforming to the Shubnikov phase. In this phase, it is energetically more favourable that the magnetic field penetrates the material in the form of fluxoids, also called Abrikosov vortices. Accordingly, the total energy is lowered by the amount of the surface energy $\Delta E \propto (\xi - \lambda_L){B_c}^2$ with the thermodynamic critical field B_c, according to the GLAG theory. Consequently, the materials remain superconducting until the so-called upper critical field B_{c2} before they transform into the normal-conducting phase. The upper critical field can be far above 10 Tesla, depending on the respective material or alloy. The flux of each fluxoid amounts to the magnetic flux quantum $\Phi_0 = h/2e$ with the Planck constant h and the elementary charge e. In general, they are arranged in a triangular lattice in parallel to the applied magnetic field. The fluxoid quantisation in superconductors was first experimentally demonstrated by B.S. Deaver and W.M. Fairbank [43] as well as R. Doll and M. Näbauer [45] in 1961. This confirmed the prediction of the GLAG theory.

  The GLAG theory, named after V.L. Ginzburg, L. Landau, A.A. Abrikosov and L.P. Gor'kov, often also called the Ginzburg–Landau theory [4, 73, 93], is the second valuable theory regarding superconductivity, which was published in the 1950s. The macroscopic theory, based on thermodynamics and valid for temperatures close to T_c, clarifies many phenomena of type-I and type-II superconductors by modelling superconductivity as a thermodynamic phase. Without going into detail, type-I and type-II superconductors are distinguishable if the corresponding Ginzburg–Landau parameter $\varkappa = \lambda_L/\xi$ amounts to more or less than $1/\sqrt{2}$, respectively. It is used to derive B_{c1} and B_{c2} from B_c, which is linked to the difference of the thermodynamic Gibbs free energy of the normal and superconducting phase.

  Unfortunately, ideal type-II superconductors cannot transport current without resistance. Transport current naturally provokes Lorentz forces on the Abrikosov vortices. This leads consequently to movements of the vortices, a so-called flux flow, described for example by the Bardeen–Stephen model [11]. According to Faraday's law, these movements induce an electrical field and hence

Table 1.1: Characteristic parameters of the A-15 compound Nb_3Sn [76, 117, 122]. *At zero temperature.

Debye temperature Θ_D	234 K
Critical temperature T_c	18 K
Ginzburg–Landau coefficient $\varkappa^*$	34
Ginzburg–Landau coherence length ξ^*	3.6 nm
Lattice parameter at RT a	0.5293 nm
London penetration depth λ^*	124 nm
Lower critical field B_{c1}	38 mT
Superconducting energy gap Δ^*	3.4 meV
Sommerfeld constant γ	13.7 mJ K^{-2} mol^{-1}
Thermodynamic critical field B_c	520 mT
Upper critical field B_{c2}^*	25 T

dissipation. The phenomenon can be modelled with the so-called flux flow resistance, which is proportional to the applied magnetic field.

- Finally, type-II superconductors with pinning centres, so-called hard superconductors, make a stationary (DC) transport current without any resistance possible and consequently feasible for technical uses. These pinning centres, which are energetically favoured defects in the crystalline structure, anchor the fluxoids and suppress the dissipative flux flow. The threshold where the Lorentz force exceeds the pinning force determines the critical current. Pinning centres are implemented intentionally in type-II superconductors to achieve high critical currents, which is the primary objective of optimisations for superconducting wires. In the case of Nb_3Sn wires, grain boundaries form the pinning mechanism primary. Consequently, it is desirable to decrease the grain size during the phase formation, which is investigated here. The achieved critical current determined by the pinning ability is an extrinsic property, compared to the intrinsic critical temperature and critical fields of the superconductor. It is bound by the substantially higher intrinsic depairing current density J_d predicted by the GLAG theory.

  However, the pinning mechanism is also responsible for irreversible magnetisation and hence causes hysteresis losses, described for example by Bean's critical-state model [19] (cf. Section 3.4.1). Moreover, the above-mentioned disorder and impurities in hard superconductors, which are intended for the flux pinning, inherently affect the electronic mean free path l of the material. Consequently, the superconducting behaviour and its intrinsic parameters are significantly changed. For instance, the electronic specific heat coefficient γ (i.e. the Sommerfeld constant) and the resistive state resistivity ρ_n are dominated by l. They influence the Ginzburg–Landau parameter $\varkappa$ according to the Gor'kov–Goodman relation, which is coupled again to the critical fields B_{c1} and B_{c2}. The influence of the electronic mean free path l is further elaborated in the works of P.G. deGennes [44], L.P. Gor'kov [74] and K. Maki [104, 105]. Without going into detail, one can distinguish between superconductors in the clean and dirty limit, i.e. $l \gg \xi_{BCS}$ and $l \ll \xi_{BCS}$ with the BCS coherence length ξ_{BCS}, respectively. Technical superconductors can be assumed as superconductors in the dirty limit, where the electronic mean free path is much smaller than the BCS coherence length due to their impurities and disorder. This also justified the use of the Werthamer–Helfand–Hohenberg (WHH) [78, 79, 179] method for dirty superconductors in this work (cf. Section 3.4.2).

- The discovery of superconductivity in cuprate compounds, often called high-temperature superconductors (HTS) with critical temperatures above the boiling point of nitrogen 77.4 K, in 1987 [20] should be mentioned for magnet applications [174]. Moreover, magnesium diboride and iron-based compounds, discovered in 2001 [119] and 2006 [84], respectively, are considered to be promising materials for technical applications in the future.

Today, the most important technical superconductors in commercial composite wires are the alloy Nb-Ti and the intermetallic compound Nb_3Sn, which belong to the so-called low-temperature superconductors (LTS). Their superconducting behaviour was discovered in 1961 [81] and 1954 [109], respectively. Nb-Ti has an A-2 crystal structure, a critical temperature of 9.2 K and an upper critical field of 14.5 T. The properties of Nb_3Sn are summarised in Table 1.1. Although Nb_3Sn was discovered first and has more attractive properties for magnet application, the brittle A-15 material is technologically challenging, so that many applications are implemented preferably with the more ductile Nb-Ti.

1.2.2 Superconducting composite wires

In order to build a superconducting coil for a high-field magnet, the hard superconductor is fabricated in "stabilised" composite wire [85]. An SEM micrograph of a typical Nb_3Sn wire is shown in Figure 2.2. The primary reasons for the concept are analysed briefly as follows:

- First, the superconductor within the wire is arranged in filaments or sub-elements with a preferable size smaller than 70 µm and embedded in a matrix of highly conductive metal such as copper (Cu). This high surface-to-volume ratio surrounded by copper aims primarily to achieve a good thermal stabilisation of the superconductor. It provides a good cooling of the superconducting filaments and allows the transport current to flow temporarily in the copper and prevents a local quench[2] from propagating over the entire wire or coil. A local resistive transition can be caused by short-term current overload, mechanical damage or flux jumps and is mitigated by the stabilised design. The ratio of copper to superconductor is a typical design decision resulting in a trade-off between thermal stability and current density of the coil. It is experimentally quantified, for example, by the normal propagation zone (NPZ) or minimum quench energy (MQE).

- The second reason for a multi-filamentary design is to reduce loss regarding changing magnetic fields, e.g. ramping the magnet to its nominal field or generating alternating magnetic fields. The pinning mechanism, which is instrumentalised to achieve a high critical current, causes the mentioned magnetic hysteretic behaviour. The magnetisation and its associated loss are reduced by the smaller filament size. Moreover, the field error in magnets caused by the hysteretic behaviour as well as flux jumps are decreased, and the design decision regarding the filament size is based on such aspects.

- According to Faraday's Law, applied changing magnetic fields generate circular screening currents in the filaments, which are coupled via the copper matrix. This phenomenon poses an additional load in the filaments without contributing to the transport current. Hence, it decreases the stability regarding the current overload. To counteract the so-called interfilament coupling, the bundle of filaments is twisted. This transposition is apparent in the SEM micrograph of the chemically extracted Nb_3Sn sub-elements in Figure 2.7.

- Eddy currents in the copper matrix of wires within a magnet coil lead to undesired Joule heating and hence also lower the stability of the particular wire. Consequently, wires are bundled into twisted cable, e.g. Rutherford cables in the case of LHC accelerator magnets. In general, a compromise has to be made between a sufficiently high interstrand contact resistance to suppress the aforementioned eddy currents and a low interstrand contact resistance to allow current sharing in the case of a local quench within the cable.

Commercial wires are typically fabricated by extrusion processes. In the case of Nb-Ti, the superconducting rods are embedded in the copper cylinder ingots having a significantly larger diameter and lower length compared to the final wire. Subsequently, the composite is extruded to the desired diameter and length.

The fragile nature of Nb_3Sn inhibits a winding without damage or performance degradation. Hence, the necessary components for forming the Nb_3Sn are summarised in sub-elements and extruded within a wire. Consequently, many Nb_3Sn wire designs are implemented with higher sub-element diameters compared to Nb-Ti filaments. The non-reacted wire can be deformed and wound into a coil. Afterwards, a reaction heat treatment (RHT) of the wound coil up to roughly 650 °C transfers the components into Nb_3Sn ("wind and react" technique), as discussed in Section 1.3. In addition to the A-15 formation of the sub-elements, the copper stabiliser of the wire becomes highly annealed at these temperatures, which increases its conductivity and hence leads to better thermal stability. Today's three most renowned state-of-the-art Nb_3Sn wire architectures for accelerator magnets are listed in Table 1.2.

Wires used in this work are exclusively distributed-barrier internal tin wires fabricated according to the Restacked-Rod Process (RRP) discussed in Section 2.1. The primary advantage of this wire architecture is the high critical current. However, the relatively large sub-elements of typically 50 µm are responsible for high irreversible magnetisation, resulting in high loss during the ramping of a magnet built with RRP wires. RRP and PIT wires are investigated within the 11 T dipole and MQXF quadrupole working packages of the HL-LHC.

In order to assess and compare the essential performance of superconducting wires phenomenologically, the IEC61788-2 standard [159] defines the "DC critical current measurement for Nb_3Sn composite

[2] A quench denotes an uncontrolled transition between the superconducting and the resistive state generating heat dissipation.

Table 1.2: Overview of renowned state-of-the-art Nb_3Sn wire architectures [136].

Type	Sub-element size µm	$J_{c,nonCu}(12\,T, 4.2\,K)$ $A\,m^{-2}$
Bronze process	2 to 4	$\sim 0.9 \cdot 10^9$
Internal tin (single barrier)	3 to 6	$\sim 1.0 \cdot 10^9$
Internal tin (distributed barrier)	30 to 50	$\sim 2.9 \cdot 10^9$
Powder-In-Tube (PIT)	40 to 70	$\sim 2.7 \cdot 10^9$

superconductors". The superconducting wire is transferred from the superconducting to the resistive state in a controlled way by ramping the transport at a constant temperature. The resistive transition follows a power law and defines the critical current I_c as well as the resistive transition index n, as described in Sections 3.2.3 and 3.3.3. In order to assess the copper stabiliser, which embeds the sub-element, the residual resistance ratio (RRR) is often cited [158].

1.2.3 Unified scaling law for flux pinning in technical superconductors

The essential behaviour of Nb_3Sn wires is described by the Unified Scaling Law (USL) of J.W. Ekin [55] based on experimental data and further elaborated in references [56, 59, 58]. It is commonly used to derive the function $I_c(B,T)$, which is also known as the critical surface in magnet design. It is illustrated in Figure 1.5 and frequently used to define the nominal operation point of a superconductor within a magnet as well as to assess load or temperature margins. By using the USL, the most essential properties of a superconductor for magnet design are taken into account:

- The *critical current density* J_c, an extrinsic property depending on the volume pinning force F_p, determined by the micro-structure of the material and additional alloy components.
- The *critical temperature* T_c and the *upper critical field* B_{c2} are intrinsic properties of the material. They depend primary on the crystal structure and atomic scale characteristics. They vary by only a few percent by depending on the fabrication process and the ratio of additional alloy components.
- In addition to the three primary parameters, the *mechanical strain* ε, influences the superconducting behaviour significantly. Wires in coils are pre-tensioned in the coil winding process and additionally exposed to high Lorentz forces during magnet operation. Moreover, the wires are loaded inherently with thermal-induced pre-compression ε_m, considering the formation of the A-15 phase at roughly 650 °C and an operating temperature below 18 K. Consequently, the intrinsic strain $\varepsilon_0 = \varepsilon - \varepsilon_m$ is defined. The thermal-induced pre-compressive pre-strain $\varepsilon_m \approx 0.3\,\%$ is strongly dependent on the architecture and material of the composite wire. With the introduction of strain ε, the four-dimensional critical surface $I_c(B,T,\varepsilon)$ can be defined as shown in Reference [54].

In this work, interpolations and scaling are performed on the basis of the USL and described as follows. The pinning mechanism is quantified by the volume pinning force F_p, as mentioned above. It counteracts the Lorentz force F_L to prevent depinning and movements of the fluxoids. The threshold, where the Lorentz force $F_L = J \times B$ exceeds the maximal pinning force F_p, defines the end of the lossless transport current and hence the critical current density J_c. This can be expressed as

$$F_p = F_L = J_c B. \tag{1.2}$$

Equation 1.2 implies that **J** is perpendicular to **B**, which describes the dominant situation within a magnet. The USL formulates the pinning force

$$F_p = J_c B = C\,K(t,\varepsilon_0)\,f(b) \tag{1.3}$$

with a constant C, the pre-factor $K(t,\varepsilon_0)$ and the general pinning force function $f(b)$. The reduced temperature t is defined as

$$t = \frac{T}{T_c{}^*(\varepsilon_0)}, \tag{1.4}$$

where $T_c{}^*(\varepsilon_0)$ is the effective critical temperature depending on the intrinsic strain ε_0. The reduced field b is defined as

$$b = \frac{B}{B_{c2}{}^*(t,\varepsilon_0)}, \tag{1.5}$$

where $B_{c2}{}^*(t,\varepsilon_0)$ is the effective upper critical field depending on the reduced temperature t and the intrinsic strain ε_0. The effective values $T_c{}^*$ and $B_{c2}{}^*$ are determined by the particular extrapolated scaling functions intercepting with the respective abscissa. In general, they are not identical to the critical temperature T_c and the upper critical field B_{c2}, respectively. The effective values do not consider inhomogeneity effects of the respective wire architecture occurring by temperatures close to T_c or vanishing magnetic field.

The general pinning force function for constant temperature t and strain ε is described by

$$f(b) = b^p(1-b)^q, \tag{1.6}$$

where the parameters p and q dominate the low-field and high-field part, respectively. The two parts are split by the maximum of the function at $b_{max} = p/p+q$. In particular, the pinning theory of Kramer [88] predicts $p = 0.5$ and $q = 2$, which is in good agreement with the measurement data of Nb_3Sn wires. Thus, the equation $F_p = J_cB = C\,b^{0.5}(1-b)^2$ is frequently used for interpolating the critical current at particular applied fields. Therefore, the fit approximation $I_c = C'\,b^{-0.5}(1-b)^2$ with C', b as fitting parameters is applied to the measurement data. Moreover, the Kramer model is used to extrapolate the effective upper critical field $B_{c2}{}^*$, which is located in a difficult-to-access measurement region in the case of Nb_3Sn. The above-mentioned relation

$$J_cB = C\,b^{0.5}(1-b)^2 \qquad \text{can be transferred to} \qquad {J_c}^{0.5}B^{0.25} \propto 1 - \frac{B}{B_{c2}{}^*}. \tag{1.7}$$

The expression ${J_c}^{0.5}B^{0.25}$, which can be obtained from the measurement data, forms a straight line over B. It intersects the abscissa at $B_{c2}{}^*$ and can be calculated accordingly. Under the assumption that $B_{c2} \approx B_{c2}{}^*$, this method can be used to assess the upper critical field B_{c2} and is also known as the Kramer plot or Kramer extrapolation.

The effective upper critical field $B_{c2}{}^*(t,\varepsilon)$ is dependent on temperature t and strain ε. Therefore the behaviour is separated into two functions

$$B_{c2}{}^*(t,\varepsilon_0) = B_{c2}{}^*(0,0)\,b_{c2}(t)\,b_{c2}(\varepsilon_0) \quad \text{with} \quad B_{c2}{}^*(0,0) = B_{c2}{}^*(0) \tag{1.8}$$

and

$$\begin{aligned} B_{c2}{}^*(t) &= B_{c2}{}^*(0)\,b_{c2}(t), \\ B_{c2}{}^*(\varepsilon_0) &= B_{c2}{}^*(0)\,b_{c2}(\varepsilon_0). \end{aligned} \tag{1.9}$$

The temperature dependency is known to be

$$b_{c2}(t) = (1-t^\nu), \tag{1.10}$$

where $\nu \approx 1.5$ is in good agreement with the experimental data for Nb_3Sn wires. Within the so-called moderate strain region $-0.5\,\% < \varepsilon_0 < \varepsilon_{0,irr} \approx 0.4\,\%$, the strain dependency is modelled by the power law approximation

$$b_{c2}(\varepsilon_0) = (1 - a|\varepsilon_0|^u). \tag{1.11}$$

An extraction of J.W. Ekin [55] in Figure 1.3 shows the correlation of the fit function with the measurement data of binary multi-filamentary Nb_3Sn wires. The exponent parameter can be assumed with $u \approx 1.7$, and the strain-sensitivity parameter a is in the range of 900 to 1250 for Nb_3Sn [54]. The experimental data for tension ($\varepsilon_0 > 0$) are slightly steeper than for compression ($\varepsilon_0 < 0$). Consequently, the parameters a^+ and a^- for tension and compression strain, respectively, are defined for detailed scaling.

The strain dependence of the effective critical temperature within the moderate strain region can be expressed with the strain behaviour of the upper critical field

$$T_c{}^*(\varepsilon_0) = T_c{}^*(0)\left[\frac{B_{c2}{}^*(\varepsilon_0)}{B_{c2}{}^*(0)}\right]^{1/w} = T_c{}^*(0)(1-a|\varepsilon_0|^u)^{1/w} \tag{1.12}$$

with $w \approx 3$ for Nb_3Sn as shown in Figure 1.4(a).

Under the assumption that the pre-factor $K(t,\varepsilon_0)$ can also be separated into a strain and a temperature-dependent part $K(t,\varepsilon_0) = g(\varepsilon_0)\,h(t)$, the USL can be expressed in its separable form

$$F_p = J_cB = C\,g(\varepsilon_0)\,h(t)\,f(b). \tag{1.13}$$

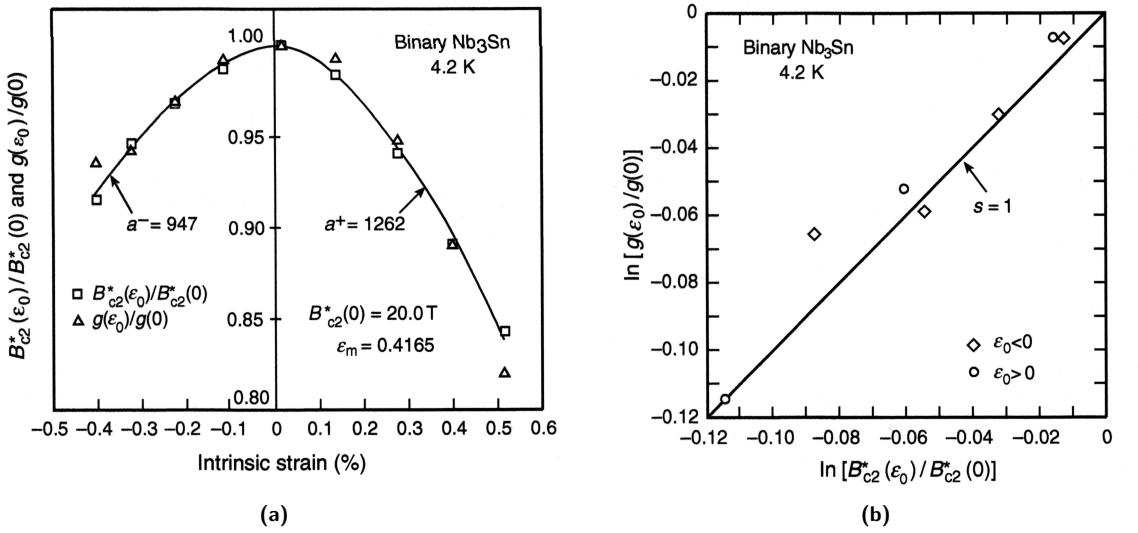

Figure 1.3: **(a)** Strain dependency of the normalised intrinsic parameter $B_{c2}{}^*(\varepsilon_0)/B_{c2}{}^*(0)$ and the normalised strain scaling function $g(\varepsilon_0)/g(0)$ within moderate strain. **(b)** Logarithmic plot of $g(\varepsilon_0)/g(0)$ versus $B_{c2}{}^*(\varepsilon_0)/B_{c2}{}^*(0)$ for evaluation of parameter s. Information taken from Reference [55, p.451].

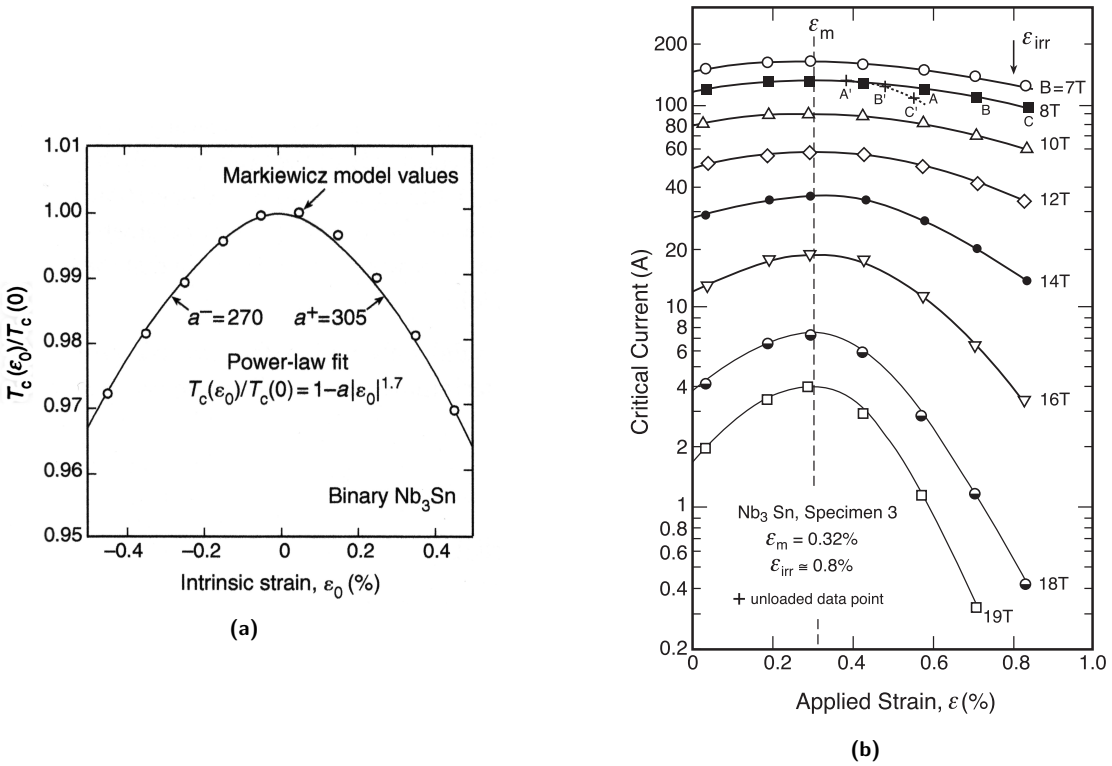

Figure 1.4: Strain dependency of **(a)** the normalised intrinsic parameter $T_c(\varepsilon_0)/T_c(0)$ and **(b)** the critical current $I_c(\varepsilon)$. Information taken from Reference [55, p.445] and [55, p.435], respectively.

The temperature scaling law $h(t)$ is defined as

$$h(t) = h(0)\left[\frac{B_{c2}{}^*(t)}{B_{c2}{}^*(0)}\right]^{\eta} = h(0)\left(1 - t^{\nu}\right)^{\eta} \tag{1.14}$$

with $\eta \approx 2.5$ for Nb_3Sn and is in good agreement with the transport current measurements $I_c(T)$ within the wire investigated in Section 4.2.2.

Finally, the strain scaling function $g(\varepsilon_0)$ can be expressed within the moderate strain region by the obtained strain dependency of the upper critical field

$$g(\varepsilon_0) = g(0)\left[\frac{B_{c2}{}^*(\varepsilon_0)}{B_{c2}{}^*(0)}\right]^{s} = g(0)(1 - a|\varepsilon_0|^u)^s, \tag{1.15}$$

where $s \approx 1$ can be identified for Nb_3Sn, shown in Figure 1.3. The nearly consistent power-law behaviour of $T_c{}^*(\varepsilon_0)$, $B_{c2}{}^*(\varepsilon_0)$ and $g(\varepsilon_0)$ within the moderate strain region is assumed to arise from the phonon anharmonicity of the crystal lattice. This reversible effect is further discussed in Section 1.4.

After a certain stress level, the conductor no longer recovers from the load, which can be observed by the degradation of a subsequent non-loaded measurement. Hence, an additional irreversible effect influences the I_c performance, which is illustrated in Figure 1.4(b) as follows. After the wire is exposed to a strain $\varepsilon = 0.6$ (measurement point A), the subsequent non-loaded measurement still shows a residual strain (measurement point A'). This can be explained by the fact that materials of the wire, e.g. the copper stabiliser, are plastically deformed and exert a residual strain on the superconductor. As long as the performance of the wire recovers on a particular point on the $I_c(\varepsilon)$ curve, the superconductor is unharmed conclusively. This also implies measurement point B followed by non-loaded measurement point B'. After a threshold, i.e. measurement point C, the wire does not recover fully, which can be seen by a subsequent non-loaded measurement (point C'). Hence, the wire is degraded irreversibly, which is assumed to be caused by fractures of the superconducting material. This so-called irreversible strain limit ε_{irr}, i.e. in the present case at point C ($\varepsilon \approx 0.8$), is an essential threshold for magnet design and should not be reached in any case after the RHT. Despite the fact that high-compressive strain in coils should not be an intended state in a magnet, the regime $\varepsilon_0 < -0.5\,\%$ is also investigated and modelled with a power law approximation [56].

1.2.4 NearT_c concept

Within the wire investigation, transport critical current measurements were performed exclusively in magnetic self-field. This was decided due to the following restrictions:

- In order to protect the specimen from undesired damage during the measurements, the use of an applied field was excluded.
- An alternative cost-efficient measurement method should be demonstrated and verified, which would enable low-temperature measurements without a background magnet and continuous supply of liquid helium (^{4}He).

In order to support and explain the chosen measurement principle, some established background knowledge is introduced. Based on the USL for constant strain, the mentioned critical surface $I_c(B, T)$ can be expressed as

$$I_c = \frac{F_p}{B} = C\,B^{-1}\,h(t)\,f(b), \tag{1.16}$$

and is shown in Figure 1.5. Underneath that surface, the conductor is superconducting and above it reverts to the resistive state. By using critical current tests at specific applied fields and temperatures, the surface can be scaled and is frequently used for assessments in magnet design.

The most common critical current evaluation is the measurement of $I_c(B)$ at a constant temperature T, i.e. I_c-B curves labelled in Figure 1.5. This is implemented primarily by winding the Nb_3Sn wire on a barrel, e.g. a VAMAS barrel [25], and subsequently reacted within the RHT process. Afterwards, the sample is cooled below its critical temperature in a cryostat equipped with the necessary instrumentation, e.g. current leads and a background solenoid magnet. Considering the thermodynamic properties of liquid (^{4}He I) and superfluid helium (^{4}He II), helium at the temperature of 4.2 K or 1.9 K is preferred as a coolant.

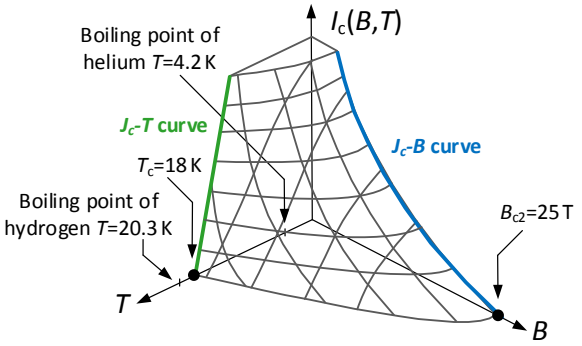

Figure 1.5: Critical surface $I_c(B,T)$ derived from the USL for assessment of the conductor's operation point and margin within magnet design. In addition, the boiling points of hydrogen and helium are annotated. Helium is the most commonly used cryogenic liquid to test and use LTS composite wires, such as Nb_3Sn wires.

One of the advantages of cooling the sample with boiling ^{4}He I is the quasi-isothermally absorption of heat energy by the latent heat of vaporisation, which stabilises the sample temperature naturally. Moreover, the specific heat capacity of liquid helium is several orders of magnitude higher than that of commonly used metals at these temperatures. The outstanding properties of ^{4}He II as a coolant are its very high specific heat capacity and thermal conductivity besides the absence of boiling and viscosity.

To shift the critical current $I_c(B)$ in an experimentally accessible range, i.e. below the maximum current of the power supply, the applied field is increased. The resulting measurement range achieved by using a 300 A current source and a 15 T background magnet is labelled in Figure 1.6(a). This is performed by setting the applied field and subsequently ramping the current during voltage recording until the resistive transition occurs. The quench protection cuts the current supply to prevent damage of the wire due to Joule heating. The critical current is determined preferably according to the IEC61788-2 standard [159]. The measurement point $I_c(12\,\mathrm{T}, 4.2\,\mathrm{K})$ is often used to compare the performance of different wires (cf. Table 1.2).

In the present work, a background magnet was not available. Consequently, the above-mentioned shift of I_c with high applied fields was not utilisable. Instead, the temperature was raised in an alternative manner and stabilised. Hence, variable-temperature measurements of the critical current $I_c(T)$ were chosen, as illustrated by the I_c-T curve in Figure 1.5. Test currents of up to 150 A require a temperature shift close to the critical temperature T_c, which gives the NearT_c concept its name. This stands in contrast to the frequently used measurement temperatures 4.2 K and 1.9 K mentioned above. The typical measurement range is labelled within the critical surface in Figure 1.6(b). The chosen measurement range provides certain technological advantages:

- The absence of the background magnet has primary economical reasons. It also has the advantage that the sample does not have to fit into the relatively small aperture of a background magnet, which is often the spatial boundary for $I_c(B)$ measurement test stations. The concept presented here enables comparatively more space in the low-temperature measurement chamber for the sample and instrumentation. Moreover, a sophisticated mounting of the sample is not mandatory.

- Owing to the high operation temperature far above the boiling point of helium, an implementation of a cryogenic refrigerator system (cryocooler) can be taken into account. In this case, the cooling power of the system is the limiting factor regarding the maximal test current. A closed-loop refrigerator system would supersede the continuous supply of liquid helium and enable a high measurement throughput considering the cooling duration of established systems.

However, the NearT_c concept also has inherent drawbacks. Shifting the temperature instead of the magnetic field leads to higher requirements regarding temperature stability, which has to satisfy the slope $\mathrm{d}I_c/\mathrm{d}T$ in the respective measurement range.

I_c-T curves are frequently used to assess the temperature margin of a superconducting wire. In principle, there is more than one way to implement a variable-temperature measurement. One solution is to put the sample in a cryogenic liquid bath and regulate the pressure of the cryostat. The temperature of the sample can be reduced by evacuating the gas space of the cryostat. Accordingly, increasing the cryostat's pressure raises the boiling temperature. Hence, the boiling point of the liquid and consequently the sample temperature is reduced as a function of the pressure along the saturation vapour pressure curve. Helium is thus called saturated (two-phase) helium while operating in this two-phase

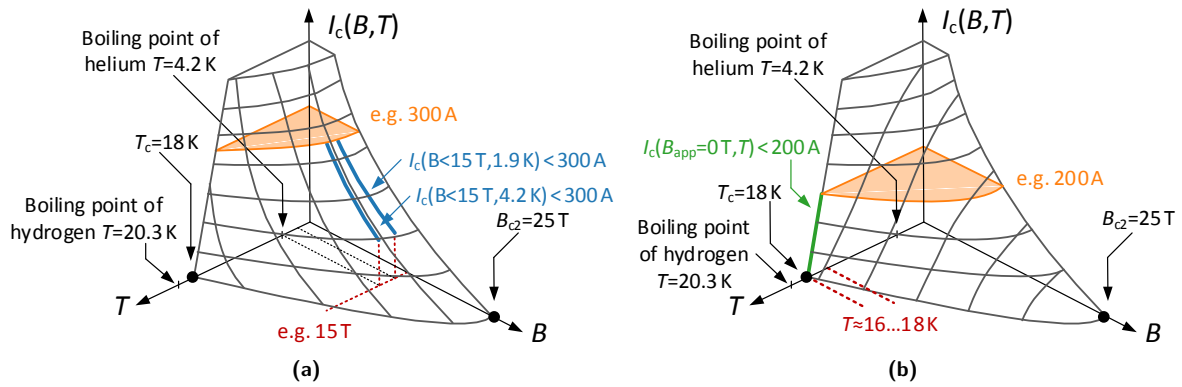

Figure 1.6: Illustration of the measurement region aided by the critical surface $I_c(B,T)$. **(a)** Measurement range for a background magnet of up to 17 T at 4.2 K or 1.9 K with liquid or superfluid helium, respectively. **(b)** Measurement range in self-field by adjusting the sample temperature close to the critical temperature, i.e. the so-called NearT_c concept.

region of the phase diagram. In general, the upper boundary of this evacuating–pressurising technique is given by the critical point of the respective cryogenic liquid. However, the pressure of the cryostat or dewar vessel is limited in practice by the recommended safety limits, e.g. in the range of the double atmospheric pressure. The bottom temperature limit is reached at the triple point of the particular coolant.

The temperature of this targeting concept amounts roughly to the range of 15 K to 20 K determined by the properties of Nb_3Sn. Consequently, the number of selectable liquid coolants is restricted. Nitrogen (N_2) has a triple point of 63.2 K and hence cannot be used for these temperatures. In the case of ^{4}He, the critical point is reached at 5.2 K and 2.2 bar. Hence, without an applied field, the critical current of Nb_3Sn wires in this temperature range is technologically difficult to reach. Nevertheless, saturated helium is often used to reach temperatures below its lambda point at 2.17 K and 0.05 bar by evacuation. Hydrogen (H_2) has a triple point at 13.8 K and 0.07 bar, and the required temperature range can be achieved with the experimentally accessible pressure. Unfortunately, hydrogen is rarely used as a coolant due to the risk of the boiled-off gas exploding when mixed with air. A mixture of hydrogen with air in the ratio of 4 % to 75 % is flammable and must be handled appropriately.

In this work, a cryostat setup based on a pressure-regulated helium phase separator was designed and implemented to emulate and test the feasibility of a refrigerator-based cooling system (two-stage cryocooler) for the NearT_c concept. The conductively-cooled sample, a Nb_3Sn wire with test currents of up to 150 A, was mounted on a portable sample holder in a vacuum atmosphere. The specific construction is described in Section 3.3 and its operation is discussed in Section 4.2. Former and similar experiments of Nb_3Sn close to the critical temperature T_c are mentioned in the literature review in Section 1.4.

1.3 Accelerator magnets & their manufacturing

This section briefly introduces superconducting accelerator magnets and the production of Nb_3Sn accelerator magnets. It focuses on the necessary technological background for the presented thesis. Considering that the field of accelerator magnets is well established, the literature of L. Rossi *et al.* [131] and S. Russenschuck [135] is recommended for additional background information.

1.3.1 Accelerator magnets

The dipole magnets of a circular collider steer the charged particles, i.e. the beam, on the desired bent trajectory according to the Lorentz force. The maximal achievable bending field in the beam aperture implemented by the dipole magnets determines the bending radius of the beam and hence the radius of the collider. It is one of the significant factors regarding the estimation of costs. Based on the calculated motion of a charged particle in a constant magnetic field, the beam energy of a circular collider can be assessed in practical units by

$$E_{\text{beam}} \approx 0.3\, R\, B_0 \tag{1.17}$$

in TeV [135]. The variable R identifies the radius of the beam trajectory inside the bending field in km and B_0 defines the magnetic bending field in Tesla. Thus, in order to raise the achievable beam energy

of a particle collider, either the radius or the magnetic bending field must be increased. In practice, the radius R of the beam implemented by the dipole magnets must be smaller than the actual radius of a collider. This is necessary because the entire circumference of a collider is not available for dipole magnets, e.g. the intersection regions, which is usually described by the dipole filling factor of a particle collider.

Moreover, the focusing magnets, in particular the low-β^* quadrupole magnets, influence the luminosity L at the interaction point, which, broadly speaking, affects the efficiency of a collider. Thus, the development of magnets is essential for the advancement of particle colliders.

Most normal-conducting magnets for colliders are commonly implemented by copper coils around a flux-leading yoke, which is also often called an iron yoke. The yoke consists of laminations of magnetically soft ferromagnetic material, e.g. iron or soft ferrites, as shown in Figure 1.8. The particle beam is exposed to the magnetic field by locating it in the air gap of the yoke. The current density of the copper coils is limited by the generated Joule heating to several $10^6\,\mathrm{A\,m^{-2}}$, whereby the engineering current density is generally used in magnet design[3]. The generated magnetic field is concentrated and guided by the iron yoke and is technologically limited by the saturation flux density of the ferromagnetic material, which is typically between 1 T to 1.8 T. The decisive field quality is determined by the shape of the yoke poles or pole shoes, which is also why they are often called iron-dominated magnets.

Although superconducting magnets replaced normal-conducting in large colliders with high-rigidity particle beams, they are still broadly used and optimised within high-energy physic experiments. Pulsed kicker and septa magnets, which are used to extract and inject particle bursts within the CERN accelerator infrastructure (cf. Figure 1.1), are normal-conducting. Moreover, the FCC-ee is considered to be implemented with twin-aperture normal-conducting magnets [113].

Owing to the demand of high-energy physics experiments to reach still higher nominal fields and gradients in bending and focusing magnets, respectively, it was necessary to search for higher current densities. This barrier of accelerator technology could be overcome by the research and development of superconducting magnets. By operating coils made of superconducting composite wires underneath its critical current, located in a cryostat, engineering current densities above $5 \cdot 10^8\,\mathrm{A\,m^{-2}}$ became feasible with vanishingly small Joule heating. One of the first superconducting accelerator magnets went into operation at CERN in the late 1970s [23]. Nb-Ti quadrupole magnets with a peak field of 5.3 T were used in the intersection region of Intersecting Storage Rings (ISR) to raise luminosity. The first entirely superconducting collider was the Tevatron at the FNAL, which operated from 1983 to 2011 using Nb-Ti composite wires.

Conventional superconducting accelerator magnets are so-called coil-dominated magnets. Hence, the field shape is formed primarily by the layout of the coil as shown in Figure 1.9. This means the distribution of the current density in the two-dimensional space perpendicular to the beam direction is responsible for the field shape, due to the absence of a flux-leading yoke. An adequate coil modelling is mandatory to achieve an appropriate field quality. Correspondingly, I. Rabi [128] demonstrated that a pure transverse dipole field $\mathbf{B} = B\,\mathbf{e}_\mathrm{y}$ as well as higher-order multipoles can be achieved by combining the intersection ellipse with opposite current polarity. The corresponding configuration shown in Figure 1.7(a) generates a perfect uniform dipole field in the aperture

$$\mathbf{B} = \mu_0\, J_0\, c\, \frac{b}{a+b}\, \mathbf{e}_\mathrm{y}. \tag{1.18}$$

Moreover, it can be demonstrated that a ring of thickness t with a current density distribution of $J = -J_0 \cos(\vartheta)$ also generates a pure dipole field in the aperture with a magnitude of

$$\mathbf{B} = \frac{\mu_0 J_0}{2}\, t\, \mathbf{e}_\mathrm{y}, \tag{1.19}$$

as illustrated in Figure 1.7(b). Accordingly, the current distribution $J = -J_0 \cos(n\varphi)$ generates a field of a $2n$-multipole, where n is a positive whole number. The $\cos(\varphi)$-dependent current density in a ring is barely technically feasible, but a block-wise approximation can be implemented to approach the ideal current density distribution, as can be seen in Figure 1.7(c). The field inside the coil shell of this arrangement is not a perfect dipole and is generally written as

$$\mathbf{B}(\rho, \varphi) = B_\rho(\rho, \varphi)\, \mathbf{e}_\rho + B_\varphi(\rho, \varphi)\, \mathbf{e}_\varphi. \tag{1.20}$$

[3]The engineering current density $J_{\mathrm{c,ENG,coil}}$ of magnets is defined as the current of the coil divided by the entire cross section of the coil (cf. Section 3.2.3).

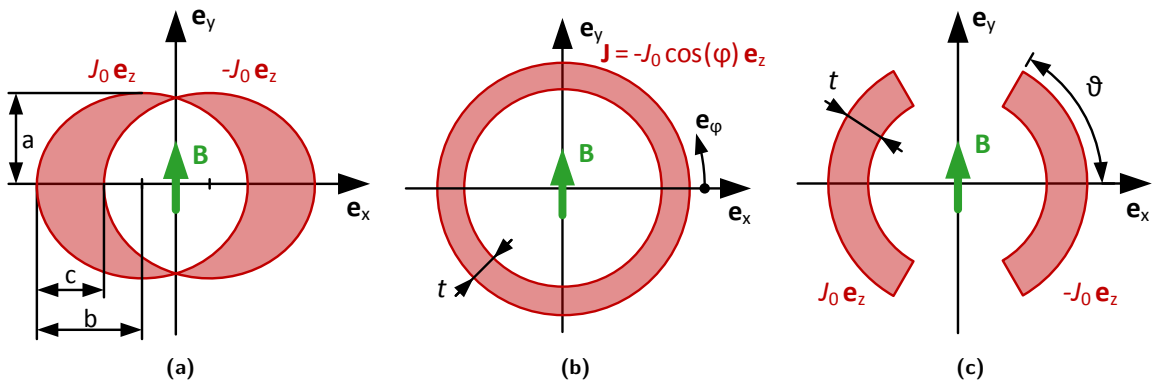

Figure 1.7: Two-dimensional layout of current density distributions to achieve a transverse dipole field with coil-dominated magnets. **(a)** Perfect uniform dipole field generated by intersecting ellipse of current densities. **(b)** Dipole field by generated by a ring with $\cos(\vartheta)$-dependent current density. **(c)** Arc-shaped shell segments with constant current distribution to technically implement the dipole field of (b).

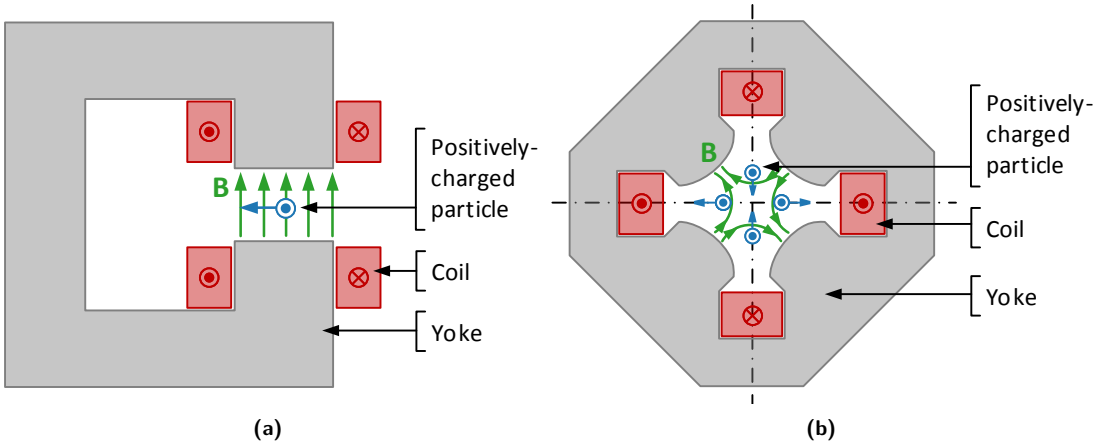

Figure 1.8: Iron-dominated accelerator magnets with a moving positively charged particle in the aperture affected by the Lorentz force. The magnetic field is guided in the ferromagnetic yoke, and the field quality in the air gap is dominated primarily by the iron pole shape. **(a)** C-shaped dipole magnet to bend the particle beam. **(b)** Quadrupole magnet to focus the particle beam vertically.

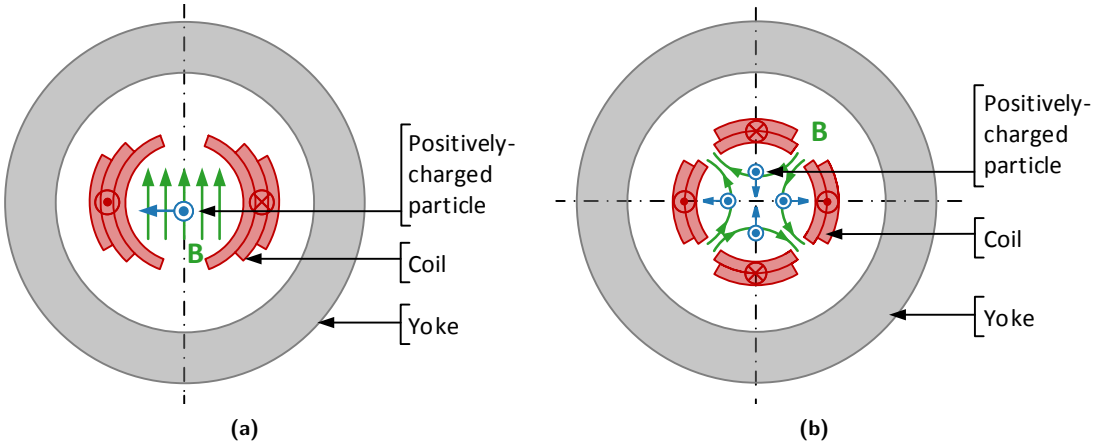

Figure 1.9: Coil-dominated accelerator magnets with a moving positively charged particle in the aperture affected by the Lorentz force. The magnetic field distribution is dominated primarily by the coil layout, and the yoke is used only for shielding. **(a)** Dipole magnet to bend the particle beam. **(b)** Quadrupole magnet to focus the particle beam vertically.

It can be shown that fields in accelerator magnets, i.e. two-dimensional magnetic fields generated by a transverse current distribution surrounding the aperture, are describable by coefficients of a Fourier series expansion along the circle. This method is commonly used and often called multipole coefficients or field harmonics. For example, errors of the particular design from the ideal field distribution are often assessed by field harmonics at a particular reference radius, e.g. in the case of the 11 T dipole development [86]. The desired dipole component B_1, i.e. Fourier coefficient $n = 1$, of Figure 1.7(c) leads to a field inside the aperture of

$$\mathbf{B} = B_1 \mathbf{e}_y = \frac{2\mu_0}{\pi} J_0 \, t \, \sin(\vartheta) \, \mathbf{e}_y, \tag{1.21}$$

whereby the dipole coefficient is clearly higher than the undesired multipole coefficients of higher orders. To achieve an optimal conductor arrangement concerning a specific optimisation criterion, e.g. field quality or energy efficiency, nested layers (cf. Figure 1.9) or block coil arrangements (cf. Figure 1.13) are widely used implementations.

To design the desired two-dimensional coil layout based on the laws of electromagnetism, numerical methods such as finite-element and boundary-element methods are used in state-of-the-art tools for magnet design. At CERN, the electromagnetic simulation and optimisation programme ROXIE for accelerator magnets was developed for this purpose [132, 8]. However, analytical approaches were also developed and used in the past. For instance, R.A. Beth [22] introduced the concept of complex multipoles by employing the complex analysis. At this point, it should be mentioned that the usual conceptual design of magnets is based on blocks or cables with homogeneously distributed engineering current density, such as the field calculation of the cable specimen in Section 3.2.2. Hence, current variations within these blocks are often excluded in the optimisation of the magnetic field distribution.

A significant drawback of coil-dominated magnets is that the coils are unavoidably located within high-field regions of the generated magnetic field, which is also an important fact for the work presented here. This implies that the coils, i.e. the current-carrying conductors, are exposed to high magnetic fields and thus to high electromagnetic forces. A dedicated mechanical design including force-restraining structures is necessary to counteract the Lorentz force and to prevent the destruction of the magnet. The mechanical design, which is especially crucial when using the brittle Nb_3Sn superconductor, is discussed in more detail in the next section.

One of the broadly used implementations of coil-dominating superconducting accelerator magnets is the $\cos(\vartheta)$-design, i.e. the LHC dipoles and quadruples as well as the above-mentioned 11 T dipole magnet for the HL-LHC. It aims to approximate this above-explained current distribution with shell-shaped coils. In simplified terms, two-curved saddle coils are located around the beam aperture, as shown in Figure 1.10. To approach the desired $\cos(\vartheta)$-layout, nested layers and insulated wedges are placed, according to the field optimisation results. For instance, four layers are discussed for the FCC 16 T dipole conceptual design [107]. The final coil design of the 11 T dipole magnet consists of two layers with four inner blocks and two outer blocks, as illustrated in Figures 1.13(b) and 1.14(b). These nested coil packs are surrounded and pre-stressed by a non-magnetic austenitic steel collar to ensure mechanical support. Furthermore, the collared coil assemblies are enclosed by a ferromagnetic yoke to protect the surrounding area from the generated magnetic field. This is further encased by stainless steel shells and constitutes the helium vessel, the so-called cold mass. The cold mass is placed in a cryostat vacuum vessel after being assembled with cryogenic insulation material, so-called superinsulation. A typical implementation of a $\cos(\vartheta)$-magnet, the LHC main dipole magnet, is schematically shown in Figure 1.15 at the end of this section.

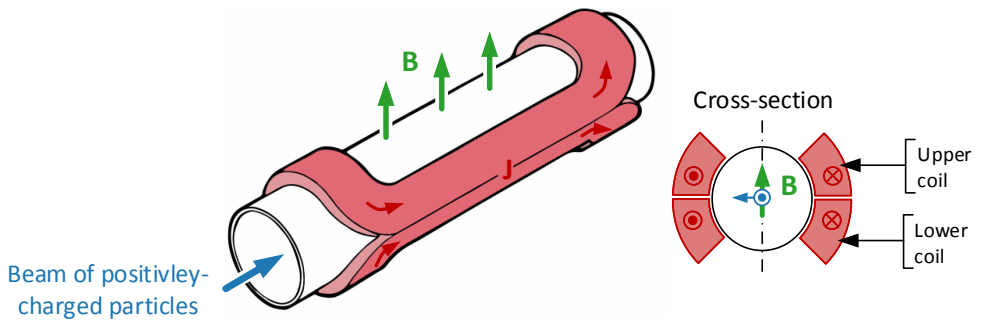

Figure 1.10: Schematic of the $\cos(\vartheta)$ dipole magnet design. Two-curved saddle coils surround the particle beam aperture and generate a magnetic dipole field. Information taken from Reference [181] and edited by the presenting author.

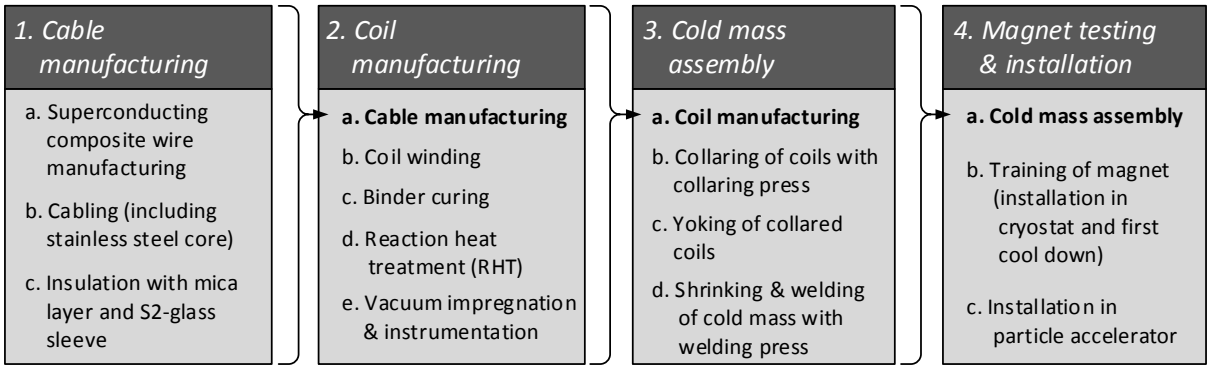

Figure 1.11: Fabrication processes of the Nb_3Sn 11 T dipole magnets at CERN according to the "wind and react" manufacturing technique.

1.3.2 Manufacturing of the Nb_3Sn 11 T dipole magnet

After an introductory description of the design and structure of superconducting coil-dominated magnets, their fabrication is discussed. The HL-LHC 11 T dipole production is well established, and most samples of the thesis originate from the corresponding development. Consequently, Nb_3Sn accelerator magnet production will be discussed based on the example of 11 T dipole production [89, 138, 139], which also provides valuable knowledge for the planned FCC magnet development. The primary steps are illustrated in Figure 1.11 and described as follows:

1. Cable manufacturing

First, the delivered Nb_3Sn composite wires are "cabled" to so-called Rutherford cables at CERN (TE-MSC-SCD) as shown in Figure 1.12 [31, 133]. This highly compacted cable type was proposed in the early 1970s by the Rutherford laboratories for magnet design. Thus, 40 non-reacted Nb_3Sn wires are rolled into a hollow, twisted tube and subsequently pressed into two fully-transposed layers, as shown in the micrograph in Figure 1.12(b).

The periodical transposition pitch aims to lower induced eddy currents during the ramping of the magnet. Additionally, a non-magnetic austenitic steel core is placed in the centre to increase the adjacent resistance between the two layers and hence enable fast cycling of the magnet [157]. For comparison, the Nb-Ti wires used for the LHC magnets were also fabricated to Rutherford cables and coated additionally with a tin alloy to increase the interstrand contact resistance [129, 5].

As a final conductor for the 11 T dipole magnet, the wire RRP108/127 with 108 superconducting Nb_3Sn sub-elements and an average size of 46 µm was chosen (cf. Table 2.3). The Restacked-Rod Process is further described in Section 2.1, and the final cable properties are listed in Table 2.2 (column "Specimen 2"). In order to wind a coil into an arc segment shape, the Rutherford cable is flatted at the so-called keystone angle α. According to the "wind and react" technique mentioned above, the wires are cabled in the non-reacted condition. Otherwise, the brittle Nb_3Sn sub-elements would be demolished during the cabling or winding process, resulting in poor superconducting performance. However, the necessary substantial deformation of the wire on the cable edges during cabling can rupture the niobium barrier (cf. Figure 1.12(b)) [64]. Consequently, the tin core of the sub-elements could leak out during the reaction heat treatment above 230 °C. This would contaminate the high-purity copper matrix, resulting in a degradation of the *RRR* and hence loss of stabilisation performance.

After cabling, the Rutherford cable is insulated with a S-2 glass sleeve braided over a C-shaped mica layer as shown in Figure 1.12(a) to ensure electrical insulation up to a breakdown voltage of 10 kV after a reaction heat treatment of up to 650 °C [152].

2. Coil manufacturing

In the next step, the cables are wound into $\cos(\vartheta)$-coils, i.e. curved saddle coils, with a four-degree-of-freedom winding machine at CERN (TE-MSC-LMF) [124, 125]. The first and second layers of the 11 T dipole coils are wound around a mandrel with saddle-shape ends including the filling wedges according to the magnet design. Respectively, two coils are combined to surround the beam aperture completely in order to generate the designed field distribution.

Subsequently, after the coil layers are wound and equipped with the necessary instrumentation, e.g. voltage taps, they are cured under moderate thermal treatment in the range of 150 °C to 190 °C. The ceramic binder for the curing process aims to achieve the necessary stabilisation support of the double-

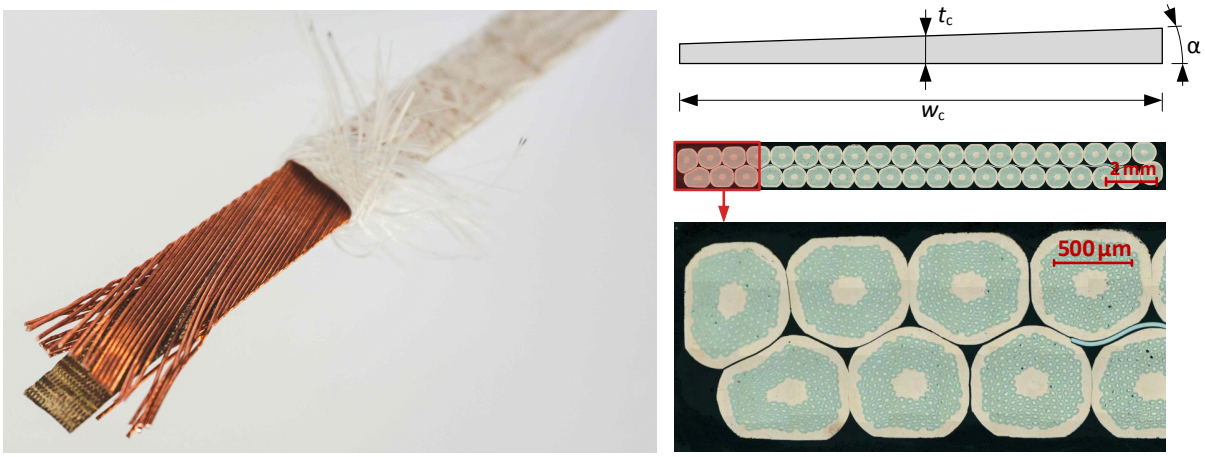

Figure 1.12: Rutherford cable for 11 T dipole development made of 40 Nb_3Sn strands with a nominal cross-section dimension of $w_c \times t_c = (14.7 \times 1.25)\,mm^2$, a keystone angle of $\alpha = 0.79°$ and a transposition pitch of 100 mm. **(a)** Picture of the slightly untwisted non-reacted cable with the austenitic steel core and S-2 glass sleeve. The C-shaped mica foil for additional insulation is not pictured. **(b)** Schematic and optical microscopy of the transverse cross section after reaction heat treatment and impregnation. The resulting deformation of the wires and sub-elements as well as the core at the thin edge are shown enlarged in the bottom micrograph.

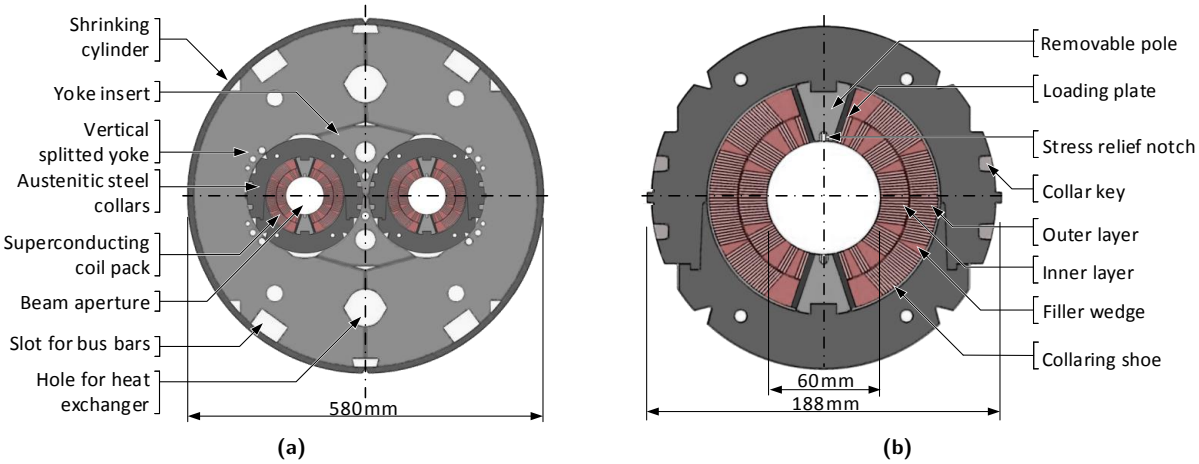

Figure 1.13: Schematic of the 11 T dipole magnet cross section. **(a)** Final cold mass assembly. **(b)** Collared coils from a single aperture enlarged from (a). Information taken from Reference [35] and edited by the presenting author.

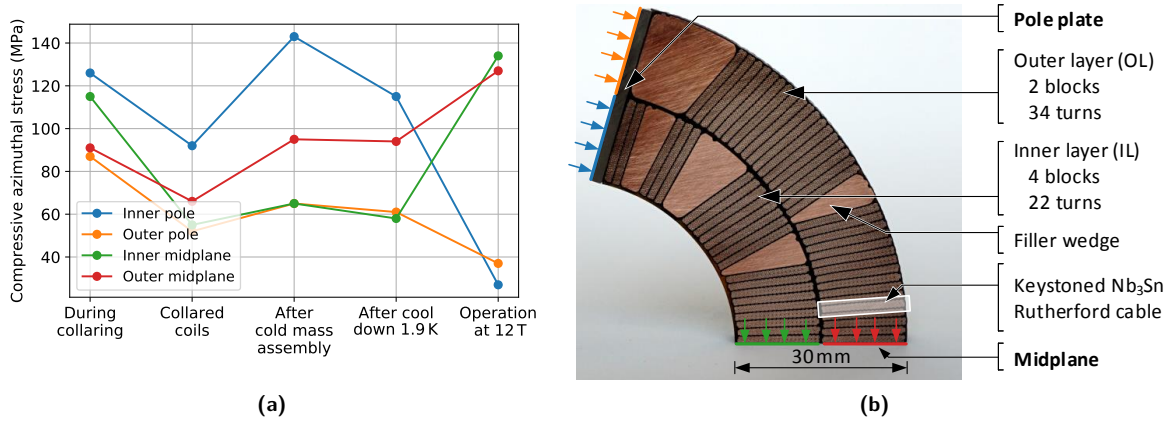

Figure 1.14: Stress distribution within a coil quadrant of the 11 T dipole magnet. **(a)** Assessment of the coil pre-stress in pole and mid-plane region during the manufacturing steps with the aid of FEM. Information taken from Reference [86]. **(b)** Extracted coil quadrant of the reacted and impregnated coils.

layer coils for the following manipulations.

After the the coils are wound, they are subjected to the necessary RHT, according to the "wind and react" technique. The approximately 5.4-m-long coils are placed into a reaction mould and transported into a heat treatment furnace [92]. The RHT is performed according to the wire manufacturer in three temperature dwells up to 650 °C with a specified homogeneity down to ±3 °C [139]. Including the temperature ramps of 50 °C h^{-1}, the RHT has a duration of approximately 200 h, which is further described in Section 2.1.

After the Nb_3Sn A-15 phase is formed, the coil should not be deformed to prevent breakage of the sub-elements, which would affect the superconducting performance negatively.

Subsequently, the coils are impregnated with epoxy resin CTD101K and placed in an impregnation mould for vacuum pressure impregnation (VPI) to guarantee the necessary mechanical stability of the brittle Nb_3Sn superconductor for the magnet assembly. The 11 T dipole design enables a mounting of the necessary quench heaters after impregnation. An extracted part of a reacted and impregnated coil is pictured in Figure 1.14(b).

3. Cold mass assembly

After the successful manufacturing of the four double-layer coils for the twin aperture, they are placed in groups into the helium vessel, i.e. the so-called cold mass assembly.

In order to withstand the high electromagnetic forces during operation, the two coils per aperture are pre-strained by force-restraining structures, known as collars. These collars are made of packs of austenitic steel laminations with vanishing magnetic susceptibility. The coils, including the beam pipes, are placed between an intermeshing collar. A finished collared coil group is shown in Figure 1.13(b). In order to pre-stress the coils, pressure is exerted by a hydraulic press on the collared coils, which is the so-called collaring press. The collaring keys are inserted under pressure so that a residual pre-stress is maintained after releasing the collaring press.

The magnet assembly process, in particular the collaring process, is considered to be one of the most crucial steps of magnet manufacturing with regard to mechanical design. The local stress distribution within the coil must locally not exceed the irreversible strain limit of the Nb_3Sn superconductor. Considering that this has to be guaranteed over the entire length of the 5.4-m-long coils, a complex composite material, it is a technological challenge that requires components with low manufacturing tolerances. The mechanical concept of the 11 T dipole magnet considered transferring the stress azimuthally by removable poles with stress relief notches [86, 6]. This guarantees a local azimuthal compressive stress of less than 150 MPa during all manufacturing steps and operation, which is commonly used as the pre-stress limit without irreversible damage.

Afterwards, the collared coils are equipped with the yoke insert and subsequently surrounded by the vertically split yoke. The yoke insert applies a symmetric load on the collared coils during the subsequent shrinking process. The yoke, made of ferrite laminations, shields the magnetic field. Afterwards, the entire assembly is placed between two 10-mm-thick stainless steel shells, known as the shrinking cylinder. The two shells are closed and welded under a hydraulic press, a so-called welding press, to guarantee an additional compaction of the assembly. The finished assembly can be seen in Figure 1.13(a).

After the cold mass assembly is closed, it is covered with a super-insulation and placed in a vacuum vessel with the necessary feed-through for electrical connection and subjected to the first tests at low temperatures.

4. Magnet testing and installation

Before the magnet is ready for installation and operation, it is tested at CERN (TE-MSC-TF). The magnet is cooled with superfluid helium to its operation point of 1.9 K. Every superconducting magnet must be trained to reach its nominal or ultimate performance level. This consists of iteratively ramping the current of the superconducting coils until a quench occurs. In order to prevent damage, every superconducting magnet is equipped with voltage taps and so-called quench heaters. This safety facility is used to perform a safe and spatially homogeneous transition of the entire coil to the normal-conducting state in the case of a local quench. The residual stored energy of the magnet is absorbed and dissipated by an external resistor, which prevents further temperature rise of the coil. The iterative quenching of a virgin magnet is followed by progressive improvement. This saturating training process is repeated several times until the nominal performance of the magnet is reached [139].

The origin of the training phenomenon is assumed to be caused by slight movements of the conductor within the virgin coil compound under the influence of tremendous electromagnetic forces. These quenches caused by such movements are reduced as the conductor reaches a more stable position after repetitive training runs, i.e. it becomes extensively embedded. The behaviour varies widely and depends on the conductor type, the coil geometry and the manufacturing of the magnet. The training

procedure was also applied to the impregnated cable specimens, as described in Section 4.1.2.

After training, the superconducting magnet is ready to be installed in the LHC in the DS region during the future long shutdown of the LHC, as mentioned in Section 1.1.

The substantial mechanical concept of the cold mass considers the coil pre-stress process in two parts: collaring and shrinking. The first FEM analysis by M. Karppinen *et al.* [86] regarding the stress distribution within the coil cross section indicated that the stress peak values during manufacturing are similar to those at full operation at 1.9 K and 12 T. The FEM is based on a model that uses cables with homogeneous material properties, meaning that local stress concentration effects of wires or even sub-elements with voids are not studied. The maximal values at the inner and outer mid-plane as well as pole plate of a quarter section after the crucial manufacturing steps are extracted and summarised in Figure 1.14.

Considering that the mechanical properties are temperature-sensitive and that manufacturing uncertainties must be accepted to a certain extent, damage to the brittle conductor can occur due to manufacturing. Moreover, the need for higher pre-stress of the 16 T magnets is discussed for the current designs to counteract the higher electromagnetic forces on the conductor. In combination with the high strain sensitivity of the Nb_3Sn wires, this was the original motivation to study the irreversible degradation of the superconductor caused by necessary applied stress during manufacturing. The investigation is covered by the 16 T dipole development programme, wound conductor task [90], which includes the presented work. The concretisation of the arising problem as well as the reason for the chosen experiments to investigate this topic are discussed in Section 1.5.

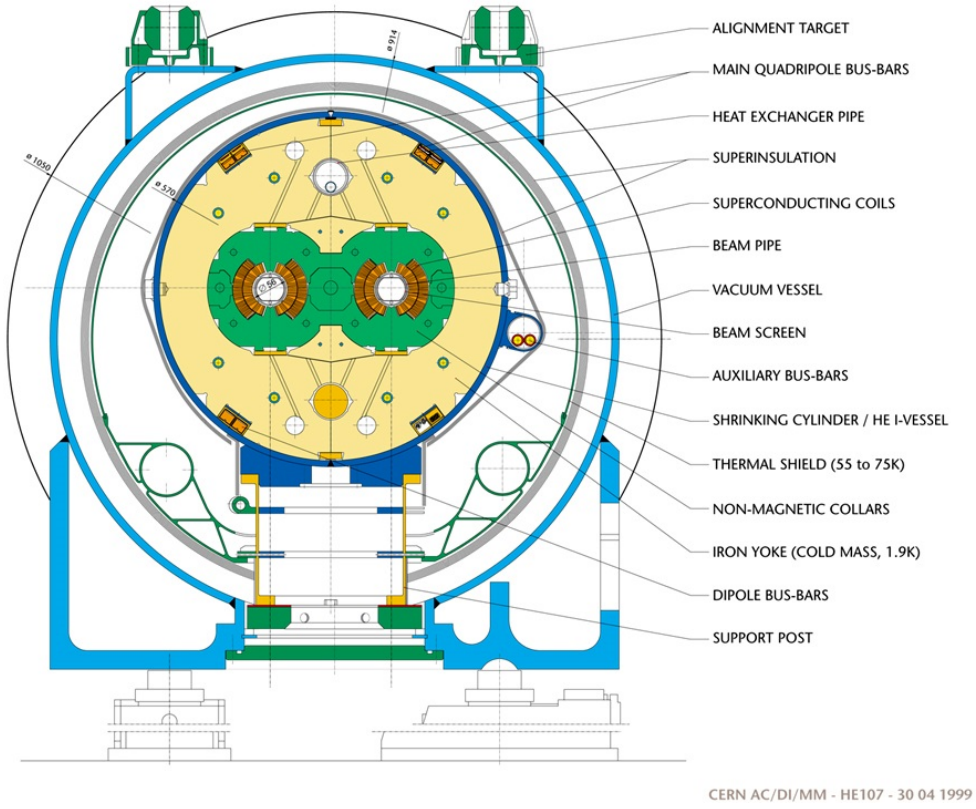

Figure 1.15: Cross section of the LHC dipole magnet. Twin-aperture coil-dominated made of Nb-Ti superconductors. Information taken from Reference [35].

1.4 Former investigations & literature research

Owing to the technological importance of strain dependency within magnet design, broad-based studies on wires and cables with different purposes and arrangements have been performed. Many load cases and identification measurements performed on **superconducting composite wires** were found during the author's literature research.

- J.W. Ekin [53] performed I_c-ε measurements with a stress-free cooling cryostat. The superconducting wire is not soldered or constrained in any other way during cooling, which allows measurements at the intrinsic pre-strain condition.
- In order to test the superconducting properties as a function of axial load, two common types are established to investigate stress, e.g. caused by the winding process of a magnet coil.

  The so-called Walter's spring [176] is a coil sample holder, which can apply axial tension or compression on a long superconducting wire by twisting or untwisting the spring, respectively. Researchers at the University of Geneva have published several experiments based on Walter's spring, including a modification to exert transverse stress on impregnated and non-impregnated Nb_3Sn wires [32, 36, 116, 147, 170].

  Another established possibility to apply axial stress was designed by B. ten Haken *et al.* [161] using a U-bending beam. The sample is soldered on the back of a U-spring, which can emulate axial tension or compression on the soldered wire by applying force on the arms on the other side. Although the sample length is limited, it performs the stress in axial direction with almost no undesired bending effects and was further used in recent experiments by M.G.T. Mentink [112]. Owing to the short sample length of the U-spring configuration, which inherently reduces the accuracy of the I_c measurements, A. Godeke *et al.* [68, 69] designed an additional bending device in a cylindrical shape called Packman.
- An experimental cryostat setup to analyse the hoop stress on wires within a ring coil was designed by J.W. Ekin [53]. It emulates the dominant load case within solenoid magnets.
- W. Goldacker *et al.* [70] designed a bending strain rig for continuous bending of high-temperature superconductors at 77 K, which can be used to determine essential properties for magnet design, e.g. maximal bending radius.

The properties of **superconducting cables** have been extensively tested as a function of transverse stress. The dominating load case on a superconducting coil compound in a $\cos(\vartheta)$-magnet (cf. Section 1.3) is in azimuthal direction. In order to simplify the experimental arrangement, cables are exposed to transverse stress.

- The University of Twente houses a cryogenic press that can load superconducting cables with more than 250 MPa perpendicular to an applied field of up to 15 T [42, 28, 163, 172, 188].
- At CERN, B. Bordini *et al.* [27, 26] performed measurements with a FRESCA-compatible sample holder for transverse stress up to 155 MPa parallel to an applied field of 10 T, based on an aluminium shell and a bladder-and-key system.
- A short sample test facility was used in the Fermi National Accelerator Laboratory (FNAL) to apply transverse stress on Nb_3Sn Rutherford cables [14].
- The Karlsruher Institute of Technology (KIT) implemented a setup for high-temperature superconductors to measure samples exposed to transverse stress [18].

All mentioned experiments are optimised for a specific purpose, and the respective stress application has to be considered when comparing results. The constraints due to the different thermal contraction of the sample and the material of the respective sample holder also have to be taken into account [165]. Some of the experiments focused on the fundamental reason behind the physical behaviour. Others were designed to be as close as possible to the final operation conditions within a magnet in order to deliver reliable parameters for magnet design.

Despite the ongoing investigations regarding strain at cryogenic temperatures, the impact of stress on the superconducting properties caused by the manufacturing of magnets has scarcely been investigated. In the author's literature research, only a few tests could be found, although FEM analyses showed high stresses on Nb_3Sn coils during the mechanical force-restraining procedure [86]. For instance, B. Jakob *et al.* [82] performed tests on impregnated Nb_3Sn Rutherford cables made of a bronze-process wire for the design of a 1 m Nb_3Sn demonstrator magnet within the context of the LHC investigations in 1990. In addition, tests of entire coils with different pre-stress were performed by H. Felice *et al.* [61] for US-LARP.

Regarding the developed **experimental NearT_c concept**, some former alternative implementations to reach variable-temperature measurements have been published. They are aimed primarily at evaluating the temperature margin of a wire's performance or confirming the temperature dependency of the

USL using a gaseous helium environment. For instance, B. ten Haken *et al.* [162] performed variable-temperature measurements above the atmospheric boiling point of helium with currents of up to 120 A. L.F. Goodrich *et al.* [72] implemented a variable sample temperature in the range of 4 K to 20 K with test currents of up to 200 A using a helium gas flow cryostat. Subsequently, L.F. Goodrich *et al.* [71] also implemented an apparatus with current leads for up to 400 A and a sample temperature range of 4 K to 200 K.

Based on this introduction, **the influence of stress and strain on the performance of Nb_3Sn composite wires** can be divided into three categories:

1. The **intrinsic properties of superconductivity material** are influenced by stress and strain. In conventional superconductors, superconductivity depends on the coupling of phonons and on the electronic system. Phonons are a property of the crystal lattice, which is directly affected by stress and strain. It is presumed that the cause of the strain dependency of the intrinsic properties is strain-induced phonon anharmonicity. For instance, D.F. Valentinis *et al.* [171] provided a model of strain dependency by means of the Eliashberg theory [60], especially the formulation by W.L. McMillan [110]. That publication emphasizes a broadening of the phonon spectrum due to anharmonic phonon generation. Consequently, electron-phonon coupling is reduced, which leads to a decrease of the intrinsic properties. Recently, W.D. Markiewicz [108] devised a model of $T_c(\varepsilon)$ with the help of the phonon spectrum and the Eliashberg function (cf. Figure 1.4(a)). Additionally, M.G.T. Mentink [112] performed a microscopy computation that complements experimental data.

2. In the case of state-of-the-art Nb_3Sn wires, the **flux pinning**, which is decisive for the **critical current**, is created primarily by the grain boundaries. Strain on the superconducting material influences its micro-structure, i.e. disorder or dislocation, and hence its pinning behaviour. For comparison, pinning centres in commercial Nb-Ti wires, which are primary α-Ti precipitates, are generated by a thermo-mechanical treatment. Additionally, $J_c(B, T)$ is indirectly influenced by the strain dependency of the upper critical field B_{c2} and critical temperature T_c.

3. High stress deforms the **copper matrix, and residual pre-stress** can be induced. Further exposure to stress yields **fractures and hence interruptions of the superconducting sub-elements** in transport current flow direction and reduces locally the effective superconducting cross section. The current has to flow alternatively in the normal-conducting part of the composite wire and generates Joule heating, which affects its stability margin. Consequently, the **thermal stabilisation of the wire is indirectly harmed**. These extrinsically irreversible processes are strongly dependent on the mechanical properties of the particular material, e.g. Young's modulus or yield strength. It should be noted that the sub-elements already suffer from pre-strain by design of the composite wire, namely the thermal-induced pre-compression ε_m.

The impact regarding these phenomena is dependent on the geometric structure of the composite wire, i.e. how stress is distributed and effectively applied to the superconducting material, i.e. the sub-elements. High-energy X-ray diffraction experiments and analysis of the lattice parameter revealed a mixture of hydrostatic and deviatoric deformation during the application of stress [118]. Generally, the irreversible impact of stress is given by the plastic deformation of the copper matrix and the fracture of the superconducting material, which is also the focus of the presented work.

1.5 Scope & overview of thesis

The topic of the thesis belongs to one of three subtasks of the wound conductor task of the FCC 16 T dipole development programme, which is further described in Section 1.1.

The original objective of this thesis was to determine the performance loss of the superconductor due to the manufacturing of accelerator magnets. It can be assumed that the degradation of the conductor is provoked after the RHT of the Nb_3Sn coil, which forms the brittle A-15 phase and makes the compound conductor vulnerable to mechanical damages, i.e. it then has a very low acceptance of induced mechanical stress. As emphasised in the above sections, the most critical part of the magnet assembly is the application of pre-stress on the coils. In the case of the 11 T dipole magnet, discussed in Section 1.3, the pre-stress is applied by the force-restraining procedure including welding the shrinking cylinder (collared coils). The required high pressure of up to 150 MPa is then applied to the superconducting coils. For the manufacturing of magnets with higher nominal fields, higher pre-stresses are contemplated to counteract the higher Lorentz forces during operation.

The dominating load case on a coil of the most common accelerator magnets during magnet assembly is in azimuthal compressive or transverse compressive direction, depending on the magnet type.

In general, the dominating force on an individual cable in the coil can be assumed to be in transverse direction. This **concretises the topic on quantification and cause analysis of the degradation of Nb_3Sn cables and wires due to transverse stress at room temperature**. Consequently, the investigation stands in contrast to the currently well-investigated stress at low temperature, which is annotated in the literature research. The manufacturing and testing of the entire coils were excluded for economical and experimental reasons, and hence the investigation was split into the following parts to fulfil the objectives sketched in Figure 1.16:

- **Development of homogeneous stress application**
  Stress was applied to the cables and wires by applying pressure with a hydraulic press. Therefore, the hydraulic system was refurbished, including calibrated load cells, to measure the force applied to the specimens. In order to measure and further optimise the stress distribution, pressure-sensitive films were used. An evaluation script was developed to analyse and overlap the multilayer films.

- **Cable investigation**
  Impregnated Rutherford cable double stacks were loaded with transverse stress at RT and subsequently tested in the FRESCA cable test station at CERN. This experiment provides results similar to the actual application in a magnet coil, which is considered to be a valuable contribution to magnet design and refinement of the manufacturing process. Moreover, the results include mechanical effects of the coil and cable compound, e.g. mechanical behaviour of the epoxy resin and cable geometry. In parallel, the working group performed an X-ray tomography for a FEM model to estimate the partial stress within the compound conductor.

  Therefore, three state-of-the-art Nb_3Sn cable specimens from the HL-LHC were prepared and tested, which included fabricating inaccuracies of the cables. A loaded and non-loaded part of the first specimen was metallographically prepared and investigated with an SEM, as described below.

- **Wire investigation and research of alternative measurement methods**
  Although the cable experiment is similar to the actual application, it only delivers information about a specific cable configuration and must be repeated if the cable properties are changed. The results include electrodynamic effects of the cable, which makes it difficult to analyse the actual cause. Moreover, cables or coil tests are highly demanding, and only the critical current I_c could be evaluated in the experiment mentioned above. For that reason, a simplified experiment based on a single wire was conducted to perform a root cause analysis about the degradation of the superconducting material independent of the actual cable or coil configuration.

  This investigation comprised the following parts. First, a cryostat insert was developed to perform transport current measurements up to 150 A on a straight wire in self-field. This should prevent damage of the specimen due to the Lorentz force and, furthermore, it should demonstrate alternative measurement methods. A characterisation of superconducting wires without the need of a background magnet and a continuous supply of liquid helium (LHe) should be verified. The latter is achievable because the system must not necessarily be cooled to the boiling point of helium and hence can be operated preferably with a cryogenic refrigerator system (cryocooler). These measurements were complemented by low-resistance measurements, and consequently by the evaluation of the critical temperature T_c and residual resistance ratio RRR. The second part was a confirmation of the transport current measurements by magnetisation measurements with a SQUID magnetometer, which was used to determine the critical current density J_c, the critical temperature T_c and the upper critical field B_{c2}. This should also clarify the suitability of magnetometric methods for crack detection because magnetometry is also a less demanding characterisation method for superconductors. An additional part was a microscopy investigation to detect and analyse cracks in the sub-elements caused by transverse stress. This reflects the behaviour of the measured (macroscopic) superconducting properties.

  Moreover, the working group subjected loaded wires to an X-ray tomography in order to develop a FEM model. Subsequently, a FEM simulation was performed to assess the stress condition within the wire, especially the residual strain due to plastic deformations. This links the local stress to the measured I_c degradation and observed crack initiation. This universal information could be further used to estimate the I_c degradation based on a FEM stress analysis of any specific cable or coil cross section, which tracks the local stress values on the sub-elements [41]. It was provided a preliminary assessment of crack formations and I_c degradation caused by transverse stress at RT of various configurations, e.g. different impregnation materials and strand diameters without costly cable or coil tests.

- **Microscopy investigations and development of a metallographic procedure**
  In order to obtain more information on the presumed leading cause of degradation, the fracture of the Nb_3Sn, a further microscopy investigation was mandatory. Initial non-destructive X-ray tomography turned out to be insufficient, which triggered metallographic investigations to observe the formation of cracks in the sub-elements. Metallographic techniques were developed to detect and characterise cracks in transversal and longitudinal layers. Furthermore, chemical extraction with nitric acid was performed to confirm the reliability of the mechanical preparation.

This document is structured as follows:

- **Chapter 1** presents the technical and physical background upon which this thesis is based. Furthermore, it gives an overview of ongoing investigations within the research community of Nb_3Sn material and accelerator magnets. Finally, it introduces the topic and describes the experiments performed for this thesis.
- **Chapter 2** lists all analysed specimens including their properties as well as the metallographic preparation process for SEM developed within the scope of this thesis.
- **Chapter 3** provides a detailed description of the methods to achieve the results. All systems, especially the self-designed cryostat insert for the wire investigation, are described. Furthermore, all procedures for measurements and data evaluation are discussed.
- **Chapter 4** presents all relevant data and provides a detailed discussion of the measurements. It presents the achieved results, puts them into context with previous publications and refers to the corresponding published theories. The conclusion and outlook are summarised in the last sections.

The work presented in this thesis was published to a great extent in two journal articles [48, 49] by the presenting author as main author and a conference publication [182] as co-author. Moreover, internal technical notes were composed at CERN [47, 67].

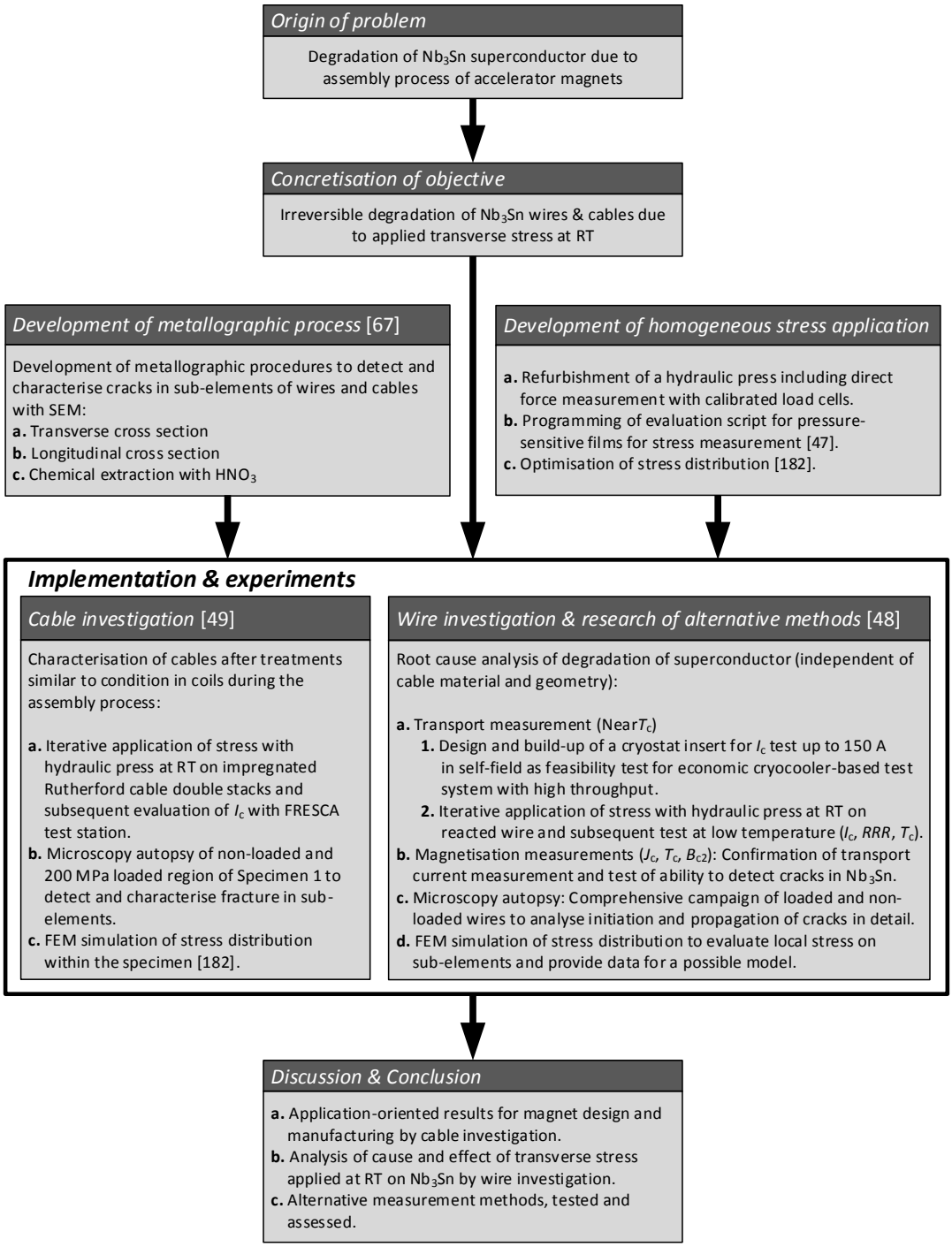

Figure 1.16: Overview of presented work.

Chapter 2

Specimen specification & preparation

This chapter describes the measured specimens and preparations to investigate the degradation process of the superconductor caused by transverse stress applied at RT. Section 2.1 presents the wire specimen for the NearT_c transport current measurements and the magnetisation measurements with the SQUID magnetometer. The cable specimens, i.e. impregnated Rutherford cable double stacks produced to be tested in the FRESCA cable test station, are discussed in Section 2.2. Finally, Section 2.3 summarises the metallographic techniques, which were employed for the autopsy of the specimens. A scanning electron microscope was used especially to characterise crack formation in the sub-elements.

2.1 Wire for transport current & magnetisation measurements

For the wire investigation, the Nb_3Sn compound wire RRP144/169 with the specifications summarised in Table 2.1 was chosen. Owing to the brittleness of Nb_3Sn, it cannot be directly processed from bulk to a usable superconducting compound wire, as emphasised in Section 1.2. Thus, the wires were subjected to the RHT in argon atmosphere according to the manufacturer's instructions. This was performed by putting 160-mm-long pieces of the wire in straight ceramic cavities and inserting them into the horizontal tube furnace *Carbolite GHC 12/750* at CERN.

Table 2.1: Specifications of the wire RRP144/169 for the wire investigation and the first cable specimen HT15OC0190. OST has been part of Bruker Energy and Supercon Technologies (BEST) since the end of 2016.

Manufacturer	Oxford Superconducting Technology (OST)
Type	RRP144/169
Cu/nonCu ratio	1.08
No. of sub-elements	144
Wire diameter	0.7 mm
Sub-element diameter	41 µm
Sub-element shape	hexagonal
Pitch length	14 mm (right-hand)
RHT	48 h at 210 °C 48 h at 400 °C 50 h at 650 °C

2.1.1 Wire type & reaction heat treatment

A microscopy of the chosen wire before and after reaction heat treatment (RHT) can be seen in Figure 2.1 and 2.2, respectively. Figure 2.1(b) shows the non-reacted sub-elements in detail. Every distributed-barrier internal tin wire, in the present case a RRP wire, houses a tin (Sn) core. The core is surrounded by niobium (Nb) filaments, embedded in copper (Cu) and surrounded by a niobium barrier. The primary purpose of the barrier is to avoid the diffusion of tin into the high-purity copper matrix during RHT. This would reduce the *RRR* and impair the thermal stability of the wire.

In the first steps of the RHT, i.e. in the range of 200 °C to 500 °C, the tin of the core diffuses in radial direction and mixes with the inter-filamentary copper. This is performed to achieve a homogeneous tin

concentration of 18 to 25 at.% within the sub-element, which is mandatory to form a stable Nb_3Sn phase later on [33, 115]. The desired A-15 phase Nb_3Sn is formed with the niobium filaments in the following final high-temperature step at approximately 650 °C. Additional doping agents, titanium rods in the presented case, are implemented among niobium filaments to optimise intrinsic properties such as the critical temperature T_c and upper critical magnetic field B_{c2} [65].

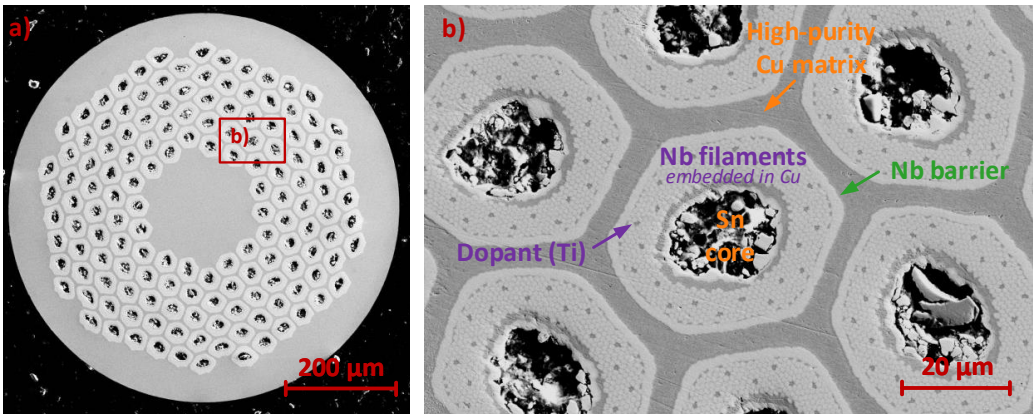

Figure 2.1: SEM micrographs of the non-reacted wire specimen RRP144/169. **(a)** Overview of the wire with a diameter of 0.7 mm and 144 sub-elements. **(b)** Detailed view of the non-reacted sub-elements with their labelled components, obtained by an energy dispersive X-ray analysis (EDX).

Figure 2.2 shows the fully reacted wire after RHT, especially the superconducting Nb_3Sn sub-elements in the right-hand part. The outer brighter layer of the sub-elements is superconducting Nb_3Sn, and the core consists of residual α-bronze. As discussed in Section 1.2, the critical current is determined by pinning the Abrikosov vortices. Without going into detail, it should be mentioned that the volume pinning force is primarily dependent on the micro-structure of the material, especially on the grain boundaries in the case of Nb_3Sn wires [142, 166]. Owing to the reaction process during RHT, the average grain boundary size is roughly 100 nm to 200 nm. Consequently, the refinement of the grain size is currently the subject of further research [185, 186] and serves as a possible strategy to achieve the FCC Nb_3Sn target performance of $1.5 \cdot 10^9$ A m^{-2} at 16 T and 4.2 K [169]. However, large grains with an average size of 2 µm also formed on the inner border of the sub-elements. Their contribution to transport current is minimal, which could especially be observed in Power-In-Tube (PIT) Nb_3Sn wires [160].

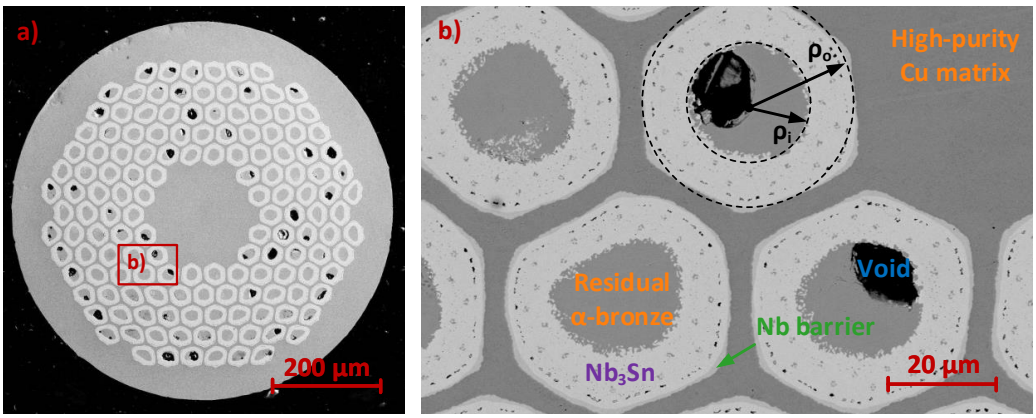

Figure 2.2: SEM micrographs of the reacted wire specimen RRP144/169. **(a)** Overview. **(b)** Detailed view of the reacted superconducting sub-elements including the inner and outer radius ρ_i and ρ_o used for the calculation in accordance with the magnetisation measurements.

Another undesired effect caused by the reaction process is the formation of so-called Kirkendall voids [140, 141], see Figure 2.2. This inherent phenomenon is also the objective of recent research regarding the optimisation of the RHT [13, 36, 187]. Kirkendall voids are formed mainly during the mixture of tin and copper in the lower temperature dwells and can be traced back to a volume density change during the phase transformations. These cavities in the centre of the reacted sub-elements have an essential impact on mechanical properties and the irreversible I_c degradation, as further discussed in Chapter 4.

2.1.2 Specimens

The reacted 160-mm-long specimen for the NearT_c transport current measurements was soldered with Sn-Pb solder alloy on the sample holder with no additional preparation steps, as further described in Section 3.3. The wire and the current plates, connected with the transport bars, were heated homogeneously and only slightly above the solder's liquidus temperature (roughly 200 °C) to avoid any thermal gradients during soldering. Subsequently, the wire was placed carefully in the intended grooves filled with solder. Afterwards, the voltage leads made of enamelled copper wire were soldered, as can be seen in Figure 3.14.

It should be noted that the current connector length of 40 mm and the voltage-tap spacing of 64 mm is a multiple of the sub-element pitch length (cf. Table 2.1) in order to guarantee a homogeneous current distribution within the voltage-tap placements [52, 57].

Specimens for the magnetisation measurement and microscopy autopsy were cut into small pieces with a *Diamond WireTech DWS 250* saw. Therefore, reacted 60-mm-long wires were exposed to transverse stress, as described in Section 3.1. Later, small pieces of the middle of the stressed region were extracted by cutting. This ensured that the same amount of stress was applied as for the NearT_c specimen, and avoided using short samples extracted from the end of the stress region. Figure 2.6 shows a longitudinal autopsy of the cut, which revealed a crack penetration depth of the cut of less than 50 µm.

Wires for the magnetisation measurement were cut into approximately 4-mm-long specimens, as can be seen in Figure 3.22(b). The length was chosen in order to fulfil the requirements of the models discussed in Section 3.4. Wires for the microscopy observation as well as the sawing procedure are further discussed in Section 2.3.

2.2 Impregnated cables for transport current measurements

The cable investigation implies the measurements of three specimens, which were specially prepared for cable performance characterisation. The Rutherford cable types, used in the first two specimens, were designed for the 11 T dipole project, and the latter originates from the MQXF quadrupole development. The cables are manufactured at CERN [31, 133], and their specifications are listed in Table 2.2.

The cables used for Specimen 1 and Specimen 2 are both from the 11 T dipole development, and consequently had the same cross-section dimensions and transposition pitch. Specimen 1 was made of the same strand as used in the wire investigations (cf. Table 2.1). The specifications of the strands used in the other two cables are summarised in Table 2.3 and 2.4, respectively. The strand of Specimen 3 had a larger diameter, which resulted in a larger cable cross-section dimension. All cables were keystoned, equipped with a stainless steel core and insulated with a braided S-2 glass sleeve [152], as applied for the coil production.

Table 2.2: Specification of the cables used for the specimens in the cable investigation.

	Specimen 1	Specimen 2	Specimen 3
Cable ID	HT15OC0190	HT15OC0210	HT16OC0217
Manufacturer	CERN		
Project	11 T dipole	11 T dipole	MQXF quadrupole
Strand type	RRP144/169	RRP108/127	RRP108/127
Strand diameter	0.7 mm	0.7 mm	0.85 mm
Number of strands	40		
Transposition pitch	100 mm	100 mm	109 mm
Transposition direction	left-handed		
Width	14.7 mm	14.7 mm	18.15 mm
Middle thickness	1.25 mm	1.25 mm	1.525 mm
Keystone angle	0.79°	0.79°	0.4°
Thin edge compaction	17.95 %	17.95 %	15.42 %
Thick edge compaction	3.48 %	3.48 %	5.17 %
Core material	316LN (austenitic steel)		
Core dimension	12 mm × 24.3 µm		
Insulation material	S-2 glass braiding sleeve		
Insulation thickness	0.2 mm		
Additional insulation	none	C-shape mica	none

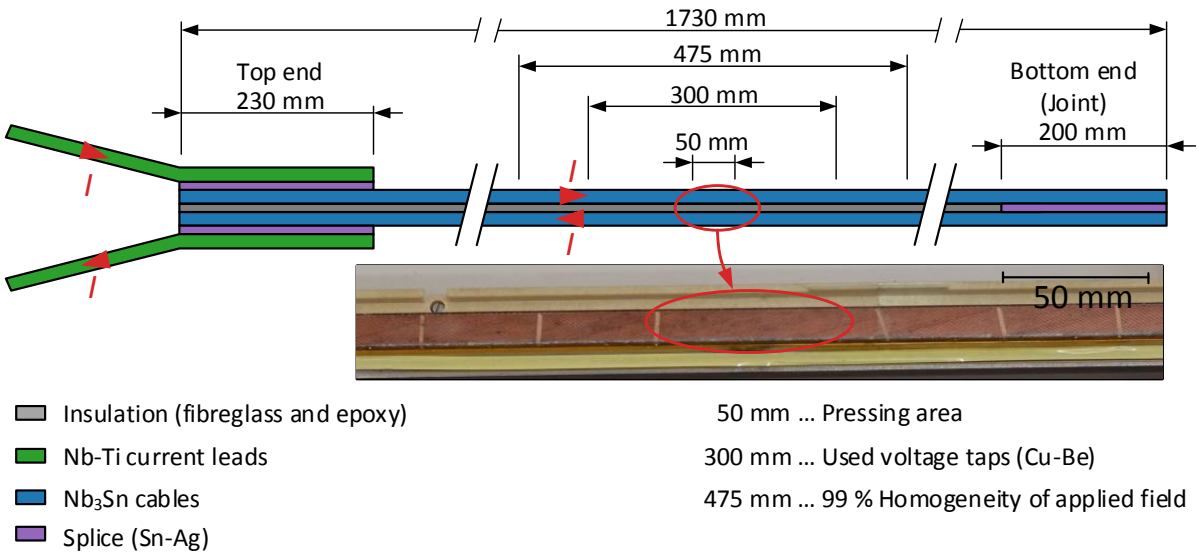

Figure 2.3: Schematics including dimensions of the FRESCA-compatible cable specimens, keystone-compensated Rutherford cable double stacks with Nb-Ti current leads. An image of Specimen 1 including voltage taps (cable type HT15OC0190) in the opened FRESCA sample holder is shown in the bottom right part.

2.2.1 FRESCA-compatible specimens

The specimens were made as shown in Figure 2.3 to meet two requirements: applying transverse stress on the reacted and impregnated specimen and characterising it in the FRESCA test station. An approximately 1.7-m-long keystone-compensated Rutherford cable double stack was made of a single cable type. The typical cross section can be seen in Figure 2.4. This arrangement allowed a planar surface to apply transverse stress and ensured a closed measurement circuit for the I_c measurements. The samples were manufactured at CERN as described:

1. The already insulated non-reacted cables were wrapped together with a 0.2-mm-thick S-2 glass braided band. Subsequently, voltage taps made of copper-beryllium (Cu-Be) were laterally placed over the entire cable width, underneath the sleeve at certain locations. The location and purpose of the specific voltage tap is further described in Section 3.2. In order to prevent short-circuits between the cables, the voltage taps of the upper and lower cables were mounted with a shift of 20 mm. The insulation on the bottom end was removed, and a 200-mm-long copper foil was placed between the cables to create an electrical connection.

2. The prepared specimen was subjected to the mandatory RHT to form the superconducting A-15 phase in the sub-elements. This was performed by housing the samples in a dedicated reaction mould and using the furnace *Carbolite GLO 750KE/09-1G*. Additionally, the voltage taps and the copper foil were bonded inherently by diffusion at these high temperatures.

3. In the next step, the bottom ends were soldered together with Sn-Ag solder alloy to form the so-called bottom joint. Next, the specimen was impregnated in a dedicated impregnation mould by vacuum pressure impregnation (VPI) with epoxy resin CTD101K, whereby the top end was covered for further processing. The average gap between the two cables within the stack was approximately 0.3 mm.

4. In the last step, the required ductile Nb-Ti current leads were soldered to the top end of the double stack over a length of 230 mm. They were subsequently used to electrically connect the specimen with the sample holder insert of the FRESCA test station. Finally, the lateral part of the voltage taps was revealed for soldering with the signal wiring.

As indicated in Figure 2.3, the test current I was fed by the current leads, and the bottom parts of the cables were soldered together. Hence, by connecting the specimen to the current source, an anti-parallel current flow was generated. Both cables were equipped with voltage taps to allow simultaneous measurement and analysis. An area with a length of 50 mm was defined for pressing in the centre of the specimen. This ensured a pressing area over a half pitch length without voltage taps. Moreover, this placement guaranteed I_c measurements in the desired high-homogeneity region of the applied field of

the FRESCA test station. According to the test run at the beginning of each measurement session, the splices on the top and bottom ends had a resistance in the range of 0.3 nΩ at low temperature [21].

Specimens 1 and 2 were impregnated without additional layers and had a nominal cross section area of $(15.6 \times 1.8)\,\mathrm{mm}^2$, which can be seen in Figure 2.4(a). Thus, the stress exertion was performed on the epoxy resin.

At the end of the investigations, another test configuration was chosen for Specimen 3 by impregnating additional titanium bars parallel to the cable stack in a sandwich arrangement, as can be seen in Figure 2.4(b). The titanium bars with a cross section of $(18.7 \times 2.1)\,\mathrm{mm}^2$ as well as the larger MQXF cable type enlarged the specimen cross section to $(19.3 \times 9.0)\,\mathrm{mm}^2$.

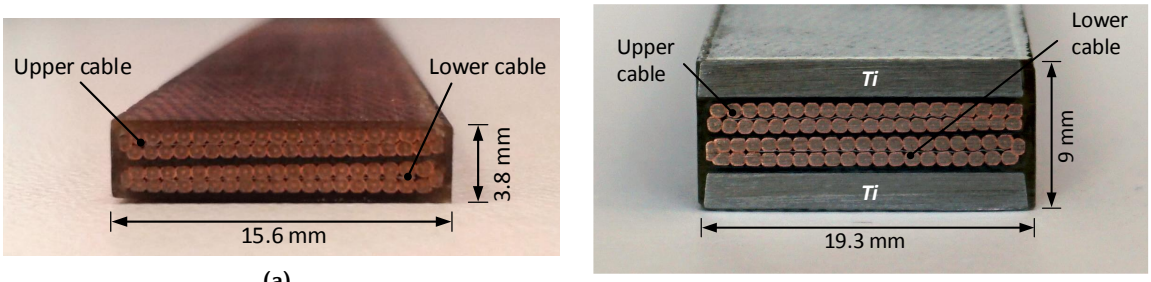

Figure 2.4: Images of the specimens' cross sections, impregnated Rutherford cable double stacks. **(a)** Specimens 1 and 2 with cable types HT15OC0190 and HT15OC0210, respectively (for the 11 T dipole development). **(b)** Additional Specimen 3 with cable type HT16OC0217 (for the MXQF quadrupole development) and titanium shims in sandwich arrangement.

Table 2.3: Specification of the wire RRP108/127 (Ø=0.7 mm) used for the second cable specimen HT15OC0210.

Manufacturer	see Table 2.1
Type	RRP108/127
Cu/nonCu ratio	1.15
No. of sub-elements	108
Wire diameter	0.7 mm
Sub-element diameter	46 µm
Sub-element shape	hexagonal
Pitch length	14 mm (right-handed)
RHT	see Table 2.1

Table 2.4: Specification of the wire RRP108/127 (Ø=0.85 mm) used for the second cable specimen HT16OC0217.

Manufacturer	see table 2.1
Type	RRP108/127
Cu/nonCu ratio	1.2
No. of sub-elements	108
Wire diameter	0.85 mm
Sub-element diameter	55 µm
Sub-element shape	hexagonal
Pitch length	19 mm (right-handed)
RHT	see Table 2.1

2.3 Metallographic preparation techniques

Previous publications indicated that crack formation in the high-stress range of brittle Nb_3Sn sub-elements is the leading cause of performance loss [32], [55, p.436]. Hence, it was essential to investigate the cracks in sub-elements and the search for proper tools

- to detect cracks and analyse their propagation,
- to determinate the stress threshold of crack initiation and
- to investigate their relevance to the critical current degradation.

Initial non-destructive X-ray tomography of loaded specimens delivered only insufficient resolution for crack detection and analysis [49], which was the reason to pursue the metallographic research and development described here.

Considering that the already very brittle Nb_3Sn sub-elements with potential cracks host cavities, i.e. voids, and are embedded in a soft-annealed copper matrix, it is a metallographic challenge to reveal cracks unequivocally without causing polishing damage. Sophisticated polishing is necessary to reliably reveal the sub-elements and in particular the cracks, which are in the range of a few micrometres, from

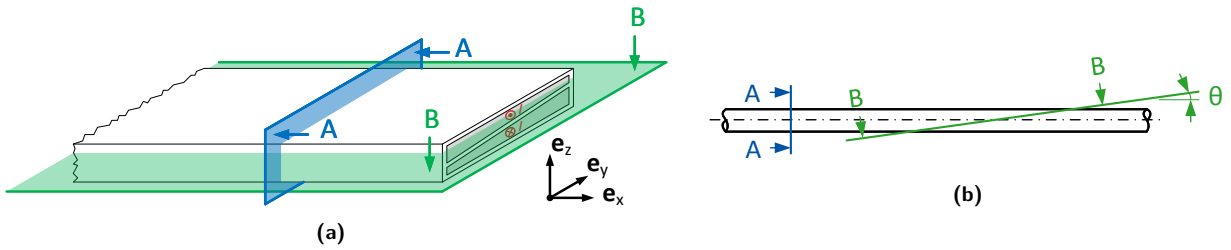

Figure 2.5: Schematics of the prepared layers to detect and characterise cracks in the Nb_3Sn sub-elements (A-A: transverse cross section, B-B: longitudinal cross section). **(a)** Layers in the case of the cable specimen. **(b)** Layers in the case of the wire specimens. To explore the entire cross section longitudinally, the preparation of the longitudinal cross section was performed with a tilt angle of approximately $\theta = 2°$.

this given surface with fluctuating hardness. Furthermore, the behaviour of crack formation, especially caused by transverse stress, has only barely been investigated in the past.

The author's literature research found only a few investigations of metallographic extraction of cracks in Nb_3Sn compound wires, e.g. regarding cracks caused by axial and bending stress by M.C. Jewell *et al.* [83] and electromagnetic forces by C. Sanabria *et al.* [137]. On the base this information, the following three supplementary techniques were chosen, further developed and evaluated for crack examination:

1. Preparation of the **transverse cross section**, i.e. perpendicular to the current flow, which is denoted by A-A or YZ-plane in Figure 2.5. This common method delivers general information about the wire, e.g. the number of sub-elements, average sub-element size and condition of the superconducting area, after only rudimentary polishing. In the presented work, more extensive polishing was necessary for crack detection. The transverse cross section was used primarily to detect cracks as well as to reveal the crack distribution and density within the cable and the wire.

2. Preparation of the **longitudinal cross section**, which is denoted by B-B or XY-plane in Figure 2.5. This method was used to characterise the shape and propagation of the cracks. For the latter wire investigation, the longitudinal cross section was made with a tilt angle of approximately $\theta = 2°$ to explore several layers simultaneously.

3. **Chemical extraction of the sub-elements with nitric acid (HNO_3)**. Nitric acid reacts with and especially dissolves copper, which reveals the sub-elements without applying any mechanical treatment. This method was used only within the wire investigation to confirm the results obtained with the methods described above.

After completing the final load step of 200 MPa of Specimen 1 cable, a metallographic preparation for crack examination was launched. In order to exclude ambiguities and misinterpretation, a non-loaded part of the approximately 1.7 m specimen was metallographically prepared as well.

On the basis of this success, a metallographic campaign within the wire investigation was developed. Wires of the same type as for the transport current and magnetisation measurement were loaded with particular stress from 0 MPa to 200 MPa and metallographically prepared for the microscopy investigation to detect the crack initiation and analyse the crack formation and behaviour in detail. Therefore, Nb_3Sn was chemically extracted to confirm the results of transversal and longitudinal cross sections. Similar to the cable specimen examination, the non-loaded case was also examined to guarantee an unobjectionable preparation, which does not cause cracks.

The following metallographic steps were performed to prepare the transverse and longitudinal cross section of cables and wires for electron microscopy:

1. The specimens were carefully cut with the above-mentioned diamond wire saw at a speed less of than 2.5 m s^{-1}. The specimens were cut into approximately 25-mm-long pieces. A later observation shows a penetration depth of the cracks caused by the cut of less than 50 µm, which can be seen in Figure 2.6. Considering that the following grinding and polishing steps removed more than 0.7 mm of the surface vertically and the longitudinal cross sections were observed only in the centre of the sample, this circumstance did not influence the investigation.

2. The specimens were embedded in cold epoxy resin by vacuum pressure impregnation.

3. Subsequently, the surface was ground with fine-grained silicon carbide (SiC) grinding paper up to the target level.

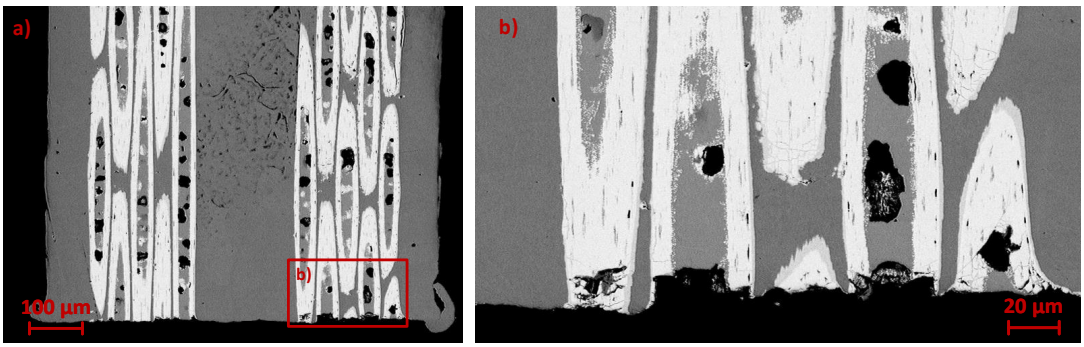

Figure 2.6: SEM micrographs of the end of the specimen. One can see that the cracks influenced by the cut propagate less than 50 µm. This result can be regarded as a quality check because the observed cracks in the centre of the specimen are not influenced by the cut with the diamond wire saw.

4. The surface was polished with polishing paper in combination with water-based diamond paste as well as a vibratory polisher with colloidal silica.
5. As the last step, the surface was automatically cleaned with a mixture of water rinsing and ultrasound, then dried.
6. Prior to the electron microscopy session, the sample was sputter-coated with several nanometres of a gold-palladium alloy (Au-Pd), to preventively improve the signal-to-noise ratio and hence obtain a better quality of the SEM micrographs.

Wire specimens for chemical extraction of the sub-elements were exposed to HNO_3 50 vol.%, rinsed with distilled water, dried and subsequently also studied in a scanning electron microscope. Embedded samples were sprinkled with a few drops of HNO_3, which dissolved the copper by roughly 300 µm after an exposure time of 60 min. A typical result is shown in Figure 2.7, observed at a slightly tilted view. Furthermore, the outer surface of the niobium barrier and the inner boundary of the Nb_3Sn area, the diffusion zone, can be observed. Moreover, loose wires with a length of approximately 25 mm were dipped in a bath of HNO_3 for 20 min. These wires were only dipped half way into the acid and for a relatively short time to prevent the copper matrix from dissolving entirely by capillary attraction. The metallographic processes described in this section are additionally summarised in Reference [67] and made it feasible to evaluate the cracks down to a size of 0.5 µm.

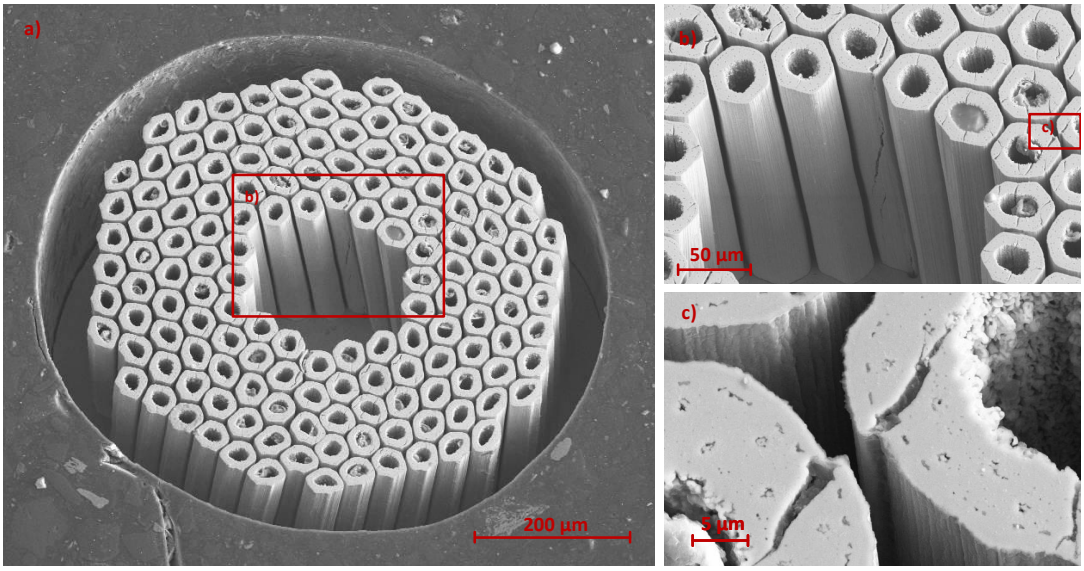

Figure 2.7: SEM micrographs of sub-elements of a loaded and embedded wire chemically extracted with nitric acid. This metallographic technique allowed the examination of the sub-elements with no mechanical treatment. Owing to the dissolution of the cooper, the intended twist of the sub-elements as well as their inner and outer border are clearly visible.

Chapter 3

Measurement procedures

This chapter presents the measurement methods and procedures used in this thesis. Section 3.1 describes the hydraulic press system, the self-programmed evaluation script for pressure-sensitive films as well as the stress application on cable and wire specimens. The FRESCA cable test station to determinate the degradation on impregnated cables after a certain stress level at RT is described in Section 3.2. The implementation of the transport current measurement near the critical temperature for loaded wires, so-called NearT_c, is elaborated in Section 3.3. Section 3.4 describes the measurement methods used with the SQUID magnetometer to obtain the critical current as well as the intrinsic parameter T_c and B_{c2} of wires after a particular transverse stress at RT.

3.1 Application of transverse stress at room temperature

In order to apply a well-defined homogeneous transverse compressive stress on Rutherford cables and wires at RT, a hydraulic press was refurbished and can be seen in Figure 3.1. The hydraulic jack with a maximal force of 200 kN is powered by a hydraulic circuit with a nominal pressure of 150 bar. The resulting pressure on the piston can be controlled by an analogue proportional valve with a 4–20 mA current loop. Major renewals have been implemented to the system allowing adequate loading of the specimens:

- A new state-of-the-art proportional valve with an integrated digital axis controller (*Bosch Rexroth 4WRPDH*) was purchased to ensure an accurate feedback-controlled adjustment of the hydraulic pressure.
- A new pressing insert was designed to apply homogeneous pressure distribution on the specimens, which is also highlighted in Figure 3.1 [182]. The applied force was evaluated by implementing four calibrated load cells (*Burster Druckkraftsensor 8526*) with a measurement range from 0 MPa to 200 MPa and an accuracy of 0.05 %. They were arranged in a planar rectangle with a side length of 85 mm. The support points of the load cells were aligned horizontally with stainless steel shims to an accuracy of 5 µm in order to achieve equivalent load balance. Furthermore, the pressing die was manufactured with a radius of 3 mm to prevent stress peaks at the end of the pressing area.
- In addition to the direct force measurement, pressure-sensitive films from the *FujiFilm Corporation* [66] were used to analyse and optimise the stress distribution on the surface of the specimen. These so-called *Prescale films* can be placed as an intermediate layer on the pressure surface and deliver a two-dimensional red-colour density imprint of the pressurised area. This allows an evaluation of the pressure independently of the force measurement.

Prescale films are available in certain measurement ranges, whereby the types MS (10 MPa to 50 MPa), HS (50 MPa to 130 MPa), HHS (130 MPa to 300 MPa) were used in the presented work. They have a spatial resolution of 0.1 mm and the pressure accuracy is ±10 % according to the manual. The two-dimensional red-colour density imprint is proportional to the applied pressure. The available manual allows a comparison with the reference colour samples, and the measured pressure can be visualised in a diagram.

To evaluate the stress distribution quantitatively, the Prescale films were scanned and the digital images were analysed with a self-designed script written in *MathWorks MATLAB* using the *Image Processing Toolbox* [164]. Every pixel i of the image is associated with a colour density value x_i. This value is subsequently transferred to an intermediate quantity $y_i = g(x_i)$ by using the spline-interpolation function

Figure 3.1: Setup for applying transverse compressive stress on the cable and wire specimens. 1. Pressing insert, 2. Hydraulic jack, 3. Hydraulic circuit, 4. Supports with support bar, 5. Control unit, 6. Load cells.

$g(x)$, which is obtained from the scanned reference colour samples. The intermediate quantity is further converted into the required pressure value $\sigma_i = f(y_i)$ in MPa by the spline-interpolation function $f(y)$, which is derived from the plot in the manual. Hence, the software uses the composition function

$$h(x_i) = (f \circ g)(x_i) = \sigma_i \tag{3.1}$$

to determinate the measured pressure σ_i out of a colour density value x_i of the pixel i. Owing to the necessary bijectivity of $h(x)$, the inverse function $x = h^{-1}(\sigma)$ can be derived. Pixels that are too bright or dark for the evaluation can consequently be deleted in advance. Figure 3.2 shows a typical input and output of the programmed software, whereby pressure values outside the measurement range of the film are shown in white.

Moreover, the stress values of the entire pressing area A_P can be used to integrate the force F_P numerically. It can be compared with the entire force $F_{\mathrm{LC},\Sigma}$ measured by the calibrated load cells

$$F_{\mathrm{LC},\Sigma} = \sum_{j=0}^{3} F_{\mathrm{LC},j} \approx F_\mathrm{P} = \sum_{i=0}^{n} h(x_i)\, A_\mathrm{P}, \tag{3.2}$$

where $F_{\mathrm{LC},j}$ is the force measured by the load cell j and used for confirmation. The algorithm above is further described and verified in Reference [47].

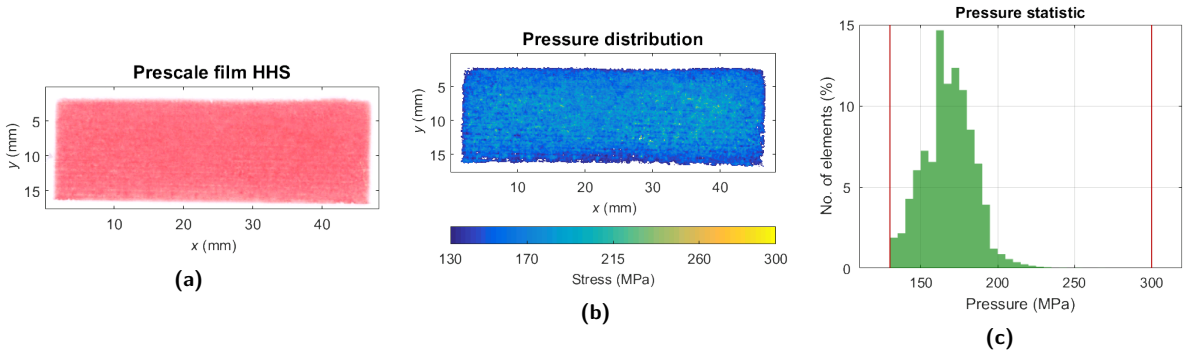

Figure 3.2: **(a)** Typical input, a loaded Prescale film, and **(b, c)** output of the self-written evaluation script for pressure-sensitive Prescale films. The analysed HHS film originates from the application of 175 MPa on Specimen 1. The white areas in (b) are points outside of the range of the films function provided in the manual, i.e. either too high or too low for the film.

3.1.1 Transverse stress on cables

The FRESCA-compatible cable specimens were exposed to a certain stress level for a duration of approximately 2 min. This allows a high reliability of the pressure-sensitive films to be achieved, as recommended in the manual [66]. Afterwards, the sample was transported to the FRESCA cable test station to measure the critical current. This procedure was performed iteratively with increasing stress levels until a critical current degradation of around 10 % could be observed.

For the stress application on the nearly 2-m-long specimens, a 2-m-long and 35-mm-wide portable support bar and supports were established to prevent any damage due to handling (cf. Figure 3.1). The specimens, including current leads, were placed on the support plate and slid into the pressing insert. After aligning the specimens to the defined pressing area with an effective length of 44 mm (cf. Figure 2.3) the pressing procedure was performed, which can be seen in Figure 3.4(a). The load cell signals as well as the pressure-sensitive films were used to evaluate the applied load on the specimen. The measured stress, represented in Section 4.1, was recorded from the calibrated force measurement and the nominal pressing area. The pressure-sensitive films served as a quality indicator to validate that the stress was distributed uniformly during the stress exertion. The pressing arrangement was chosen

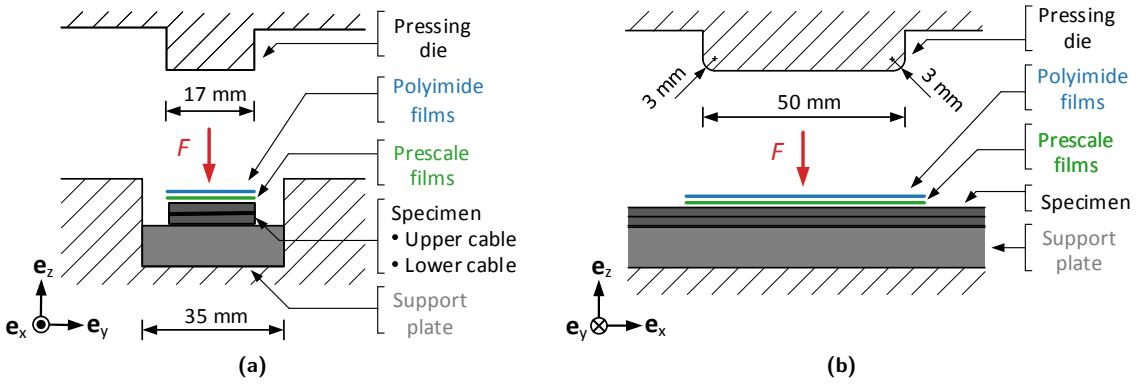

Figure 3.3: Schematic view of pressing configuration for applying transverse stress on the Rutherford cable stacks. **(a)** Side view. **(b)** Front view.

as shown schematically in Figure 3.3. In the beginning, several intermediate layers of different materials (In, Sn-Ag and Sn-Pb) were tested to improve further the homogeneity of the stress on the specimen. It was concluded that a 1-mm-thick intermediate layer of eight polyimide foils achieved the best result. Accordingly, the final pressing arrangement was defined with pressure-sensitive films underneath the polyimide foils. In order to extend the stress measurement range, films of types HHS, HS and MS were stacked. Figure 3.4(b) shows the configuration of polyimide and Prescale films after stress exertion.

Furthermore, a non-destructive X-ray tomography of equivalent specimens was performed by the working group to develop an FEM model and investigate with *ANSYS* the stress distribution within the cross section of the specimen, a complicated composite compound [87, 182].

Figure 3.4: **(a)** Specimen 1 (cable HT15OC0190) in the pressing tool and **(b)** 1-mm-thick polyimide foil stack intermediate layer (top) with pressure-sensitive films (bottom) after applying a nominal stress of 175 MPa.

3.1.2 Transverse stress on wires

The wire specimens were exposed to transverse stress for 2 min with the same hydraulic system and pressing die that was used for the cable specimens.

Samples for the magnetisation measurements and the microscopy campaign were exposed to stress by putting them on the ground plate of the pressing tool and afterwards cut into pieces with a wire diamond saw for further investigations.

The specimen for the transport current measurement was loaded while already assembled into the sample holder, as shown in Figure 3.14. It was exposed to a certain stress at RT, after which the electrical properties were measured with the NearT_c setup, as described in Section 3.3. This was performed iteratively until heavy degradation could be detected. For the stress procedure, the sample holder current connector plates were fixed via stainless steel bars to prevent any movement of the wire during the press procedure. Afterwards, the middle plate was exchanged with a stainless steel plate to ensure a planar and aligned pressing surface. The pressing area was defined in the middle of the sample within the voltage taps to prevent stress peaks due to the soldering points.

The final pressing configuration, as sketched in Figure 3.5, was defined to have no intermediate layers, which is the result of a previously executed test study. The objective was to apply well-defined stress and a similar crack distribution along the transverse cross section, as observed in the loaded strands within the cables (cf. Figure 4.9). Based on a microscopy investigation of loaded wires from different pressing arrangements, the approach could be achieved by the absence of intermediate layers. For this reason, it was refrained from using the concepts of past investigations. For instance, G. Mondonico *et al.* [116] sought a hydrostatic stress configuration within an impregnation. C. Calzolaio *et al.* [32] achieved a shape-conforming stress by using a cylindrical groove. Both experiments implemented the stress application during operation at low temperatures. For the analysis in Section 4.2, the direct force measurement and the projected area, i.e. $(0.7 \times 44)\,\mathrm{mm}^2$, were used to determine the stress on the wire.

In order to investigate the stress distribution further, an X-ray tomography of loaded and non-loaded wires was performed by the working group to develop an FEM model for *ANSYS*. Subsequently, an FEM analysis was performed to assess the stress distribution within the wire, especially the local stress on the sub-elements [41, 48].

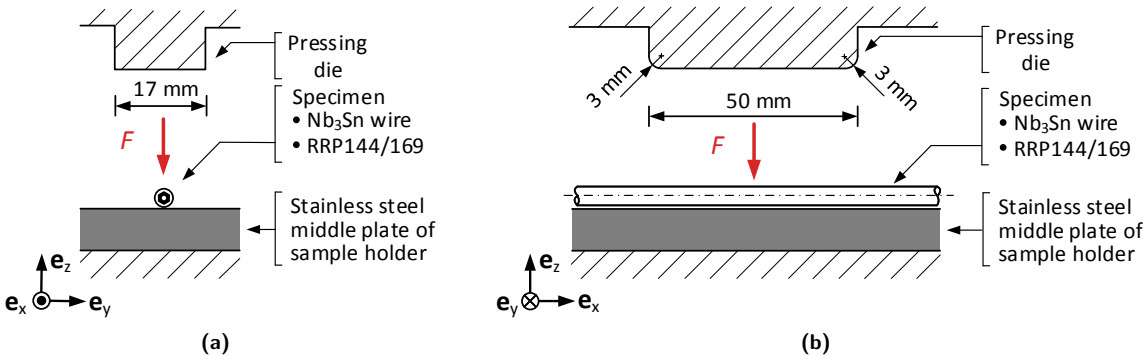

Figure 3.5: Schematic view of pressing configuration for applying transverse stress on the wires. **(a)** Side view. **(b)** Front view.

3.2 Measurements of cables with the FRESCA test station

The transport critical current measurements of the cable specimens after application of a certain stress level were performed with the FRESCA cable test station at CERN (TE-MSC-SCD). The Facility for Reception test of Superconducting Cables (FRESCA) was built for the R&D of superconducting cables for LHC magnets [175]. It can be seen in Figure 3.6, and the key properties are:

- A current source of up to 32 kA for the sample measurement circuit.
- A background magnet with an operating field of up to 9.6 T and a 99 % homogeneity within approximately 0.5 m perpendicular to the sample current.
- A specimen cooling at 4.3 K with saturated liquid helium and at 1.9 K with pressurised superfluid helium (sub-cooled), both slightly above the atmospheric pressure.

(a) (b)

Figure 3.6: FRESCA cable test station. **(a)** Overview. 1. Embedded vertical double-bath cryostat, 2. Power source for sample (32 kA) and Nb-Ti background magnet, (16 kA) 3. Water-cooled current leads, 4. Helium liquefier for the CERN building 165, 5. Liquid helium buffer dewar (6000 L), 6. Crane for changing the sample, **(b)** Detailed view of the FRESCA cryostat.

A schematic of the system can be seen in Figure 3.7(a). The test station is a "double cryostat concept", and both are vertical double-bath cryostats, which have an entire helium consumption of roughly 200 L h^{-1} in full operation. The upper baths operate at 4.3 K, and the lower baths can be operated down to 1.9 K cooled by heat exchangers. Lambda plates thermally separate the 4.3 K baths from the 1.9 K parts.

The Nb-Ti dipole magnet [94] is housed in the outer cryostat independently and only warmed for maintenance reasons. The magnet generates the applied field up to 9.6 T and is equipped with 18 kA current leads. Although it was designed for 10 T at a temperature of 1.9 K, a maximal value of 9.6 T is recommended for continuous operation. The approximately 1.7-m-long magnet with an aperture of 88 mm was designed to ensure field homogeneity of $B_{\mathrm{app}}/\max(B_{\mathrm{app}}) = 99\,\%$ in the centre along 475 mm. The inner cryostat houses the cylindrical sample chamber with an aperture of 77 mm and is equipped with 32 kA current leads. Furthermore, the test station is assembled with a rotating system to turn the sample over 90°.

In order to perform measurements, the cable specimen, which is described in Section 2.2, is placed in the sample holder. It is pre-strained in a sandwich of fibreglass laminate spacer (G10) and stainless steel plates. Afterwards, the equipped sample holder is mounted in a cylindrical collar to avoid movements of the sample due to the electromagnetic forces, which is illustrated in Figure 3.7(b). The sample holder is fixed by a cardan joint including current leads, helium transfer line and signal wiring to the sample insert and subsequently inserted into the inner cryostat. The current leads of the specimens are clamped with indium foils to the sample insert, which leads to a contact resistance of typically below 3 nΩ. The cold part of the measurement circuit has an entire resistance in the range of 10 nΩ at low temperatures.

The acquisition system consists of a low- and a high-frequency system. The former provides high voltage resolution and is used to record the voltage-current ($V-I$) and voltage-field ($V-H$) curves, respectively, during transport current measurements. Voltage taps in the high-field region and the direct current–current transformers (DCCT) signal of the sample current are connected to two nanovoltmeters with a resolution of 1 nV and a sampling time down to 350 ms. The high-frequency system with a lower voltage resolution is used for monitoring and interpreting the quench behaviour. It consists of a 15-channel acquisition system with a sampling time down to 50 µs per channel in the mV range. Additional "Potaim" cards, bipolar comparator circuits made by CERN, are used for quench detection. The temperature of the sample holder is evaluated by calibrated *LakeShore Cernox CX-1050* NTC temperature sensors. The current of the background magnet and the sample is also regulated and measured by using DCCT. Figure 3.8 illustrates the location of the most important voltage taps mounted on the cable specimens. The pressed area was defined in the middle of the Nb_3Sn sample and thus the voltage taps labelled with GLx, FMx, ENx with $x = 1$ for cable 1 (upper) and $x = 2$ for cable 2 (lower), respectively,

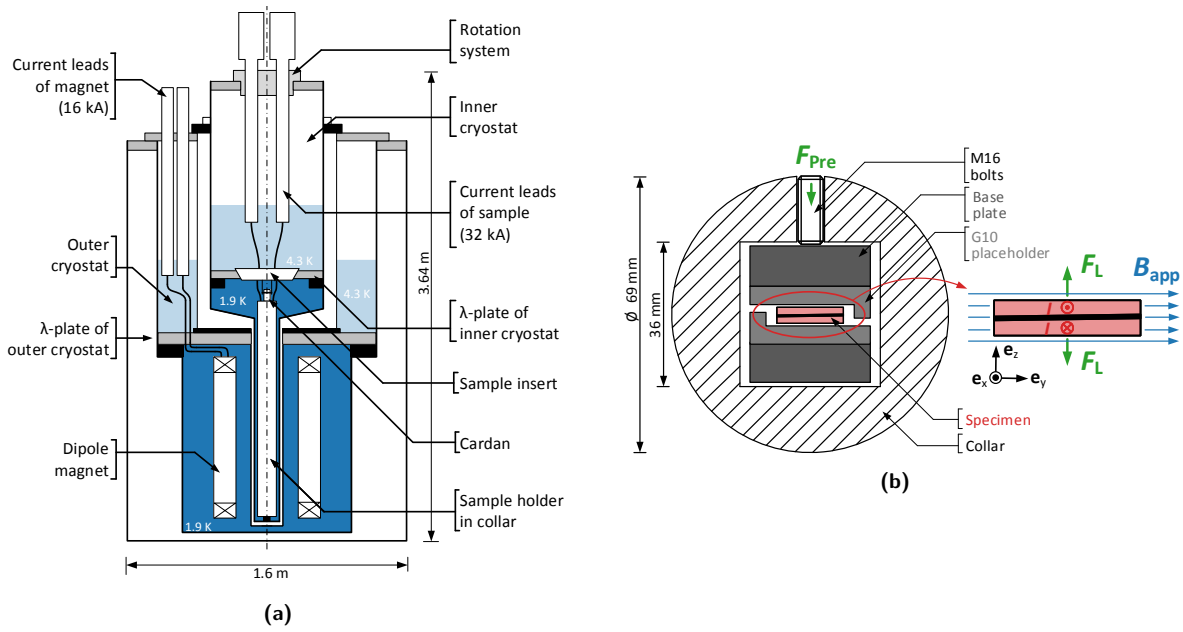

Figure 3.7: **(a)** Schematic view of the FRESCA test station. **(b)** Specimen in sample holder consisting of sandwich configuration in collar during the final experimental condition.

are intended for the recording of the $V - I$ curves. Primarily the voltage-tap pairs within the high-homogeneity field region were used, i.e. GLx with a spacing of 300 mm. The current-transfer length is consequently approximately 500 mm after a current contact length of 230 mm and 200 mm, respectively. Moreover, the specimen is equipped with additional voltage taps to detect a premature quench outside the pressing area and consequently a corruption of the measurement. Therefore, the voltage drops of the following parts were observed during every measurement, which can also be seen in Figure 3.8 and will be discussed in the next section:

- Bottom end (joint): $1VT05 - 2VT05$
- Top end of cable x: $xVT17 - xV014$
- Clamping of cable x: $xVT19 - xV017$
- Nb_3Sn cables: $1VT14 - 2VT14$
- Specimen: $1VT17 - 2VT17$
- System: $1VT19 - 2VT19$

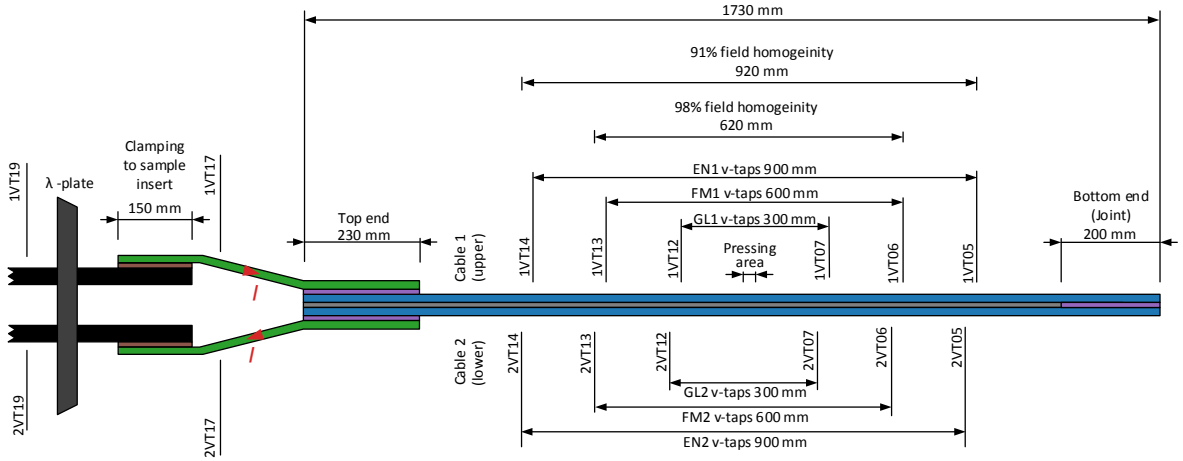

Figure 3.8: Schematic view of the specimen including voltage-tap placements in relation to the location of the high-homogeneity region of the applied magnetic field. In the present work, only voltage-tap signals within the region of a field homogeneity of $B_{app}/\max(B_{app}) \geq 98\,\%$ were used for the analysis.

3.2.1 Experimental condition & measurement procedure

After loading the specimen described in Section 3.1.1, it was assembled into the sample holder for the I_c measurement in the FRESCA cable test station.

The necessary pre-stress of 50 MPa was applied at RT by using M16 bolts every 40 mm of the collar, which is illustrated with F_{Pre} in Figure 3.7(b). Subsequently, it was inserted into the aperture of the test station and the specimen was cooled. The I_c measurements were performed with current ramps of 100 A s^{-1} during 4.3 K and in the virgin state also at 1.9 K. The background field from 7 T to 9.6 T was applied perpendicular to the current and parallel to the long edge of the cable (cf. Figure 3.7(b) right).

Figure 3.9 gives an overview of the typical measurement and monitoring signals during a recording of a $V-I$ relation. The corresponding embedded plots magnify the essential part of the original plot. Figures 3.9(a) show the raw data of the low-frequency acquisition system with the higher accuracy used for the analysis. The following voltage measurement points, after stopping the current supply, were not used for the analysis and can be traced back to electrodynamic and thermal processes within the cables, e.g. inter-strand current sharing, due to the sharp current cut. The monitoring signals obtained with the high-frequency acquisition system give information about the quench location to prevent misinterpretation, which are drawn in Figure 3.9(b). The additional small plot shows the signals during the resistive transition in detail. It is clear that the Nb_3Sn cables equipped with voltage taps ENx, FMx, GLx become resistive before the top and bottom splices, which indicates a successful measurement process of the cables. Therefore, the delay between the resistive transition of each cable was observed to ensure an independent quench occurrence of the cables. The delay has to be shorter than 7.4 ms to guarantee that the heat transfer or the quench propagation in one cable did not cause the quench in the other, which was the objective in earlier research activities [62].

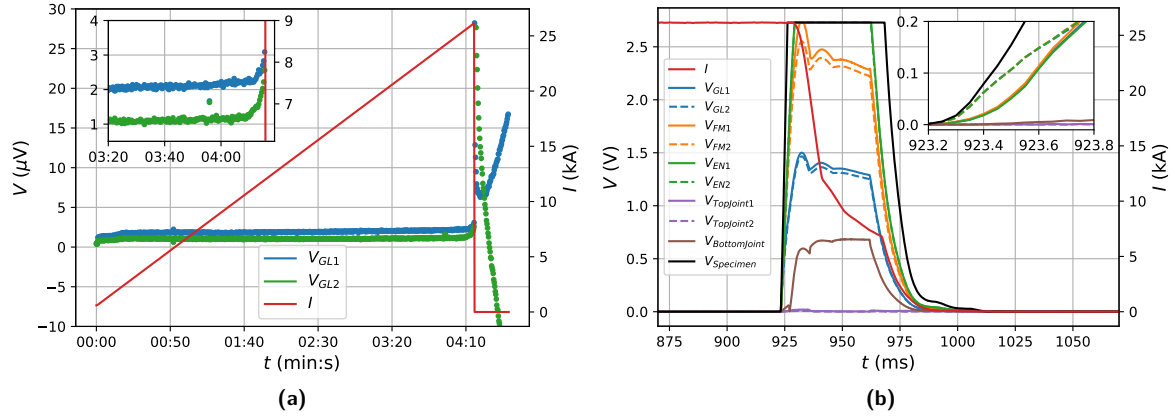

Figure 3.9: **(a)** Measurement and **(b)** monitoring signals during a typical $V-I$ recording. The magnified plot in (b) clearly shows that the current leads on the top ($V_{\text{TopJoint}x}$) and the joint on the bottom ($V_{\text{BottomJoint}}$) are not quenching or are quenching after the actual specimen ($V_{\text{GL}x}$, $V_{\text{FM}x}$, $V_{\text{EN}x}$). The measurement range of the fast monitoring system is limited to 3 V. The small plot in (a) enlarged the resistive transition used for the analysis before the quench detection was triggered.

3.2.2 Self-field correction

The peak field B_{peak} within the specimen on the superconductor was used for the analysis of the cable results in Section 4.1.

The magnetic self-field $B_{self}(\mathbf{r})$ of the specimen, which is linearly proportional to the current I, is non-uniform. Its local peak value can be more than 20 % of the applied field $B_{app}(\mathbf{r})$ during the measurements. Hence, the self-field has to be considered in the results to present the critical currents with respect to the actual magnetic condition within the specimen, especially of the superconductor. Based on the electromagnetic situation of the specimen's cross section shown in Figure 3.7(b), the entire magnetic field at a specific location can be computed by superpositioning the homogeneous applied field and the inhomogeneous self-field

$$\mathbf{B}(\mathbf{r}) = \mathbf{B}_{app}(\mathbf{r}) + \mathbf{B}_{self}(\mathbf{r}, I) \tag{3.3}$$

with the applied field $\mathbf{B}_{app}(\mathbf{r}) = \mathbf{B}_{app} = B_{app}\mathbf{e}_y$, the self-field $\mathbf{B}_{self} = B_{self}\mathbf{e}_{B_{self}} = B_{self,y}\mathbf{e}_y + B_{self,z}\mathbf{e}_z$, the specimen current I and the position vector $\mathbf{r}$. The peak field B_{peak}, which is used for the analysis, is

Table 3.1: FEM results for the 11 T and MQXF cable specimen configuration.

I (kA)	$\max_{\mathbf{r}}(B_{\text{self,11 T}})$ (T)	$\max_{\mathbf{r}}(B_{\text{self,MQXF}})$ (T)
10	0.80	0.65
20	1.60	1.29
32	2.55	2.07

further defined as the sum of the applied field and the maximum value of the self-field

$$B_{\text{peak}} := B_{\text{app}} + \max_{\mathbf{r}}[B_{\text{self}}(\mathbf{r}, I)]. \tag{3.4}$$

In order to estimate the magnetic self-field, a two-dimensional magneto-static FEM of the specimen's cross section including its environment was performed with *ANSYS Maxwell*. It solves numerically the Biot—Savart law for every location on the surface (YZ-plane). Therefore, the following idealisations of the specimen were made:

- Reduction of the cable to a trapezoidal cross section with homogeneous current density $J = {}^{I}/_{A}$ with the nominal cross-section area A, i.e. effects of a particular strand or sub-element are neglected.
- The twist pitch of the cable is ignored, i.e. the current is parallel to the x-axis, which restricts the magnetic self-field to the YZ-plane.
- The environment of the cables, e.g. epoxy resin, stainless steel and liquid helium, was idealised as vacuum atmosphere, i.e. $\mu_r = 1$.
- The field is constant in x direction, which represents the high-field region in the middle of the specimen.

Figures 3.10 and 3.11 show the FEM results of the two specimen types, the 11 T cable and MQXF cable configuration, respectively. They have a maximal magnetic field of 2.55 T and 2.07 T, respectively, at a current of $I_{\text{max}} = 32$ kA. The highest magnetic field concentration is formed within the 0.3-mm-wide gap between the cables due to the anti-parallel current flow, which can be easily checked by using Ampere's Law $\nabla \times \mathbf{B} = \mu_0 \mathbf{J}$.

The location of the maximum value $\max_{\mathbf{r}}[B_{\text{self}}(\mathbf{r}, I)]$ is in the centre region of the specimen, more precisely on the border of the cables, due to the point-symmetric layout of the specimen. This implies that the maximal field in the specimen is also the maximal field in the cables' superconducting area, which was the final reason to use it for the analysis. This means also that the earliest quench can be expected in the middle centre strands of the specimen, which can be checked by using the Kramer relation of superconductors $J_c(b) \propto b^{-0.5}(1-b)^2$ with $b = {}^{B}/_{B_{c2}{}^*}$. The maximal field gradient within the cables, carrying the maximal current of 32 kA, is approximately 2.2 T mm^{-1} and 1.4 T mm^{-1} for the 11 T and the MQXF cable configuration, respectively.

In order to achieve the maximum magnetic self-field as a function of the current, the simulation was performed with 10 kA, 20 kA and 32 kA and their results are listed in Table 3.1. Thus, the linear behaviour

$$\max_{\mathbf{r}}[B_{\text{self}}(\mathbf{r}, I)] = k_{\text{I}} I \tag{3.5}$$

with a correction factor k_{I} of 80 mT kA^{-1} and 65 mT kA^{-1} for the 11 T dipole and MQXF cable specimen, respectively, was confirmed. Consequently, the parameter derived above were used to present the results of the cables $I_c(B_{\text{peak}})$ with $B_{\text{peak}} = B_{\text{app}} + k_{\text{I}} I$ in Section 4.1.

As a reference for the cable measurements, the critical currents $I_c(B)$ of the virgin wires, i.e. strands in non-cabled condition, are also presented in Section 4.1. These results were obtained by transport current measurements with an ITER VAMAS barrel at CERN (TE-MSC-SCD) according to the standard [159]. The superconducting wire is wound on the barrel with a diameter of roughly 20 mm and measured with an applied field parallel to the barrel axis. The angle between the wound wire and the applied field is approximately 88°. In order to compare these results with the cable results, the actual magnetic field during the measurements must be determined, which consists also of the applied field of the background magnet and the self-field of the measured wire. Obtained by B. Bordini [25] using an FEM simulation, the actual local peak field on the superconductor during the measurement is given by

$$B_{\text{peak,wire}} = B_{\text{app}} + B_{\text{self,wire}}(I) \tag{3.6}$$

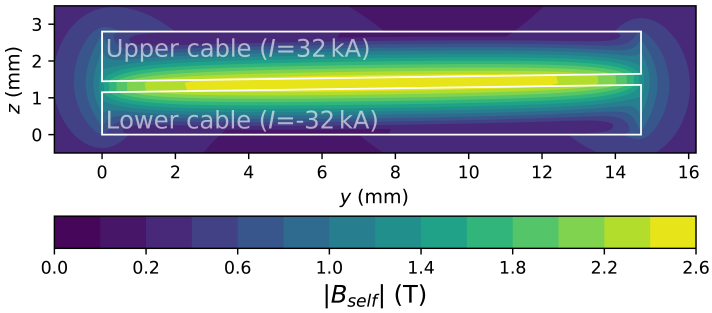

Figure 3.10: Magnetic self-field of the 11 T cable configuration with a current of $I_{\text{max}} = 32\,\text{kA}$ obtained by an FEM simulation. The maximum is located in the centre region of the specimen, more precisely on the border of the cables, and is on the order of 2.55 T.

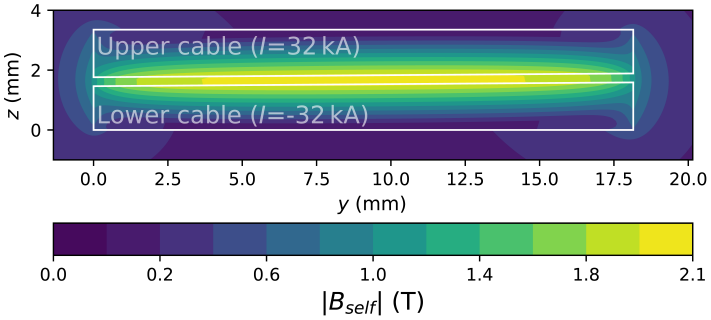

Figure 3.11: Magnetic self-field of the MQXF cable configuration with a current of $I_{\text{max}} = 32\,\text{kA}$ obtained by an FEM simulation. The maximum is located in the centre region of the specimen, more precisely on the border of the cables, and is on the order of 2.07 T.

with $B_{\text{self,wire}}(I) = \mu_0 I/2\pi r - 9 \cdot 10^{-5}\,\text{T A}^{-1} \cdot I$, where r is the outer radius of the sub-element array within the cylinder wire and I is the test current. In addition to the self-field correction, the critical current $I_c(B_{\text{peak,wire}})$ of the wire was multiplied by the number of strands of the respective cable and plotted together with the cable results.

In order to compare the transverse stress applied at RT with the force during the electrical measurements, the entire electromagnetic respectively Lorentz force F_L on the cables in the specimen was calculated. In general, the local electromagnetic force density on an infinitesimal element in a current-carrying conductor is defined as

$$\mathbf{f}(\mathbf{r}) = \mathbf{J}(\mathbf{r}) \times \mathbf{B}(\mathbf{r}). \tag{3.7}$$

The cumulative force on the conductor, e.g. wire or cable, can be obtained by integration over its volume $\mathcal{V}$

$$\mathbf{F} = \int_{\mathcal{V}} \mathbf{J}(\mathbf{r}) \times \mathbf{B}(\mathbf{r})\,\mathrm{d}\mathcal{V}. \tag{3.8}$$

Taking the above idealisations into account, the problem can be described independently of the length of the conductor, and the common length-related force

$$\mathbf{F}' = \frac{\mathbf{F}}{l} = \int_{\mathcal{A}} \mathbf{J}(\mathbf{r}) \times \mathbf{B}(\mathbf{r})\,\mathrm{d}\mathcal{A} \tag{3.9}$$

was further derived, where A is the cross section of the conductor, i.e. a single cable in the present case, perpendicular to the current flow. The current density of a single cable is defined as $\mathbf{J} = I/A\,\mathbf{e}_x$ and with the magnetic field $\mathbf{B}(\mathbf{r}) = \mathbf{B}_{\text{app}} + \mathbf{B}_{\text{self}}(\mathbf{r})$ computed above, the entire length-related force $F_L{}'$ on a single cable can be written as

$$\mathbf{F}_L{}' = \int_{\mathcal{A}} \mathbf{J}(\mathbf{r}) \times \mathbf{B}(\mathbf{r})\,\mathrm{d}\mathcal{A} = \int_{\mathcal{A}} \frac{I}{A}\mathbf{e}_x \times \mathbf{B}(\mathbf{r})\,\mathrm{d}\mathcal{A} = \frac{I}{A}\int_{\mathcal{A}} \mathbf{e}_x \times \left[\mathbf{B}_{\text{app}} + \mathbf{B}_{\text{self}}(\mathbf{r})\right]\mathrm{d}\mathcal{A}. \tag{3.10}$$

The applied magnetic field, i.e. $\mathbf{B}_{\text{app}}(\mathbf{r}) = \mathbf{B}_{\text{app}} = B_{\text{app}}\mathbf{e}_y$, and the magnetic self-field can be written as

Table 3.2: Length-related forces in y and z direction of the upper cable within the specimen derived from FEM simulation for $I_{max} = 32\,\mathrm{kA}$ and $B_{app,max} = 9.6\,\mathrm{T}$.

	$F_{L,z}{}'$ $\mathrm{kN\,m^{-1}}$	$F_{L,y}{}'$ $\mathrm{kN\,m^{-1}}$
11 T dipole	341.4	1.9
MQXF	336.0	0.6

$\mathbf{B}_{self}(\mathbf{r}) = B_{self,y}(\mathbf{r})\mathbf{e}_y + B_{self,z}(\mathbf{r})\mathbf{e}_z$ due to the current flow explicitly in x direction, which leads to

$$\begin{aligned}\mathbf{F}_L{}' &= I\left[\frac{1}{A}\int_{\mathcal{A}} \mathbf{e}_x \times B_{app}\mathbf{e}_y \,\mathrm{d}\mathcal{A} + \frac{1}{A}\int_{\mathcal{A}} \mathbf{e}_x \times B_{self,y}(\mathbf{r})\mathbf{e}_y + \mathbf{e}_x \times B_z(\mathbf{r})\mathbf{e}_z \,\mathrm{d}\mathcal{A}\right] \\ &= I\left[\underbrace{\frac{1}{A}\int_{\mathcal{A}} B_{app}\,\mathrm{d}\mathcal{A}}_{B_{app}}\,\mathbf{e}_z + \underbrace{\frac{1}{A}\int_{\mathcal{A}} B_{self,y}(\mathbf{r})\,\mathrm{d}\mathcal{A}}_{\overline{B}_{self,y}(\mathcal{A})}\,\mathbf{e}_z + \underbrace{\frac{1}{A}\int_{\mathcal{A}} B_{self,z}(\mathbf{r})\,\mathrm{d}\mathcal{A}}_{\overline{B}_{self,z}(\mathcal{A})}(-\mathbf{e}_y)\right].\end{aligned} \tag{3.11}$$

The defined quantities $\overline{B}_{self,y}(\mathcal{A})$ and $\overline{B}_{self,z}(\mathcal{A})$ can be assumed as the average value of the self-field over the cable cross section in y and z direction, respectively. Hence, the length-related force on a single cable can be summarised as

$$\mathbf{F}_L{}' = \underbrace{I\left[B_{app} + \overline{B}_{self,y}(\mathcal{A})\right]}_{F_{L,z}{}'}\mathbf{e}_z - \underbrace{I\overline{B}_{self,z}(\mathcal{A})}_{F_{L,y}{}'}\mathbf{e}_y. \tag{3.12}$$

Consequently, the z and y components of the magnetic field cause an electromagnetic force in y and z direction, respectively. This circumstance can be easily checked by applying the common Lorentz force law for a current-carrying wire $\mathbf{F}_L = Il\mathbf{e}_I \times \mathbf{B}$, where l is the length of the wire within the magnetic field $\mathbf{B}$ and $\mathbf{e}_I$ is the direction of electrical current I.

Nevertheless, the self-field B_{self} is only a fraction of the applied field B_{app}, as derived above. Hence, the primary share of the force is in z direction ($F_{L,z}{}' \gg F_{L,y}{}'$) driven by the applied field B_{app}, which can be obtained from the FEM results listed in Table 3.2. The cable-independent part due to the applied field amounts to $32\,\mathrm{kA} \cdot 9.6\,\mathrm{T} = 307.2\,\mathrm{kN\,m^{-1}}$.

The two cables repel each other due to the anti-parallel current flow (cf. Figure 3.7(b)), and the self-field contributes only marginally to the force parallel and anti-parallel to the z-axis, respectively. The length-related force component $F_{L,y}{}'$ represents the lateral force, which is sensitive to the keystone angle of the cables.

The most interesting force for this investigation is in z direction, because the applied stress at RT is also in z direction. The highest electromagnetic force can be assumed with the maximal current of 32 kA during the maximal applied field 9.6 T. The high-field region in the middle of the specimen has a length of $l = 475\,\mathrm{mm}$, and hence the entire force within this area can be derived by $F_{L,z} = F_{L,z}{}'l$. In order to estimate the maximal stress parallel to the long edge on a cable, which can be compared to the stress application at RT, the maximal force with the cable width w is used to derive

$$\sigma_L \approx \frac{F_{L,z}}{l \cdot w} = \frac{F_{L,z}{}'}{w} = \begin{cases} 23.2\,\mathrm{MPa}, & \text{for 11 T dipole configuration} \\ 18.2\,\mathrm{MPa}, & \text{for MQXF quadrupole configuration} \end{cases} \tag{3.13}$$

with a current $I_{max} = 32\,\mathrm{kA}$, an applied field of $B_{app,max} = 9.6\,\mathrm{T}$ and the nominal cable width w of 14.7 mm and 18.5 mm for the 11 T dipole and MQXF cable, respectively. Considering that the highest current is barely reached during the I_c measurements, the estimated maximal stress σ_L on a cable (XY-plane) during the measurement is lower than half the lowest stress level applied at RT and hence not considered in the results.

3.2.3 Data evaluation

As described above, the critical current was determined by recording $V(I)$ curves to evaluate the degradation due to transverse stress at RT. The standard for evaluating the critical current of Nb_3Sn composite superconductor [159] recommends an electrical field or a resistivity criterion. The most common criterion is the electrical field criterion, which is also chosen for the present work. Accordingly, the $V(I)$

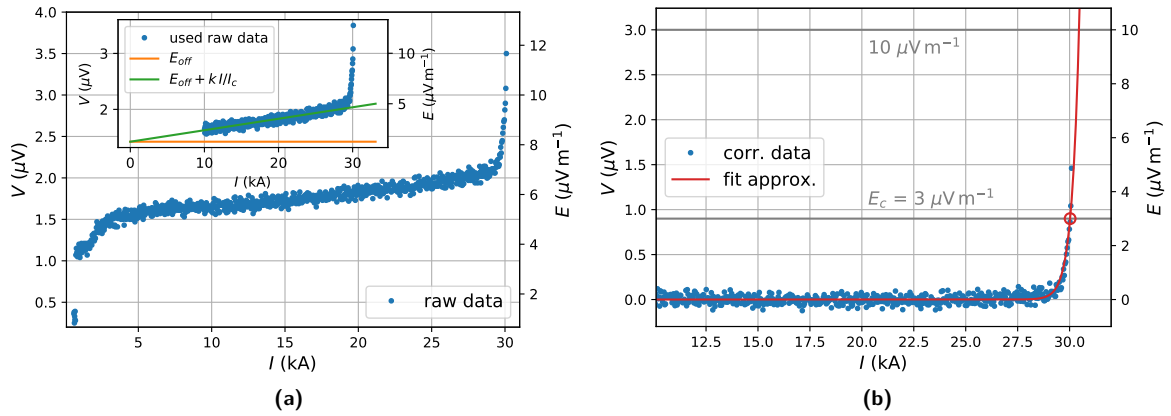

Figure 3.12: Critical current evaluation of a typical cable $V(I)$ recording. **(a)** Raw data points of a $V-I$ recording at $T = 4.3\,\mathrm{K}$ until the quench. The small plot shows the estimation of the undesired constant and linear part caused by experimental condition in contrast to the raw data above 10 kA used for the analysis. **(b)** Critical current determination according to electrical field definition $E(I = I_c) = E_c$ with $E_c = 3\,\mu\mathrm{V\,m^{-1}}$ from the corrected data, i.e. after reassessment of the undesired thermoelectric, the induction voltage (constant) and the resistive part (linear).

relations at a particular and constant temperature can be expressed by the power law

$$E(I) = E_c \left(\frac{I}{I_c} \right)^n . \tag{3.14}$$

Therefore, the electrical field along the specimen is defined by $E = V/l$ with the voltage of the specimen V and the voltage-tap spacing l. Hence, the critical current is defined as the current when the electrical field E transcends the constant threshold E_c, i.e. $E(I = I_c) = E_c$. A threshold of $10\,\mu\mathrm{V\,m^{-1}}$ is recommended for LTS such as Nb_3Sn and Nb-Ti and is restricted practically by the noise level of the voltage signal and the precision of the measurement equipment. The resistive transition index n, the so-called n value, is derived by the slope of the $E(I)$ relation in a double-log reference frame in the region of the I_c determination point.

Experimental measurements are not perfect, and undesired systematic influences must be reassessed retrospectively. In practice, constant and linear effects caused by the experimental arrangement are relevant:

- The constant component appears unavoidable by the thermoelectric and inductive voltage. The latter is dependent on the current ramp rate.
- The linear component is caused primarily by the current-transfer voltage. It represents the resistive junction from the current leads contact points to the superconducting sub-elements of the specimen and can be minimised a priori by a sufficiently long current-transfer length [52, 57].

In general, cable measurements had to be performed inherently with higher currents, resulting in higher energy dissipation during the measured resistive transition, which led to an earlier stop of the recording compared to wire measurements. Thus, only data points far below the recommended criterion were recorded, which is visualised by the corrected $V(I)$ relation of a typical cable measurement in Figure 3.12(b). Moreover, the undesired constant and linear components of the corresponding raw data in Figure 3.12(a) are recognisable.

Owing to the facts presented above, it was decided to evaluate the critical current of cables by using a curve fitting as follows. Initially, the criterion E_c was reduced from the recommended $10\,\mu\mathrm{V\,m^{-1}}$ to $3\,\mu\mathrm{V\,m^{-1}}$ in order to prevent extrapolation uncertainties, i.e. to ensure that measurement points are available around the I_c determination point. Figure 3.12(a) shows a typical $V-I$ raw curve, from which data points above 10 kA were used to fit the function

$$E(I) = E_c \left(\frac{I}{I_c} \right)^n + E_{\mathrm{offset}} + k\,\frac{I}{I_c} \tag{3.15}$$

with I_c in A, E_{offset} in $\mu\mathrm{V\,m^{-1}}$, k in $\mu\mathrm{V\,m^{-1}}$ and n as fitting parameters. The first term represents the desired "pure" resistive transition of the superconductor. The latter two represent undesired constant and linear effects caused by the experimental conditions. The small plot in Figure 3.12(a) shows the

Table 3.3: Inner and outer radii, ρ_o and ρ_i, respectively, as well as the superconducting area $A_{\text{A-15}}$ of all wires used in this work, obtained by SEM.

Wire type	d_{nom} (mm)	N (-)	ρ_o (µm)	ρ_i (µm)	$A_{\text{A-15}}$ (mm^2)	Utilisation
RRP 144/169	0.7	144	20.4	11.1	0.133	Wire investigation and specimen 1 cable
RRP 108/127	0.7	108	23.0	11.5	0.135	Specimen 2 cable
RRP 108/127	0.85	108	27.5	13.5	0.195	Specimen 3 cable

estimation of these terms, which were used to achieve the corrected data in Figure 3.12(b). Finally, the critical current was determined as the interpolated current value of the corrected fit function at 3 µV m^{-1}, which is annotated by the red marker.

All I_c values are additionally converted into the critical current density J_c, given primarily by a secondary axis in Chapter 4. Therefore, the effective superconducting area $A_{\text{A-15}}$ is used, i.e. the Nb_3Sn area of all N sub-elements within a wire. For that purpose, the sub-elements are idealised as annuli with ρ_o and ρ_i as the outer and inner radius, respectively, which is illustrated in Figure 2.2. Thus, the used critical current density within this work is defined as

$$J_c = J_{c,\text{A-15}} = \frac{I_c}{A_{\text{A-15}}} \quad \text{with} \quad A_{\text{A-15}} = N\pi({\rho_o}^2 - {\rho_i}^2), \tag{3.16}$$

which is in agreement with the derived magnetisation model (cf. Equation 3.41). The radii ρ_o and ρ_i of the specimens, which were obtained by the microscopy investigation, are summarised with the calculated $A_{\text{A-15}}$ in Table 3.3. In the case of the cable results, the area $A_{\text{A-15}}$ was consequently multiplied by the number of strands to consider the entire Nb_3Sn area within the cable compound. The number of strands was in all cables equals 40, i.e. $A_{\text{A-15,cable}} = 40\, A_{\text{A-15}}$.

Nevertheless, the nonCu critical current density $J_{c,\text{nonCu}}$ is frequently mentioned in the referenced publications. The Cu/nonCu ratio $\varkappa_{\text{Cu/nonCu}}$ indicates the ratio of the copper to non-copper materials, e.g. tin and niobium, within the cross section of a non-reacted wire and is given in its specification. Hence, the corresponding critical current density is defined as

$$J_{c,\text{nonCu}} = \frac{I_c}{A_{\text{nonCu}}} \quad \text{with} \quad A_{\text{nonCu}} = \frac{A_{\text{wire}}}{1 + \varkappa_{\text{Cu/nonCu}}}, \tag{3.17}$$

where $A_{\text{wire}} = \pi r^2$ is the area of the wire cross section with a radius of r. Basically, it includes besides the Nb_3Sn also the tin core and the residual α-bronze after RHT, which does not distribute to the current transport. Owing to the fact that $A_{\text{nonCu}} > A_{\text{A-15}}$ it follows that $J_{c,\text{nonCu}} < J_{c,\text{A-15}}$.

Within the magnet design, the engineering critical current density of the wire $J_{c,\text{ENG,wire}}$ and the cable $J_{c,\text{ENG,cable}}$ are often used. They are defined as the critical current over the entire cross section of the wire A_{wire} and the cable A_{cable}, respectively. The relation between these two is dependent on the packing factor of the cable, which is also listed in Section 2.2 for the investigated types.

3.3 Measurements of wire with the NearT_c setup

After the application of stress on the wire described in Section 3.1, the electrical properties were measured with a self-built cryostat setup, which is described in this section. The setup was built and the measurements were performed in the CryoLab at CERN (TE-CRG-CI). The measurement concept, so-called NearT_c, foresees $I_c(T)$ measurements in magnetic self-field near the critical temperature up to 150 A and leads consequently to higher demands on the control accuracy of the sample temperature. This concept was chosen on the one hand to demonstrate an alternative measurement method and, on the other hand, to prevent any Lorentz force during the measurement, which would cause additional damage to the sample. The concept and its assets and drawbacks are discussed in more detail in Section 1.2.4. The key design requirements for this transport current measurements were:

- The stress application and I_c measurements using the same specimens, i.e. iterative experiment procedure, as performed on the cable specimens.
- No removal of the voltage taps at all process steps to ensure the same voltage-tap spacing after every stress level.

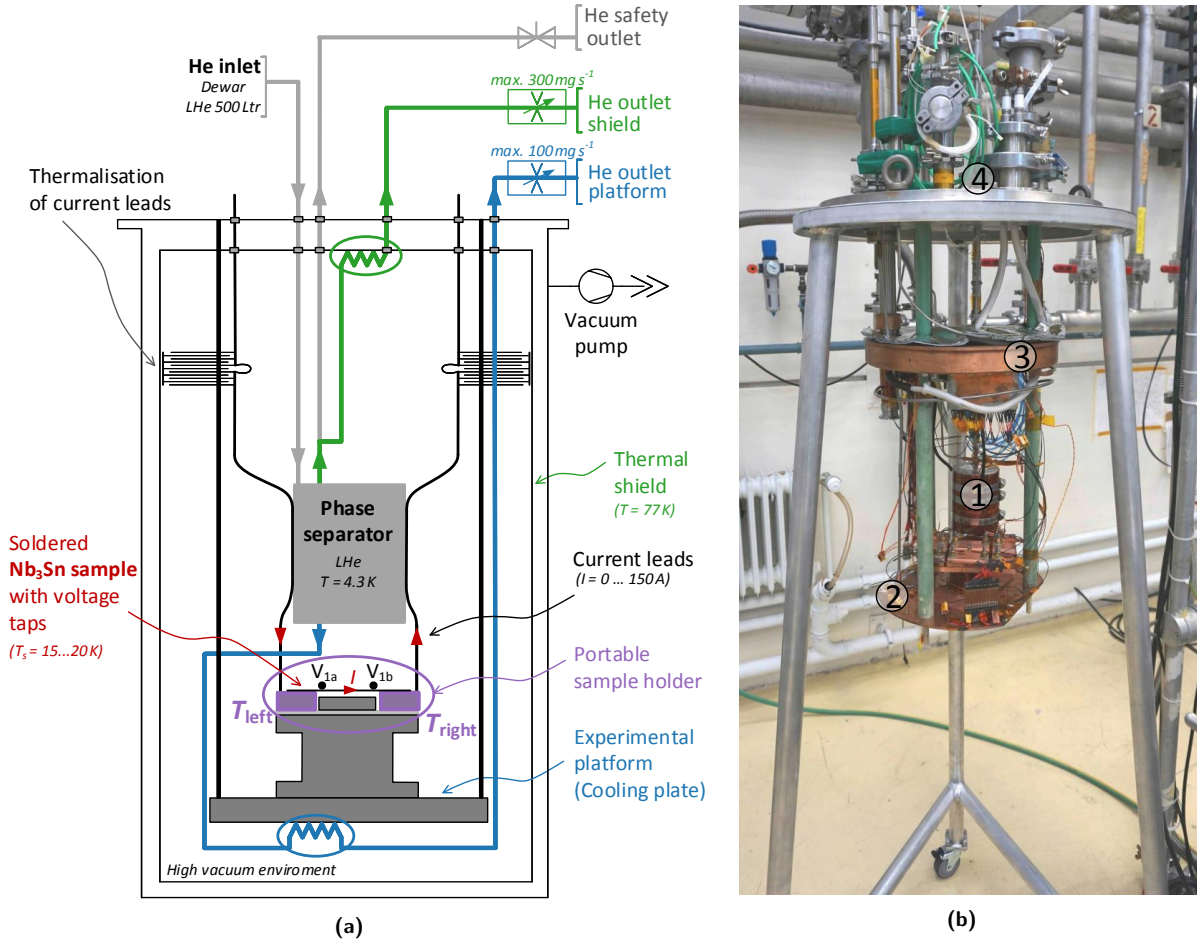

Figure 3.13: **(a)** Schematic of cryostat setup assembled in a vacuum chamber including sample holder and cryogenic peripheral. **(b)** Cryostat setup outside the vacuum chamber. 1. Phase separator, 2. Experiment platform, 3. Fixation for thermal shield, 4. Electrical and cryogenic feed-throughs.

- The hydraulic press described in Section 3.1.1 has to be used to exert uniform transverse stress at RT. Moreover, the specimens should not be disassembled from the sample holder during all iterations to prevent damage due to handling operations.

Therefore, an adequate sample holder was designed as described below. Moreover, a low-resistance measurement was established to extend the investigation of the critical temperature T_c and the RRR.

3.3.1 Cryogenic sub-system & sample holder

The setup consists of a cryostat insert including a phase separator with one inlet, which was connected steadily to a 500 L liquid helium dewar, as indicated in Figure 3.13(a). For the measurements, the entire setup was transferred to a vacuum chamber and sealed. Subsequently, an insulation vacuum atmosphere below 10^{-6} mbar was established to suppress thermal convection and conduction through the residual gas content.

The phase separator had two outlets. The upper vapour outlet, drawn in green in Figure 3.13(a), was connected to the heat exchanger of the thermal shield, which additionally thermalised the current leads. The bottom liquid outlet, drawn in blue in Figure 3.13(a), was connected to the heat exchanger of the experimental platform, which carried the sample holder. Hence, the specimen was cooled by conduction via the two connector plates, which are shown in purple in Figure 3.13(a). By using two helium mass flow controllers (*Bronkhorst Low-Δ-Flow controller*) at the outlets as described above, the sample was cooled to slightly below T_c. The pressure of the dewar was controlled to ensure proper operation of the flow controller and to avoid pressure-dependent temperature variations.

The fine stabilisation of the sample temperature close to the critical temperature was performed at the base temperature of approximately 13 K, ensured by the mass flow controllers. This was achieved by controlling the temperature of each connector plate independently with a 5 W heater resistor and a

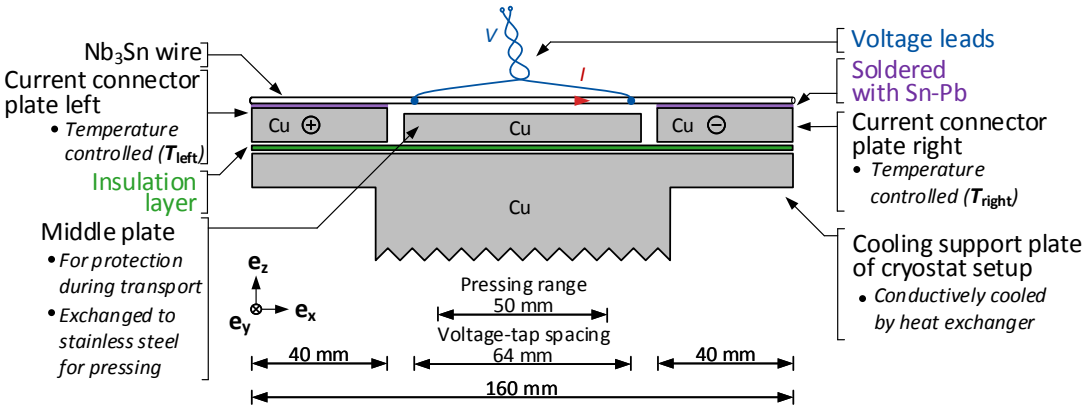

Figure 3.14: Schematic of sample holder including sample assembled in the cryostat setup.

calibrated NTC temperature sensor (*LakeShore Cernox CX-1070*) with a calibration accuracy of ±4 mK. The plate temperatures T_{left} and T_{right} were feedback-controlled by a *Lakeshore temperature controller 336*. The sample temperature T_{s} was further defined as the arithmetic mean value

$$T_{\text{s}} = \frac{T_{\text{left}} + T_{\text{right}}}{2}, \tag{3.18}$$

and consequently regulated indirectly by the plate temperatures. The temperature difference

$$\Delta T_{\text{s}} = |T_{\text{left}} - T_{\text{right}}| \tag{3.19}$$

served as a homogeneity parameter of the plates.

The portable sample holder shown in Figure 3.13 had a size of $(160 \times 100 \times 10)\,\text{mm}^3$ and a detailed sketch is shown in Figure 3.14. The specimen, a 160-mm-long Nb_3Sn RRP144/169 wire, was soldered on the two current connector plates made of copper $(40 \times 100 \times 10)\,\text{mm}^3$. The sample was soldered on each plate with a contact length of 40 mm, and the current leads were clamped on the back. The voltage taps with a spacing of 64 mm were placed symmetrically outside the pressing zone and never removed to ensure the same measurement length. For the transport and pressing, the three plates were connected by stainless steel bars to prevent the specimen from moving and sustaining damage. After the pressing procedure described in Section 3.1.2, the sample holder was mounted again in the cryostat setup for low-temperature measurements. The connector plates were screwed on with low torque only in order to prevent unwanted strain due to thermal contraction. The assembled sample holder in the cryostat setup can be seen in Figure 3.15, including mounted current leads and temperature sensors.

In order to monitor the system, additional voltage taps and temperature sensor, e.g. Pt100 (PTC), were placed at appropriate positions of the system and measured by the four-lead-measurement method using a measurement current of 1 mA. The entire cryostat setup, with all functionalities used here, is summarised in the Piping and Instrumentation Diagram (PID) in Figure 3.21 at the end of this section.

3.3.2 Electrical sub-system & current leads estimation

Figure 3.13(a) shows the electrical measurement circuit. The setup was equipped with passively-cooled current leads made of copper and designed for 150 A. They are clamped with indium foils to the current connector plates, which provide the connection of the high-current feed-through connectors outside the vacuum chamber. The electrical measurement circuit was powered by a 200 A current source (*Delta Elektronika SM30-200*), and the specimen current was measured by using a shunt resistor with $0.25\,\text{m}\Omega \pm 0.25\,\%$. The twisted voltage leads made of Cu, for recording the $V - I$ and $V - T$ curves, were routed directly to the low-temperature vacuum chamber. The other signal wiring of low-temperature coefficient material was collectively transferred to the chamber by two 40-pin electrical vacuum connectors.

Nanovoltmeters (*Keithley multimeter model 2001*) with a resolution of 10 nV were used to measure the specimen and the shunt voltage. The superconducting transport properties were characterised by performing critical current measurements $I_{\text{c}}|_{T=\text{const.}}$ at specific temperature steps $T_{\text{s}} = T_{\text{c}} \ldots T_{\text{c}} - 1\,\text{K}$ and current-sharing temperature measurements $T_{\text{cs}}|_{I=\text{const.}}$ during specific current steps $I = 1\,\text{A} \ldots 100\,\text{A}$. The latter had the advantages that the Joule energy of the remaining part of the electrical measurement circuit stayed constant during the entire recording, which led to higher stability. The measurements were performed with a recording sampling time of 200 ms.

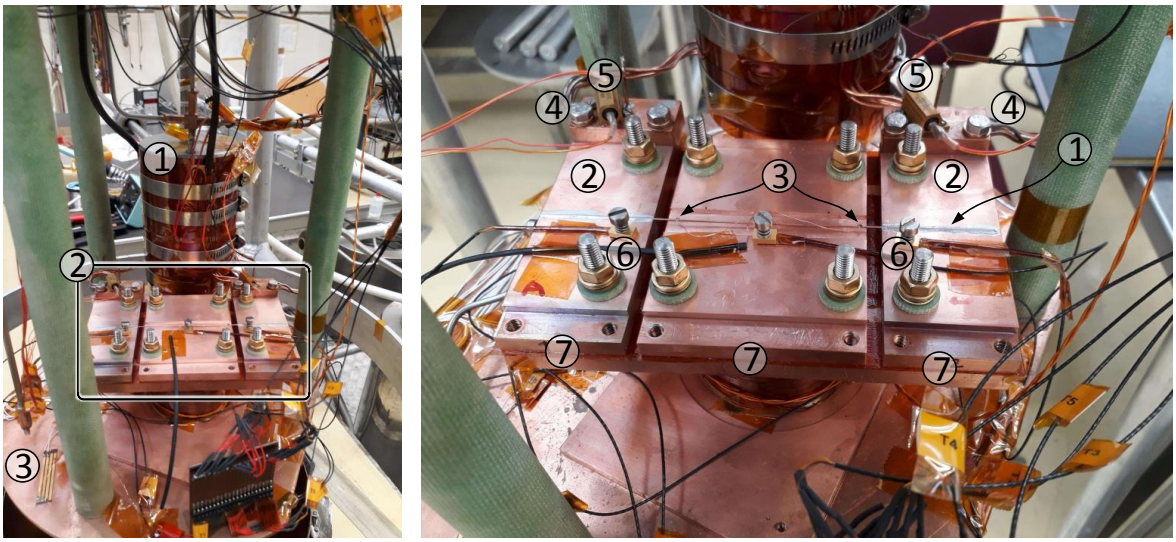

(a) (b)

Figure 3.15: Sample holder in the cryostat setup. **(a)** Setup with phase separator in the rear and assembled sample holder in the front, 1. Phase separator, 2. Sample holder including sample, 3. Cooling plate. **(b)** Installed sample holder, 1. Specimen, 2. Current connector plates, 3. Voltage taps, 4. Current leads connections, 5. Heaters, 6. Temperature sensor, 7. Groove for transport lock (stainless steel bars).

In order to evaluate also the critical temperature T_c and to estimate the temperature range for the high-current measurements, a thermovoltage-compensated resistance measurement was carried out. The thermoelectric voltage V_{EMF} is constant and inherently associated with low-temperature measurements. Thus, compensation within the resistance measurements was necessary. In the present work, this was implemented by making two measurements with currents of opposite polarity within a single measurement cycle. Each final measurement point was a result of a voltage measurement of the specimen with positive current polarity $V_{M+} = V_{EMF} + RI$ and a negative polarity $V_{M-} = V_{EMF} - RI$. In the end of the 1.5-s-long measurement cycle, the thermoelectric voltage was cancelled by combining these measurements and calculating the actual voltage drop at the sample

$$V_M := \frac{V_{M+} - V_{M-}}{2} = IR. \tag{3.20}$$

The resistance of the specimen was then obtained by $R = {}^{V_M}/_{I}$. The measurement current I was 100 mA, which led to a current density of $J = 0.75\,\mathrm{A\,mm^{-2}}$ within the sub-elements. Considering that only low temperature ramps up to $0.2\,\mathrm{K\,min^{-1}}$ were used, the temperature-dependent change of V_{EMF} was neglected. Figure 3.20 shows typical data recording obtained by using the established measurement routines, including the corresponding analysis.

Further instrumentation, e.g. additional voltage taps and temperature sensors, was acquired by using a nanovoltmeter (*Keithley multimeter model 2001*) equipped with a scanner card. Consequently, the contact resistance and the resistance of the current leads were analysed by using the installed voltage taps, which is presented in Section 4.2.

All measurement and control devices were connected via GPIB or USB with a PC, which is schematically shown in Figure 3.17. For controlling and data recording, a software written in Python using the instrumentation library PyVISA [126] and the scientific library SciPy [146] was developed. The measurement environment, including the operating cryostat, can be seen in Figure 3.16.

In order to install the current leads, a first estimation was made. The passively-cooled two-stage current leads were thermalised at the thermal shield by using interception electric breaks and at the phase separator, which is illustrated in Figure 3.13. This leads to the separation of a warm and a cold part modelled with fixed temperatures at their ends. The warm part was installed from the outside, $T_{warm,upper} = 290\,\mathrm{K}$, to the thermal shield, assumed with $T_{warm,lower} = 77\,\mathrm{K}$. The cold part was connected from the thermal shield $T_{cold,upper} = 77\,\mathrm{K}$ to the phase separator, $T_{cold,lower} = 4\,\mathrm{K}$. The objective of the estimation was to find the optimal cross section A of the current lead to minimise the heat influx from outside. This leads to a compromise of heat conduction, which decreases by reducing the cross section, and the Joule heating, which decreases with increasing cross section.

An overview of this matter was provided by modelling a single current lead as an one-dimensional

(a) **(b)**

Figure 3.16: Measurement environment. **(a)** Measurement station. **(b)** Cryostat setup in vacuum chamber during operation including vacuum pump system in the background.

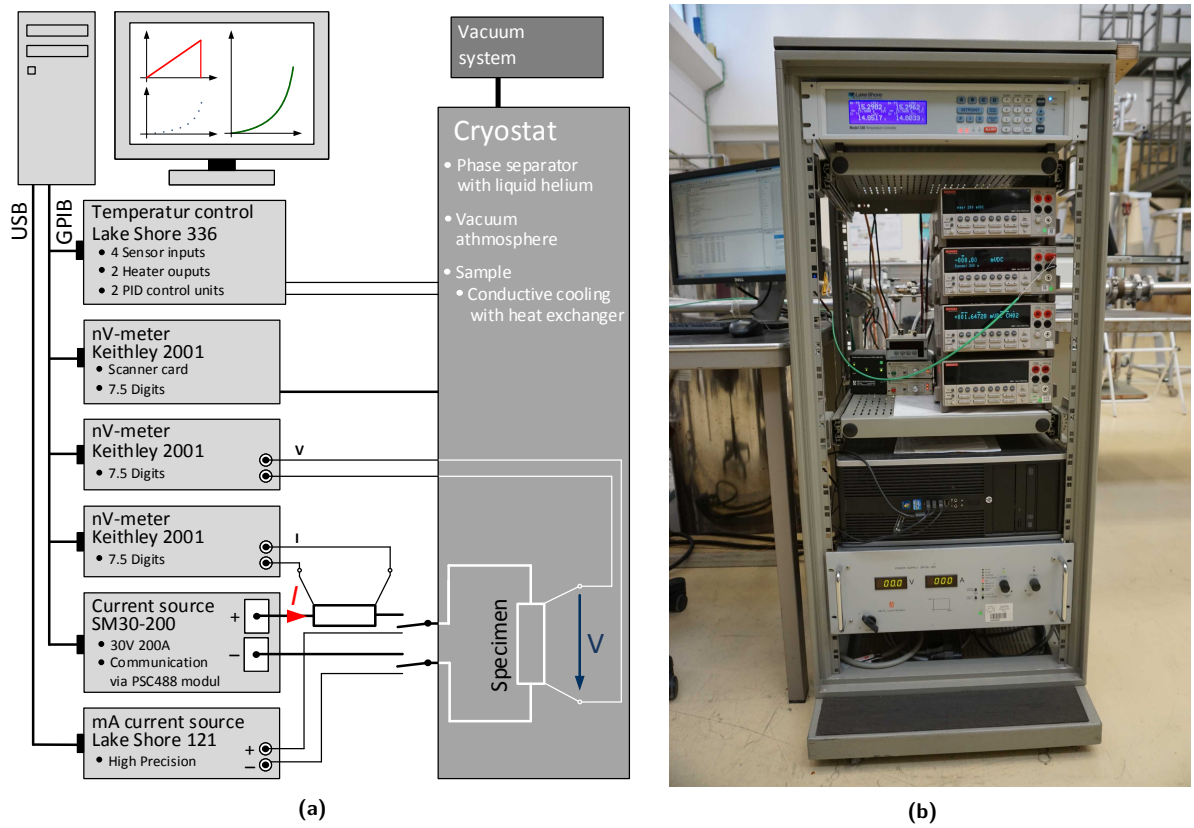

(a) **(b)**

Figure 3.17: Measurement and control system. **(a)** Schematics and wiring of equipment. **(b)** Measurement tower installed next to the cryostat.

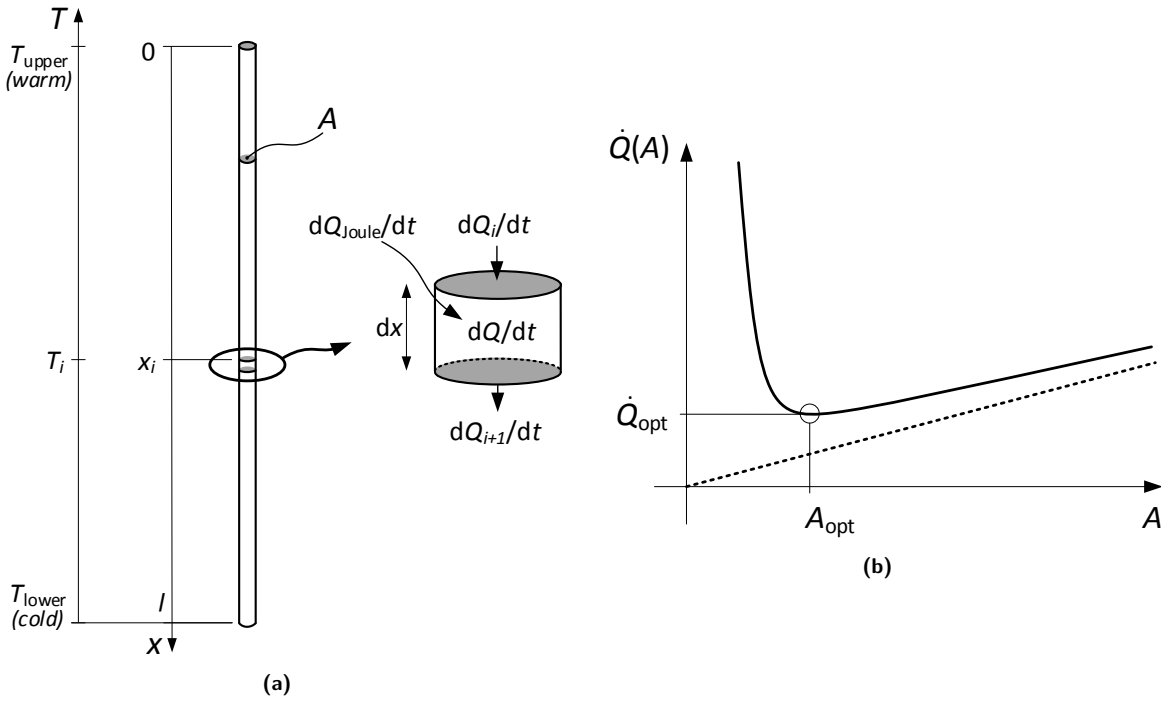

Figure 3.18: Model of a passively-cooled current lead. **(a)** Idealised infinitesimal model to derive the heat influx of a high-current lead. **(b)** Heat transfer at the cold end as a function of the cross section with (solid line) and without (dashed line) a constant current.

conductor with cross section A, length l and current I as illustrated in Figure 3.18(a). The steady-state heat power equation for an infinitesimal slice $\mathrm{d}V = A\,\mathrm{d}x$ of the current lead can be postulated as

$$\frac{\mathrm{d}Q}{\mathrm{d}t} = \frac{\mathrm{d}Q_i}{\mathrm{d}t} - \frac{\mathrm{d}Q_{i+1}}{\mathrm{d}t} + \frac{\mathrm{d}Q_{\mathrm{Joule}}}{\mathrm{d}t} \tag{3.21}$$

with

- the total heat energy stored in the slice $\mathrm{d}Q$ with the specific heat capacity $c = \frac{1}{\rho_\mathrm{m}\mathrm{d}V}\frac{\mathrm{d}Q}{\mathrm{d}T}$ and volume mass density ρ_m,
- the incoming heat energy from the warm end by heat conduction $\frac{\mathrm{d}Q_i}{\mathrm{d}t} = -\lambda A\frac{\partial T(x_i)}{\partial x}$ with thermal conductivity λ and temperature T,
- the outgoing heat energy to the cold end by heat conduction $\frac{\mathrm{d}Q_{i+1}}{\mathrm{d}t} = -\lambda A\frac{\partial}{\partial x}\left[T(x_i) + \frac{\partial T(x_i)}{\partial x}\mathrm{d}x\right]$ and
- the Joule heating $\frac{\mathrm{d}Q_{\mathrm{Joule}}}{\mathrm{d}t} = I^2\rho\frac{\mathrm{d}x}{A}$ caused by electrical current I with electrical resistivity ρ.

By using the above-listed aspects, Equation 3.21 can be written for the general case ($x = x_i$) and in the settled condition ($\dot{T} = 0$) as

$$\frac{\partial^2 T}{\partial x^2} = -\frac{I^2\rho}{\lambda A^2}. \tag{3.22}$$

The temperature along x of the one-dimensional model can be derived from the linear ODE second-order (Equation 3.22) with $\Delta T = T_\mathrm{upper} - T_\mathrm{lower}$ and the boundary conditions $T(x = 0) = T_\mathrm{upper}$ and $T(x = l) = T_\mathrm{lower}$

$$T(x) = -\frac{\rho I^2}{2A^2\lambda}x^2 + \left(-\frac{\Delta T}{l} + \frac{\rho I^2 l}{2A^2\lambda}\right)x + T_\mathrm{upper}. \tag{3.23}$$

To get the desired heat flux through the cross section of the cold end ($x = l$), one must use the heat conductivity equation

$$\dot{Q}\big|_{x=l} = -A\lambda\frac{\partial T}{\partial x}\bigg|_{x=l} = A\lambda\frac{\Delta T}{l} + \frac{\rho I^2}{2}\frac{l}{A} = \dot{Q}(A), \tag{3.24}$$

Table 3.4: Optimisation of the cross-section area A of the current leads, made of copper ($RRR = 100$) to minimise heat influx.

	warm part	cold part
T_{upper}	290 K	77 K
T_{lower}	77 K	4 K
l	0.6 m	0.6 m
I	150 A	150 A
A_{opt}	25 mm^2	9 mm^2
$\dot{Q}_{\text{opt}}$	6.15 W	1.2 W
A_{used}	25 mm^2	10 mm^2

which can be interpreted as a function of the cross section as shown in Figure 3.18(b). For a large cross-section area, the Joule heating has only a minor impact, and the entire influx converges to an exclusive thermal transfer. If the cross section area is chosen to be small, the influx is dominated by the Joule heating. The local minima of this function, hence the desired optimal cross-section area A_{opt}, and the corresponding minimum heat input $\dot{Q}_{\text{opt}}$ are given by

$$A|_{\min_{A>0} \dot{Q}(A)} = A_{\text{opt}} = \sqrt{\frac{\rho}{2\lambda\Delta T}}\, Il \quad \text{and} \tag{3.25}$$

$$\min_{A>0} \dot{Q}(A) = \dot{Q}_{\text{opt}} = I\sqrt{2\rho\lambda\Delta T}, \quad \text{respectively.} \tag{3.26}$$

The optimal cross-section area is often reported independently of the application-dependent quantities as the shape factor

$$SF = \left(\frac{Il}{A}\right)_{\text{opt}} = \sqrt{\frac{2\lambda\Delta T}{\rho}}, \tag{3.27}$$

and can be looked up in graphs for given material properties in the relevant specialised literature, see for example in Reference [55]. For the present work and under consideration of the temperature dependence of thermal conductivity $\lambda(T)$ and the resistivity $\rho(T)$ of copper assumed to be $RRR = 100$, the shape factor $SF = 3.6 \cdot 10^6\,\text{A m}^{-1}$ for the warm part with $T_{\text{upper}} = 290\,\text{K}$ and $T_{\text{lower}} = 77\,\text{K}$ was chosen based on R. McFee [127]. For the cold part, $SF = 10 \cdot 10^6\,\text{A m}^{-1}$ was used. This led to an optimum cross section of 25 mm^2 and 9 mm^2 for the warm and the cold part, respectively, for a current of 150 A and a length of 0.6 m. The results are summarised in Table 3.4. In this context, it should be mentioned that an increase of the RRR of the copper evokes almost no advantage above 77 K, hence only the cold part can be improved by increasing the RRR [155].

3.3.3 Data evaluation & measurement procedure

Within the NearT_c measurements, the critical current $I_c|_{T=\text{const.}}$ of the recorded $V(I)|_{T=\text{const.}}$ curves were evaluated. As described in Section 3.2.3, the electrical field criterion $E(I = I_c) = E_c$ with $E = V/l$ and the voltage-tap spacing l was chosen for this work to determine the critical current I_c. Based on the resolution of the nanovoltmeters and the noise level, it was decided to increase the electrical field criterion E_c to 100 µV m^{-1}. As an abort criterion, i.e. quench criterion, 250 µV m^{-1} was defined.

$V(I)$ curves were recorded with a typical current ramp rate of 1 A s^{-1}, whereas the sample temperature T_s was stabilised at certain levels in the range of T_c to $T_c - 1\,\text{K}$ with steps of 0.1 K. On average, five $V(I)$ curves were recorded at every temperature level. A typical $V - I$ recording and the subsequent I_c evaluation is shown in Figures 3.20(a) and 3.20(b). No significant current-transfer voltage could be observed and consequently only the offset voltage was corrected. In contrast to the cable measurements, recording clearly above the threshold E_c could be performed. Hence, the critical current could be evaluated by interpolating the recording with a sampling rate of 200 ms. The actual sample temperature at the I_c determination point was also obtained by interpolating the temperature recording, annotated in the I_c analysis (cf. Figure 3.20(b)). The n value was evaluated according to the standard of I_c measurement for Nb_3Sn wires [159] by fitting a slope in the double-log depiction around the criterion, as shown in Figure 3.19.

Owing to initial stabilisation problems, the current-sharing temperature $T_{cs}|_{I=\text{const.}}$ was analysed redundantly by recording $V(T)|_{I=\text{const.}}$ curves with a typical temperature ramp rate of 0.2 K min^{-1}. Therefore, the sample current I was set to certain value in the range from 1 A to 100 A with steps greater than 5 A. At least three $V(T)$ curves were measured at every current level to check the repeatability of the

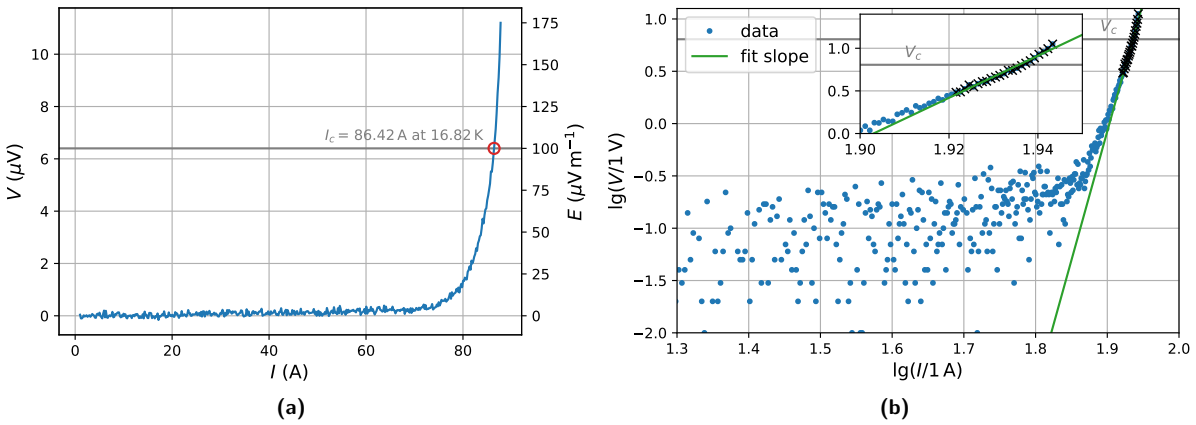

Figure 3.19: Illustration of the I_c and n value evaluation, according to the standard [159]. **(a)** Offset-corrected $V(I)$ relation to determine the critical current I_c (red marker) at the critical field criterion $E_c = 100\,\mu V\,m^{-1}$. **(b)** Evaluation of the n value by fitting the linear slope in double-log depiction around the voltage criterion $V_c = E_c\,l$ with the voltage-tap spacing l. Data points used for the fitting are marked with crosses. The evaluation of the n value is enlarged in the small plot.

measurement procedure. A typical $V - T$ measurement and the subsequent T_{cs} evaluation are shown in Figures 3.20(c) and 3.20(d). Analogous to the I_c evaluation, the current-sharing temperature as well as the actual current were interpolated at the determination point $E(T = T_{cs}) = E_c$ annotated in the analysis (cf. Figure 3.20(d)).

The low-resistance measurement developed in this work facilitated the evaluation of the resistive transition, i.e. the critical temperature T_c, and the RRR. A resistance recording, including the sample temperature, in the transition region is shown in Figure 3.20(e). In order to trace possible delays of heat transfer, the resistive transition was measured with an increasing and a decreasing temperature ramp, designated as R_{up} and R_{down}, respectively. The subsequent analysis is plotted in Figure 3.20(f), which reveals no hysteresis effect. At least three $R(T)$ measurements with a typical temperature ramp of $0.1\,K\,min^{-1}$ were performed to test the reliability of the measurement. For the data interpretation, the "mid-point" criterion was used. Hence, the resistive plateau and the transition were fit linearly. The temperature at the intersection of the two fits, labelled $T_{c,tan}$, and the temperature at the zero point of the transition fit, labelled $T_{c,zero}$, are used to characterise the resistive transition. The "mid-point" critical temperature $T_{c,midpoint}$ and transition width ΔT_c are defined as

$$T_{c,midpoint} = \frac{T_{c,tan} + T_{c,zero}}{2} \quad \text{and} \quad \Delta T_c = T_{c,tan} - T_{c,zero}, \tag{3.28}$$

and were used for the analysis in Section 4.2.2. Additionally, the RRR was evaluated to obtain information about the copper matrix after transverse stress applied at RT. It was performed in the course of the cool down of the system. The residual resistance ratio RRR [158] was defined as

$$RRR := \frac{\rho(T_s = 293\,K)}{\rho(T_s = 19\,K)}. \tag{3.29}$$

In the end, it must be mentioned that the transition width ΔT_c as well as the n value depend strongly on the definition, particularly the n value on the threshold E_c, and have to be taken into account when comparing the reported results with the values reported by other authors.

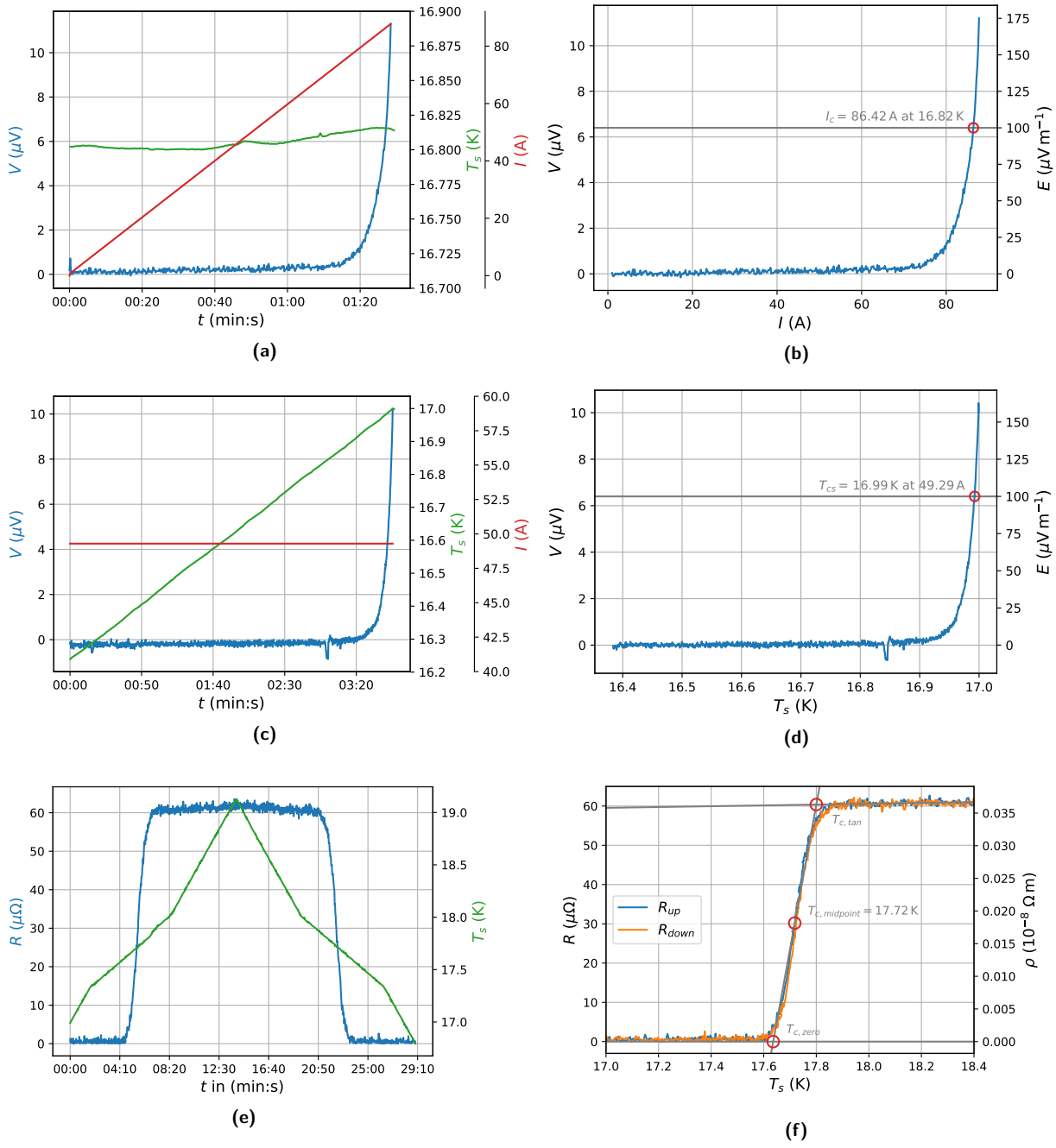

Figure 3.20: Typical measurement recordings and analyses performed with the NearT_c setup. **(a)** $V - I$ recording at $T_s = 16.8\,\mathrm{K}$ with ${}^{dI}/_{dt} = 1\,\mathrm{A\,s^{-1}}$. **(b)** I_c analysis of (a) with an electrical field criterion $E_c = 100\,\mu\mathrm{V\,m^{-1}}$. **(c)** $V - T$ recording at $I = 50\,\mathrm{A}$ with ${}^{dT}/_{dt} = 0.2\,\mathrm{K\,min^{-1}}$. **(d)** T_{cs} analysis of (b) with an electrical field criterion $E_c = 100\,\mu\mathrm{V\,m^{-1}}$. **(e)** Thermovoltage-compensated resistance measurement around $T = T_c$ with ${}^{dT}/_{dt} = \pm 0.1\,\mathrm{K\,min^{-1}}$. **(f)** Resistive transition on the base of (e).

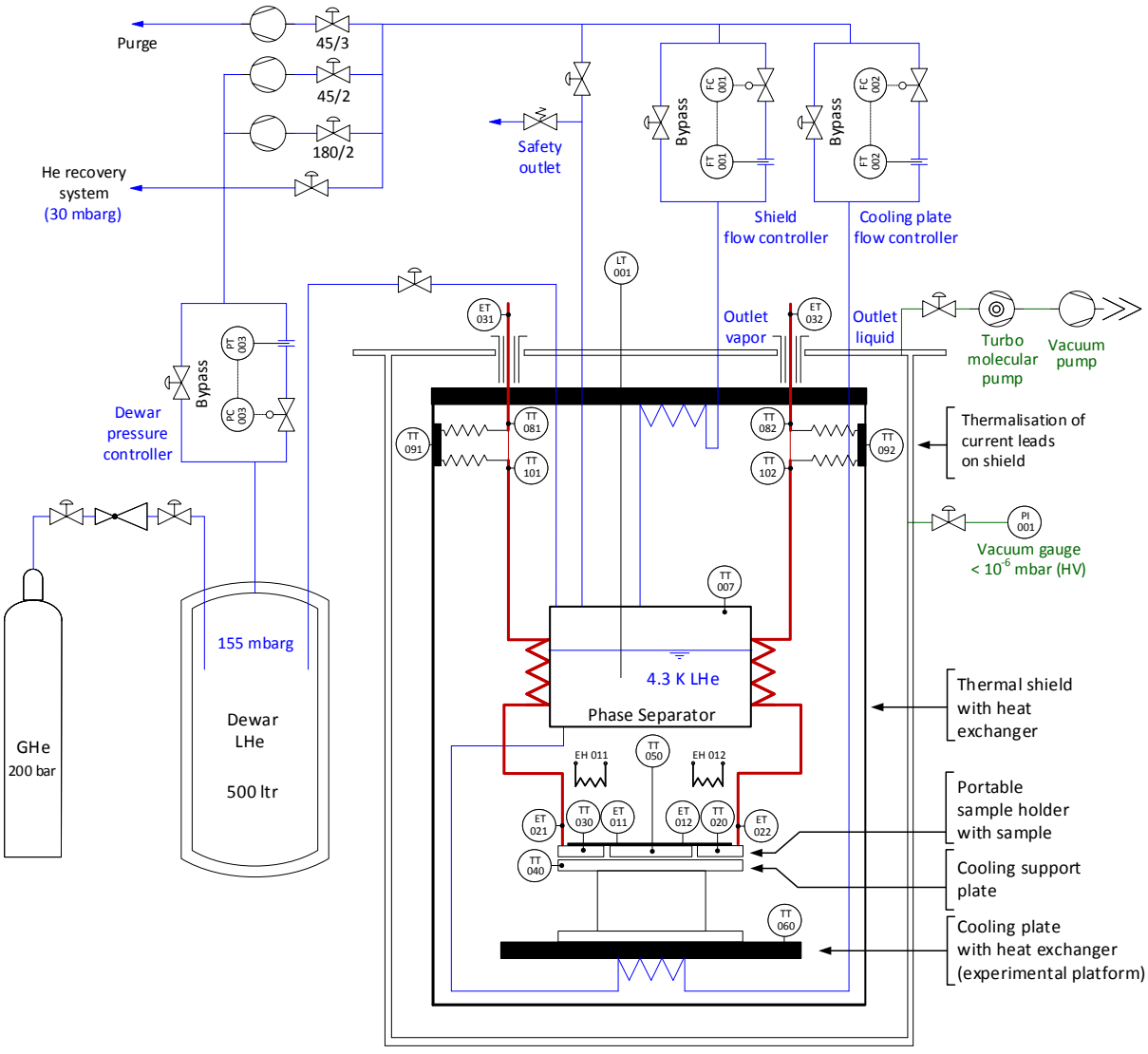

Figure 3.21: PID of the setup in the cryostat showing the thermalisation of the current leads at the thermal shield and at the LHe phase separator before reaching the variable temperature platform housing the sample.

3.4 Measurements of wires with the SQUID magnetometer

Additional magnetisation measurements were performed to confirm the results of the transport current measurements of the wire. It extended the measurement range of the wire investigation to lower temperatures and various applied fields. Moreover, this campaign also aimed at clarifying the suitability of magnetometric methods for crack detection. Magnetisation measurements are a common and efficient tool to investigate the properties of superconductors.

The magnetisation of a superconductor, especially the irreversible magnetisation of a hard superconductor, indirectly contains information about additional quantities, e.g. intrinsic properties and the critical current. With the help of sufficiently accurate models, the desired variables can be derived quantitatively. In general, magnetometry has substantial advantages over transport current measurement:

- Heating of the specimen is negligible, and sample contacts are not necessary. Hence, no current-transfer length has to be respected.
- Measurements can be performed in temperature and field ranges, which usually are not accessible by transport current measurements due to extremely high critical currents (several kA).
- Magnetisation measurements are less time consuming, which implies a lower consumption of liquid helium.

Nevertheless, magnetometry also has drawbacks:

- Weak control of underlying assumptions, e.g. granularity of sample.
- Models are only valid under certain requirements, e.g. assumption of a point-like sample requires a much smaller sample length than the pickup coil assembly.
- Careful data analysis is mandatory to avoid misinterpretation.

In this work, magnetisation measurements were performed on transverse loaded and non-loaded samples with a length of approximately 4 mm. The SQUID magnetometer *Quantum Design MPMS XL* and the sample holder at TU Wien (Atominstitut) used for present investigation can be seen in Figure 3.22. The system facilitates magnetisation measurements in a temperature range from 1.9 K to 400 K with a stability of ±0.5 %. Moreover, it provides an applied field of up to 7 T with 0.01 % non-uniformity in the measurement region. The system has a liquid helium consumption of roughly $5\,\mathrm{L\,d^{-1}}$ when operating at low temperatures. The samples were always installed perpendicular to the applied field to simulate similar conditions to those observed in a magnet.

The SQUID magnetometer employs a second-order gradiometer pickup assembly, which houses the sample during the measurement. It is further linked to the shielded RF SQUID device via a flux transformer. Such gradiometers house a single coil with two turns clockwise and two coils of one turn counter-clockwise spaced symmetrically outside (20 mm coil diameter, 30 mm between top and bottom coil), as illustrated in Figure 3.23(b). They are optimised to reject outer disturbance fields and detect the dipole moment of the sample within the gradiometer. The SQUID device functions as a magnetic flux-to-voltage converter of unsurpassed sensitivity that measures the net flux of the sample, which is modelled as a point-like object. The magnet dipole moment m of the sample is evaluated by analysing the voltage obtained from the SQUID device. The MPMS XL exhibits the following three basic measurement modes:

1. *DC measurement with standard sample holder:*
   This method represents the most basic measurement. It moves the sample through the 30-mm-long gradiometer in small steps while the SQUID response voltage and the corresponding sample position is recorded. The desired magnetic moment m of the sample can then be obtained from the recorded voltage over the position curve (raw data) by fitting the data points to the theoretical curve
   $$V(z) = -\frac{ma^2}{2}\left[\frac{1}{((z+d)^2+a^2)^{3/2}} - \frac{2}{(z^2+a^2)^{3/2}} + \frac{1}{((z-d)^2+a^2)^{3/2}}\right], \tag{3.30}$$
   with the actual coil radius of $a = 10.1\,\mathrm{mm}$ and length between the upper and lower coil of $2d = 30.4\,\mathrm{mm}$ as shown in Figure 3.23(a). The Quantum Design MPMS XL software calculates the magnetic moment m from the fit function amplitude. Hence each value m is related to a raw curve $V(z)$. By default, the final value $m(B_{\mathrm{app}}, T)$ is obtained as an average over three measurements taken under the same conditions with the standard deviation. As shown by past investigations by T. Baumgartner in Reference [15, p.70], the additional RSO is less vulnerable to undesired disturbance fields and hence delivers more reliable results. Thus, this mode was avoided for the final measurements presented in this work.

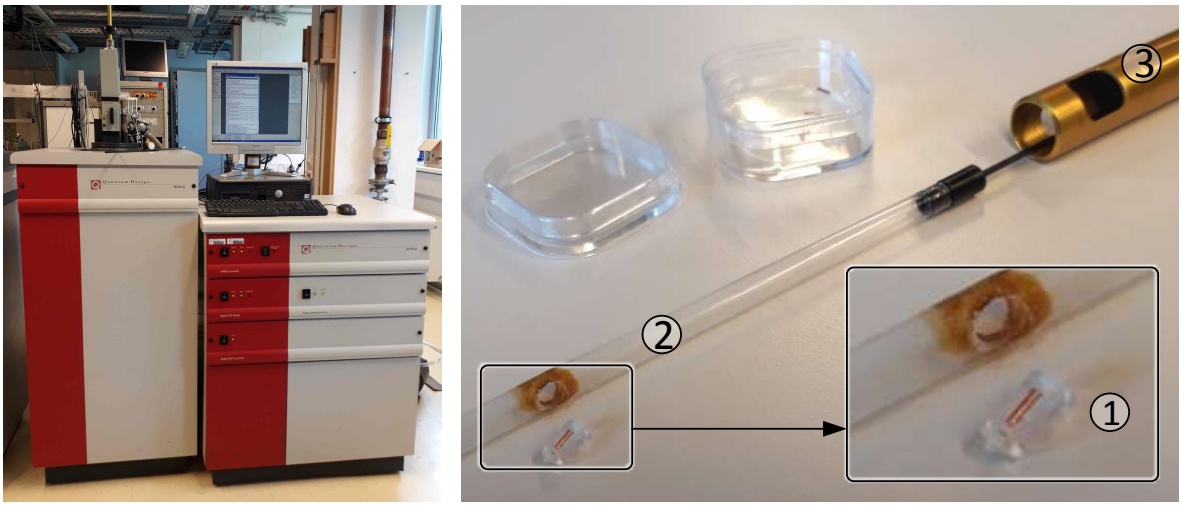

(a) (b)

Figure 3.22: Equipment for the magnetisation measurements. **(a)** SQUID magnetometer Quantum Design MPMS XL with the installed RSO. **(b)** RSO rod and sample holder made from a 180-mm-long transparent straw and a 6-mm-long silica glass tube housing the typical 4-mm-long sample for magnetisation measurements to place the sample perpendicular to the applied field. 1. Sample in glass tube, 2. Sample holder, 3. RSO rod.

2. *DC measurement with the Reciprocating Sample Option (RSO):*
   This method was used to evaluate the critical current density $J_c(B, T)$ of wire specimens, based on the measurement of magnetisation loops. It is discussed in Section 3.4.1.

3. *AC susceptibility measurement:*
   This method was used to evaluate the critical temperature T_c and to extrapolate the upper critical field B_{c2} of loaded and non-loaded wires. It is further described in Section 3.4.2.

3.4.1 DC measurement with the RSO

The RSO is an extended mode for DC measurements and increases the sensitivity of the system, as mentioned above. Therefore, the RSO appliance is attached to the top of the MPMS XL cryostat and the brass RSO rod must be used as shown in Figure 3.22. After assembling the sample holder, the sample is placed between the centre pickup coil and the upper pickup coil, where the SQUID response function has its maximal slope (cf. Figure 3.23(a)). While the measurements are being taken, the sample rapidly oscillates around the centre position, which converts the system into a vibrating sample magnetometer (VSM) with a SQUID sensor. The SQUID magnetometer collects data within the selected amount of cycles. As long as the periodical displacement of the sample stays within the linear range of the SQUID response function $V(z)$, the received voltage-to-sample-position relation will remain linear. In the end, the MPMS XL software computes the magnetic moment by linearly fitting the data point collected during the cycles. The final value $m(B_{app}, T)$ is an average over three measurements taken under the same conditions. Amplitude and frequency of the oscillation can be set in a range of 0.5 mm to 50 mm and 0.5 Hz to 4 kHz, respectively. The parameters chosen for the presented work are listed in Table 3.5.

The sample holder was made of an approximately 180-mm-long straw with a diameter of approximately 7 mm, as recommended by Quantum Design, and glued with vacuum grease to the sample rod for the RSO measurements. The sample was placed transversely in the middle of the sample holder by using a small silica glass tube, which ensures a reproducible installation of the sample, perpendicular to the applied field during the measurements. The sample was additionally fixed with vacuum grease.

In order to obtain the critical current density, the magnetisation loops $m(B_{app})$ at a certain constant temperature T of the sample were measured automatically. Therefore, the sample was previously magnetised with an applied field of −3 T. Subsequently, the applied field B_{app} was ramped from zero to the maximum and back to zero. Hence, two-quadrant magnetisation loops were recorded. The irreversible magnetic moment is given approximately by

$$m_{irr}(B) = \frac{m_{dec}(B = B_{app} + B_{self}) - m_{inc}(B = B_{app} - B_{self})}{2}, \tag{3.31}$$

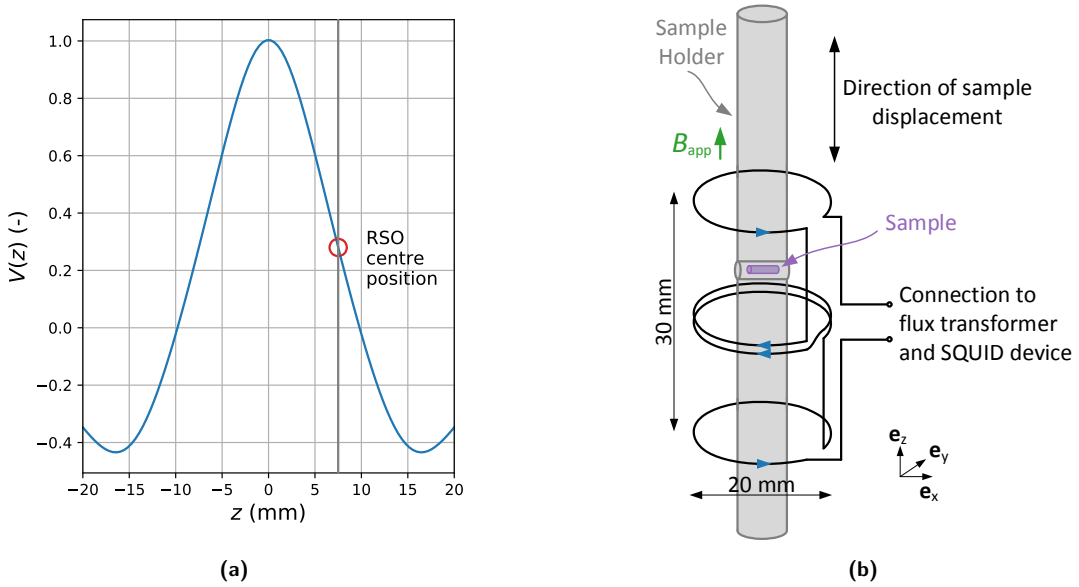

Figure 3.23: **(a)** SQUID sensor response as a function of the sample position in the gradiometer with the middle coil as the centre $z = 0\,\text{mm}$. **(b)** Second-order gradiometer of the SQUID magnetometer used to measure the dipole moment of the sample.

where $m_{\text{dec}}(B)$ and $m_{\text{inc}}(B)$ are the magnetic moments measured in the decreasing and increasing applied field, respectively. The quantity B_{self} is the magnetic self-field of the sample, which depends on the irreversible currents in the sample having different signs on the decreasing and increasing measurement loop. Consequently and as indicated in Equation 3.31, the self-field contributes either positively or negatively to the magnetic field B in the case of the decreasing or increasing loop. Hence, the calculation of the irreversible magnetisation $m_{\text{irr}}(B)$ inherently implies a first-order self-field correction and only higher-order components are not considered. Previous investigations of RRP wires concluded that the self-field B_{self} stays below 0.15 T even at high critical currents above $5 \cdot 10^{10}\,\text{A m}^{-2}$ and thus makes only a minor contribution to the entire magnetic field B for $B > B_{\text{self}}$ [15, p.90]. For these reasons, it was decided that the first-order self-field correction is sufficient for the present evaluation, i.e. $m_{\text{irr}}(B)$ defined by Equation 3.31 was assumed for the following analysis.

The relation between irreversible magnetisation $m_{\text{irr}}(B)$, which is indirectly measured with the magnetometer, and the critical current density $J_c(B,T)$ depends only on geometric factors, which will be demonstrated as follows.

In general, the magnetic moment $\mathbf{m}$ of a current distribution $J(\mathbf{r})$ within a closed volume $\mathcal{V}$ is defined as

$$\mathbf{m} = \frac{1}{2}\int_{\mathcal{V}} \mathbf{r} \times \mathbf{J}(\mathbf{r})\mathrm{d}\mathcal{V}. \tag{3.32}$$

The circumstances within the superconductor during the above-explained magnetisation measurement can be described with the Bean's critical state model[1] [19]. This assumes that the superconductor is a fully penetrated hard superconductor and $J(\mathbf{r}) = J_c$ throughout the entire superconducting volume, which leads to

$$\mathbf{J}(\mathbf{r}) = J_c\,\mathbf{e}_J(\mathbf{r}), \tag{3.33}$$

with $\mathbf{e}_J(\mathbf{r})$ as the local direction of the current. Using Equation 3.33 in Equation 3.32 delivers

$$\mathbf{m}_{\text{irr}} = J_c\,\frac{1}{2}\int_{\mathcal{V}} \mathbf{r} \times \mathbf{e}_J(\mathbf{r})\,\mathrm{d}\mathcal{V}, \tag{3.34}$$

and implies that the irreversible magnetic moment of the superconductor is proportional to its critical current density and the proportional factor is dependent only on the geometric matter, as was assumed before.

In order to derive a relation between the magnetic dipole moment and the critical current, the subelements were modelled to generate an analytical solution. A detailed model would be helical tubes

[1] The model assumes an ideally hard superconductor and is used to assess the critical current of technical superconductors from their irreversible magnetisation. It implies the Shubnikov phase with a macroscopic homogeneous magnetic field distribution. The field generates a current density within the material, which is assumed to be constant and equal to the critical current density.

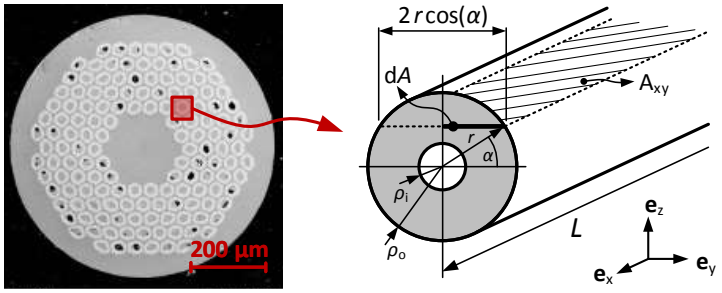

Figure 3.24: Modelling of the superconducting sub-elements as straight, parallel and hollow cylinders without magnetic coupling to yield an analytical relation between the magnetic dipole moment (z direction) and the corresponding planar current loop (XY-plane). Considering that the length and diameter of the samples are small with respect to the sub-element twist pitch, these simplifications are reasonable.

oriented transversely to the applied field, which are coupled magnetically. Considering that the analytical description of helical tubes are quite complex and the sample's dimensions are much smaller than the sub-element twist pitch, some helpful simplifications without major deviation from reality can be made. Hence, the sub-elements are idealised as straight, parallel and hollow cylinders with no coupling. The model, including the coordinate system, is illustrated in Figure 3.24.

The following discussion derives the relation between the magnetic dipole moment and the critical current of a single idealised sub-element and, in the end, is extrapolated to the moment of the entire wire by multiplying it with the number of sub-elements.

Considering that the applied field is parallel to the z-axis, the current loops, which produce the magnetic moment, flow parallel to the XY-plane with the amount J_c according to the Bean model. It can be calculated by splitting the sub-element into infinitesimally flat slices parallel to the XY-plane, carrying a circular-flowing infinitesimal current $\mathrm{d}I = \mathrm{d}I_c$. Hence, the moment $\mathrm{d}\mathbf{m}$ of the infinitesimal slice is defined as

$$\mathrm{d}\mathbf{m} = \underbrace{J_c \mathrm{d}A}_{\mathrm{d}I_c} \; \underbrace{A_{xy}\mathbf{e}_z}_{\mathbf{A}_{xy}}, \tag{3.35}$$

with the infinitesimal cross section $\mathrm{d}A$, through which the current density J_c flows. The vector area $\mathbf{A}_{xy} = 2\,r\cos(\alpha)\,L$ with the sample length L is illustrated in Figure 3.24. In the next step, the entire magnetic dipole moment of an idealised sub-element can be calculated by accumulating $\mathrm{d}\mathbf{m}$ of all slices, hence integrating the entire cross section (YZ-plane) of the sub-element. Therefore the infinitesimal cross section $\mathrm{d}A$ is translated into polar coordinates by using the Jacobian determinant

$$\mathrm{d}A = \mathrm{d}x\,\mathrm{d}y = \left|\det\frac{\partial(x,y)}{\partial(r,\alpha)}\right| \mathrm{d}r\,\mathrm{d}\alpha = r\,\mathrm{d}r\,\mathrm{d}\alpha, \tag{3.36}$$

and leads to

$$\mathrm{d}\mathbf{m} = J_c\,2\,L\,r^2 \mathrm{d}r\,\mathrm{d}\alpha\cos(\alpha)\,\mathbf{e}_z. \tag{3.37}$$

The integration over the half annulus with ρ_i and ρ_o as the inner and outer radii yields the irreversible magnetic moment of a single sub-element:

$$\begin{aligned}
\mathbf{m}_{irr} &= \int_{\rho_i}^{\rho_o}\int_{-\frac{\pi}{2}}^{\frac{\pi}{2}} d\mathbf{m} = 2\int_{\rho_i}^{\rho_o}\int_{0}^{\frac{\pi}{2}} d\mathbf{m} \\
&= 4J_cL\int_{\rho_i}^{\rho_o}\int_{0}^{\frac{\pi}{2}} r^2\cos(\alpha)\,\mathrm{d}r\,\mathrm{d}\alpha\,\mathbf{e}_z = 4J_cL\,\frac{\rho^3}{3}\Big|_{\rho_i}^{\rho_o}\sin(\alpha)\Big|_0^{\frac{\pi}{2}}\mathbf{e}_z \\
&= \frac{4}{3}J_cL({\rho_o}^3 - {\rho_i}^3)\,\mathbf{e}_z.
\end{aligned} \tag{3.38}$$

Finally, the result is multiplied by the number of sub-elements N to achieve the irreversible magnetic moment of the entire wire

$$\mathbf{m}_{irr} = \frac{4}{3}J_cNL({\rho_o}^3 - {\rho_i}^3)\mathbf{e}_z. \tag{3.39}$$

For the present measurement condition, the irreversible magnetic moment can be obtained by evaluating the magnetic moment parallel to the applied field, hence m' (z direction), and leads to

$$m_{irr} = \frac{4}{3}J_cNL({\rho_o}^3 - {\rho_i}^3). \tag{3.40}$$

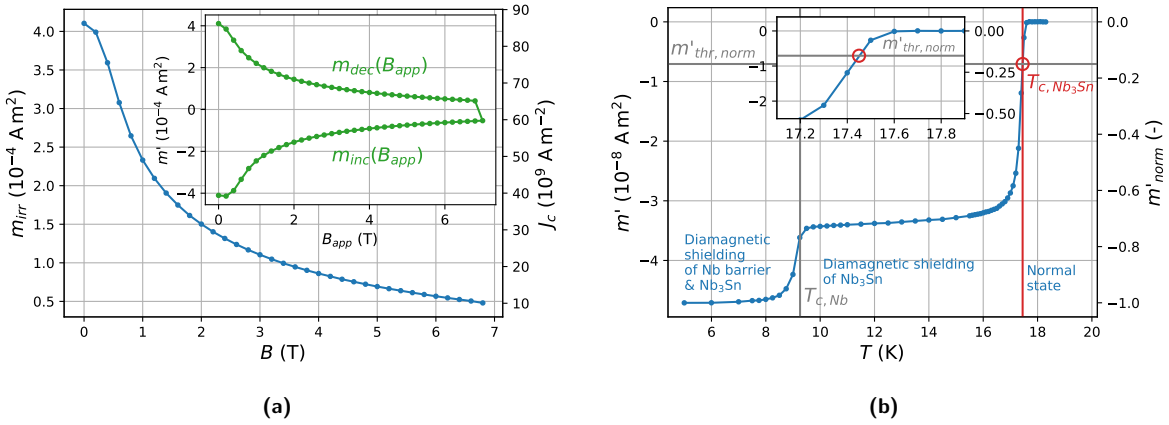

Figure 3.25: Typical measurement data obtained with a SQUID magnetometer. **(a)** Two quadrants of the magnetisation loop of the non-loaded sample after a pre-magnetisation of −3 T (small plot) measured with the RSO and related calculation of the irreversible magnetisation. **(b)** AC susceptibility measurement (in-phase component) of a non-loaded sample for T_c evaluation of Nb_3Sn according to a defined threshold m'_{thr}. The transition of the Nb at $T = 9.3$ K as well as the transition of the reacted Nb_3Sn at 17.45 K are marked by vertical lines. The evaluation of T_{c,Nb_3Sn} is magnified in the small plot.

The final hollow cylinder relation for the RSO measurement in this work was

$$J_c = \frac{3}{4}\frac{m_{irr}}{NL(\rho_o{}^3 - \rho_i{}^3)} = \gamma(N, L, \rho_o, \rho_i)\, m_{irr}, \tag{3.41}$$

with the scalar geometry factor $\gamma(N, L, \rho_o, \rho_i)$ in m^{-4} dependent only on easily determinable variables. The length L was obtained individually for every specimen with a micrometre gauge and the number of sub-elements N as well as the outer and inner radii of the superconducting A-15 phase, ρ_o and ρ_i, respectively, were identified by a SEM and annotated in Figure 2.2. The practical use of Equation 3.41 is demonstrated by the secondary axis in Figure 3.25(a). The postulation of the model and the derivation were firstly done by T. Baumgartner *et al.* [16]. Similar investigations were performed for Nb_3Sn PIT wires by Lindenhovius *et al.* [100].

Table 3.5: Settings for RSO measurements to evaluate the critical current density J_c.

Parameter	Setting
Amplitude	2 mm
Frequency	4 Hz
Number of cycles	20
Measurements per data point	3

Table 3.6: Settings for AC susceptibility measurements to determine the critical temperature T_c.

Parameter	Setting
Amplitude	30 µT
Frequency	33 Hz
Block per measurements	3
Measurements per data point	3

3.4.2 AC susceptibility measurement

An AC susceptometer is established in the form of the AC measurement option, which is frequently used to detect and characterise thermodynamic phase changes, e.g. the transition of Nb_3Sn wires at T_c. A small copper coil around the sample chamber is installed to generate an alternating magnetic field within a frequency range from 0.01 Hz to 1 kHz and an amplitude $B_{app,AC}$ of up to 0.4 mT. The alternating field can be optionally superimposed by the applied DC field $B_{app,DC}$. It should be mentioned here that the magnetic field on the surface of the sample can be up to $(1/1-\eta)$-higher than the macroscopic applied field[2], which is important, for example, for evaluating the lower critical field B_{c1}. Therefore, the effective magnetic field $B_{eff} = (1/1-\eta)B_{app}$ is often established, which represents the maximal value of the magnetic field on the surface of the sample.

[2]The demagnetising factor $0 < \eta < 1$, which depends only on the sample's geometry, considers the enhanced magnetic field at the surface caused by the magnetisation of the sample (shielding currents). Long cylinders transverse to the applied field, i.e. the idealised sub-element, have a demagnetising factor of $\eta = 1/2$ [167, p.25].

The AC field causes a time-dependent magnetic moment in the sample. The field of the time-dependent moment induces a current in the pickup coils, which allows measurements without sample motion. AC fields with low frequency are commonly used to evaluate more precisely the slope $\chi = {\mathrm{d}M}/{\mathrm{d}H}$ of a sample's DC magnetisation curve $M(H)$, called susceptibility. In combination with a DC bias field, different parts of the magnetisation curve are accessible.

For the purpose of the present work, higher frequencies were used, and the entire settings are summarised in Table 3.6. Owing to the hysteretic behaviour of a hard superconductor in the Shubnikov phase, the magnetic moment may lag behind the applied AC field $B_{\mathrm{app,AC}}\cos(\omega t)$. Therefore, the so-called AC susceptibility χ is defined as a complex quantity with magnitude and phase, which can be split into a real part χ' (in-phase) and imaginary part χ'' (out-of-phase). The latter indicates dissipative processes in the sample. The MPMS XL measures the first harmonics of the in-phase component m' and out-of-phase m'' of the magnetic moment and, with the relation $M = {m}/{V} = {\chi B}/{\mu_0}$, it follows that

$$m(t) = \underbrace{\chi' V \frac{B_{\mathrm{eff,AC}}}{\mu_0}}_{m'} \cos(\omega t) + \underbrace{\chi'' V \frac{B_{\mathrm{eff,AC}}}{\mu_0}}_{m''} \sin(\omega t). \tag{3.42}$$

The volume AC susceptibility $\chi = \chi' - i\chi''$ can then be calculated by

$$\chi' = \frac{\mu_0}{V B_{\mathrm{eff,AC}}} m' \qquad \text{and} \qquad \chi'' = \frac{\mu_0}{V B_{\mathrm{eff,AC}}} m'', \tag{3.43}$$

with the superconducting volume V of the sample and the imaginary number i. At this point, it should be noted that the assumption of ideal diamagnetism and accordingly the calculation of B_{eff} using the demagnetisation factor η is only valid if the sample is in the Meißner phase. In the Shubnikov phase, the magnetic field penetrates the material, as discussed in Section 1.2. Consequently, the magnetic self-field of the sample based on its geometry has to be calculated, e.g. numerically and by using the Bean model. The sample's self-field and the applied field can then be superimposed to obtain the effective field B_{eff}.

The measurement procedure can be broken down into blocks, each of which corresponds to a two-point measurement. A certain number of blocks are summarised into one measurement. Each final data point is a result of three repetitive measurements. The average value, including standard deviation, is stored in the output file. According to the MPMS XL manual, the RSO rod can also be used for the AC option. Consequently, it was used to avoid possible inaccuracies by using the standard sample holder, as mentioned at the beginning of this section. The sample was also placed perpendicular to the applied field. In fact, the RSO and AC measurements were performed automatically and subsequently without disassembling the sample from the magnetometer. In addition, the temperature resolution of the measurements was increased around the transition point up to 0.02 K and reduced during the remaining duration of the temperature scan to save measurement time.

Evaluation of the critical temperature T_c

Although the AC susceptibility provides a lot of additional information, it was used only to determine T_c. For that reason, only the corresponding magnetic dipole moments m' and m'' were analysed, which are proportional to χ' and χ'', respectively. As long as the conditions $T < T_\mathrm{c}$ and $B_{\mathrm{app,AC}} < (1-\eta)B_{\mathrm{c1}}(T)$ are valid, the sample stays in the Meißner state, hence it is ideally diamagnetic with a susceptibility of $\chi' \approx -1$ and $\chi'' \approx 0$. Above the critical temperature, a superconductor typically has a low susceptibility $|\chi'| \approx 0$. The transition between these two states can be used to determinate the critical temperature T_c.

Therefore, the sample temperature was typically ramped up from 5 K to 19 K during an applied AC field with an amplitude of 30 µT. A typical response of a 4-mm-long sample can be seen in Figures 3.25(b) and 3.26(a), and the effects are described as follows.

- At the start temperature, the Nb_3Sn and the niobium barrier of the sub-elements are superconducting. Meißner screening currents generate a magnetic moment. Above the transition of Nb, which can be clearly identified at $T_{\mathrm{c,Nb}} = 9.3\,\mathrm{K}$, only the Nb_3Sn parts are superconducting. The critical temperature of niobium was not essential for the scope of the thesis and hence not further investigated. At around $T \approx 17.5\,\mathrm{K}$, the A-15 phase transfers into the normal state, resulting in $m' \approx 0$, which was the part of interest.

- The behaviour of Nb_3Sn in the superconducting state above $T_{\mathrm{c,Nb}}$ and until the actual transition of the A-15 phase reveals information about the homogeneity and micro-structure morphology of

the reacted Nb_3Sn. A continuous creeping rise of the in-phase component m' until the transition T_{c,Nb_3Sn}, in contrast to a sharp jump at T_{c,Nb_3Sn}, is an indication that some parts of the Nb_3Sn area have already turned into the Shubnikov or normal phase.

- Moreover, the AC method delivers the out-of-phase component m''. It is shown with the complete information of a typical scan of a non-loaded sample in Figure 3.26(b). It is almost zero, except slightly below the transition of niobium and Nb_3Sn. As mentioned above, the out-of-phase component indicates the dissipation process in the sample. Thus, the peak of m'' represents the maximum energy loss due to flux flow and absorption, and indicates the beginning of the Shubnikov phase just below where the sample transforms into the normal state.

In order to determine the critical temperature utilizing AC measurements, all measured scans m' were normalised and evaluated at a normalised threshold ${m'}_{\mathrm{thr,norm}} = -0.15$, as indicated in Figure 3.25(b).

Evaluation of the upper critical field B_{c2}

Motivated by the measured difference of T_c of wires loaded with particular transverse stress at RT, the upper critical field B_{c2} was estimated with the help of AC susceptibility measurements. In order to measure the temperature dependency of $B_{c2}(T)$, the critical temperature T_c at different DC bias fields $B_{\mathrm{app,DC}}$ was measured. Unfortunately, the accuracy of the above-described threshold criterion turned out to be insufficient for scans with applied DC fields. Consequently, the peak criterion was used to estimate B_{c2}. Therefore, the transition of selected samples was measured repeatedly with higher resolution. Subsequently, the peak of m'' was used to determine T_c during a particular applied bias field, as indicated in Figure 3.26(b). Owing to the limitation of the applied DC field of 7 T, $B_{c2}(T)$ was evaluated only at high temperatures ($T \geq 3/4\, T_c$).

Nb_3Sn sub-elements within superconducting composite wires can be identified as so-called superconductors in the dirty limit, due to their impurities and disorder. Without going into detail, dirty superconductors are characterised by an electronic mean free path much smaller than the BCS coherence length, i.e. $l \ll \xi_{\mathrm{BCS}}$. Under consideration of the dirty limit and without the Pauli paramagnetic limit[3], the WHH expression for the zero-temperature value of the upper critical field $B_{c2}(0)$ can be simplified to

$$B_{c2}(0) = 0.693\ {T_c}^* \left(-\frac{\mathrm{d}B_{c2}}{\mathrm{d}T}\right)_{T={T_c}^*} \tag{3.44}$$

with the effective critical temperature ${T_c}^*$. Equation 3.44 is commonly used to estimate $B_{c2}(0)$ based on $T_c(B)$ measurements. The effective critical temperature ${T_c}^*$ was used instead of the measured critical temperature T_c at zero applied DC field to reduce the influence of inhomogeneities. The critical temperatures measured at applied DC fields in the range of 2 T to 7 T were used to fit the linear behaviour of $B_{c2}(T)$ at high temperatures

$$\left(-\frac{\mathrm{d}B_{c2}}{\mathrm{d}T}\right)_{T={T_c}^*}. \tag{3.45}$$

The received linear fit was further used to determine ${T_c}^*$, which is known as the extrapolated intercept with the temperature axis.

A typical evaluation of the slope and ${T_c}^*$ can be seen in Figure 3.26(b). The critical temperatures, measured at certain applied fields, are plotted in the $B-T$ diagram (coloured dots). The linear fit of the slope is plotted as a dashed black line. Points that were used for the fit approximation are additionally marked with black crosses. The difference between the extrapolated effective ${T_c}^*$ (black triangle) and T_c (blue dot) is apparent. The small plot shows the peak of the out-of-phase components m'' at a certain DC bias field in the corresponding colour. At an applied field greater than $(1-\eta)B_{c1}(T)$, the samples are explicitly in the Shubnikov phase during the temperature scan, which arises in a lower and more widespread peak of m'' at the transition to the normal state.

[3]This means that the paramagnetic limitation parameter α, also called the Maki parameter, is zero [104, 105]. The complete WHH theory [78, 79, 179] is used to derive the temperature dependence of B_{c2} including the Pauli spin paramagnetism and spin-orbit scattering based on the GLAG theory.

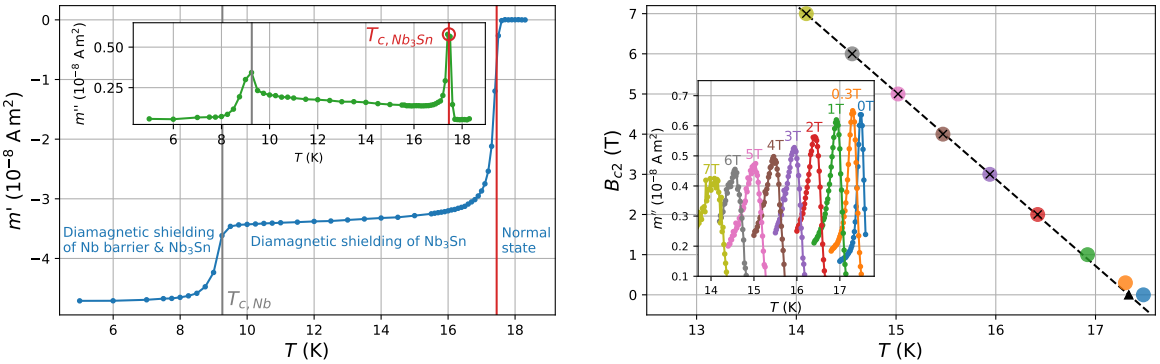

(a) **(b)**

Figure 3.26: Typical estimation of the upper critical field $B_{c2}(0)$ using AC measurements and the WHH expression for dirty superconductors. **(a)** AC susceptibility scan with T_c evaluation according the m'' peak criterion. The peak of m'' indicates the dissipation within the sample slightly below the transition. **(b)** Evaluation of the slope $\mathrm{d}B_{c2}/\mathrm{d}T$ at high temperatures for the WHH expression. The measured T_c at a certain DC bias field (cf. (a)) are plotted in the $B-T$ diagram (coloured dots) as well as the linear fit (dashed line). The points for fitting the slope are marked with a black cross. The effective critical temperature $T_c{}^*$ is marked with a black triangle. The corresponding out-of-phase component m'' at a certain DC bias field used for the T_c is shown in the small plot with the same colour.

3.5 Microscopy of metallographically prepared cables & wires

For the presented work, a field emission gun scanning electron microscope (FEG-SEM) was chosen to perform the microscopy, specifically a *FEI Quanta 250 FEG* for the cable investigation and a *ZEISS FEG Sigma* for the wire investigation.

Both back-scattered electron (BSE) imaging and secondary electron (SE) imaging were used. The BSE imaging yields an image proportional to the atomic number of the observed material. Owing to its high contrast, it was primarily used for an overview of the specimen and the different material components, e.g. niobium diffusion barrier. The SE imaging, implemented with an Everhart–Thornley detector (ETD) in the present case, delivers information mainly about the surface of the specimen. Hence, it was used to analyse the shape of the cracks or to expose initial polishing problems. Additionally, an energy-dispersive X-ray analysis (EDX) was used to identify the components of a sub-element.

In general, an accelerator voltage of 10 kV with a working distance from 8 mm to 12 mm was used with magnifications from 100 to 2000 to characterise cracks with widths as small as approximately 0.2 µm. An accelerator voltage of 40 kV and a magnification of up to 4000 were used to inspect the crack surfaces.

Owing to the average size of cracks, the magnification range of optical microscopes (OM) was sufficient for prior or intermediated inspection. In this case, the digital OM *Keyence VHX-1000E* with the universal lens *VH-Z100UR* was used.

Chapter 4

Results & discussion

All results achieved within the framework of this thesis are summarised and interpreted in this chapter. The results of the critical current measurements and the complementary microscopy investigations on the cable experiment are provided in Section 4.1 and contain information about degradation similar to the actual situation in a magnet. Section 4.2 presents the results of the wire investigations, i.e. the transport and magnetisation measurements as well as the microscopy. It will present and discuss the measured data about the cause and effect of the transverse stress exposed at RT on Nb_3Sn as well as the feasibility of the NearT_c concept. Finally, the conclusion in Section 4.3 summaries the essential achievements, and an outlook in Section 4.4 contributes suggestions for further investigations.

4.1 Results of cable investigations

This section presents the results of the cable investigations, which are based on the stress application at RT and the subsequent I_c measurement of three specimens. In order to provide microscopy information for the cause analysis, the final 200 MPa loaded measured area and a non-loaded area of Specimen 1 were metallographically prepared for an SEM autopsy. In addition, a load study with remaining parts of Specimen 1 was performed to analyse the behaviour of the sub-elements after certain stress at RT.

4.1.1 Stress exertion

Tables 4.1, 4.2 and 4.3 summarise the recordings during the pressing procedure at RT prior to the critical current measurement with the FRESCA test station. This procedure was iteratively performed with increasing load and a minimum step size of 10 MPa until the specimen showed a critical current degradation of approximately 10 %. These tables compare the targeted (nominal) stress $\sigma_{\mathrm{nom}} = {}^{F_{\mathrm{nom}}}/_{A_{\mathrm{nom}}}$ with the stress $\sigma_{\mathrm{LC},\Sigma} = {}^{F_{\mathrm{LC},\Sigma}}/_{A_{\mathrm{nom}}}$ determined by the direct force measurements using the load cells and the nominal pressing area A_{nom}. The maximal measured force within the approximately 2-min-long stress exertion was used for this evaluation. As the error of the actual stress from the nominal stress was less than 2.1 %, the nominal values represent the results in Section 4.1.2. Additionally, the load balance reports the force allocation among the support points of the four load cells. It holds information about the deviation from the desired evenly distributed force ${}^{F_{\mathrm{nom},\Sigma}}/_4$ for each support point, which was adjusted in advance for the high-pressure region within the hydraulic press refurbishment.

In the experiments with Specimens 1 and 2, all pressure steps were performed with the same pressing die described in Section 3.1.1. The difference of the specimens' width originates from the different impregnation mould used for the preparation of Specimen 2. The experiment with the wider Specimen 3 including titanium bars in a sandwich structure (cf. Figure 2.4(b)) exceeded unexpectedly the capacity of the hydraulic system of maximal 180 kN. Accordingly, a shorter die with an equal radius of 3 mm on the edges was made to allow an exertion above 210 MPa with a smaller nominal pressing area.

Additional to the force measurement, pressure-sensitive films were used for the stress measurement, as described in Section 3.1. Figures 4.1, 4.2 and 4.3 show the HHS type films after the stress exertion of the last three steps on the particular specimen. Some stress peaks were observed, which are caused by the surface roughness of the impregnated specimen and can be traced back to the impregnation process. The almost symmetric stress distributions result from the optimisation of the load balance and the stress distribution.

Despite the valuable contribution of Prescale films during optimisation, it was decided to make only a local analysis with these films in the final experiments. Derived global values were deceptive, due to the measurement range of the films, and a comparison with the force $F_{\mathrm{LC},\Sigma}$ was debatable. Stress values outside the measurement range are not included in the statistics, which resulted in a sharp constraining cut of the almost Gaußian-shaped stress distribution in the histogram in Figure 3.2(c). Consequently, the spatial average value of the two-dimensional stress map of stress exertions with a target stress σ_{nom} near the measurement range boundary was inherently falsified, as was the integrated entire force F_{p}. As discussed in Reference [47], the reliability of F_{p} increases with the effective area and the distance of the nominal stress to the measurement range boundaries. Furthermore, the Prescale film exposed to a stress above 250 MPa became deformed so that only a limited local assessment could be made.

Table 4.1: Results of Specimen 1 (HT15OC0190, 11 T dipole project) with a nominal pressing area of $A_{\mathrm{nom}} = (44 \times 15.6)\,\mathrm{mm}^2$.

Nominal		Force measurement					
σ_{nom}	F_{nom}	$F_{\mathrm{LC},\Sigma}$	$\sigma_{\mathrm{LC},\Sigma}$	Load balance			
(MPa)	(kN)	(kN)	(MPa)	(-)	(-)	(-)	(-)
50	34.32	33.60	48.95	1.29	1.13	0.82	0.76
100	68.64	69.37	101.06	1.17	1.09	0.87	0.86
125	85.80	85.59	124.69	1.16	1.07	0.91	0.86
150	102.96	104.12	151.69	1.14	1.07	0.93	0.86
175	120.12	118.74	172.99	1.11	1.06	0.93	0.89
200	137.28	138.16	201.28	1.11	1.05	0.93	0.92

Table 4.2: Results of Specimen 2 (HT15OC0210, 11 T dipole project) with a nominal pressing area of $A_{\mathrm{nom}} = (44 \times 15.8)\,\mathrm{mm}^2$.

Nominal		Force measurement					
σ_{nom}	F_{nom}	$F_{\mathrm{LC},\Sigma}$	$\sigma_{\mathrm{LC},\Sigma}$	Load balance			
(MPa)	(kN)	(kN)	(MPa)	(-)	(-)	(-)	(-)
50	34.76	34.88	50.17	1.03	0.93	0.97	1.07
100	69.52	69.63	100.16	1.00	0.99	0.99	1.02
125	86.90	86.99	125.13	0.99	1.00	1.00	1.01
150	104.28	104.21	149.90	0.99	1.02	0.99	1.00
170	118.18	118.45	170.38	0.98	1.00	1.01	1.01
180	125.14	125.48	180.49	0.99	1.02	0.99	0.99

Table 4.3: Results of Specimen 3 (HT16OC0217, MQXF project) with a nominal pressing area of $A_{\mathrm{nom},1} = (44 \times 19.3)\,\mathrm{mm}^2$ until 210 MPa and $A_{\mathrm{nom},2} = (35 \times 19.3)\,\mathrm{mm}^2$ from 225 MPa, respectively.

Nominal		Force measurement					
σ_{nom}	F_{nom}	$F_{\mathrm{LC},\Sigma}$	$\sigma_{\mathrm{LC},\Sigma}$	Load balance			
(MPa)	(kN)	(kN)	(MPa)	(-)	(-)	(-)	(-)
125	106.15	106.78	125.74	0.98	0.98	1.03	1.01
150	127.38	127.42	150.05	0.98	0.98	1.03	1.01
170	144.36	144.41	170.05	0.98	0.98	1.03	1.01
185	157.10	157.38	185.33	0.98	0.98	1.03	1.00
200	169.84	169.91	200.08	0.96	0.97	1.04	1.03
210	178.33	178.59	210.30	0.98	0.99	1.02	1.01
225	151.99	152.44	225.67	0.98	0.99	1.02	1.01
240	162.12	162.59	240.70	0.98	1.00	1.01	1.01
255	172.25	172.40	255.22	0.97	1.00	1.01	1.02

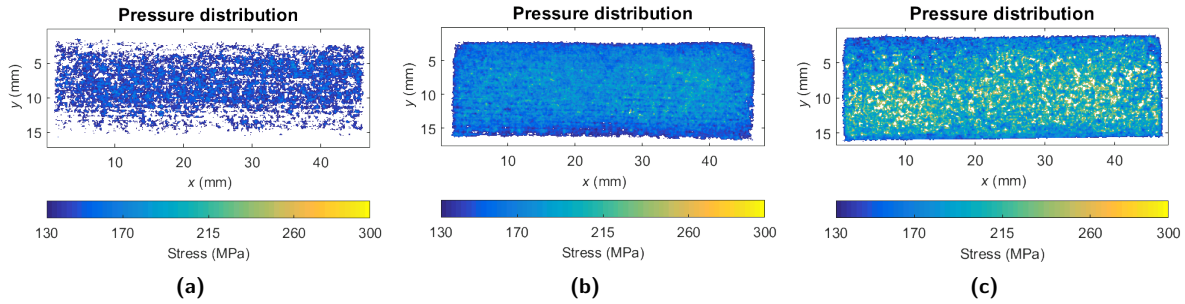

Figure 4.1: Evaluation of pressure-sensitive films (type HHS) of Specimen 1 after application of a nominal stress of **(a)** 150 MPa **(b)** 175 MPa **(c)** 200 MPa.

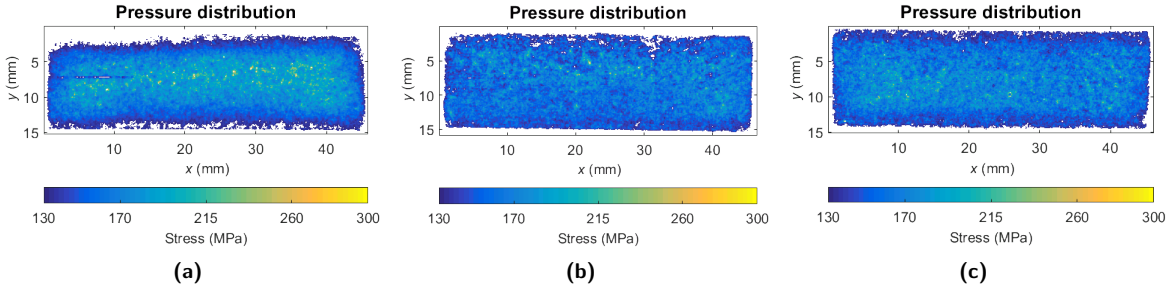

Figure 4.2: Evaluation of pressure-sensitive films (type HHS) of Specimen 2 after application of a nominal stress of **(a)** 150 MPa **(b)** 170 MPa **(c)** 180 MPa.

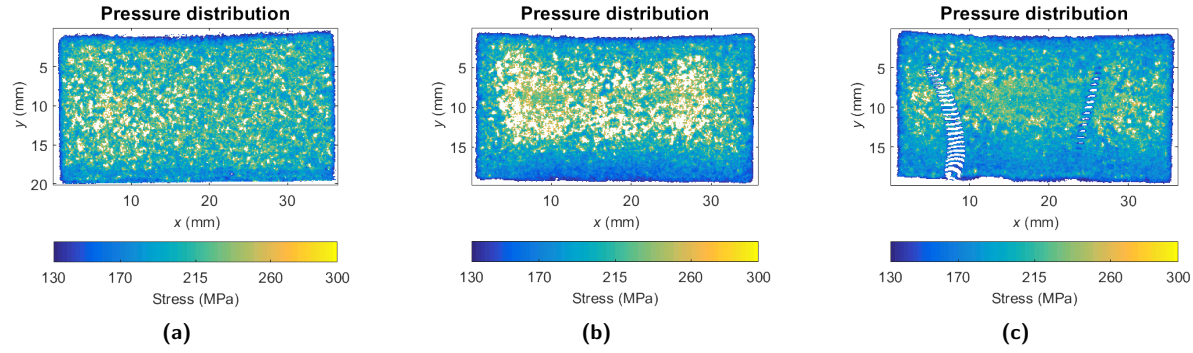

Figure 4.3: Evaluation of pressure-sensitive films (type HHS) of Specimen 3 after application of a nominal stress of **(a)** 225 MPa **(b)** 240 MPa **(c)** 255 MPa. Films exposed to stress greater than 250 MPa became deformed, which can be observed in (c). This led to a restricted assessment of the stress distribution.

4.1.2 Transport current measurements

After every pressure step at RT reported in the above section, the critical current of the specimens was measured with the FRESCA cable test station. In order to perform a relative analysis, all virgin specimens were measured at the beginning shortly after an extensive training phase. As every specimen was made of a single cable type, the analysis focuses on the upper cable, and the lower cable was evaluated merely for confirmation.

The critical current of the specimens was evaluated at 4.3 K with current ramps of 100 A s^{-1}. Specimen 1 and 2 were measured at applied fields from 7 T to 9 T in steps of 0.5 T and additionally at the maximum $B_{\mathrm{app,max}} = 9.6\,\mathrm{T}$. Specimen 3 had a higher critical current due to the different cable and strand properties listed in Table 2.2 and 2.4. In combination with the FRESCA measurement window, constrained by a maximal applied field of 9.6 T and a maximal operation current of 32 kA, Specimen 3 could only be characterised at 9.0 T and 9.6 T. The non-loaded specimens were also tested at 1.9 K. Owing to constraints, further load steps were not measured at this temperature, which did not allow us to interpret the results.

Figures 4.4(a), 4.5(a) and 4.6(a) show the completed critical current results I_c (markers) of the particular specimen as a function of the peak field $B_{\mathrm{peak}}(I)$. The latter is derived in Section 3.2.2 for the present specimen geometries. Additionally, the scaling law curves (lines) derived by using the Kramer relation $I_c = C\,b^{-0.5}(1-b)^2$ with $b = {}^{B}/_{B_{c2}{}^*}$ and C and $B_{c2}{}^*$ as fitting parameters were plotted for the virgin state and the highest pressure step [88]. The critical current of the corresponding non-cabled virgin wires was plotted additionally as a reference. These results, provided by CERN (TE-MSC-SCD), were measured in compliance with the IEC61788-2 standard [159] and presented according to Section 3.2.2.

The recorded $V-I$ curves including corresponding fit functions at the highest applied field of all pressure steps are plotted in Figures 4.4(b), 4.5(b) and 4.6(b) for the respective specimen, representing the closest measurement case to the situation in a magnet. As pointed out in Section 3.2.3, the $V-I$ curves were corrected for the analysis, i.e. the undesired induction offset voltage and the ohmic part in the virgin measurement data were substituted. Owing to the few measurement points within the resistive transition, a reduction of the criterion E_c to 3 µV m^{-1} was obligatory to prevent extrapolation uncertainties, i.e. to ensure that measurement points are available around the I_c determination point. Every specimen was measured at a distinct condition at least three times. The recording with the most points at the transition was taken for the presented analysis to prevent uncertainties of the fit approximation.

Owing to the substantial degradation of Specimen 1, it was decided that data points above 5 kA would be included in the evaluation. Specimens 2 and 3 were analysed with data points above 10 kA, as defined in Section 3.2.3. The dependency of the effective upper critical field $B_{c2}{}^*(4.3\,\mathrm{K})$ on the transverse stress was not clearly determinable by using the Kramer plot. This can be attributed to the limitation of the applied field to 9.6 T, which is significantly smaller than $B_{c2}(4.3\,\mathrm{K})$ of Nb_3Sn composite superconductors.

Tables 4.4, 4.5 and 4.6 summarise the results of the particular specimen. In order to present the degradation, the values are normalised to the virgin measurement and listed in an additional column. Figure 4.7 visualises an overview of the achieved results.

Table 4.4: Results of Specimen 1 at $T = 4.3\,\mathrm{K}$ and $\max(B_{\mathrm{app}}) = 9.6\,\mathrm{T}$.

Stress σ_{nom} (MPa)	Upper cable I_c (kA)	(-)
0	22.10	–
50	22.25	1.01
100	22.23	1.01
125	22.18	1.00
150	22.19	1.00
175	21.54	0.97
200	7.77	0.35

Table 4.5: Results of Specimen 2 at $T = 4.3\,\mathrm{K}$ and $\max(B_{\mathrm{app}}) = 9.6\,\mathrm{T}$.

Stress σ_{nom} (MPa)	Upper cable I_c (kA)	(-)
0	20.50	–
50	20.80	1.01
100	20.79	1.01
125	20.84	1.02
150	20.95	1.02
170	20.40	1.00
180	18.84	0.92

Table 4.6: Results of Specimen 3 at $T = 4.3\,\mathrm{K}$ and $\max(B_{\mathrm{app}}) = 9.6\,\mathrm{T}$.

Stress σ_{nom} (MPa)	Upper cable I_c (kA)	(-)
0	30.45	–
125	30.40	1.00
150	30.30	1.00
170	30.21	0.99
185	30.29	0.99
200	30.26	0.99
210	30.29	0.99
225	30.07	0.99
240	29.74	0.98
255	28.40	0.93

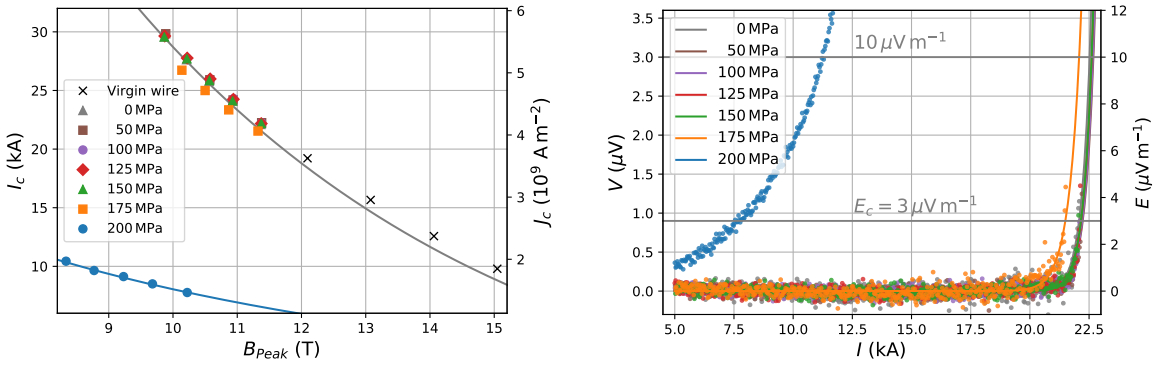

(a) **(b)**

Figure 4.4: Results of Specimen 1. **(a)** Critical current of the upper cable as a function of the peak field at $T = 4.3\,\mathrm{K}$ after each pressure level with a Kramer law fit for the virgin and the highest pressure step in the corresponding colour. The black crosses without a Kramer law fit refer to the I_c measurements of the non-cabled wire of the same type. **(b)** Comparison of corrected $V - I$ characteristics of the upper cable at $T = 4.3\,\mathrm{K}$ and $\max(B_{\mathrm{app}}) = 9.6\,\mathrm{T}$ after each pressure level.

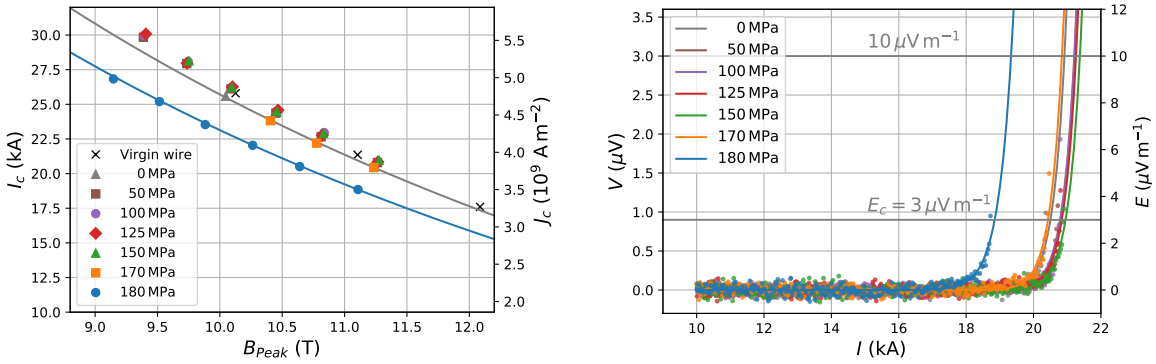

(a) **(b)**

Figure 4.5: Results of Specimen 2. **(a)** Critical current of the upper cable as a function of the peak field at $T = 4.3\,\mathrm{K}$ after each pressure level with a Kramer law fit for the virgin and the highest pressure step in the corresponding colour. The black crosses without a Kramer law fit refer to the I_c measurements of the non-cabled wire of the same type. **(b)** Comparison of corrected $V - I$ characteristics of the upper cable at $T = 4.3\,\mathrm{K}$ and $\max(B_{\mathrm{app}}) = 9.6\,\mathrm{T}$ after each pressure level.

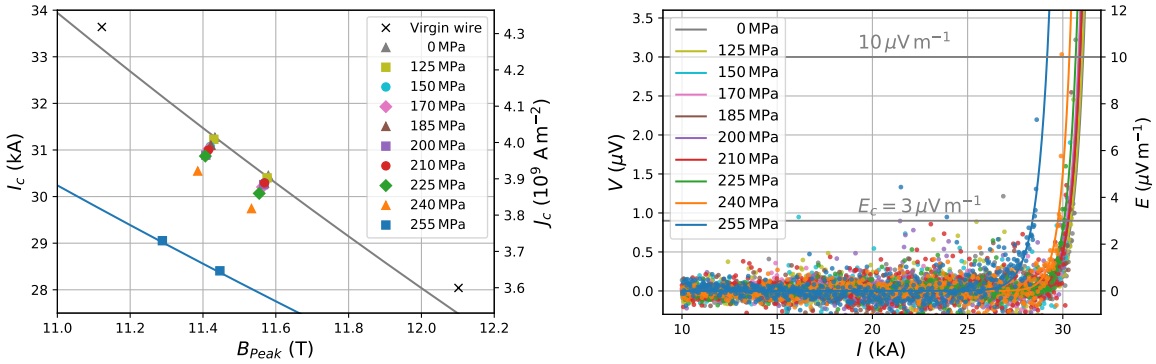

(a) **(b)**

Figure 4.6: Results of Specimen 3. **(a)** Critical current of the upper cable as a function of the peak field at $T = 4.3\,\mathrm{K}$ after each pressure level with a Kramer law fit for the virgin and the highest pressure step in the corresponding colour. The black crosses without a Kramer law fit refer to the I_c measurements of the non-cabled wire of the same type. **(b)** Comparison of corrected $V - I$ characteristics of the upper cable at $T = 4.3\,\mathrm{K}$ and $\max(B_{\mathrm{app}}) = 9.6\,\mathrm{T}$ after each pressure level. Owing to the greater dimension of the cable type, higher test currents were necessary to reach I_c.

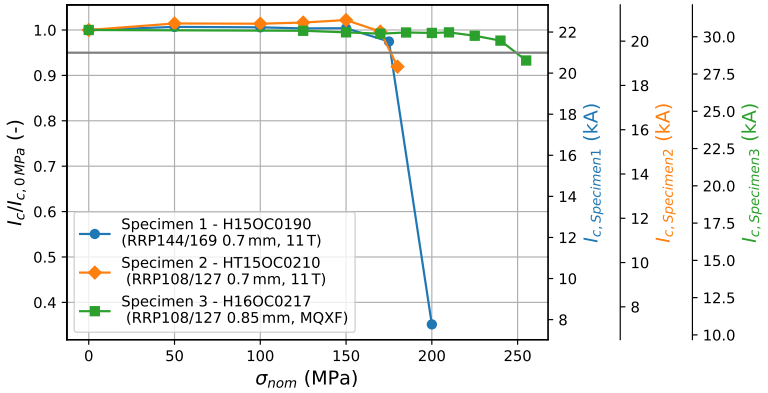

Figure 4.7: Comparison of critical currents normalised to the non-loaded performance of respective specimens (upper cable) at $T = 4.3\,\mathrm{K}$ and $\max(B_{\mathrm{app}}) = 9.6\,\mathrm{T}$ including a 5 % degradation threshold. The better performance of Specimen 3 can be justified with the change of stress arrangement by using titanium bars in a sandwich configuration.

4.1.3 Microscopy investigations

After the I_c measurements of Specimen 1 were completed up to a nominal stress of 200 MPa, the sample was cut and metallographically prepared. The originally measured loaded region as well as a non-loaded region were subjected to a microscopy investigation. As described in Figure 2.5(a), the transverse (XZ-plane) and longitudinal (XY-plane) cross sections were metallographically prepared for autopsy to observe the mechanical consequence of the transverse stress.

The centre part of the transverse cross section of the non-loaded region can be seen in Figure 4.8, including the labelling of the components. It revealed several known facts, for example the pre-reacted deformation of the strands due to cabling and the partial hemming bends of the core, which are further investigated by J. Fleiter *et al.* [63]. The primary purpose of this observation was to confirm a doubtless metallographic process without generating misleading cracks. In the transverse and longitudinal cuts of the non-loaded sample, the absence of cracks could be approved within the observed area.

The transverse cross section of the loaded part revealed many cracks. The highest crack density was observed in the centre part, which can be seen in Figure 4.9. Cracks with a typical width down to 0.5 µm were taken into account in the presented inspection. A characteristic spatial X-shape crack pattern within the strands was observed as shown in the magnified micrograph Figure 4.9(b). Depending on the former deformation due to cabling, the pattern was slightly asymmetrical. However, this pattern helped to estimate at which depth of the longitudinal cross section the sample must be prepared for a further crack investigation. Figure 4.9(d) shows a cracked sub-element in detail. The cracks tend to be parallel to the applied transverse stress and extend from the inner residual α-bronze to the niobium diffusion barrier. Voids tend to act as stress concentrators that induce larger cracks.

The longitudinal cross sections were further prepared to identify the shape and propagation of the cracks detected in the transverse cross section described above. Therefore, the upper row of strands (upper cable) was examined. About one-third of the row was removed planarly by metallographic preparation. Figure 4.10 presents the non-loaded part, including the labelling of the components. An overview of the loaded sample is provided in Figure 4.11, which displays part of the cross section of a damaged strand. The examined cracks preferred to propagate in longitudinal direction, i.e. longitudinal cracks, and ultimately drifted to the outer border of the sub-elements.

The remaining parts of the approximately 1.7-m-long Specimen 1 with no voltage taps or heaters were further used to estimate the crack initiation threshold experimentally. For this purpose, it was necessary to inspect the transverse cross section of different loaded samples. Consequently, the pieces were loaded according to the same procedure, as described in Section 3.1.1. Subsequently, a transverse cross section of the pressing area was prepared with the same procedure as the samples described above. Then, the region with the highest expected crack density, the centre upper part according to the above SEM analysis, was observed for every piece with an optical microscope (OM). No cracks in the mentioned region were observed in samples loaded with less than 175 MPa.

Figure 4.12 shows a comparison of a strand from the same position in the centre part of the upper cable (upper row of strands) after stress levels of 150 MPa, 175 MPa and 200 MPa. Sub-elements of the

150 MPa load case (Figure 4.12(a) and (d)) are undamaged. The 175 MPa load case (Figure 4.12(b) and (e)) can be considered to be the threshold of crack initiation followed by the 200 MPa load case (Figure 4.12(c) and (f)) with clearly ruptured sub-elements. Hence, the observed crack initiation after a specific stress correlates with the results of the particular I_c measurements presented in Section 4.1.2.

The FEM analysis based on a model obtained by X-ray tomography provided an overview of the spatial stress distribution in the specimen [182]. A 1.6 times higher stress on the actual cables compared to the externally applied stress on the compound specimen was estimated. Unfortunately, the resolution of the X-ray tomography only facilitates a FEM modelling on strand level. Consequently, the wires were simulated as a homogeneous material with an elastic modulus of 108 GPa.

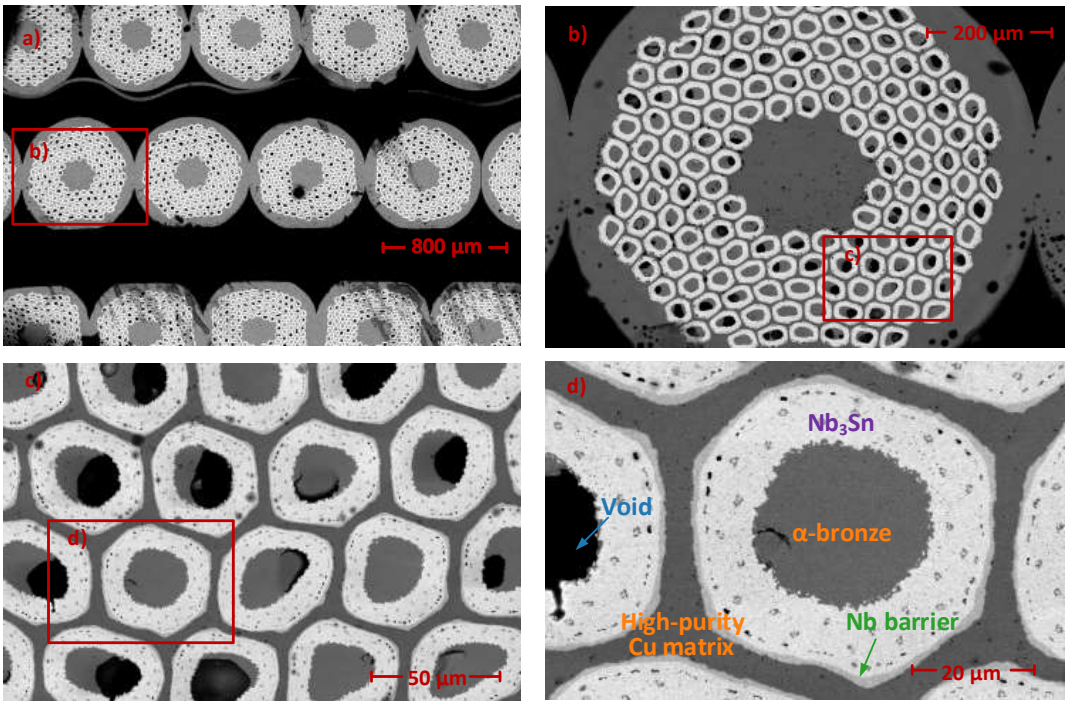

Figure 4.8: SEM micrographs of transverse cross section of a non-loaded region of Specimen 1 (centre part).

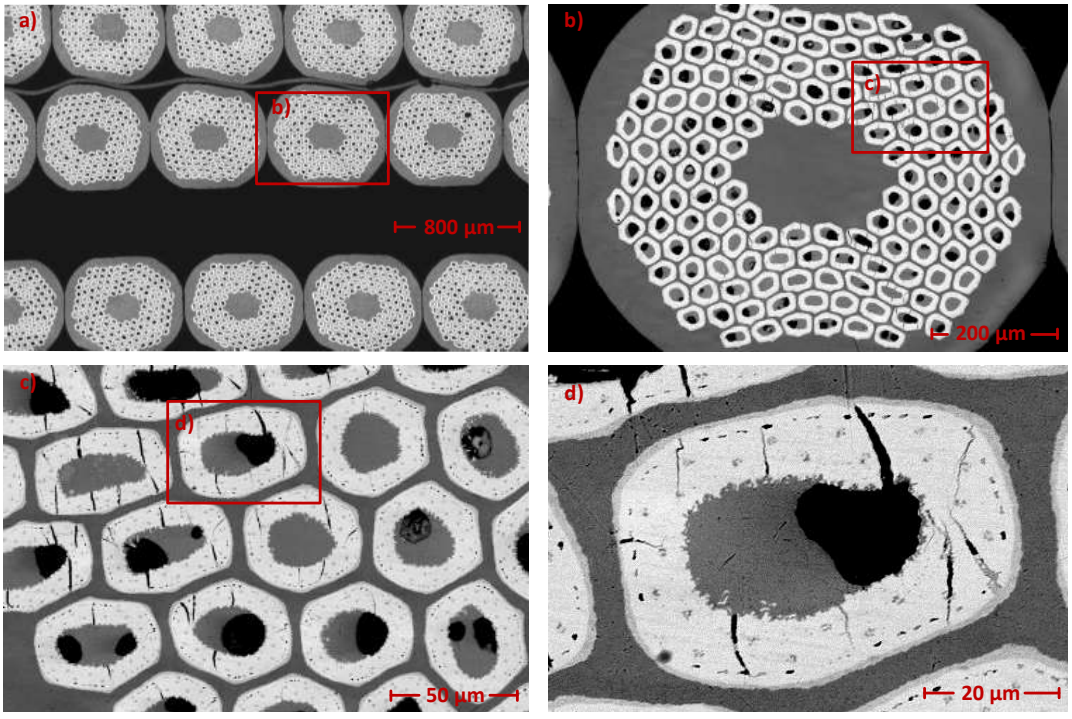

Figure 4.9: SEM micrographs of transverse cross section of the 200 MPa loaded region of Specimen 1 (centre part).

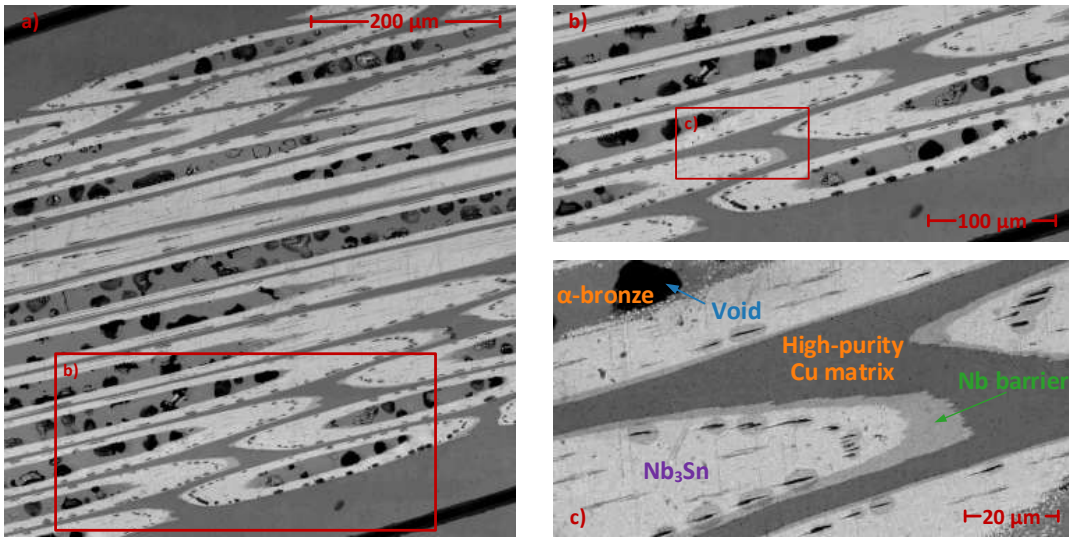

Figure 4.10: SEM micrographs of longitudinal cross section of a non-loaded region of Specimen 1 (centre of upper strand layer of upper cable).

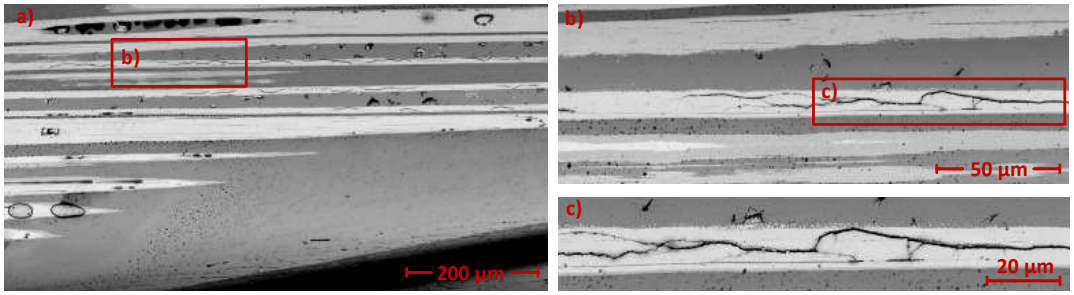

Figure 4.11: SEM micrographs of longitudinal cross section of the 200 MPa loaded area of Specimen 1 (centre of upper strand layer of upper cable).

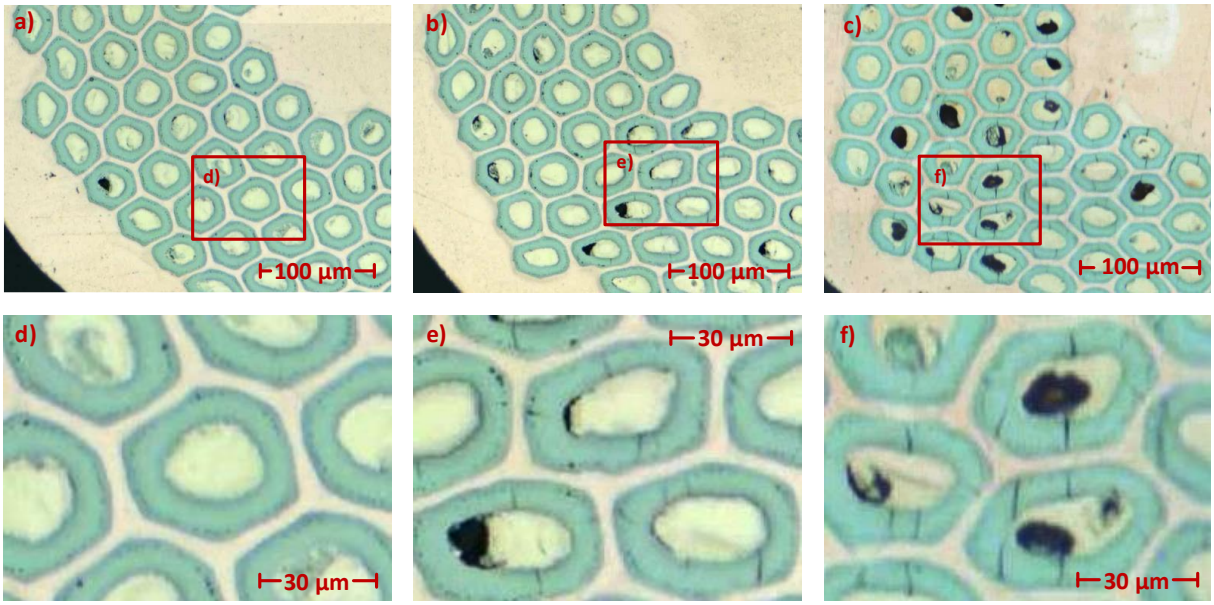

Figure 4.12: OM micrographs of a transverse metallographic cross section of the same located strand within remaining pieces of Specimen 1 after exertion of **(a,d)** 150 MPa, **(b,e)** 175 MPa and **(c,f)** 200 MPa (centre of upper strand layer of upper cable). The first crack initiation was detected at the 175 MPa loaded sample, which correlates with the I_c results.

4.1.4 Discussion

Critical current measurement and stress distribution

Specimens 1 and 2 showed similar behaviours due to their identical mechanical arrangement. An irreversible degradation of less than 5 % after a nominal load of 175 MPa directly applied on the bare impregnated cables at RT was specified. This confirms the conventional limitation of 150 MPa for collaring a magnet coil with an additional margin. Nevertheless, local deviations from the coil dimensions due to the accepted production tolerances shall not be exposed to local stress above 175 MPa during the force-restraining procedure to ensure less than 5 % degradation. Considering that the currently produced 11 T dipole coils have a nominal length of 5.4 m, it is a technical challenge to monitor and control this requirement while collaring the coil and welding the shrinking cylinder.

Specimen 1 was additionally exposed to 200 MPa, which shows a tremendous degradation resulting in a very low n value in combination with a severe I_c degradation. This could be traced independently of the applied field to current sharing, arising from a confirmed fracture of the sub-elements. For Specimen 2, the pressure steps were defined in smaller steps around the expected degradation. The particular results and hence the drop of performance in the range of 175 MPa confirmed the results of Specimen 1, considering that they have similar dimensions. No significant difference were measured due to the different sub-element size and additional C-shaped mica insulation of the particular specimen.

In order to yield an outcome close to the situation in a coil during magnet assembly, impregnated Rutherford cables were chosen for the experiment. This allowed to create a load case similar to the one observed in full-size loaded coil assemblies. Nevertheless, the homogeneous stress on the specimen's surface, which is also the aim during the collaring process for magnet coils, yields only an indirect statement about the intrinsic stress threshold on the superconducting sub-elements. The latter is finally accountable for the observed cracks and the crucial performance loss. The mechanical properties, e.g. Young's modulus, Poisson's ratio and yield strength, of

- the relatively soft epoxy resin and additional insulation layers,
- the annealed copper stabiliser,

as well as the dimensional properties of the composite compound, such as

- the cable configuration,

influence mainly the relationship between the externally applied stress on the surface and the local stress on the sub-elements. The mentioned FEM analysis by F. Wolf *et al.* [182] correlates the stress distribution with the crack pattern, but unfortunately could not be used to evaluate the decisive stress on the sub-elements. In addition, the determination of the material parameters has been investigated within the FCC 16 T dipole programme [143, 144, 183] and HL-LHC project [41, 134].

Strain caused degradation due to the residual stress resulting from the plastic deformations of the soft copper matrix beneath the crack initiation level of 175 MPa could not be clarified unequivocally based on the presented results [56]. A similar experiment performed by B. Bordini *et al.* [27] applying transverse stress on cables during operation at 4.3 K revealed a significant field dependency, which is evidence of strain effects. A small degradation at 90 MPa and a 24 % degradation of the quench current at 11.6 T and 155 MPa was measured in this experiment. Unfortunately, it does not provide information about the irreversible degradation at low temperatures.

It must also be taken into account, for comparing these results with those of other publications, that the mechanical properties of Nb_3Sn composite compounds differ at RT and low temperature. Hence, the performance loss of Nb_3Sn cables caused by stress at RT differs from that caused by stress at low temperatures [120].

Specimen 3 was additionally tested with another mechanical structure, which makes it difficult to compare it with Specimens 1 and 2. By adding the titanium bars in a sandwich arrangement, the spatial stress situation within the specimen is changed, thus also on the cables. The solid titanium bars homogenise the stress distribution, which made the polyimide foils dispensable, and the Prescale films yielded only a slight estimation regarding the situation on the epoxy resin or the cable. The applied force on the specimen in the XZ-plane is distributed over a broader range than the actual pressing die profile, and a lower average stress on the cables within a larger area at equal force can be assumed. The latter may be the reason for the lower sensitivity of stress with a degradation of less than 5 % after a nominal stress of 240 MPa at RT.

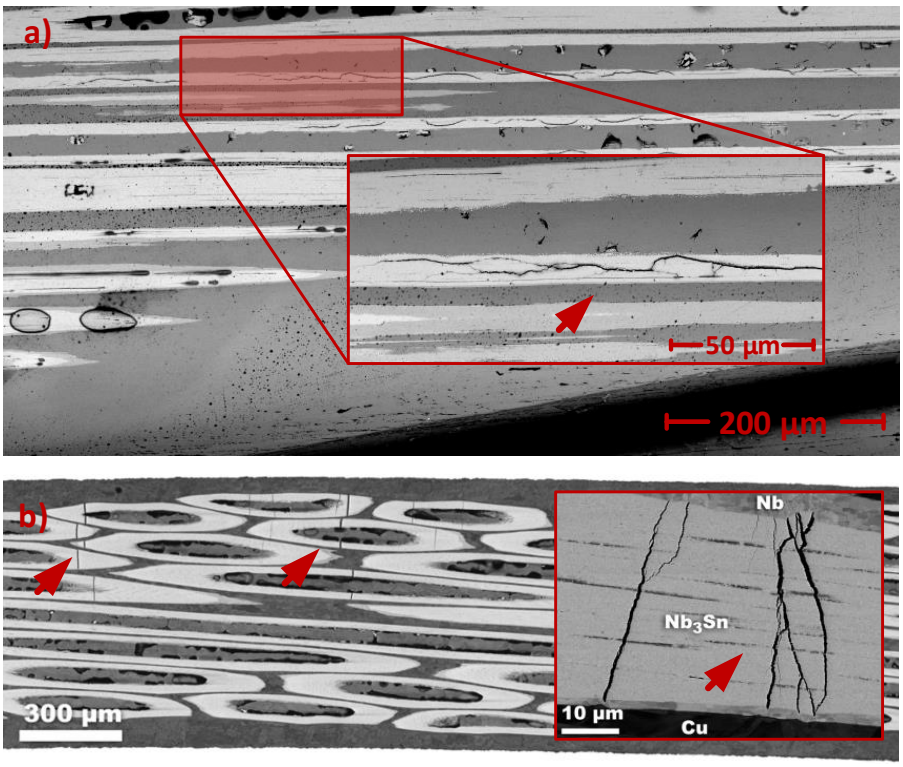

Figure 4.13: Comparison of SEM micrographs. **(a)** Longitudinal cracks caused by transverse stress in impregnated Rutherford cable double stack of RRP wires. **(b)** Transverse cracks caused by bending stress of a single RRP wire (Information taken from Reference [103, p.83-84] with marks by the present author).

Nevertheless, the high requirements of cable tests with currents above 10 kA restricted the investigation, so that finally only the critical current at an electrical field criterion of $E_c = 3\,\mu V\,m^{-1}$ could be used unequivocally. This was also the trigger to investigate the degradation process on single wires, which is described in Section 4.2.

Microscopy investigation

The microscopy investigations of Specimen 1 revealed cracks in the superconducting sub-elements. Furthermore, their spatial distribution within the specimen was inspected. They can be assumed to be the main reason for I_c degradation, particularly due to the following stress study (cf. Figure 4.12). The transverse cross section yielded information about crack distribution. This also gave an estimate of the stress distribution within the cable and the wire. In general, the systematic crack distribution in the observed region was overlaid by statistical variation due to fabrication uncertainties, e.g.

- the hemming fold of the core,
- the gap between the upper and lower row of strands due to impregnation,
- the pre-reacted deformation on the cable edges due to cabling and
- Kirkendall voids,

which makes a local stress analysis within the composite compound challenging. Voids encourage cracks due to the stress concentration at the cavities' surface. The research community is aware of this optimisation potential regarding mechanical improvements by the RHT and was further investigated by C. Scheuerlein *et al.* [141], C. Barth *et al.* [13], Y. Zhai *et al.* [187].

The longitudinal cross section revealed the typical shape of the cracks, which are mostly in longitudinal direction and drift to the border of the sub-elements. They differ from cracks generated by bending or tensile stress, which cause transverse cracks in sub-elements published, for instance, by M.C. Jewell *et al.* [83, 103] and C. Sanabria *et al.* [137]. In most cases, the longitudinal shape of the inspected cracks caused only a shrinkage of the effective superconducting cross section and not an entire interruption of the superconducting material in transport current direction. Figure 4.13 clarifies this matter by comparing the presented results with the earlier investigation mentioned above.

Table 4.7: Results of the load application of all wires used in this investigation by the mean of the projected area $A_{\mathrm{proj}} = (44 \times 0.7)\,\mathrm{mm}^2$.

Nominal			Transport	Magnetisation	Microscopy
σ_{nom} (MPa)	$F_{\mathrm{nom}}{}'$ (kN m^{-1})	F_{nom} (kN)	$\sigma_{\mathrm{LC},\Sigma}$ (MPa)	$\sigma_{\mathrm{LC},\Sigma}$ (MPa)	$\sigma_{\mathrm{LC},\Sigma}$ (MPa)
25	17.50	0.77	29.19	26.55	27.11
50	35.00	1.54	50.90	50.22	50.97
75	52.50	2.31	74.94	75.54	76.43
100	70.00	3.08	100.07	99.96	101.06
112.5	78.75	3.47	113.57	112.53	–
125	87.50	3.85	125.49	125.32	125.74
150	105.00	4.62	150.97	150.55	150.80
200	140.00	6.16	–	199.70	200.09

Summing up the evidence, i.e. the presence of cracks and the absence of a measurable field-dependency, gives rise to the assumption that the degradation process is purely a mechanical effect. Consequently, this indirectly affects the thermal stability of the cable negatively. The applied stress at RT influences the superconducting performance of the cable indirectly due to mechanical fractures of the sub-elements. The verified cracks evoke an allocation of the transport current from the superconductor to the copper stabiliser, which causes dissipation and hence instability. This behaviour, so-called current sharing, can further quantitatively be modelled by an electrical network of a normal and a superconducting path to yield a prediction of the stability loss, e.g. as introduced by Z.J.J. Stekley *et al.* [156].

4.2 Results of wire investigations

This section presents the results of the wire investigation, which was launched after completing the measurements of Specimen 1 cable. It consists of three supplementary parts:

- the transport current measurements with the self-designed NearT_{c} setup,
- the magnetisation measurements with a SQUID magnetometer and
- the microscopy investigations.

They were performed to identify the cause and effect of a specific amount of applied transverse stress at RT on the superconducting Nb_3Sn as a simplified case of the cable experiment. Furthermore, the feasibility of the NearT_{c} concept is assessed on the basis of the presented data.

4.2.1 Stress exertion

The stresses on the specimens used for these investigations are listed in Table 4.7. In order to allow a better comparison with the cable results in Section 4.1, the nominal pressure $\sigma_{\mathrm{nom}} = {}^{F_{\mathrm{nom}}}/_{A_{\mathrm{proj}}}$ is defined as the force divided by the central longitudinal cross section $A_{\mathrm{proj}} = (44 \times 0.7)\,\mathrm{mm}^2$ with the pressing die length of 44 mm and the nominal wire diameter of 0.7 mm. In addition, the length-related force $F_{\mathrm{nom}}{}' = {}^{F_{\mathrm{nom}}}/_{l}$ is listed together with the absolute nominal force F_{nom}. The right part of the table lists the evaluated stress $\sigma_{\mathrm{LC},\Sigma}$ of every specimen used in the corresponding sub-studies. The high error of the 25 MPa load case is attributed to the fact that values below 1 kN are close to the lower limit of the hydraulic system. Except for that, only minor errors of the actual stress from the nominal stress smaller than 2 % were observed. This justifies using the nominal values present the superconducting results in the next sections.

The transport current measurements were stopped after a nominal load of 150 MPa applied at RT. The microscopy study was performed before the transport and magnetisation measurements. The additional load case of 112.5 MPa was inserted afterwards. The results showed that the load case was not essential for microscopy characterisation. Thus, it was decided to disregard this case in the microscopy investigation. Owing to the restriction discussed in Section 3.3, the stresses for the transport current measurement were always performed on the same specimen. The magnetisation and microscopy observations were performed for every stress level on a particular specimen of the same RHT, which also enabled the metallographic preparation in a single embedment.

Although the external force on the wire was measured, it yields only indirect information about the stress within the wire. In terms of contact mechanics, the presented situation can be idealised two-dimensionally as the touch of a confirming half space, the pressing die, with a non-conforming cycle, the multi-filamentary wire, at a single point. This leads to a stress concentration at the contact point and can be identified as a Hertzian contact problem [80, 177].

Accordingly, the nonlinear stress distribution, especially the local maxima, within the wire is significantly higher than the measured external force. Furthermore, the inhomogeneity of the idealised cycle due to the sub-elements, consisting of other materials such as Nb_3Sn and α-bronze, must be considered. The FEM simulation by P. Ebermann *et al.* [48] provides further information on this topic.

4.2.2 Transport current measurements with the NearT_c setup

Feasibility study of measurement concept and experimental setup

The chosen principle, characterising the critical current of Nb_3Sn wires in self-field close to the critical temperature, could be validated successfully by conductive cooling of the wire mounted on the base of a liquid helium heat exchanger.

The crucial experimental temperature stability was appropriate to measure $I_c(T)$ reliably at the chosen temperature steps of 100 mK and $T_{cs}(I)$ with the chosen current levels. The data obtained to characterise the wire after a certain stress level is shown in Figure 4.14. As shown in Figure 4.14(a), five determinations of the critical current $I_c(T)$ at a defined set temperature T were typically performed. This was done to improve the reliability of the measurement, which was influenced especially at the beginning of the work by temperature instabilities. It was also the trigger to establish current-sharing temperature measurements as illustrated in Figure 4.14(b). The temperature-dependent disturbances of the measured voltage $V(t)$ are inherently compensated by the analysis, i.e. plot of $V(t)$ over T obtained by recording $T(t)$. This led to higher repeatability in contrast to the $V(I)$ curves of Figure 4.14(a), so that typically only three repetitions were performed for a particular $T_{cs}(I)$.

Subsequently, the results of both measurement types are plotted over the measured temperature in Figure 4.15. A fit approximation $I_c(T) \propto [1-(T/T_c)^{1.5}]^{\eta}$ with $\eta = 2.5$ derived from the USL [56] is added to the plot and shows good agreement.

The control accuracy of the sample temperature T_s was established within a band of ±10 mK to ±20 mK at roughly 13 K with the mass flow controllers and the heat exchanger on the experimental platform. It was finally improved to a band of ±2.5 mK to ±5 mK close to T_c by using the feedback control with heaters on both current connector plates.

Within the feasibility check, the profile of the sample temperature was recorded, and their AC parts are shown in Figure 4.16 to assess the error. The blue and orange signals were recorded before and after enabling the temperature control, respectively. The periodicity of the signals is evident, which could be traced back to flow-driven thermal instabilities in the helium tubes of the system. In general, they can occur in tubes of cryogenic systems having a temperature gradient and containing helium, e.g. from the dewar vessel filled with liquid helium (4.3 K) to the recovery line (approximately 300 K) in the present case. The tubes of the setup comprised an unavoidable two-phase helium flow due to the heat load generated by the required temperature of the sample platform range of 15 K to 20 K.

The density ratio of liquid and vapour helium at the boiling point is 7.4, and the density ratio of liquid helium and gaseous helium at 0 °C and atmospheric pressure is 698.6 [55]. Considering the different densities of helium in the two thermodynamic phases presented here, the pressure and consequently the temperature in the tubes changed periodically with a noticeable magnitude.

These oscillations were reduced preventively by the pressure regulator of the dewar vessel with a nominal pressure of 155 mbar (gauge), as indicated in Figure 3.21. The frequency of the fundamental oscillation was similar at every measurement, i.e. 20 mHz to 40 mHz. The fundamental oscillation and the corresponding harmonics are determined primarily by the setup-dependent properties, e.g. length and diameter of the transfer line and helium tubes inside the cryostat.

On the basis of an approximately 5-min-long capture of the recorded temperature signals with a sampling time of 240 ms, a power spectral density (PSD) estimate was performed. This was done by using Welch's method [178] and applying a Hann window function to reduce the spectral leakage of the discrete Fourier transformation. Figure 4.16 shows the sample temperature including its spectral distribution with and without temperature controller. It is clear that the active temperature control on the connector plates reduced primarily low-frequency oscillations, which is discussed further in Section 4.2.5.

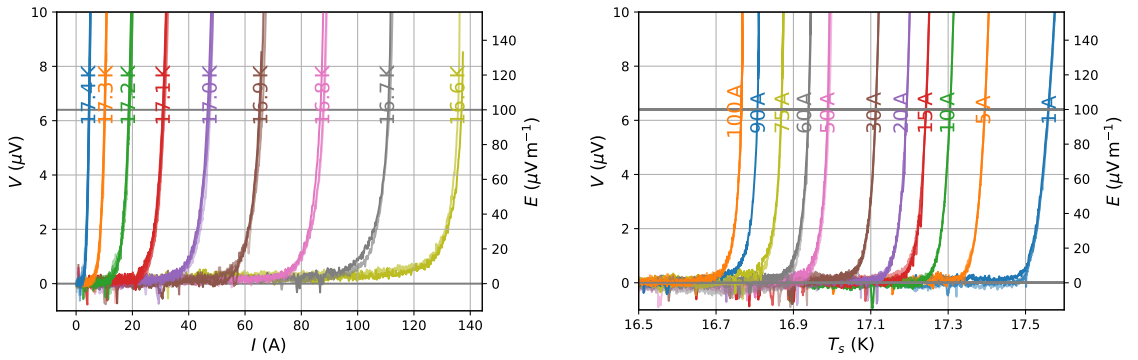

Figure 4.14: Measurements performed with the NearT_c setup to characterise the specimen after a specific applied stress at RT. **(a)** $V(I)$ curves at certain nominal set temperature levels and **(b)** $V(T)$ curves during a certain nominal current of the wire specimen. Every condition was measured at least three times, and the results are plotted in the same colour overlapped in different brightness. A clear and repeatable difference can be seen between the chosen nominal set temperature and current levels for the $V(I)$ and $V(T)$ recordings, respectively (cf. labels in the plot).

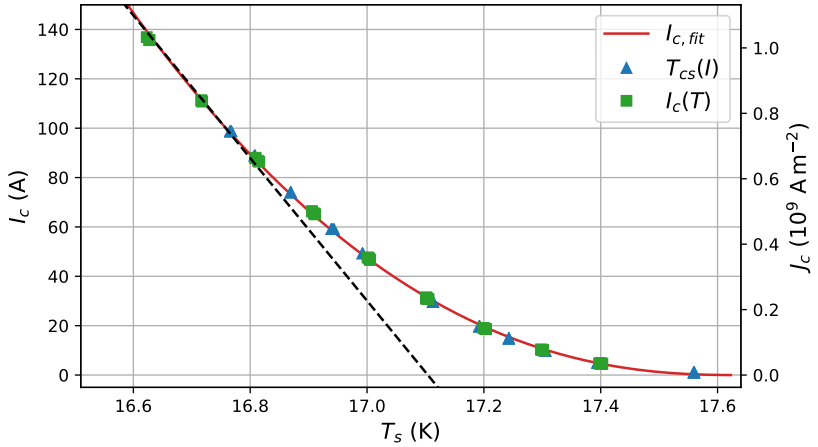

Figure 4.15: Evaluated $I_c(T)$ and $T_{cs}(I)$ of recordings shown in Figure 4.14 as a function of the measured temperature with the fit approximation function $I_c(T) \propto [1-(T/T_c)^{1.5}]^{\eta}$ with $\eta = 2.5$. The black dashed line represents the slope $-\mathrm{d}I_c/\mathrm{d}T$ based on the fit approximation in the upper operation range of 90 A to 150 A.

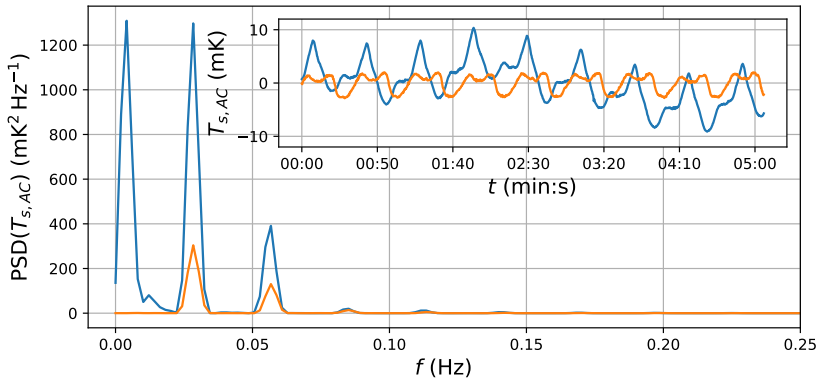

Figure 4.16: Observation of the sample temperature stability. The small plot shows the AC component of $T_s(t)$ without (blue) and with (orange) temperature controller with a sampling time $T_a = 240$ ms. The recording without temperature controller had a DC component of 12.614 K and a peak-to-peak value of 20 mK. The recording with the temperature controller had a DC component of 16.500 K, the nominal set temperature, and a peak-to-peak value of 5 mK. The larger plot shows the power spectral density of the corresponding time signals in the small plot. The active temperature regulation is primarily intended for a low-frequency rejection.

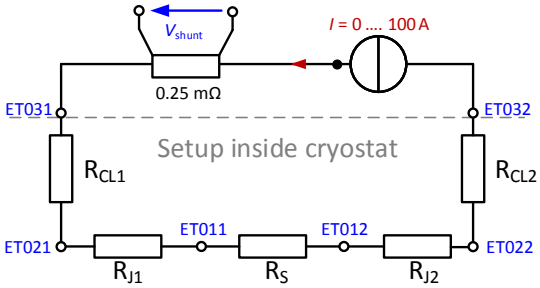

Table 4.8: Schematics of the electrical measurement circuit to estimate the Joule heating. The voltage taps can be checked in the PID (cf. Figure 3.21).

Table 4.9: Results of the system identification test with $T_s = 15.5\,\mathrm{K}$

$R_{J,x}$	$6\,\mu\Omega$
$R_{CL,x}$	$767\,\mu\Omega$
$P_J(I = 100\,\mathrm{A})$	$120\,\mathrm{mW}$
$P_\Sigma(I = 100\,\mathrm{A})$	$15.5\,\mathrm{W}$

The average liquid helium consumption was approximately $7\,\mathrm{L\,h^{-1}}$. A system test with $T_s = 15.5\,\mathrm{K}$ and a current of up to $I = 100\,\mathrm{A}$ was used to estimate the electrical parameter of the measurement circuit. Owing to the additional voltage taps on the top and bottom end of every current lead (cf. Figure 3.21), the following voltages

- $V_1 = \mathrm{ET011} - \mathrm{ET012}$,
- $V_2 = \mathrm{ET021} - \mathrm{ET022}$ and
- $V_3 = \mathrm{ET031} - \mathrm{ET032}$

were defined as illustrated in Figure 4.8. Assuming a symmetrical structure, the resistance of the low-temperature junctions to the specimen $R_{Jx} = {}^{V_2 - V_1}/_{2I}$, and the resistance of current leads $R_{CLx} = {}^{V_3 - V_2}/_{2I}$, with x for the left and right part, were acquired. The resistance R_{Jx} represents the soldering joint of the sample and the contact resistance from the current leads to the sample holder implemented by clamping with indium foils. The evaluated Joule dissipation $P_J = (V_2 - V_1)I$ on the sample holder and the entire setup $P_\Sigma = (V_3 - V_1)I$ are also evaluated and summarised in Table 4.9. The additional heating of a few Watt compared to the current lead estimation is based on several modifications performed before the initial commissioning. First, the installation was performed with copper, which has a lower RRR. Second, it was necessary to bend the copper rods during construction, which also affects the RRR negatively. It represents the entire Joule heating measured from the outside of the cryostat, which includes additional contact resistances. The thermal optimisation of the setup was not the further focus of the investigation.

The sample temperature T_s was defined as the arithmetic mean of the connector plate temperatures T_{left} and T_{right}, which were feedback-controlled independently by using the mounted heaters and temperature sensors (cf. Figure 3.15). The temperature along the sample was not monitored, and a linear temperature profile between the two electrical connections of the sample was assumed. This raised the suspicion of an undetectable accumulation of heat energy in this adiabatic system and, consequently, a corruption of the measurement results.

A hidden heating of the sample would influence the temperature-dependent critical current, which contains indirect information about the sample temperature. Measurements under the same conditions as in Figure 4.14 were performed several times in sequence, but no iterative decreasing tendency of I_c was observed with the chosen settings. This proved indirectly that no hidden heat accumulation occurs. Even repetitive recording of $V(T)$ curves for T_{cs}, which implies a necessary temperature rise of up to 1.5 K, did not show iterative heating of the sample, i.e. decreasing tendency of T_{cs}.

Measurement results

After the feasibility check of the measurement principle, the specimen was characterised after every stress application at RT according to the elaborate procedure discussed in the above section.

The summary of the high-current results can be seen in the $I_c(T)$ diagram in Figure 4.17. The rectangles and the triangles represent the results of I_c and T_{cs} measurements, respectively, whereby the evaluated actual temperature at the respective transition was used. A fit approximation $I_c(T) \propto [1 - ({}^{T}/_{T_c})^{1.5}]^{\eta}$ with $\eta = 2.5$ was computed for every pressure step and added to the plot as a solid line. The slope $-{}^{\mathrm{d}I_c}/_{\mathrm{d}T}$ between 90 A and 150 A was typically in the range of 0.29 to 0.05 $\mathrm{A\,mK^{-1}}$, as listed in Table 4.10. Figure 4.18 presents the critical current and the current-sharing temperature as a function of the nominal applied stress at RT, as extracted from Figure 4.17.

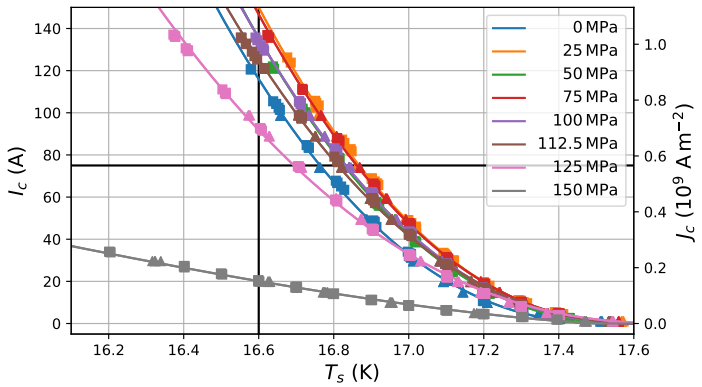

Figure 4.17: Results of high-current transport measurements in the $I(T)$ diagram. Critical current I_c (rectangles) and current-sharing temperature T_{cs} (triangles) summarised with corresponding fit approximations (solid line in corresponding colour). Values along the black lines are extracted in Figure 4.18.

Table 4.10: Results of the high-current transport measurement. Slope $-\mathrm{d}I_c/\mathrm{d}T$ on the base of the respective fit approximation between 90 A and 150 A in Figure 4.17.

σ_{nom} (MPa)	$-\mathrm{d}I_c/\mathrm{d}T$ (A mK^{-1})
0	0.28
25	0.29
50	0.29
75	0.29
100	0.28
112.5	0.26
125	0.22
150	0.05

The wire performance improved slightly until 75 MPa, followed by degradation starting from 100 MPa. The obtained degradation threshold at 100 MPa correlates with the crack initiation at 100 MPa elaborated in Section 4.2.4. Owing to high I_c degradation, the measurements were stopped after 150 MPa.

In order to allow a comparison of the recorded data after a particular stress at RT, Figure 4.19 shows an excerpt of the recordings. Three measured curves after every pressure step were plotted in the same colour and different brightness. The $V(I)$ curves for the I_c evaluation are partly influenced by temporal imperfect temperature stabilisation, which can also be seen in the more sensitive n values plotted in Figure 4.20. The points and the error bars represent the arithmetic mean values and the standard deviation of typically three to five measurements, respectively. However, the decreasing tendency of the n value with rising applied stress is recognisable. Additionally, the n value over the measured temperature range is plotted, which shows a decrease with increasing temperature.

Figure 4.21 and Table 4.11 summarise the results of the low-resistance measurements. The critical temperature improves after the application of 25 MPa transverse pressure until the wire became heavily damaged after 150 MPa. The RRR decreased after 100 MPa, which is assumed to have been caused most likely by the plastic deformation of the copper matrix.

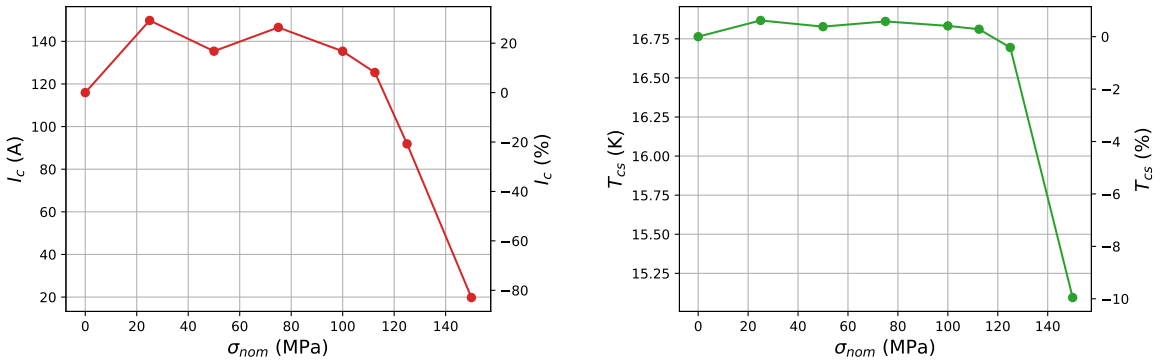

(a) **(b)**

Figure 4.18: Results of the transport current measurements. **(a)** Critical current I_c as a function of the applied stress σ_{nom} at RT during $T = 16.6$ K. **(b)** Current-sharing temperature T_{cs} as a function of the nominal applied stress σ_{nom} at RT during $I = 75$ A.

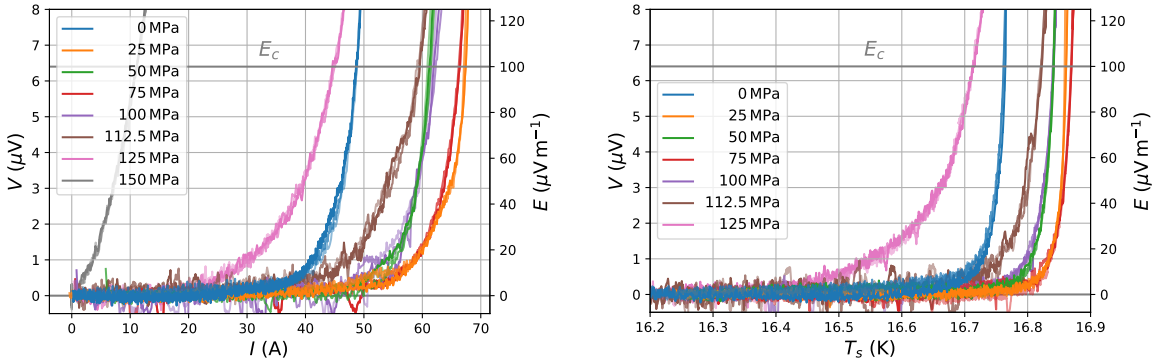

(a) **(b)**

Figure 4.19: Excerpt of the transport current measurements. **(a)** Typical $V(I)$ curves at $T = 16.9\,\mathrm{K}$. **(b)** Typical $V(T)$ curves at $I = 75\,\mathrm{A}$. A repetition of three measurements at the same condition is plotted in the same colour overlapped in different brightness.

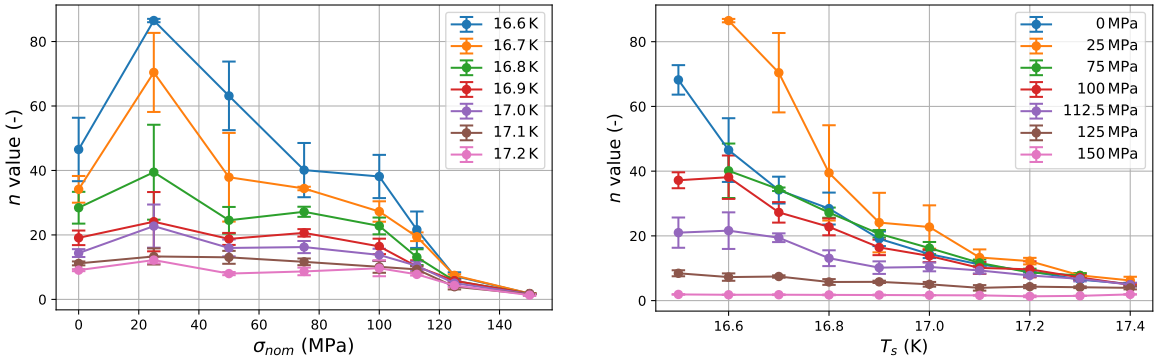

(a) **(b)**

Figure 4.20: Results of the n value analysis of the $V(I)$ curves. **(a)** n value as a function of the nominal applied stress σ_{nom} at RT. **(b)** n value as a function of the sample temperature.

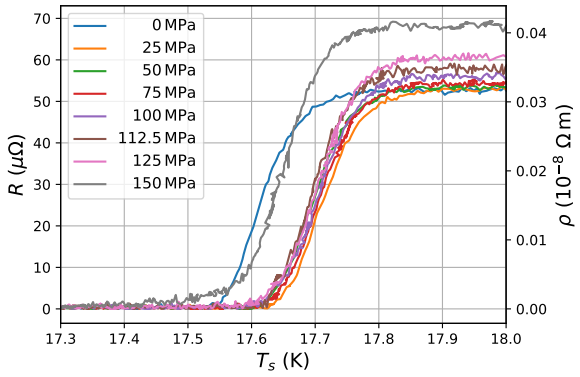

Figure 4.21: Results of low-resistance measurements for critical temperature T_c and residual resistance ratio RRR evaluation.

Table 4.11: Results of low-resistance measurements: T_c and $RRR := \rho(293\,\mathrm{K})/\rho(19\,\mathrm{K})$.

σ_{nom} (MPa)	$T_{c,\mathrm{midpoint}}$ (K)	ΔT_c (K)	RRR (-)
0	17.62	0.17	97.9
25	17.72	0.18	97.4
50	17.70	0.17	97.4
75	17.71	0.16	97.5
100	17.71	0.17	92.5
112.5	17.70	0.16	92.5
125	17.71	0.18	87.0
150	17.65	0.23	76.2

4.2.3 Magnetisation measurements

Magnetisation measurements were performed with samples exposed to transverse stress at RT up to 200 MPa, and the stress after each step on the respective sample is listed in Table 4.7.

Figure 4.22 summarises the results of the measurements at 4.2 K. It represents the behaviour at a common temperature range used for superconducting magnets, the atmospheric boiling point of helium, far below T_c, i.e. $T/T_{c,Nb_3Sn} \approx 0.2$. Figure 4.22(a) gives an overview of $J_c(B, 4.2\,\mathrm{K})$ calculated from the irreversible magnetisation $m_{irr}(B, 4.2\,\mathrm{K})$, by using the relation derived in Section 3.4.1. The corresponding magnetisation loops are shown in the small plot, and their abnormal fluctuations at low fields can be traced back to flux jumps. They show an unstable behaviour occurring during operation due to local disturbances resulting in an avalanche of depinned fluxoids, especially at low applied fields.

This well-known phenomenon was not a further objective of the work and hence not taken into consideration. Figure 4.22(b) extracts the obtained critical current density out of the stable measurement region at 6 T as a function of the stress applied on the respective sample. A degradation threshold at 100 MPa can be clearly recognised and correlates with the crack initiation threshold observed in the metallographic investigation.

Figure 4.23 shows the results of the same samples and measurement procedure but at a sample temperature of 16 K, i.e. $T/T_{c,Nb_3Sn} \approx 0.9$. The measured magnetic moment above 2 T approaches the noise level of the magnetometer, which is in the range of $5 \cdot 10^{-9}\,\mathrm{A\,m^2}$. Speaking of disturbances, flux jumps in the SQUID sensor cannot be excluded, which result in a shift of the measured flux by the magnetic flux quantum Φ_0. Figure 4.23(b) is an extraction of the stable measurement range at 0.5 T. Except for the 25 MPa case, these results show an improvement at low stress levels and degradation at stresses above 100 MPa, which confirms the behaviour found from the transport current measurements.

In summary, the results reflect qualitatively the tendency determined by the transport current measurements. In addition, the effect is exaggerated at the lower temperature, i.e. in the presented case at 16 K.

In addition, the critical current density at self-field in the range of 5 K to 18 K was assessed as shown in Figure 4.24. It represents a close situation to the performed transport current measurements near T_c in self-field. Except for the 25 MPa case, the results confirm qualitatively the performance improvement of samples, loaded with a stress below the crack threshold, and the degradation of samples, applied with stress above the observed crack initiation.

The analysis of T_c based on the AC susceptibility measurements illustrated in Figure 4.25 also shows an improvement in the low-stress range, where no cracks could be found. According to the unified scaling law $J_c(B, T)$ by J.W. Ekin [56], the critical current density changes due to variations of T_c, which generates a shift of the function along the T-axis.

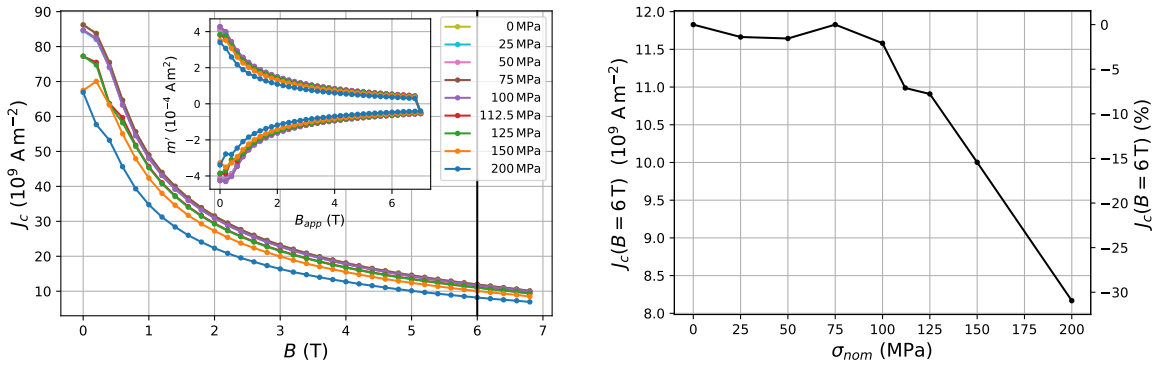

(a) **(b)**

Figure 4.22: Results of the magnetisation measurements at $T = 4.2\,\mathrm{K}$. **(a)** $J_c(B, 4.2\,\mathrm{K})$ of loaded and non-loaded samples by evaluating the irreversible magnetisation m_{irr} out of the magnetisation loops m', shown in the small plot. **(b)** Critical current density $J_c(6\,\mathrm{T}, 4.2\,\mathrm{K})$ as a function of the applied stress σ_{nom} at RT extracted from (a).

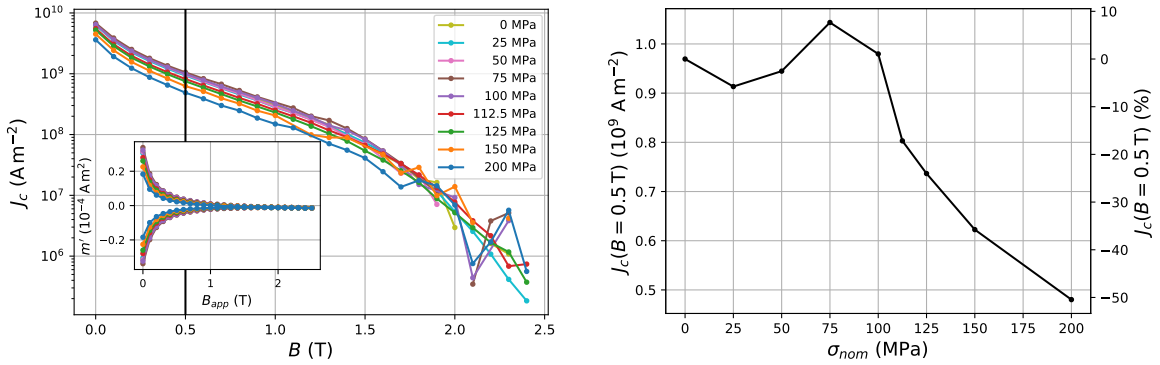

(a) **(b)**

Figure 4.23: Results of the magnetisation measurements at $T = 16\,\mathrm{K}$. **(a)** $J_\mathrm{c}(B, 16\,\mathrm{K})$ of loaded and non-loaded samples by evaluating the irreversible magnetisation m_irr out of the magnetisation loops m', shown in the small plot. **(b)** Critical current density $J_\mathrm{c}(0.5\,\mathrm{T}, 16\,\mathrm{K})$ as a function of the applied stress σ_nom at RT extracted from (a).

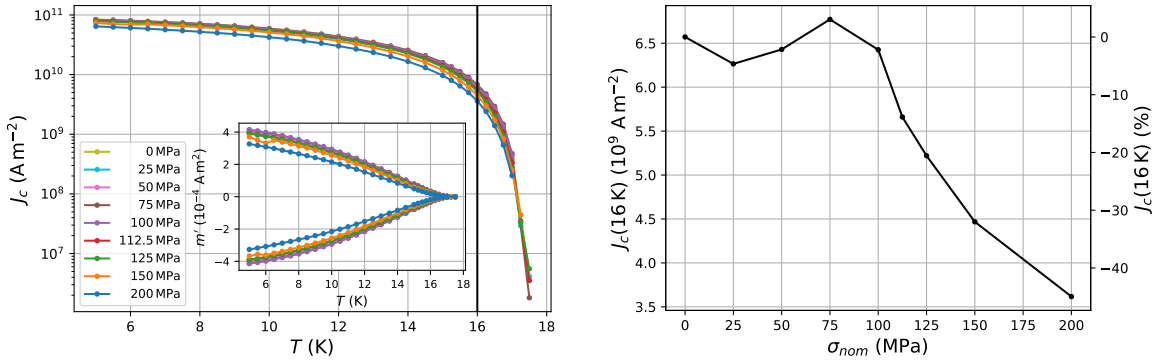

(a) **(b)**

Figure 4.24: Results of the magnetisation measurements at self-field. **(a)** $J_\mathrm{c}(B_\mathrm{self}, T)$ of loaded and non-loaded samples by evaluating the irreversible magnetisation m_irr out of the magnetisation loops m', shown in the small plot. **(b)** Critical current density $J_\mathrm{c}(B_\mathrm{self}, 16\,\mathrm{K})$ as a function of the applied stress σ_nom at RT extracted from (a).

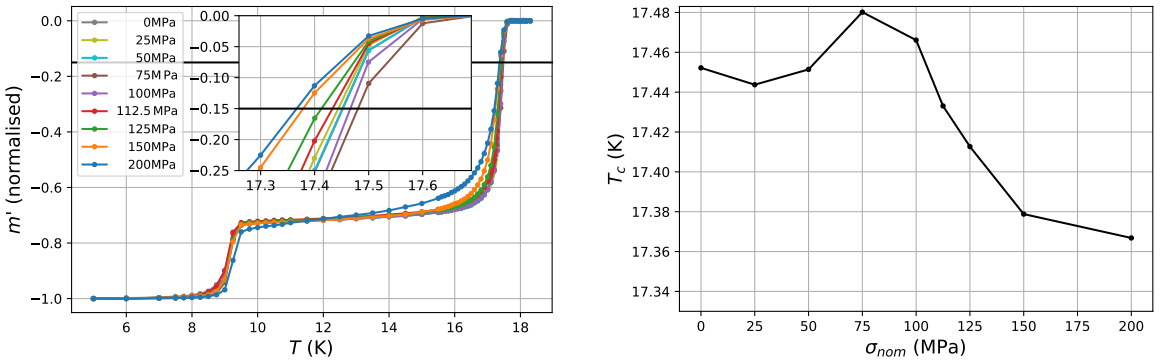

(a) **(b)**

Figure 4.25: Results of the AC susceptibility measurements. **(a)** Normalised AC magnetic moment m' of loaded and non-loaded samples with a magnified view of the area used for the criterion in the small plot. **(b)** Critical temperature T_c as a function of the applied stress σ_nom at RT extracted from (a) by using the threshold criterion at $m'_{\mathrm{thr,norm}} = -0.15$.

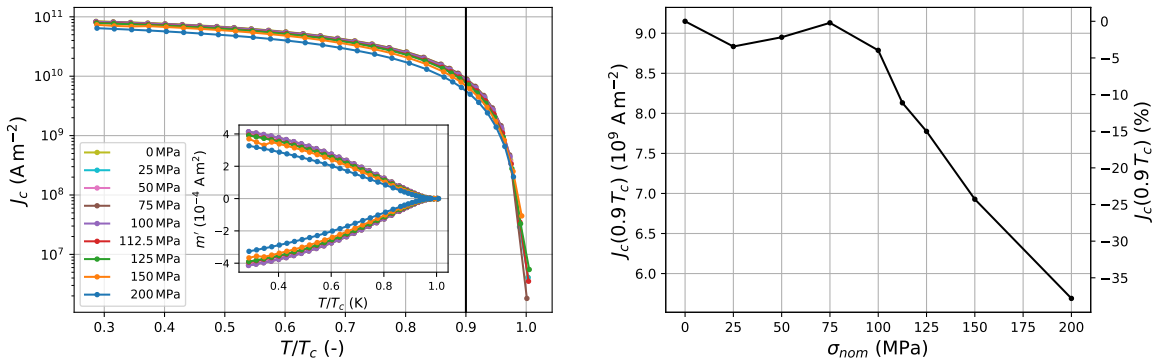

(a) **(b)**

Figure 4.26: Normalised results of the magnetisation measurements at self-field. **(a)** $J_c(B_{self}, t)$ of loaded and non-loaded samples over the reduced temperature $t = T/T_c$. The critical current, shown in Figure 4.24, is plotted as a function of t by using the T_c results, shown in Figure 4.25. **(b)** Critical current density $J_c(B_{self}, t = 0.9)$ as a function of the applied stress σ_{nom} at RT extracted from (a).

Owing to the local value of dI_c/dT, the impact is stronger near T_c in contrast to the common operation range of 4.2 K and 1.9 K. Consequently, the results of the self-field measurements were normalised to the reduced temperature $t = T/T_c$ and are shown in Figure 4.26. In order to derive t for every sample, the results of T_c shown Figure 4.25 were used. It is recognisable that the effect on the corrected $J_c(B_{self}, t)$ occurs weaker and similar to the observation at 4.2 K (cf. Figure 4.22).

After the analysis of T_c, the temperature dependence of the upper critical field $B_{c2}(T)$ of a reference wire was investigated as well as samples after applying transverse pressure of 75 MPa, 100 MPa and 200 MPa. Figure 4.27 and Table 4.12 summarise the results by applying the WHH expression, as discussed in Section 3.4.2. They also improved at 75 MPa and 100 MPa followed by a decrease, leading to a reduction of approximately 8 % at 200 MPa. In addition to the measured data (crosses), Figure 4.27 shows the respective fit approximation (line), which extrapolates $B_{c2}(T)$ outside the measurement range, i.e. above 7 T. For the fit function, the common expression

$$B_{c2}(T) = B_{c2}(0)\left[1 - \left(\frac{T}{T_c{}^*}\right)^{\nu}\right] \tag{4.1}$$

was used, where ν is a fitting parameter. $B_{c2}(0)$ was calculated from the WHH expression, and the effective critical current $T_c{}^*$ was obtained by extrapolating the slope $(dB_{c2}/dT)_{T=T_c{}^*}$ to the T-axis. Equation 4.1 is commonly used in the literature and the usually reported value of ν is on the order of 1.5 [56]. For the present data, the parameter ν was in the range of 1.50 to 1.52.

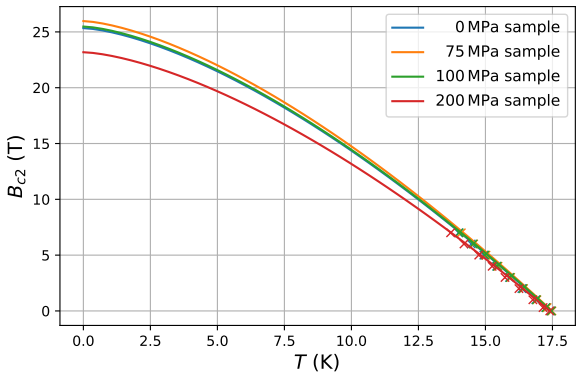

Figure 4.27: Upper critical field $B_{c2}(T)$ as a function of temperature T (solid line) based on the in-field T_c analysis (crosses) of 0, 75, 100 and 200 MPa loaded samples. The crosses refer to the peak in the imaginary part of the AC susceptibility.

Table 4.12: Results of the upper critical field evaluated by using the WHH expression.

σ_{nom}	$\left(\frac{dB_{c2}}{dT}\right)_{T=T_c{}^*}$	$T_c{}^*$	$B_{c2}(0)$	
(MPa)	(K T^{-1})	(K)	(T)	(-)
0	-2.11	17.31	25.34	–
75	-2.16	17.33	25.97	1.03
100	-2.12	17.34	25.48	1.01
200	-1.93	17.30	23.18	0.92

Table 4.13: Plastic deformation and crack formation obtained from SEM analysis. Cracks with a typical width down to 0.5 µm are considered in the presented inspection.

σ_{nom}	Transverse CS 1			Transverse CS 2			Comment
	h_{wire}	w_{wire}	$n_{damaged}$	h_{wire}	w_{wire}	$n_{damaged}$	
(MPa)	(μm)	(μm)	(-)	(μm)	(μm)	(-)	
0	710	710	0	–	–	–	Reacted
25	708	708	0	–	–	–	
50	706	713	0	703	716	0	
75	696	711	0	696	720	0	
100	694	720	4	693	721	0	
125	674	733	41	697	730	49	
150	653	736	65	656	740	59	
175	610	760	82	613	766	80	
200	589	794	88	585	700	86	
0	702	702	–	–	–	–	Non-reacted
200	654	716	–	–	–	–	

4.2.4 Microscopy investigations

Besides the transport current and magnetisation measurements, a metallographic investigation campaign was launched. It delivers additional microscopy information to determine the cause of the corresponding macroscopic behaviour. Therefore wires were exposed to transverse stress at RT according to Table 4.7.

The achieved microscopy information supports the results observed at impregnated Rutherford cables loaded with transverse stress at RT reported in Section 4.1. The characteristic spatial X-shape crack distribution in the transverse cross sections were observed as well. The crack shape, observed in the longitudinal cross section, was also in longitudinal direction.

Figure 4.28 gives an overview of the crack distribution and an indication of the stress formation, which is similar to the observed crack propagation in a Rutherford cable depicted in Figure 4.9(b). The first plastic deformation of the copper matrix was observed after 50 MPa, and the first cracks in the Nb_3Sn sub-elements were detected after a load of 100 MPa. A quantitative evaluation of the two investigated transverse cross sections (CS) at each stress level is given in Table 4.13. It comprises the remaining height h_{wire} and width w_{wire} of the wire as well as the number of damaged sub-elements labelled $n_{damaged}$.

Considering that the sub-elements are twisted for electrodynamic reasons, every sub-element passes the cracked region within the pitch length of nominal 14 mm (cf. Table 2.1). This further implies that the stress distribution in a specific cross section on the hexagonal sub-element grid changes slightly, depending on its orientation. Furthermore, it can be observed that voids promote cracks and cause a variation of the spatial distribution of the crack evolution.

For comparison, the data of a non-loaded non-reacted wire with a non-annealed copper matrix, as used during the Rutherford cabling, and a loaded non-reacted wire were added to Table 4.13. The deformation of the 200 MPa loaded non-reacted wire is comparable to that of the 150 MPa loaded reacted wire. This is an indicator that the annealed copper matrix after the RHT provides less mechanical stability for the fragile Nb_3Sn sub-elements.

The longitudinal cross sections in Figure 4.29 provide information about the shape of the cracks. Owing to the intended tilt angular of the metallographic preparation, areas with almost no cracks, i.e. horizontal middle, and areas with a high crack density can be observed (cf. Figure 2.5(b)). The cracks tend to be in longitudinal direction, but drift to the surface of the sub-elements. This leads to a reduction of the superconducting cross section and consequently a reduction of I_c. At higher loads, the sub-elements suffer strong splintering in parallel to the transport current direction.

Figure 4.30 summarises the SEM investigations of the chemically extracted sub-elements. No cracks could be found on the non-loaded sub-elements, which confirms the absence of misleading cracks caused by the metallographic mechanical preparation discussed above. On the loaded samples, cracks and broken sub-elements can be observed. The cracked sub-elements confirm the crack shape observed in the longitudinal cross section. A closer look at the cracked surface identified them as inter-granular brittle fractures along the grain boundaries.

A FEM analysis confirmed the results of the microscopy investigation [48]. The obtained crack pattern of the transverse cross section shown in Figure 4.28 correlates with the simulated stress distribution. Cracks in the sub-elements after a load of 100 MPa were confirmed by using a yield strength of 400 MPa for the sub-elements. The increasing stresses led to an increasing ovalisation of the wire by using the given pressing arrangement. Hence, the FEM simulation showed a local remaining tension strain on the sub-elements based on the plastic deformation of the copper matrix.

It should be noted that the plastic deformation also caused dislocations of the sub-elements in height. Owing to that, an additional axial tension strain on the sub-elements of the NearT_c sample between the voltage taps could not unequivocally be excluded.

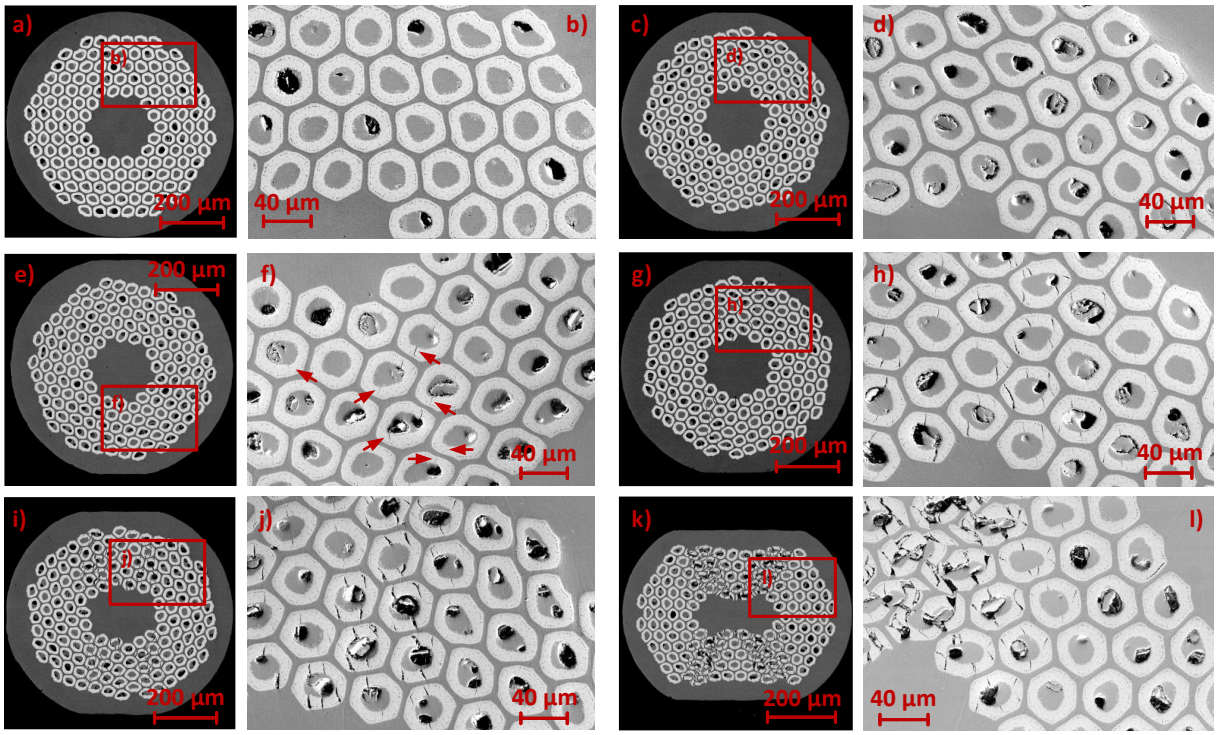

Figure 4.28: SEM micrographs of a transverse cross-sections of a reference wire **(a,b)** and wires after applying a transverse pressure of **(c,d)** 75 MPa, **(e,f)** 100 MPa, **(g,h)** 125 MPa, **(i,j)** 150 MPa and **(k,l)** 200 MPa. The first cracks observed after a nominal load of 100 MPa are marked by arrows.

4.2.5 Discussion

Change of superconducting properties caused by transverse stress at RT

The results of the transport current and magnetisation measurements in combination with the microscopy investigation allow the interpretation of the results to be split into two regimes:

- **Low-pressure regime at RT** ($\sigma_{nom} \leq 75$ MPa):
  Although no cracks could be found in this regime, a change of the extrinsic and intrinsic superconducting parameters was measured. Even an improving tendency was observed. This finding motivates the assumption that the strain situation on the superconducting sub-elements within the wire were changed. Based on the SEM micrographs and the FEM analysis mentioned above [48], the wire already became plastically deformed below the crack initiation, causing a residual strain on the Nb_3Sn sub-elements. This affects the strain situation within the wire in addition to the thermally induced pre-compression ε_m at low temperature. Hence, a change of the strain-dependent superconducting properties can be expected, which has been well elaborated and summarised, e.g. by J.W. Ekin [56] and P. Bruzzone [30]. N. Mitchell [114] modelled the thermal contraction of Nb_3Sn composite wires from the A-15 formation at approximately 650 °C to operation temperature at 4 K, whereby ε_m of internal-tin-type wires can be assumed in the range of −0.2 % to −0.25 %. As pointed out in Section 1.2.3, the strain dependency of the upper critical field $B_{c2}(\varepsilon)$ and the criti-

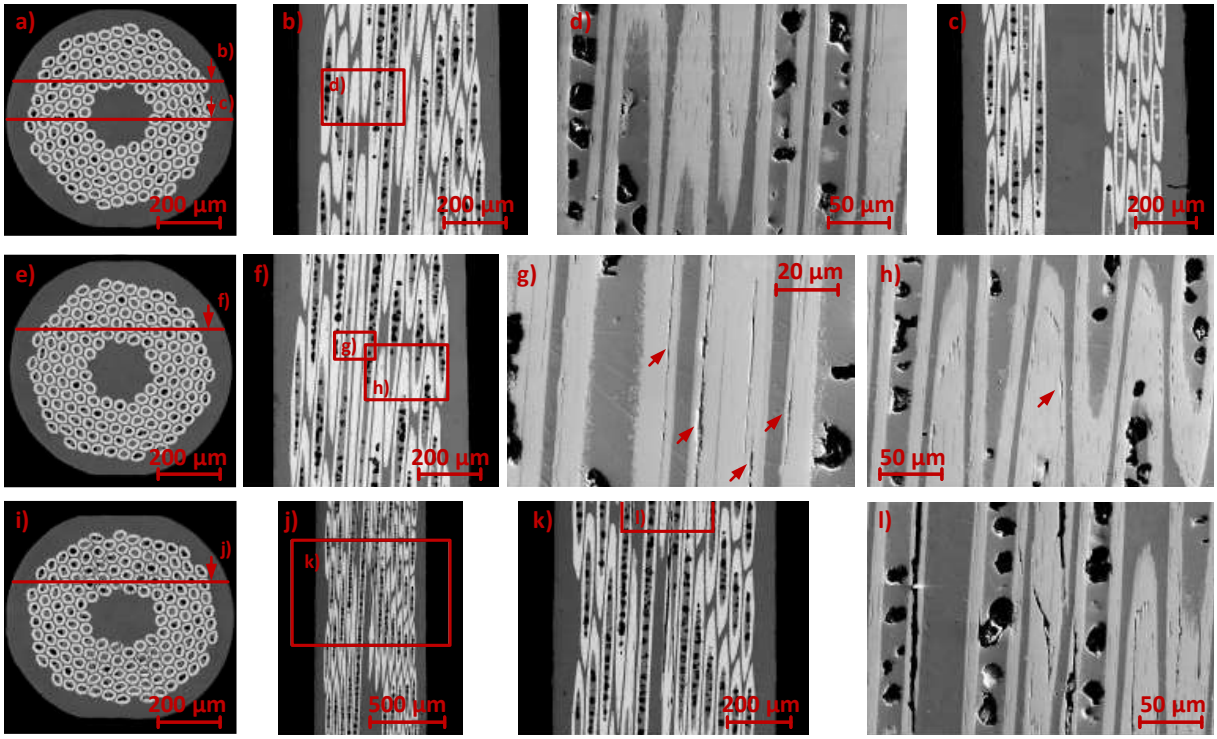

Figure 4.29: SEM micrographs of longitudinal cross sections of wires after applying a transverse pressure of **(a-d)** 75 MPa, **(e-h)** 100 MPa and **(i-l)** 150 MPa. The first cracks observed after a nominal load of 100 MPa are marked by arrows.

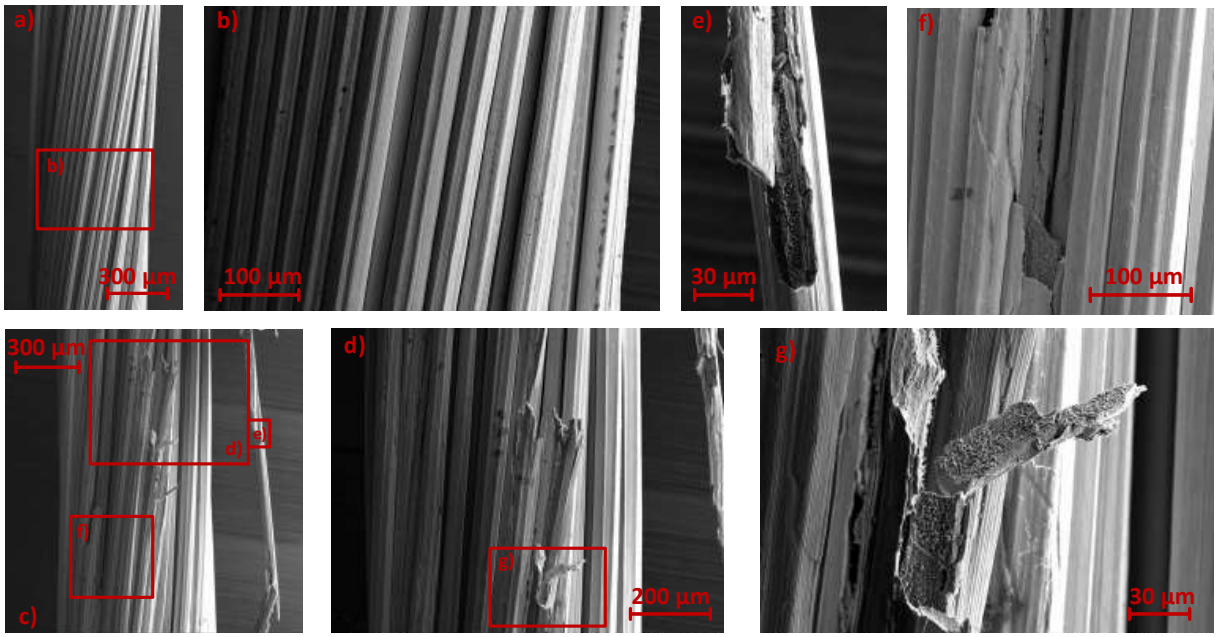

Figure 4.30: SEM micrographs of an etched **(a,b)** reference wire and an etched wire after applying a transverse pressure of **(c-g)** 200 MPa clearly revealed the splintering of the brittle Nb_3Sn sub-elements due to the transverse load as well as the surface of the fracture.

cal temperature $T_c(\varepsilon)$ can be described by a power law fit approximation within moderate strain (reversible strain effect).

The USL $F_p = I_c(B,T,\varepsilon)\,B = C\,g(\varepsilon)\,h(t)\,f(b)$ considers strain dependency within the moderate strain limit by establishing the strain scaling factor $g(\varepsilon)$ (cf. Equation 1.15). A FEM analysis showed local tension strain due to the deformation of the copper stabiliser at RT, designated as $\varepsilon_{res,RT}$. The slightly I_c improvement measured within this regime can be globally interpreted as illustrated in Figure 4.31. The intrinsic strain $\varepsilon_0 = \varepsilon - \varepsilon_m$ is shifted oppositely by the above-mentioned pre-strain $\varepsilon_{res,RT}$ caused at RT, modelled as $\varepsilon_0 = \varepsilon - \varepsilon_m + \varepsilon_{res,RT}$. Hence, it counteracts or locally relieves the pre-compression ε_m. All measurements are performed in the released situation ($\varepsilon = 0$) so that an improvement of $I_c(\varepsilon_{res,RT})$ could be measured initially. The best performance was measured after a load of 75 MPa. Hence, it can be assumed that the average residual tension strain $\varepsilon_{res,RT}$ after 75 MPa is in the range of the compression pre-strain ε_m and compensates it suitably. This behaviour stops with the irreversible strain limit $\varepsilon_{irr,RT}$ at RT, which generated fractures in the sub-elements.

Hence, this improving effect has the same origin as the effect observed in experiments with applied tension stress during the I_c measurements of wire, e.g. by G. Mondonico *et al.* [116] and B. Seeber *et al.* [148]. In these experiments, the compensating force is applied at low temperatures instead of the plastic deformation at RT as in the present case. Moreover, a permanent deformation of the copper matrix affecting the critical current during the experiment is discussed by C. Calzolaio *et al.* [32], who interpreted it as an irreversible strain effect. However, it must be considered that the mechanical properties at RT differ from those at low temperatures, i.e. $\varepsilon_{irr,RT} \neq \varepsilon_{irr}$. The residual strain of a coil assembly resulting from applied stress at RT was also investigated recently by C. Scheuerlein *et al.* [143]. At RT, the strain maps of 11 T dipole coil sections were acquired by using fast high-energy synchrotron X-ray and neutron diffraction. Such experiments can be recommended for further investigation of the present topic and may give more insight into or confirmation of the proposed interpretation (cf. Figure 4.31).

Although the Specimen 2 cable shows an improvement partly in the low-stress range, the phenomenon described above could not be observed unequivocally in the cable experiment. One of the reasons could be that the strands within the cable are spatially strongly constrained by the embedment with epoxy resin. Hence, strong deformation is prevented, which was responsible for the residual tension pre-strain and consequently improved I_c within the wire investigation.

- **High-pressure regime at RT** ($\sigma_{nom} > 75$ MPa):

  On the basis of the microscopy examination, the crack initiation starts at the load of 100 MPa, which correlates with the first continuous decrease of I_c.

  Although the decrease of B_{c2} and T_c measured by magnetometry indicates the presence of strain, the crack formation causes the primary loss of I_c. Consequently, the wire's performance degrades in this regime due to the same mechanism as observed in strands of Rutherford cables within the cable experiment (irreversible strain effect). The above-mentioned FEM analysis showed that the maximal residual strain $\varepsilon_{irr,RT}$ within a wire's cross section after a load of 100 MPa amounts to 0.44 % [48]. This is in a good agreement with the irreversible strain limit ε_{irr} in the range of 0.42 % to 0.45 % of internal-tin-type wires reported by C. Senatore [150].

  The results of the microscopy investigation confirm all conclusions of the former microscopy of the Specimen 1 cable, discussed in detail in Section 4.1.4. Cracks tend to be in longitudinal direction, i.e. parallel to transport current, and drift to the border of the sub-element. These observed longitudinal cracks are less critical concerning their I_c performance than cracks resulting from bending or axial stress, which are in transverse direction as investigated by M.C. Jewell *et al.* [83]. Similar research employing metallographic autopsy was performed by C. Sanabria *et al.* [137].

  The crack formation above a transverse load of 100 MPa found in this work can be identified as a purely mechanical process. The cracks indirectly harm the thermal stability of the wire and the I_c performance. Hence, the transport current has to evade the superconductor locally due to a crack and consequently flows in the copper stabiliser, generating dissipation and resulting in an earlier quench. This mechanism, so-called current sharing, also explains the measured decrease of the n value, observed particularly in this regime [156]. This phenomenon contrasts with the detected intrinsic strain-dependency in the low-stress regime.

At this point, it should be mentioned that investigations of reacted wires after pre-bending stress at RT were conducted by H. Oguro *et al.* [121]. The measurements with an applied field up to 18 T at 4.2 K of pre-bent Nb-rod-processed CuNb/Nb_3Sn wire also showed a clear enhancement of I_c followed by

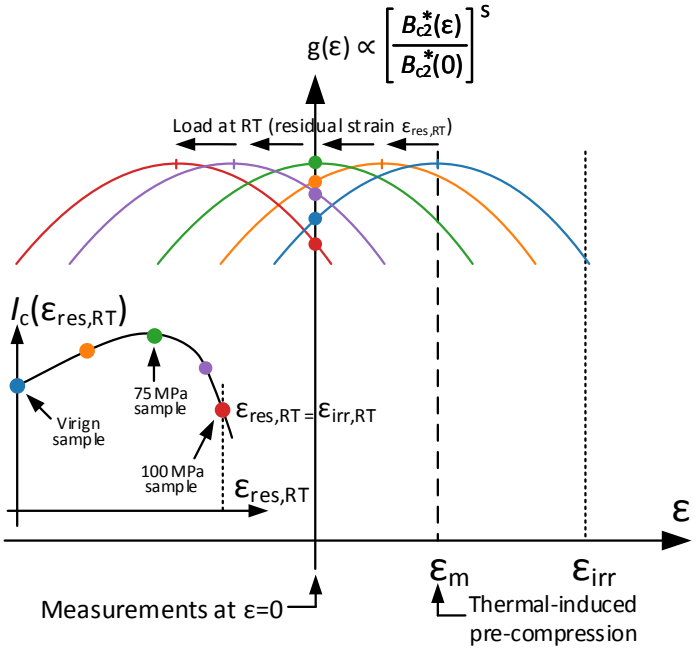

Figure 4.31: Interpretation of the results obtained with the strain scaling law $g(\varepsilon)$ of the USL $F_\mathrm{p} = I_\mathrm{c}(B,T,\varepsilon)\,B = C\,g(\varepsilon)\,h(t)\,f(b)$ for moderate strain [55, 56]. According to the SEM examination and the FEM analysis, the stress applied at room temperature causes plastic deformation of the copper stabiliser without cracks in sub-elements. Hence, a residual strain $\varepsilon_{\mathrm{res,RT}}$ within the wire is the consequence. Iterative increasing load within the experiment can be interpreted as a horizontal shift of $g(\varepsilon)$. This leads to an improvement of $I_\mathrm{c}(\varepsilon_{\mathrm{res,RT}})$ for moderate strain until cracks started to form at room temperature $(\varepsilon_{\mathrm{irr,RT}})$.

degradation at higher bending strain. They confirm the previous investigation of the "pre-bending" treatment of CuNb/(Nb,Ti)$_3$Sn wires regarding the "react and wind" coil manufacturing technique of S. Awaji *et al.* [9].

Implementation of the NearT_c concept

The NearT_c concept was implemented successfully by conductive cooling of the 160-mm-long specimen in a vacuum atmosphere with a sample temperature variation of ±5 mK. Moreover, it has been shown that the irreversible degradation of transverse stress applied at RT can be measured in the chosen temperature range of 16 K to 17.5 K.

From a more general perspective, a measurement of the $I_\mathrm{c}(T)$ behaviour up to a current of 150 A, i.e. $1.1 \cdot 10^9\,\mathrm{A\,m^{-2}}$, was performed. Compared to measurements of $I_\mathrm{c}(B)$ in liquid helium, an equal accuracy of the results is coupled to a higher technical effort, due to the required temperature control in the mK range.

Within the author's literature research, some experiments targeting the same temperature range could be found. B. ten Haken *et al.* [162] implemented a variable-temperature measurement with currents up to approximately 120 A. This was performed in a gaseous helium environment by using electrical heaters on the sample holder. Measurement results of Nb$_3$Sn wires at an applied field up to 13 T with sample temperatures in the range of 5 K to 8 K and a maximal error of ±40 mK were published.

In addition, L.F. Goodrich *et al.* [72] described an implementation of $I_\mathrm{c}(T)$ up to 200 A of Nb-Ti and Nb$_3$Sn wires. Therefore a continuous-flow cryostat based on gaseous helium with high flow rates of up to $0.3\,\mathrm{L\,s^{-1}}$ was employed to implement high-current variable-temperature measurements above 4.2 K. A linear fit of the temperature at zero field measurements was reported with a standard deviation of 10 mK. Subsequently, L.F. Goodrich *et al.* [71] published the construction and operation of a continuous-flow cryostat for measurements with test currents up to 400 A at a variable sample temperature in the range of 4 K to 120 K.

The following arguments should be taken into account when using the **NearT_c concept**:

- The NearT_c measurement principle only allows parameters that affect the $I_\mathrm{c}(T)$ diagram to be determined. Information about the upper critical field $B_{\mathrm{c}2}$, field-dependency of the observed effects as well as the impact on the pinning force $F_\mathrm{p} = {}^{I_\mathrm{c}(B)}/_{B}$ is lacking. Hence, such measurements are

often used to determine the temperature margin of the superconductors for magnet applications.

- Effects that directly influence the critical current, e.g. thermal stability, are surely traceable by evaluating $I_c(T)$. Owing to the fact that similar current densities are used as for common measurements of $I_c(B, 4.2\,\mathrm{K})$ in liquid helium, the observed effect will occur at a similar magnitude. This is also why especially influences caused by cracks are well determined by the NearT_c method. The setup was designed with 150 A, however the use of HTS current leads could extend the range to 300 A, as demonstrated by Y.S. Choi *et al.* [37].

- The magnetisation measurements confirmed the results qualitatively but also indicated a dependency of the critical current close to T_c on the variation of T_c. A comparison with Figure 4.24 and 4.26 illustrates this fact in particular. The behaviour can be explained with the high slope $\mathrm{d}I_c/\mathrm{d}T$, as mentioned in Section 4.2.3. In the present case, it exaggerated the effective impact on the critical current. Hence, for a non-relative comparison of NearT_c measurements, it is recommended to present the results $I_c(t)$ as a function of reduced temperature $t = T/T_c$ with an indication of the additionally measured T_c.

- Finally, the inhomogeneity of Nb_3Sn sub-elements within composite superconductors has to be considered. As discussed in Section 3.4, the out-of-phase magnetic moment m'' as a function of the temperature gives information about the homogeneity of the superconducting material. It is strongly influenced by the diffusion process as the A-15 phase is formed. An inhomogeneous superconducting material leads unavoidably to a spatial distribution of T_c. During critical current measurements close to T_c some parts of the sub-elements are already in the resistive state, which inherently implies a reduced effective superconducting cross section.

  Further research regarding the spatial T_c distribution of superconducting composite wires has been performed, for instance, by B. Seeber *et al.* [149]. The distribution of T_c was acquired by measuring the specific heat and using the method proposed by C. Senatore *et al.* [151]. T. Baumgartner *et al.* [17] studied the evaluation of the T_c distribution by using susceptibility measurements with confirmation by scanning Hall probe microscopy (SHPM) and EDX. These methods, which require only small samples, can be used supplementally to assess the effect of the inhomogeneity on the results received by the NearT_c measurements.

Nevertheless, within the construction, commissioning and operation of the **NearT_c setup**, several drawbacks emerged and their elaborated solutions should not be overlooked:

- In general, helium is not a convenient cooling medium for high-current measurements with operation temperature in the range of 15 K to 20 K, which comprises a large amount of Joule heating. A temperature of 4.2 K is not necessary per se for Nb_3Sn samples, based on the measurement principle discussed in Section 1.2.4. The coexistence of helium in the liquid and gaseous state in the tubes led to flow-driven thermal instabilities, which significantly affected the crucial temperature stability. Besides the actual temperature control concept, this problem was counteracted by the control of the dewar pressure and the deployment of the more robust current-sharing temperature T_{cs}. In addition, the number of repetitions of I_c measurements at the same condition was increased to improve the reliability of the measurement.

  However, it should be stated that helium is frequently used to establish a variable temperature in the range of 5 K to 300 K for application with vanish or low currents below 1 A. For instance, continuous-flow helium cryostats are often used to implement low-temperature scanning microscopes or T_c evaluations. In this case, the sample chamber, having a diameter of a few centimetres, is cooled from the bottom by a continuous helium gas flow. This is achieved by the constant supply of liquid helium through a needle valve by generating a vacuum in the chamber. Subsequently, the liquid is vaporised by a heater before entering the sample chamber. The temperature of the gas flow, and consequently of the sample chamber, can be regulated by both the flow rate and the power of the heater.

- The technological effort to obtain high-current measurement results of the same quality is much higher than for results from common measurements in liquid helium. First, the specific heat capacity $c \propto \mathrm{d}Q/\mathrm{d}T$ of liquid helium is much higher than that of copper, i.e. $5.3\,\mathrm{J\,g^{-1}\,K^{-1}}$ compared to $10^{-4}\,\mathrm{J\,g^{-1}\,K^{-1}}$ at 4.2 K, respectively [55]. This means that the occurrence of heat energy in a helium bath leads only to a minor temperature rise compared to the thermal contact to a copper plate. Moreover, the latent heat of vaporisation of saturated two-phase helium provides additional temperature stability, as discussed in Section 1.2.4. These properties make it inherently easier to stabilise the temperature in common measurements using liquid helium. However, helium can be

used to stabilise other cryogenic systems as well. R. Li *et al.* [99] utilised the high specific heat of pressured helium in a copper pot to improve temperature stability at the 4 K stage of a cryogenic refrigerator system.

Second, the temperature control of a spatially distributed system is more difficult than the current control of a background magnet. Moreover, it is closer to the common application, considering that most of the superconducting accelerator magnets are cooled with liquid or superfluid helium at a temperature of 4.2 K or 1.9 K, respectively. This is also probably why such measurements are more firmly established for characterising superconducting wires in the field of magnet development. However, the NearT_c concept with the presented setup is a lucrative alternative to achieve higher and less expensive throughput, compared to established test stations, without the need for a background magnet and a continuous supply of liquid helium.

- An alternative closed-loop cooling method would be a system based on a cryogenic refrigerator, at which this feasibility study is targeted. The Joule heating measurement of the setup showed values of 15.5 W and 120 mW for the entire system and the sample platform, respectively. The remaining radiation, conduction and convection heat influx can be estimated to be several orders of magnitude smaller than the Joule heating and heat impact due to the current leads. These test results can be further used for a heat load estimation of a two-stage cryogenic refrigerator system. The originally intended Gifford–McMahon (GM) cryocooler *Sumitomo CH210*[1] [91] has a first stage cooling capacity of 110 W at 77 K, a second stage cooling capacity 6 W at 20 K and a minimum temperature of 10 K [154]. Hence, the estimated heat load of Table 4.9 is a fraction of the nominal cooling capacity, and the results of the presented work do not rule out the use of a refrigerator system. The clear advantage of a refrigerator system for this application is the short cooling time, which allow a high measurement throughput and amounts to less than 1 h for RT to 20 K for the referred model. Moreover, it eliminates the costs due to the otherwise required continuous supply of liquid helium.
- The sample temperature analysed in the frequency domain (cf. Figure 4.16) clearly showed that an active feedback control rejects mainly low-frequency disturbances. By using an adequate PID control design on the basis of parameter identification of the system, the cutoff frequency could be further increased. Nevertheless, high-frequency disturbances, caused for instance by the mechanical cooling process of a mentioned refrigerator system at roughly 2 Hz, are barely accessible by thermal actuators. This could be done by interrupting the thermal link from the cooling plate to the sample by using materials with a higher specific heat capacity, e.g. lead (Pb). For instance, G. Dubuis *et al.* [46] demonstrated a passive suppression of the refrigerator-dependent temperature variation to the mK range without primary loss of cooling power.

Magnetisation measurement

Magnetisation measurements confirmed the transport current measurements qualitatively and contained information about the intrinsic properties. The slight improvement of B_{c2} and T_c in the low-pressure regime reinforced the assumption of rearranging the strain condition due to former force exertion at RT. Nevertheless, the model used for the magnetisation results assumes that the sub-elements are idealised straight hollow cylinders. This is ensured until roughly 112.5 MPa before the cylindrical shape of the sub-elements is no longer preserved due to the onset of splintering. Hence, magnetometry can be used only to detect cracks or stress causing cracks in sub-elements, not their quantitative influence on the practical J_c performance.

4.3 Conclusion

The effect and cause of transverse stress at room temperature on the superconducting properties of Nb_3Sn composite superconductors were measured and analysed. This was performed to study their significance in the context of manufacturing Nb_3Sn accelerator magnets.

Within the framework of the **cable investigation**, three impregnated Rutherford cable double stacks made of RRP wires were exposed to transverse stress at room temperature. Subsequently, the critical current I_c was measured, which delivers expedient information for the magnet manufacturing technology:

[1] Specification under the assumption of a three-phase 50 Hz power supply.

- In general, high stress on reacted cables at room temperature causes fractures in the superconducting sub-elements and indirectly harms the thermal stability of the strands, which results in current sharing after increased stress levels. This can be concluded from the observed irreversible I_c degradation in combination with a sharp decrease of the n value independent of the applied field.
- The first two specimens, loose impregnated double stacks, retained their integrity until 150 MPa and suffered an irreversible degradation of less than 5 % after a load of 175 MPa evaluated at 4.3 K with an applied field of 9.6 T. The first specimen showed a substantial degradation after 200 MPa. The subsequent metallographic autopsy confirmed fractures in the sub-elements as the cause of degradation. Moreover, the cracks were identified in longitudinal direction, which drifted to the surface of the sub-elements. Thus, the effective superconducting cross section was reduced. The third cable, having titanium shims for mechanical protection, showed an irreversible degradation of 5 % after a load of 240 MPa measured at 4.3 K with an applied field of 9.6 T.

In the context of the **wire investigation**, single Nb_3Sn RRP wires were exposed to transverse stress at room temperature. Subsequently, they were subjected to transport current and magnetisation measurements, which provide detailed information of the degradation process. In addition, a metallographic campaign was performed:

- The stress exertion below 100 MPa generated a plastic deformation of the copper stabiliser, thus affecting the pre-strain on the superconducting sub-elements without cracks. This counteraction of the thermal pre-compression can be concluded by the improved tendency of a few percent of the transport critical current and the strain-dependent intrinsic properties B_{c2} and T_c determined by magnetometric methods. A microscopy examination confirmed the plastic deformation without crack initiation, and the FEM analysis assessed a persistence tension strain on the sub-elements after stress exertion at room temperature.
- In the high-stress regime, the wire suffers current sharing due to cracks analogous to the observations in the cable specimens. This can be concluded from the detected onset of cracking after the stress exertion of 100 MPa determined by microscopy. This correlates also with the measured drop of I_c and T_{cs} in combination with a decrease of the n value. Regarding the characteristic crack distribution and the crack shape, the SEM results are in agreement with the cable experiment.

The implemented NearT_c concept and the applied established concepts aim to provide additional assessment possibilities besides the existing highly demanding and costly measurement infrastructure:

- **NearT_c concept and setup**
  The transport critical current $I_c(T)$ of a Nb_3Sn wire in self-field with test currents up to 150 A was successfully measured in the chosen temperature range of 16 K to 17.5 K. This was achieved by using a self-designed cryostat setup with a helium phase separator and a temperature controller to implement a sample temperature precision down to ±5 mK. Moreover, no evidence could be found that rule out the implementation of this concept using a cryogenic refrigerator system (cryocooler).

  The measurement equipment, the experimental geometric arrangement and the slope $\mathrm{d}I_c/\mathrm{d}T$ were sufficient to characterise the Nb_3Sn RRP wire. The measurement concept applied with the self-designed setup was shown to be suitable to measure the effect of the transverse stress at room temperature. In addition, a low-resistance measurement method was developed to evaluate the critical current T_c and the residual resistance ratio RRR.
- **Magnetometry**
  Magnetisation measurements were shown to be suitable to monitor an irreversible degradation after exerting transverse stress at room temperature and confirmed the transport critical current result of the chosen measurement range close to T_c.
- **Microscopy and FEM analysis**
  Metallographic procedures were developed and optimised to autopsy unequivocally cracks in Nb_3Sn sub-elements, proved by their absence in non-loaded samples. The transverse cross sections were used to obtain the crack initiation and their distribution. The longitudinal cross sections revealed the shape of the cracks. The microscopy investigation with a SEM was found to be a valuable indication tool to detect cracks without low-temperature equipment. The FEM analysis based on the X-ray tomography of samples was shown as a key tool to understand and assess the local stress and strain situation on the superconducting sub-elements caused by the externally applied force.

In summary, this work provides fundamental knowledge and adequate tools for further research on this topic and, in general, for the development of Nb_3Sn conductors for high-energy physics experiments.

4.4 Outlook

Section 1.5 outlined the purpose of the thesis and the accomplished experiments. Nevertheless, some aspects remained unfinished or were not pursued. Here are some recommendations for further research and development regarding this topic:

- **Irreversible degradation of superconducting properties caused by transverse stress applied at room temperature:**

  The degradation process was measured on a single wire type representative of all other Nb_3Sn wire types. The measurement of several equal specimens is recommended to be the next step to confirm the phenomena observed within this work. Subsequently, measurements of other wire types would be useful in order to assess the different robustness levels of the particular wire types. Consequently, this would yield applicable information for design decisions of accelerator magnets.

  Besides the minor change of superconducting properties below the onset of cracking, the leading cause of the irreversible degradation tends to be crack formation, confirmed by the cable and wire investigation. Hence, the local stress on the sub-elements is the essential cause. As emphasised in the discussion, the transfer of the externally applied force within the components is nonlinear, material-dependent and a crucial factor, which should be investigated further. A calculation of the local stress on sub-elements based on the externally applied force would standardise all experiment-dependent pressure profiles to the lowest common denominator. To implement such standardisation, FEM analyses on the basis of reliable material parameter identification and statistically based models would be essential.

  By performing a FEM simulation within the wire investigation, it was attempted to link the I_c degradation to the pre-stress on the sub-elements [48] (cf. Section 4.2). This universal information could be further used to estimate the I_c degradation based on a FEM stress analysis of any specific cable or coil cross section, which tracks the local stress values on the sub-elements. It could be used to made a preliminary assessment of crack formation and I_c degradation caused by transverse stress at room temperature of various configurations, e.g. different impregnation materials and strand diameters without costly cable or coil tests.

  One of the aspects that was not further pursued is the quantitative evaluation of cracks and crack density by using digital image processing, as performed in several other works. Automatic detection and quantification of cracks in sub-elements on SEM micrographs have been elaborated by C. Sanabria [136] and M.C. Jewell [103]. An extrapolation of this processing to SEM micrographs of loaded cables could confirm the mentioned FEM analysis [182] (cf. Section 4.1).

  It was shown that cracks mainly cause current sharing, which influences the thermal stability of the wire and cable. Considering the lengthy I_c measurements of cables and the only qualitative determination of the n value, it can be taken into account to describe this effect by common stability parameters. Hence, a statement of the stability loss could be reached by adopting the minimum quench energy, recently investigated for example by G. Willering [180] and W.M. de Rapper [42], or electrical network models, as introduced by Z.J.J. Stekly *et al.* [156].

- **Manufacturing Nb_3Sn accelerator magnets:**

  The production of Nb_3Sn accelerator magnets of the HL-LHC project still raises open questions and uncertainties, which only became evident in the final steps, the training and test procedure at low temperatures. Apparently, the production of Nb_3Sn accelerator magnets requires tighter manufacturing tolerances, compared to Nb-Ti magnets, to reach a mass-production with the necessary low drop-out rate, which fulfils the requirements for the FCC aims.

  Besides many successful research activities to imitate the manufacturing conditions within their experiments, the processes of fabrication should also be investigated in more detail. An increase of the monitoring instrumentation and automation infrastructure would improve the early detection of degradation and the reproducibility of the processes. Moreover, the obtained experimental conclusions, e.g. those of the present work, could be applied better to the actual situation in the manufacturing.

- **NearT_c concept and setup:**

  The NearT_c measurement concept was demonstrated to seek alternative experimental methods with higher throughput and lower economic effort. After the concept was put successfully into action, the next step would be optimisation. Upgrading the system to a cryocooler-based version calls for further investigation of the expected heat load of the two stages by static and dynamic heat inputs.

An obvious optimisation potential is to replace the cold parts of the current leads with commercial HTS coated conductors made for example of YBCO or BiSCCO. This would reduce the Joule heating strongly and would help to achieve a higher sample current, e.g. 300 A. In low-temperature systems with applied fields, HTS current leads have to be elaborately mounted to prevent possible quenches by Lorentz force-induced movements. Considering that the measurement concept does not imply a background magnet, mounting of the leads is not necessary. Hence, a relatively significant improvement of the setup could be achieved with relatively little effort.

Bibliography

[1] A. Abada et al. FCC Physics Opportunities – Future Circular Collider Conceptual Design Report Volume 1. *European Physical Journal C*, **79**:474, 2019.

[2] A. Abada et al. FCC-ee: The Lepton Collider – Future Circular Collider Conceptual Design Report Volume 2. *European Physical Journal Special Topics*, **228**(2):261, 2019.

[3] A. Abada et al. FCC-hh: The Hadron Collider – Future Circular Collider Conceptual Design Report Volume 3. *European Physical Journal Special Topics*, **228**(4):755, 2019.

[4] A. A. Abrikosov. On the Magnetic Properties of Superconductors of the Second Group. *Zhurnal Éksperimental'noĭ i Teoreticheskoĭ Fiziki*, **32**(6):1442, 1957. [Soviet physics, JETP **5**(6):1174 (1957)].

[5] J. D. Adam et al. Status of the lhc superconducting cable mass production. *IEEE Transactions on Applied Superconductivity*, **12**(1):1056, 2002.

[6] J. Ahlback et al. Electromagnetic and mechanical design of a 56 mm aperture model dipole for the LHC. *IEEE Transactions on Magnetics*, **30**(4):1746, 1994.

[7] G. Apollinari, I. Béjar Alonso, O. Brüning, P. Fessia, M. Lamont, L. Rossi, and L. Tavian. High-Luminosity Large Hadron Collider (HL-LHC): Technical Design Report. Report no. CERN-2017-007-M, CERN, 1211 Geneva 23, Switzerland, 2017.

[8] B. Auchmann, S. Russenschuck, and N. Schwerg. Discrete Differential Geometry Applied to the Coil-End Design of Superconducting Magnets. *IEEE Transactions on Applied Superconductivity*, **17**(2):1165, 2007.

[9] S. Awaji, K. Watanabe, and K. Katagiri. Improvement of mechanical and superconducting properties in CuNb/(Nb,Ti)3Sn wires by applying bending strain at room temperature. *Superconductor Science and Technology*, **16**(6):733, 2003.

[10] S. Balachandran, C. Tarantini, P. J. Lee, F. Kametani, Y. Su, B. Walker, W. L. Starch, and D. C. Larbalestier. Beneficial influence of Hf and Zr additions to Nb4at%Ta on the vortex pinning of Nb_3Sn with and without an O source. *Superconductor Science and Technology*, **32**(4):044006, 2019.

[11] J. Bardeen and M. J. Stephen. Theory of the Motion of Vortices in Superconductors. *Physical Review*, **140**:A1197.

[12] J. Bardeen, L. N. Cooper, and J. R. Schrieffer. Theory of Superconductivity. *Physical Review*, **108**:1175, 1957.

[13] C. Barth, B. Seeber, A. Rack, C. Calzolaio, Y. Zhai, D. Matera, and C. Senatore. Quantitative correlation between the void morphology of niobium-tin wires and their irreversible critical current degradation upon mechanical loading. *Scientific Reports*, **8**(6589), 2018.

[14] E. Barzi, T. Wokas, and A. V. Zlobin. Sensitivity of Nb_3Sn Rutherford-type cables to transverse pressure. *IEEE Transactions on Applied Superconductivity*, **15**(2):1541, 2005.

[15] T. Baumgartner. *Effects of Fast Neutron Irradiation on Critical Current and Intrinsic Properties of State-of-the-Art Nb_3Sn wires*. PhD thesis, Vienna University of Technology, Vienna, Austria, 2013.

[16] T. Baumgartner, M. Eisterer, H. W. Weber, R. Flükiger, B. Bordini, L. Bottura, and C. Scheuerlein. Evaluation of the Critical Current Density of Multifilamentary Nb_3Sn Wires From Magnetization Measurements. *IEEE Transactions on Applied Superconductivity*, **22**(3):6000604, 2012.

[17] T. Baumgartner, J. Hecher, J. Bernardi, S. Pfeiffer, C. Senatore, and M. Eisterer. Assessing composition gradients in multifilamentary superconductors by means of magnetometry methods. *Superconductor Science and Technology*, **30**(1):014011, 2016.

[18] C. Bayer, C. Barth, P. V. Gade, K. Weiss, and R. Heller. FBI Measurement Facility for High Temperature Superconducting Cable Designs. *IEEE Transactions on Applied Superconductivity*, **24**(3):1, 2014.

[19] C. P. Bean. Magnetization of High-Field Superconductors. *Reviews of Modern Physics*, **36**:31, 1964.

[20] J. G. Bednorz and K. A. Z. Müller. Possible high T_c superconductivity in the Ba-La-Cu-O system. *Zeitschrift für Physik B Condensed Matter*, **64**:189, 1986.

[21] F. Bertinelli et al. Production and Quality Assurance of Main Busbar Interconnection Splices During the LHC 2008–2009 Shutdown. *IEEE Transactions on Applied Superconductivity*, **21**(3):1786, 2011.

[22] R. A. Beth. Complex representation and computation of two-dimensional magnetic fields. *Journal of Applied Physics*, **37**(7):2568, 1966.

[23] J. Billan et al. A Superconducting High-Luminosity Insertion in the Intersecting Storage Rings (ISR). *IEEE Transactions on Nuclear Science*, **26**(3):3179, 1979.

[24] J. P. Blewett. Radial Focusing in the Linear Accelerator. *Physical Review*, **88**:1197, 1952.

[25] B. Bordini. Self-Field Correction in Critical Current Measurements of Superconducting Wires Tested on ITER VAMAS Barrels. Internal note (EDMS no. 105765), CERN, 1211 Geneva 23, Switzerland, 2010.

[26] B. Bordini, F. Regis, O. Crettiez, P. Fessia, M. Guinchard, J. C. Perez, and I. Sexton. Conceptual Design of a New Sample Holder for the FRESCA Cable Test Station. *IEEE Transactions on Applied Superconductivity*, **20**(3):1511, 2010.

[27] B. Bordini, P. Alknes, A. Ballarino, L. Bottura, and L. Oberli. Critical Current Measurements of High-J_c Nb_3Sn Rutherford Cables Under Transverse Compression. *IEEE Transactions on Applied Superconductivity*, **24**(3):1, 2014.

[28] H. Boschman, A.P. Verweij, W. A. J. Wessel, H. H. J. ten Kate, and L. J. M. van de Klundert. Effect of transverse loads up to 300 MPa on the critical currents of Nb_3Sn cables. *IEEE Transactions on Magnetics*, **27**(2):1831, 1991.

[29] O. S. Brüning, P. Collier, P. Lebrun, S. Myers, R. Ostojic, J. Poole, and P. Proudlock. LHC Design Report. URL `http://cds.cern.ch/record/782076`. [Online; Accessed September 2019]. Report no. CERN-2004-003-V-1, CERN, 1211 Geneva 23, Switzerland, 2004.

[30] P. Bruzzone. Review of Design Aspects for High Current Nb_3Sn Conductors. *IEEE Transactions on Applied Superconductivity*, **21**(3):2036, 2011.

[31] J. Cabanes, M. Garlasche, B. Bordini, and A. Dallocchio. Simulation of the cabling process for Rutherford cables: An advanced finite element model. *Cryogenics*, **80**:33, 2016.

[32] C. Calzolaio, G. Mondonico, A. Ballarino, B. Bordini, L. Bottura, L. Oberli, and C. Senatore. Electromechanical properties of PIT Nb_3Sn wires under transverse stress: experimental results and FEM analysis. *Superconductor Science and Technology*, **28**(5):055014, 2015.

[33] M. Cantoni, C. Scheuerlein, P.-Y. Pfirter, F. de Borman, J. Rossen, G. Arnau, L. Oberli, and P. Lee. Sn concentration gradients in powder-in-tube superconductors. *Journal of Physics: Conference Series*, **234**(2):022005, 2010.

[34] S. Caspi et al. Canted–Cosine–Theta Magnet (CCT)—A Concept for High Field Accelerator Magnets. *IEEE Transactions on Applied Superconductivity*, **24**(3):1, 2014.

[35] CERN Document Server. URL `https://cds.cern.ch`. [Online; Accessed September 2019]. CERN, 1211 Geneva 23, Switzerland.

[36] N. Cheggour, T. C. Stauffer, W. Starch, P. J. Lee, J. D. Splett, L. F. Goodrich, and A. K. Ghosh. Precipitous change of the irreversible strain limit with heat-treatment temperature in Nb_3Sn wires made by the restacked-rod process. *Scientific Reports*, **8**:13048, 2018.

[37] Y. S. Choi, T. A. Painter, D. L. Kim, H. S. Yang, and B. S. Lee. Semi-retractable current lead cooled by a cryocooler for high field magnet. *IEEE Transactions on Applied Superconductivity*, **19**(3):2210, 2009.

[38] N. C. Christofilos. Focusing System for Ions and Electrons. United States Patent 2736799, 1950.

[39] E. D. Courant, M. S. Livingston, and H. S. Snyder. The Strong-Focusing Synchroton – A New High Energy Accelerator. *Physical Review*, **88**:1190, 1952.

[40] E. D. Courant, M. S. Livingston, H. S. Snyder, and J. P. Blewett. Origin of the "Strong-Focusing" Principle. *Physical Review*, **91**:202, 1953.

[41] M. Daly, C. H. Löffler, D. Smekens, A. T. Fontenla, O. S. de Frutos, M. Guinchard, and F. Savary. Multiscale approach to the mechanical behavior of epoxy impregnated Nb_3Sn coils for the 11 T dipole. *IEEE Transactions on Applied Superconductivity*, **28**(3):1, 2018.

[42] W. M. de Rapper. *Thermal stability of Nb_3Sn Rutherford cables for accelerator magnets*. PhD thesis, University of Twente, Enschede, The Netherlands, 2014.

[43] B. S. Deaver and W. M. Fairbank. Experimental Evidence for Quantized Flux in Superconducting Cylinders. *Physical Review Letters*, **7**:43, 1961.

[44] P. G. deGennes. *Superconductivity of Metals and Alloys*. CRC Press, Bocan Raton, USA, 1966. ISBN 978-0738201016.

[45] R. Doll and M. Näbauer. Experimental Proof of Magnetic Flux Quantization in a Superconducting Ring. *Physical Review Letters*, **7**:51, 1961.

[46] G. Dubuis, X.He, and I. Božović. Sub-millikelvin stabilization of a closed cycle cryocooler. *Review of Scientific Instruments*, **85**(10):103902, 2014.

[47] P. Ebermann and F. Wolf. Evaluation script for analysing pressure measurement films with office scanners. Internal note (EDMS no. 188555), CERN, 1211 Geneva 23, Switzerland, 2017.

[48] P. Ebermann, T. Baumgartner, M. Daly, A. Gallifa Terricabras, T. Koettig, F. Lackner, C. Scheuerlein, and M. Eisterer. Influence of transverse stress exerted at room temperature on the superconducting properties of Nb_3Sn wires. *Superconductor Science and Technology*, **32**(9):095010, 2019.

[49] P. Ebermann et al. Irreversible degradation of Nb_3Sn Rutherford cables due to transverse compressive stress at room temperature. *Superconductor Science and Technology*, **31**(6):065009, 2018.

[50] C. Eck et al. LHC computing Grid: Technical Design Report. URL `https://cds.cern.ch/record/840543`. [Online; Accessed September 2019]. Report no. CERN-LHCC-2005-024, CERN, 1211 Geneva 23, Switzerland, 2005.

[51] M Eisterer. Towards optimized Nb_3Sn. *Superconductor Science and Technology*, **32**(4):040501, 2019.

[52] J. W. Ekin. Current transfer in multifilamentary superconductors. I. Theory. *Journal of Applied Physics*, **49**(6):3406, 1978.

[53] J. W. Ekin. Strain scaling law for flux pinning in practical superconductors. Part 1: Basic relationship and application to Nb_3Sn conductors. *Cryogenics*, **20**(11):611, 1980.

[54] J. W. Ekin. Four-dimensional *J-B-T-ε* critical surface for superconductors. *Journal of Applied Physics*, **54**(1):303, 1983.

[55] J. W. Ekin. *Experimental Techniques for Low-Temperature Measurements*. Oxford University Press, Oxford, UK, 2006. ISBN 978-0198570547.

[56] J. W. Ekin. Unified scaling law for flux pinning in practical superconductors: I. Separability postulate, raw scaling data and parameterization at moderate strains. *Superconductor Science and Technology*, **23**(8):083001, 2010.

[57] J. W. Ekin, A. F. Clark, and J. C. Ho. Current transfer in multifilamentary superconductors. II. Experimental results. *Journal of Applied Physics*, **49**(6):3410, 1978.

[58] J. W. Ekin, N. Cheggour, L. Goodrich, J. Splett, B. Bordini, and D. Richter. Unified Scaling Law for flux pinning in practical superconductors: II. Parameter testing, scaling constants, and the Extrapolative Scaling Expression. *Superconductor Science and Technology*, **29**(12):123002, 2016.

[59] J. W. Ekin, N. Cheggour, L. Goodrich, and J. Splett. Unified Scaling Law for flux pinning in practical superconductors: III. Minimum datasets, core parameters, and application of the Extrapolative Scaling Expression. *Superconductor Science and Technology*, **30**(3):033005, 2017.

[60] G. M. Eliashberg. Interactions between Electrons and Lattice Vibrations in a Superconductor. *Zhurnal Éksperimental'noĭ i Teoreticheskoĭ Fiziki*, **38**(3):966, 1960. [Soviet physics, JETP **11**(3):696 (1960)].

[61] H. Felice et al. Performance of a nb$_3$sn quadrupole under high stress. *IEEE Transactions on Applied Superconductivity*, **21**(3):1849, 2011.

[62] J. Fleiter, B. Bordini, A. Ballarino, L. Oberli, S. Izquierdo, and L. Bottura. Quench Propagation in Nb_3Sn Rutherford Cables for the Hi-Lumi Quadrupole Magnets. *IEEE Transactions on Applied Superconductivity*, **25**(3):1, 2015.

[63] J. Fleiter, A. Ballarino, A. Bonasia, B. Bordini, and D. Richter. Optimization of Nb_3Sn Rutherford Cables Geometry for the High-Luminosity LHC. *IEEE Transactions on Applied Superconductivity*, **27**(4):1, 2017.

[64] J. Fleiter, S. Peggiani, A. Bonasia, and A. Ballarino. Characterization of Nb_3Sn Rutherford cable degradation due to strands cross-over. *IEEE Transactions on Applied Superconductivity*, **28**(4):1, 2018.

[65] R. Flükiger, D. Uglietti, C. Senatore, and F. Buta. Microstructure, composition and critical current density of superconducting Nb_3Sn wires. *Cryogenics*, **48**(7):293, 2008.

[66] Fujifilm, Heesenstraße 31, 40549 Düsseldorf, Germany. Pressure measurement film – Prescale. URL `https://www.fujifilm.com/products/prescale`. [Online; Accessed September 2019].

[67] A. Gallifa Terricabras. Microscopy inspection of Nb_3Sn RRP strands and Nb_3Sn Rutherford cables after transverse compressive tests at room temperature. Internal note (EDMS no. 1994865), CERN, 1211 Geneva 23, Switzerland, 2018.

[68] A. Godeke. *Performance boundaries in Nb_3Sn*. PhD thesis, University of Twente, Enschede, The Netherlands, 2005.

[69] A. Godeke, M. Dhalle, A. Morelli, L. Stobbelaar, H. van Weeren, H. J. N. van Eck, W. Abbas, A. Nijhuis, A. den Ouden, and B. ten Haken. A device to investigate the axial strain dependence of the critical current density in superconductors. *Review of Scientific Instruments*, **75**(12):5112, 2004.

[70] W. Goldacker, S. I. Schlachter, R. Nast, H. Reiner, S. Zimmer, H. Kiesel, and A. Nyilas. Bending strain investigations on BSCCO(2223) tapes at 77 K applying a new bending technique. *AIP Conference Proceedings*, **614**(1):469, 2002.

[71] L. F. Goodrich and T. C. Stauffer. Hysteresis in Transport Critical-Current Measurements of Oxide Superconductors. *Journal of Research of the National Institute of Standards and Technology*, **106**:657, 2001.

[72] L. F. Goodrich, L. T. Medina, and T. C. Stauffer. High Critical-Current Measurements in Liquid and Gaseous Helium. *Advances in Cryogenic Engineering Materials, vol. 44. Springer, Boston, MA*, pages 873-880, 1998.

[73] L. P. Gor'kov. Microscopic Derivation of the Ginzburg-Landau Equations in the Theory of Superconductivity. *Zhurnal Éksperimental'noĭ i Teoreticheskoĭ Fiziki*, **36**(6):1918, 1959. [Soviet physics, JETP **9**(6):1364 (1959)].

[74] L. P. Gor'kov. Theory of Superconducting Alloys in a Strong Magnetic Field near the Critical Temperature. *Zhurnal Éksperimental'noĭ i Teoreticheskoĭ Fiziki*, **37**(5):1407, 1960. [Soviet physics, JETP **10**(5):998 (1960)].

[75] S. A. Gourlay et al. Magnet R&D for the US LHC Accelerator Research Program (LARP). *IEEE Transactions on Applied Superconductivity*, **16**(2):324, 2006.

[76] V. Guritanu, W. Goldacker, F. Bouquet, Y. Wang, R. Lortz, G. Goll, and A. Junod. Specific heat of Nb_3Sn: The case for a second energy gap. *Physical Review B*, **70**:184526, 2004.

[77] H. Kamerlingh Onnes. Further experiments with liquid helium. C. On the change of electric resistance of pure metals at very low temperatures etc. IV. The resistance of pure mercury at helium temperatures. *Leiden Communications*, **120b**, 1911.

[78] E. Helfand and N. R. Werthamer. Temperature and Purity Dependence of the Superconducting Critical Field, H_{c2}. *Physical Review Letters*, **13**:686, 1964.

[79] E. Helfand and N. R. Werthamer. Temperature and Purity Dependence of the Superconducting Critical Field, H_{c2}. II. *Physical Review*, **147**:288, 1966.

[80] H. Hertz. Über die Berührung Fester Elastischer Körper. *Journal für die Reine und Angewandte Mathematik*, 92:156, 1881.

[81] J. K. Hulm and R. D. Blaugher. Superconducting Solid Solution Alloys of the Transition Elements. *Physical Review*, **123**:1569, 1961.

[82] B. Jakob, G. Pasztor, M. Bona, and A. Asner. Reduced sensitivity of Nb_3Sn epoxy-impregnated cable to transverse stress. *Cryogenics*, **31**(5):390, 1991.

[83] M. C. Jewell, P. J. Lee, and D. C. Larbalestier. The influence of Nb_3Sn strand geometry on filament breakage under bend strain as revealed by metallography. *Superconductor Science and Technology*, **16**(9):1005, 2003.

[84] Y. Kamihara, H. Hiramatsu, M. Hirano, R. Kawamura, H. Yanagi, T. Kamiya, and H. Hosono. Iron-based layered superconductor: LaOFeP. *Journal of the American Chemical Society*, **128**:10012, 2006.

[85] A .R. Kantrowitz and Z. J. J. Stekly. A New Principle for the Construction of Stabilized Superconducting Coils. *Applied Physics Letters*, **6**:56, 1965.

[86] M. Karppinen et al. Design of 11 T Twin-Aperture Nb_3Sn Dipole Demonstrator Magnet for LHC Upgrades. *IEEE Transactions on Applied Superconductivity*, **22**(3):4901504, 2012.

[87] U. M. Kelly et al. Nb_3Sn Wire Shape and Cross-Sectional Area Inhomogeneity in Rutherford Cables. *IEEE Transactions on Applied Superconductivity*, **28**(4):1, 2018.

[88] E. J. Kramer. Scaling laws for flux pinning in hard superconductors. *Journal of Applied Physics*, **44**(3):1360, 1973.

[89] F. Lackner. Private conversation. CERN, 1211 Geneva 23, Switzerland, 2018.

[90] F. Lackner. Status of the wound conductor task. Presented on the FCC week 2018, Amsterdam, The Netherlands, 2018. URL `https://indico.cern.ch/event/656491/timetable/?view=nicecompact`. [Online; Accessed September 2019].

[91] F. Lackner and C. Scheuerlein. Justification for the purchase of two Sumitomo CH-210 cryocoolers. Internal purchase request (EDH-DAI no. 6414099), CERN, 1211 Geneva 23, Switzerland, 2016.

[92] F. Lackner et al. Fabrication of the 7.3-m-Long Coils for the Prototype of MQXFB, the Nb_3Sn Low-β Quadrupole Magnet for the HiLumi LHC. *IEEE Transactions on Applied Superconductivity*, **28**(3):1, 2018.

[93] L. D. Landau and V. L. Ginzburg. On the theory of superconductivity. *Zhurnal Éksperimental'noĭ i Teoreticheskoĭ Fiziki*, **20**:1064, 1950.

[94] D. Leroy, G. Spigo, A. P. Verweij, H. Boschman, R. Dubbeldam, and J. G. Pelayo. Design and manufacture of a large-bore 10 T superconducting dipole for the CERN cable test facility. *IEEE Transactions on Applied Superconductivity*, **10**(1):178, 2000.

[95] LHC Experiments Committee. ALICE: Technical Proposal. URL `https://cds.cern.ch/record/293391`. [Online; Accessed September 2019]. Report no. CERN-LHCC-95-71, CERN, 1211 Geneva 23, Switzerland, 1995.

[96] LHC Experiments Committee. ATLAS: Technical Proposal for a general-purpose pp Experiment at the Large Hadron Collider at CERN. URL `https://cds.cern.ch/record/290968`. [Online; Accessed September 2019]. Report no. CERN-LHCC-94-43, CERN, 1211 Geneva 23, Switzerland, 1994.

[97] LHC Experiments Committee. CMS: Technical Proposal. URL `https://cds.cern.ch/record/290969`. [Online; Accessed September 2019]. Report no. CERN-LHCC-94-38, CERN, 1211 Geneva 23, Switzerland, 1994.

[98] LHC Experiments Committee. LHCb: Technical Proposal. URL https://cds.cern.ch/record/622031. [Online; Accessed September 2019]. Report no. CERN-LHCC-98-004, CERN, 1211 Geneva 23, Switzerland, 1998.

[99] R. Li, A. Onishi, T. Satoh, and Y. Kanazawa. Temperature Stabilization on Cold Stage of 4 K G-M Cryocooler. *Cryocoolers 9. Springer, Boston, MA*, pages 765-771, 1997.

[100] J. H. Londenhovius, E. M. Hornveld, A. den Ouden, W. A. J. Wessel, and H. H. J. ten Kate. Progress in the development of Nb_3Sn conductors based on the "Powder in tube" method with finer filaments. *IEEE Transactions on Applied Superconductivity*, **9**(2):1451, 1999.

[101] F. London and H. London. The Electromagnetic Equations of the Supraconductor. *Proceedings of the Royal Society of London Series A*, **149**:71, 1935.

[102] C. Lorin, D. Durante, and M. Segreti. EuroCirCol 16 T Block-Coils Dipole Option for the Future Circular Collider. *IEEE Transactions on Applied Superconductivity*, **27**(4):1, 2017.

[103] M. C. Jewell. *The effect of strand architecture on the fracture propensity on niobium-tin composite wires*. PhD thesis, University of Wisconsin – Madison, Madison, Wisconsin, USA, 2019.

[104] K. Maki. The magnetic properties of superconducting alloys I. *Physics Physique Fizika*, **1**:21, 1964.

[105] K. Maki. The magnetic properties of superconducting alloys. II. *Physics Physique Fizika*, **1**:127, 1964.

[106] M. Mangano, P. Azzi, M. D'Onofrio, and M. Mccullough. Physics at its limits. *CERN Courier*, 57 (4):34, 2017. URL https://cds.cern.ch/record/2259560. [Online; Accessed September 2019].

[107] V. Marinozzi, G. Bellomo, B. Caiffi, P. Fabbricatore, S. Farinon, A. M. Ricci, M. Sorbi, and M. Statera. Conceptual design of a 16 T cos θ bending dipole for the future circular collider. *IEEE Transactions on Applied Superconductivity*, **28**(3):1, 2018.

[108] W. D. Markiewicz. Elastic stiffness model for the critical temperature T_c of Nb_3Sn including strain dependence. *Cryogenics*, **44**:767, 2004.

[109] B. T. Matthias, T. H. Geballe, S. Geller, and E. Corenzwit. Superconductivity of Nb_3Sn. *Physical Review*, **95**:1435, 1954.

[110] W. L. McMillan. Transition temperature of strong-coupled superconductors. *Physical Review*, **167**:331, 1968.

[111] W. Meißner and R. Ochsenfeld. Ein neuer Effekt bei Eintritt der Supraleitfähigkeit. *Naturwissenschaften*, **21**:787, 1933.

[112] M. G. T. Mentink. *An experimental and computational study of strain sensitivity in superconducting Nb_3Sn*. PhD thesis, University of Twente, Enschede, The Netherlands, 2014.

[113] A. Milanese and M. Bohdanowicz. Twin aperture bending magnets and quadrupoles for FCC-ee. *IEEE Transactions on Applied Superconductivity*, **28**(3):1, 2018.

[114] N. Mitchell. Finite element simulations of elasto-plastic processes in Nb_3Sn strands. *Cryogenics*, **45**(7):501, 2005.

[115] H. Müller and Th. Schneider. Heat treatment of Nb_3Sn conductors. *Cryogenics*, **48**(7):323, 2008.

[116] G. Mondonico, B. Seeber, A. Ferreira, B. Bordini, L. Oberli, L. Bottura, A. Ballarino, R. Flükiger, and C. Senatore. Effect of quasi-hydrostatical radial pressure on I_c of Nb_3Sn wires. *Superconductor Science and Technology*, **25**(11):115002, 2012.

[117] D. F. Moore, R. B. Zubeck, J. M. Rowell, and M. R. Beasley. Energy gaps of the $A-15$ superconductors Nb_3Sn, V_3Si, and Nb_3Ge measured by tunneling. *Physical Review B*, **20**:2721, 1979.

[118] L. Muzzi et al. Direct observation of Nb_3Sn lattice deformation by high-energy x-ray diffraction in internal-tin wires subject to mechanical loads at 4.2 K. *Superconductor Science and Technology*, **25**(5):054006, 2012.

[119] J. Nagamatsu, N. Nakagawa, T. Muranaka, Y. Zenitani, and J. Akimitsu. Superconductivity at 39 K in magnesium diboride. *Nature*, **410**:63, 2001.

[120] H. Oguro, S. Awaji, K. Watanabe, M. Sugimoto, and H. Tsubouchi. Mechanical and superconducting properties of Nb_3Sn wires with Nb-rod-processed CuNb reinforcement. *Superconductor Science and Technology*, **26**(9):094002, 2013.

[121] H. Oguro, S. Awaji, K. Watanabe, M. Sugimoto, and H. Tsubouchi. Prebending Effect for Mechanical and Superconducting Properties of Nb-Rod-Processed Cu–Nb Internal-Reinforced Nb_3Sn Wires. *IEEE Transactions on Applied Superconductivity*, **24**(3):1, 2014.

[122] T. P. Orlando, E. J. McNiff, S. Foner, and M. R. Beasley. Critical fields, Pauli paramagnetic limiting, and material parameters of Nb_3Sn and V_3Si. *Physical Review B*, **19**:4545, 1979.

[123] A. B. Pippard and W. L. Bragg. An experimental and theoretical study of the relation between magnetic field and current in a superconductor. *Proceedings of the Royal Society of London Series A*, **216**(1127):547, 1953.

[124] D. Pulikowski, F. Lackner, C. Scheuerlein, D. Meinel, F. Savary, D. Tommasini, and M. Pajor. Testing mechanical behavior of Nb_3Sn Rutherford cable during coil winding. *IEEE Transactions on Applied Superconductivity*, **27**(4):1, 2017.

[125] D. Pulikowski, F. Lackner, C. Scheuerlein, F. Savary, D. Tommasini, and M. Pajor. Windability tests of Nb_3Sn Rutherford cables for HL-LHC and FCC. *IEEE Transactions on Applied Superconductivity*, **28**(3):1, 2018.

[126] PyVISA – Python VISA bindings for GPIB, RS232, TCP/IP and USB instruments. URL `https://pypi.org/project/PyVISA`. [Online; Accessed September 2019].

[127] R. McFee. Optimum Input Leads for Cryogenic Apparatus. *Review of Scientific Instruments*, **30**(2):98, 1959.

[128] I. I. Rabi. A Method of Producing Uniform Magnetic Fields. *Review of Scientific Instruments*, **5**(2):78, 1934.

[129] D. Richter, J. D. Adam, D. Leroy, and L. R. Oberh. Strand coating for the superconducting cables of the lhc main magnets. *IEEE Transactions on Applied Superconductivity*, **9**(2):735, 1999.

[130] J. N. Rjabinin and L. W. Shubnikov. Magnetic Properties and Critical Currents of Supra-conducting Alloys. *Nature*, **135**:581, 1935.

[131] L. Rossi and L. Bottura. Superconducting magnets for particle accelerators. *Reviews of Accelerator Science and Technology*, **5**:51, 2012.

[132] ROXIE (Routine for the Optimization of magnet X-sections, Inverse field calculation and coil End design) programme package. URL `https://cern.ch/roxie`. [Online; Accessed September 2019]. CERN, 1211 Geneva 23, Switzerland.

[133] J. Royet and R. Scanlan. Manufacture of keystoned flat superconducting cables for use in SSC dipoles. *IEEE Transactions on Magnetics*, **23**(2):480, 1987.

[134] J. L. Rudeiros Fernandez, J. C. Perez, S. Ferradas Troitino, M. Guinchard, P. Grosclaude, M. Crouvizier, S. Langeslag, S. Izquierdo Bermudez, and F. Savary. Characterisation of the Mechanical Properties of Impregnated Nb_3Sn Coils. *IEEE Transactions on Applied Superconductivity*, **29**(5):1, 2019.

[135] S. Russenschuck. *Field Computation for Accelerator Magnet*. Wiley-VCH Verlag, Weinheim, Germany, 2010. ISBN 978-3527407699.

[136] C. Sanabria. *A new understanding of the heat treatment of Nb_3Sn superconducting wires*. PhD thesis, Florida State University, Tallahassee, Florida, USA, 2017.

[137] C. Sanabria, P. J. Lee, W. Starch, I. Pong, A. Vostner, M. C. Jewell, A. Devred, and D. C. Larbalestier. Evidence that filament fracture occurs in an ITER toroidal field conductor after cyclic Lorentz force loading in SULTAN. *Superconductor Science and Technology*, **25**(7):075007, 2012.

[138] F. Savary. WP11 in a nutshell – 11 T Dipoles. Internal note (EDMS no. 1559231), CERN, 1211 Geneva 23, Switzerland, 2015.

[139] F. Savary et al. Progress on the Development of the Nb_3Sn 11 T Dipole for the High Luminosity Upgrade of LHC. *IEEE Transactions on Applied Superconductivity*, **27**(4):1, 2017.

[140] C. Scheuerlein, M. Di Michiel, and A. Haibel. On the formation of voids in internal tin Nb_3Sn superconductors. *Applied Physics Letters*, **90**(13):132510, 2007.

[141] C. Scheuerlein, M. Di Michiel, and F. Buta. Synchrotron Radiation Techniques for the Characterization of Nb_3Sn Superconductors. *IEEE Transactions on Applied Superconductivity*, **19**(3):2653, 2009.

[142] C. Scheuerlein, M. Di Michiel, G. Arnau, R. Flükiger, F. Buta, I. Pong, L. Oberli, and L. Bottura. Coarse Nb_3Sn Grain Formation and Phase Evolution During the Reaction of a High Sn Content Internal Tin Strand. *IEEE Transactions on Applied Superconductivity*, **21**(3):2554, 2011.

[143] C. Scheuerlein, M. Di Michiel, M. Hofmann, M. Lorentzon, F. Lackner, R. Flükiger, F. Savary, and L. Bottura. Residual strain in the Nb_3Sn 11 T dipole magnet coils for HL-LHC. *Superconductor Science and Technology*, **30**(12):125002, 2017.

[144] C. Scheuerlein, F. Wolf, M. Lorentzon, and M. Hofmann. Direct measurement of Nb_3Sn filament loading strain and stress in accelerator magnet coil segments. *Superconductor Science and Technology*, **32**(4):045011, 2019.

[145] D. Schoerling et al. The 16 T Dipole Development Program for FCC and HE-LHC. *IEEE Transactions on Applied Superconductivity*, **29**(5):1, 2019.

[146] SciPy: Open source scientific tools for Python. URL `https://www.scipy.org`. [Online; Accessed September 2019].

[147] B. Seeber, A. Ferreira, V. Abacherli, T. Boutboul, L. Oberli, and R. Flükiger. Transport Properties up to 1000 A of Nb_3Sn Wires Under Transverse Compressive Stress. *IEEE Transactions on Applied Superconductivity*, **17**(2):2643, 2007.

[148] B. Seeber, A. Ferreira, F. Buta, C. Senatore, T. Boutboul, L. Oberli, and R. Flükiger. Transport Properties of a PIT-Nb_3Sn Strand Under Transverse Compressive and Axial Tensile Stress. *IEEE Transactions on Applied Superconductivity*, **18**(2):976, 2008.

[149] B. Seeber, C. Senatore, F. Buta, R. Flükiger, T. Boutboul, C. Scheuerlein, L. Oberli, and L. Rossi. Electromechanical behaviour of PIT Nb_3Sn wires for NED. *Proceedings - Workshop on Accelerator Magnet Superconductors, Design and Optimization, WAMSDO 2008*, page 37, 2009.

[150] C. Senatore. Electromechanical Properties of Technical Superconductors. Presented on the ESAS/EASITrain Summer School on Applied Superconductivity, Vienna, Austria, 2018. URL `https://indico.cern.ch/event/663949/timetable`. [Online; Accessed September 2019].

[151] C. Senatore, D. Uglietti, V. Abacherli, A. Junod, and R. Flükiger. Specific Heat, A Method to Determine the T_c Distribution in Industrial Nb_3Sn Wires Prepared by Various Techniques. *IEEE Transactions on Applied Superconductivity*, **17**(2):2611, 2007.

[152] R. S. Shankhachur, P. Potluri, S. Canfer, and G. Ellwood. Braiding ultrathin layer for insulation of superconducting Rutherford cables. *Journal of Industrial Textiles*, **46**(5):827, 2016.

[153] A. Shepelev and D. Larbalestier. The discovery of type II superconductors. *CERN Courier*, 51(9): 17, 2011. URL `https://cds.cern.ch/record/1734730`. [Online; Accessed September 2019].

[154] SHI Cryogenics Group, Daimlerweg 5a, 64293 Darmstadt, Germany. CH-210 10K Cryocooler Series. URL `http://www.shicryogenics.com/products/10k-cryocoolers/ch-210-10k-cryocooler-series`. [Online; Accessed September 2019].

[155] N. J. Simon, E. S. Drexler, and R. P. Reed. Properties of Copper and Copper Alloys at Cryogenic Temperature. *NIST Monograph*, **117**:7, 1991. URL `https://trc.nist.gov/cryogenics/materials/OFHCCopper/OFHC_Copper_rev1.htm`. [Online; Accessed September 2019].

[156] Z. J. J. Stekly and J. L. Zar. Stable superconducting coils. *IEEE Transactions on Nuclear Science*, **12**(3):367, 1965.

[157] M. D. Sumption, E. W. Collings, R. M. Scanlan, A. Nijhuis, and H. H. J. ten Kate. Core-suppressed AC loss and strand-moderated contact resistance in a Nb-Sn Rutherford cable. *Cryogenics*, **39**(1):1, 1999.

[158] Superconductivity Part 11: Residual resistance ratio measurement – Residual resistance ratio measurement of Nb_3Sn Composite Superconductors. *CEI/IEC 61788-11:2003*, 2003.

[159] Superconductivity Part 2: Critical Current Measurements – DC Critical Current of Nb_3Sn Composite Superconductors. *CEI/IEC 61788-2:2006*, 2006.

[160] C. Tarantini, C. Segal, Z. H. Sung, P. J. Lee, L. Oberli, A. Ballarino, L. Bottura, and D. C. Larbalestier. Composition and connectivity variability of the A15 phase in PIT Nb_3Sn wires. *Superconductor Science and Technology*, **28**(9):095001, 2015.

[161] B. ten Haken, A. Godeke, and H. H. J. ten Kate. The Influence of Compressive and Tensile Axial Strain on the Critical Properties of Nb_3Sn Conductors. *IEEE Transactions on Applied Superconductivity*, **5**(2):1909, 1995.

[162] B. ten Haken, A. Godeke, and H. H. J. ten Kate. The strain dependence of the critical properties of Nb_3Sn conductors. *Journal of Applied Physics*, **85**(6):3247, 1999.

[163] H. H. J. ten Kate, H. W. Weijers, and J. M. van Oort. Critical current degradation in Nb_3Sn cables under transverse pressure. *IEEE Transactions on Applied Superconductivity*, **3**(1):1334, 1993.

[164] The MathWorks Inc., Natick, USA. MATLAB R2017a. URL `https://www.mathworks.com`. [Online; Accessed September 2019].

[165] L. Thilly, C. Scheuerlein, U. Stuhr, B. Bordini, and B. Seeber. Residual Strain in a Nb_3Sn Strand Mounted on a Barrel for Critical Current Measurements. *IEEE Transactions on Applied Superconductivity*, **19**(3):2645, 2009.

[166] L. Thilly, M. Di Michiel, C. Scheuerlein, and B. Bordini. Nb_3Sn nucleation and growth in multifilament superconducting strands monitored by high resolution synchrotron diffraction during in situ reaction. *Applied Physics Letters*, **99**(12):122508, 2011.

[167] M. Tinkham. *Introduction to Superconductivity*. Dover Publications, Mineola, USA, 2004. ISBN 978-0486435039.

[168] D. Tommasini et al. The 16 T Dipole Development Program for FCC. *IEEE Transactions on Applied Superconductivity*, **27**(4):1, 2017.

[169] D. Tommasini et al. Status of the 16 T Dipole Development Program for a Future Hadron Collider. *IEEE Transactions on Applied Superconductivity*, **28**(3):1, 2018.

[170] D. Uglietti, B. Seeber, V. Abächerli, A. Pollini, D. Eckert, and R. Flükiger. A device for critical current versus strain measurements up to 1000 A and 17 T on 80 cm long HTS and LTS technical superconductors. *Superconductor Science and Technology*, **16**(9):1000, 2003.

[171] D. F. Valentinis, C. Berthod, B. Bordini, and L. Rossi. A theory of the strain-dependent critical field in Nb_3Sn, based on anharmonic phonon generation. *Superconductor Science and Technology*, **27**(2):025008, 2013.

[172] W. van de Camp. Critical Current versus Transverse Stress and Thermal Stability of a RRP Nb_3Sn Rutherford Cable. Master's thesis, University of Twente, Enschede, The Netherlands, 2012.

[173] D. van Delft and P. Kes. The discovery of superconductivity. *Physics Today*, **63**(9):38, 2010.

[174] J. van Nugteren et al. Powering of an HTS dipole insert-magnet operated standalone in helium gas between 5 and 85 K. *Superconductor Science and Technology*, **31**(6):065002, 2018.

[175] A. P. Verweij, J. Genest, A. Knezovic, D. F. Leroy, J. Marzolf, and L. R. Oberli. 1.9 K test facility for the reception of the superconducting cables for the LHC. *IEEE Transactions on Applied Superconductivity*, **9**(2):153, 1999.

[176] C. R. Walters, I. M. Davidson, and G. E. Tuck. Long sample high sensitivity critical current measurements under strain. *Cryogenics*, **26**(7):406, 1986.

[177] C. Warren, C. Young, and R. G. Budynas. *Roark's Formulas for Stress and Strain*. McGraw-Hill Education, New York, USA, 2001. ISBN 978-0070725423.

[178] P. Welch. The use of fast Fourier transform for the estimation of power spectra: A method based on time averaging over short, modified periodograms. *IEEE Transactions on Audio and Electroacoustics*, **15**(2):70, 1967.

[179] N. R. Werthamer, E. Helfand, and P. C. Hohenberg. Temperature and Purity Dependence of the Superconducting Critical Field, H_{c2}. III. Electron Spin and Spin-Orbit Effects. *Physical Review*, **147**:295, 1966.

[180] G. Willering. *Stability of Superconducting Rutherfordcables for accelerator magnets*. PhD thesis, University of Twente, Enschede, The Netherlands, 2009.

[181] M. N. Wilson. *Superconducting Magnets*. Clarendon Press Oxford, Oxford, UK, 1983. ISBN 978-0198548102.

[182] F. Wolf, P. Ebermann, F. Lackner, D. Mosbach, C. Scheuerlein, K. Schladitz, and D. Schoerling. Characterization of the stress distribution on Nb_3Sn Rutherford cables under transverse compression. *IEEE Transactions on Applied Superconductivity*, **28**(3):1, 2018.

[183] F. Wolf, F. Lackner, M. Hofmann, C. Scheuerlein, D. Schoerling, and D. Tommasini. Effect of epoxy volume fraction on the stiffness of Nb_3Sn Rutherford cable stacks. *IEEE Transactions on Applied Superconductivity*, **29**(5):1, 2019.

[184] C. Wyss. LEP Design Report. URL `https://cds.cern.ch/record/314187`. [Online; Accessed September 2019]. Report no. CERN-AC-96-01-LEP-2, CERN, 1211 Geneva 23, Switzerland, 1996.

[185] X. Xu, M. Sumption, X. Peng, and E. W. Collings. Refinement of Nb_3Sn grain size by the generation of ZrO2 precipitates in Nb_3Sn wires. *Applied Physics Letters*, **104**(8):082602, 2014.

[186] X. Xu, M. D. Sumption, and X. Peng. Internally Oxidized Nb_3Sn Strands with Fine Grain Size and High Critical Current Density. *Advanced Materials*, **27**(8):1346, 2015.

[187] Y. Zhai, L. D'Hauthuille, C. Barth, and C. Senatore. Finite-Element Analysis of Transverse Compressive and Thermal Loads on Nb_3Sn Wires With Voids. *IEEE Transactions on Applied Superconductivity*, **26**(4):1, 2016.

[188] C. Zhou, M. Dhallé, H. H. J. ten Kate, and A. Nijhuis. The Effect of Strain on the Transport Properties of Superconducting Strand and Cable in a Conduit Conductor. *IEEE Transactions on Applied Superconductivity*, **29**(1):1, 2019.